Quantitative Susceptibility Mapping in Human Brain: Short Echo Timing, Thin Slab, and Non-harmonized Multisite Applications

by

Nashwan Ameen Mohammed Naji

A thesis submitted in partial fulfillment of the requirements for the degree of

Doctor of Philosophy

Department of Biomedical Engineering
University of Alberta

Abstract

Quantifying tissue magnetic susceptibility provides a non-invasive way to monitor iron and myelin abnormalities associated with several neurodegenerative diseases. Quantitative susceptibility mapping (QSM) is a post-processing technique that retrieves the susceptibility distribution from the phase of T_2*-sensitive magnetic resonance (MR) images, providing localized and discriminative contrast of the underlying sources. QSM is typically obtained from a three-dimensional (3D) multi-echo gradient-echo sequence, though it can also be produced from single-echo sequences such as echo-planar imaging with some sacrifice on resolution and/or quality of the resultant map.

QSM methodology has improved notably over the last decade addressing several technical challenges. However, it is still not commonly included in clinical protocols, mostly due to the burden of its lengthy acquisition time. Moreover, even focal acquisitions require extended 3D coverage beyond the region of interest, that otherwise might be imaged in a few slices. This acquisition burden becomes much heavier when exploring higher spatial resolution. Furthermore, QSM multisite reproducibility has been studied mainly under the assumption that the parameters of the imaging sequence are fixed and replicable, which does not consider possible sequence variations typically found in large-scale multisite studies. Using in-vivo and simulated MR data of human brain, this thesis investigates the above-mentioned limitations and introduces new approaches to further facilitate QSM integration into clinical applications. To minimize the acquisition burden, producing QSM from 3D magnetization-prepared rapid gradient-echo (MPRAGE) phase data was proposed and possible applications were explored. In addition, a new method was introduced to allow QSM from thin slabs aided by a rapid low-resolution scan.

Furthermore, QSM multisite reproducibility was investigated in the presence of sequence variations.

The MPRAGE sequence is widely used in clinical studies to segment gray and white matter regions. Only MPRAGE magnitude is utilized for segmentation and its phase is abandoned. In Chapter 2, producing QSM from the MPRAGE phase was introduced and investigated, and possible applications were explored. Despite the limited contrast at 3T and very-short echo time (TE), MPRAGE-QSM was found useful for improving segmentation of iron-rich regions and roughly quantifying their susceptibility. Thus, producing MPRAGE-QSM adds value to volumetric studies at no additional cost. Also, the quality of MPRAGE-QSM can be improved notably if extending TE to 4.4 ms at 3T is tolerable.

Another important application of MPRAGE-QSM is assessing the load of cerebral microbleeds (CMBs) without adding an extra sequence (dedicated to QSM) to the imaging protocol. Being mainly hemosiderin deposits, CMBs introduce strong contrast on QSM within a few milliseconds of echo time. Utilizing MPRAGE-QSM for quantifying microbleeds was explored in Chapter 3 and the results showed that it is promising at field strength of 3T and above.

In Chapter 4, a new method is proposed to accelerate QSM data acquisition by allowing QSM from thin slabs. To achieve this, a rapid low-resolution scan with wider coverage is used to roughly inform the reconstruction algorithm of the expected susceptibility distribution outside the imaged slab. Compared to the standard approach, simulation and in-vivo results showed that applying the new method improved QSM measurements from as few as 8 slices with aid from low-resolution data of at most 4-times larger voxel dimensions, potentially allowing up to 7-fold reduction in acquisition time.

Studying QSM reproducibility with non-harmonized sequence parameters is an important step toward clinical integration as matching sequence specification in each site is not always possible due to hardware and/or software limitations. In Chapter 5, QSM and R_2* reproducibility were studied using 24 subjects who travelled between three sites and were scanned using 3T scanners from two vendors. Each site optimized the sequence parameters independently. Cross-site and within-site measurements for QSM and R_2* were found to be reproducible and highly correlated. Certain post-processing choices for QSM helped in reducing cross-site variability, such as excluding less reliable regions, matching spatial resolution and echo-timings, and minimizing streaking artifacts.

To conclude, this thesis proposed new methods to minimize the time burden of including QSM in clinical protocols by utilizing phase from a common MPRAGE volumetric acquisition to examine iron-rich regions and microbleeds, or by speeding up focal QSM acquisitions. In addition, QSM multisite reproducibility was examined when the acquisition sequence is not harmonized, and insights were provided on reducing the effects of cross-site variations via post-processing techniques.

Preface

All control and patient subjects included in this thesis provided informed consent after the internal Institutional Review Board approved the study design. For all the published and unpublished chapters in this thesis, Dr. Alan Wilman (supervisor) shared unique ideas, helpful discussion, and careful editing of the manuscripts. In all cases, first drafts were written by the author.

The second chapter of this thesis has been published: Naji N, Sun H, and Wilman AH. On the value of QSM from MPRAGE for segmenting and quantifying iron-rich deep gray matter. Magnetic Resonance in Medicine. 2020; 84(3):1486–1500. All simulations, reconstructions and analyses of this work were performed by the author. The manuscript was proofread by Hongfu Sun, who helped strengthen the content.

Some of the results of the third chapter were presented as an abstract: Naji N, Gee M, Jickling GC, Camicioli R, and Wilman AH. Quantifying Cerebral Microbleeds using MPRAGE-based QSM. ISMRM 28th Annual Meeting & Exhibition, online, 2020: abstract #1760. All simulations, reconstructions and analyses of this work were performed by the author. All co-authors contributed to abstract edits.

Some of the results of the fourth chapter were presented as an abstract: Naji N and Wilman AH. Towards fast single-slice QSM: Challenges and possible solutions. ISMRM 31st Annual Meeting & Exhibition, London, UK, 2022: abstract #3559. The method was invented by the author, who performed all simulations, experiment design and reconstructions.

The fifth chapter has been published: Naji N, Lauzon ML, Seres P, Stolz E, Frayne R, Lebel C, Beaulieu C, Wilman AH. Multisite reproducibility of quantitative susceptibility mapping and effective transverse relaxation rate in deep gray matter at 3 T using locally optimized sequences in 24 traveling heads. NMR in Biomedicine. 2022; 35(11):e4788. All reconstructions and analyses were conducted by the author. Michel Louis Lauzon provided technical information for GE scanners and insightful discussions to improve the manuscript. Other co-authors contributed to improving the manuscript.

All MRI sequences were standard provided by the manufacturers. MPRAGE phase images were saved by Peter Šereš, who has also carried out all MRI acquisitions for the volunteer subjects included in chapters 2 and 4. In-vivo patients included in Chapter 3 were from research studies of

Dr. Richard Camicioli and Dr. Eric Smith. In-vivo data of chapters 2 and 5 were part of the Alberta 300 study of Dr. Christian Beaulieu. For susceptibility mapping, processing codes used in chapters 2 and 3 were inherited from past graduate student Hongfu Sun. For chapters 4 and 5, mapping codes included functions from publicly available toolboxes: MEDI toolbox (6 November 2017 release) and STI Suite v3. All mapping reconstructions were performed by the author.

Acknowledgements

My PhD journey could not have been accomplished without the help and support of many people, and I would like to thank them all for their invaluable efforts and time. First, words cannot express my gratitude to my supervisor, Dr. Alan Wilman, who was always supportive and understanding. His guidance and insightful feedback carried me through all the phases of this research work. I feel fortunate to have him as my supervisor.

I would like to thank my committee members, Dr. Nicola De Zanche and Dr. Richard Thompson, for their valuable feedback and suggestions. I am thankful also to my examiners Dr. Ferdinand Schweser, Dr. Christian Beaulieu, and the exam chair Dr. Nikolai Malykhin, who shared scientific ideas about my research work and helped me broadening my horizons.

Special thanks are due to Peter Šereš who was an unfailing source of support and technical knowledge throughout my studies and MRI experiments. I would also like to thank Dr. Jeff Snyder, past and current lab members for their insightful feedback and help with MRI scans. To all my friends back home and abroad, I wanted to take a moment to thank you for your continued support and encouragement. I am very lucky to have such caring people surrounding me.

Finally, my deepest gratitude and thanks are due to my family: my parents, brothers, sisters and wife, for providing me infinite and continuous support, love and care throughout this journey. I love you so much!

Table of Contents

List of Tables

List of Figures

Chapter 1: Introduction

1.1 MAGNETIC RESONANCE IMAGING (MRI)

Magnetic resonance imaging (MRI) is a noninvasive imaging modality that is capable of creating high-resolution three-dimensional (3D) images of human soft tissue with great contrast, providing anatomical and/or functional information. A powerful feature of MRI is that its acquisition parameters can be tuned to emphasize different tissue properties and add complementary information that are useful for diagnosis. Furthermore, these qualitative images can be transformed into quantitative maps and used to facilitate tracing and recognizing age- and/or pathology-related changes.

MRI emerged from a physical phenomenon known as nuclear magnetic resonance (NMR), in which atoms nuclei excited under an applied external field respond by emitting unique signals reflecting their magnetic and chemical environments (1). NMR was first utilized to produce unique spectra to identify and explore structures of complex molecules (2), and then applications evolved into 2D and 3D spatial imaging through a series of technical advances that received multiple Nobel prizes (3). Although MRI can be tuned to different atoms, it mainly relies on signals from hydrogen (^{1}H) atoms, exploiting the abundance of water molecules in the human body.

MRI applications grew rapidly and so the related literature (4–17), and its basics have been explained in several textbooks (2,18–20). The aim of this section is to introduce the basic concepts touched in this thesis, more specifically: signal formation and acquisition, and the factors affecting MR signal.

1.1.1 Signal Formation and Acquisition

Creating an MR signal that can be received and resolved into an image in the spatial domain undergoes through three preparation steps that will be described briefly in this subsection. But first, the source of this signal needs to be explained. Zooming into the nuclear level, both protons and neutrons have an intrinsic magnetic moment known as "spin", but each pair of similar type have opposite magnetic moment in the nucleus. Therefore, only if at least one of these subatomic particles has an odd number, the nucleus will have a net magnetic moment (m in A·m^2) with a random orientation, and this net moment can be modulated to produce a measurable signal (20,21).

In human imaging applications, this signal comes mainly from the hydrogen nuclei in water molecules, as each nucleus has only one proton and thus nonzero magnetic moment.

1.1.1.1 Polarization

The first step required in producing a meaningful signal that can be detected is exposing the object of interest to an external static field (B_0 in T), which will exert a torque upon the spins trying to align them along its direction. The result of this interaction and conservation of angular momentum causes spin precession around B_0 direction (conventionally z-axis). The precession frequency (f_0 in Hz, also called Larmor frequency) is proportionally related to the static field strength with a nucleus-specific constant called gyromagnetic ratio (γ in Hz/T):

$$f_0 = \gamma B_0 \tag{1.1}$$

For hydrogen, γ is 42.6 MHz/T. The effect of applying the external field is known as magnetization resulting in a non-zero net magnetic moment over a defined spatial coverage (i.e., voxel at $\vec{r}$ location) along B_0 direction referred to as bulk magnetization (M_0 in A/m) and estimated as (18):

$$M_0(\vec{r}) = \frac{\gamma^2\, \hbar^2\, B_0}{4\, K\, T} N\,(\vec{r}) \tag{1.2}$$

where $\hbar$ is Planck's constant (in J·s), N is the spin density (in m^{-3}), K is Boltzmann's constant (in J/K), and T is the absolute temperature (in K). Thus, M_0 magnitude becomes larger at higher field strength, higher spin density, or lower temperature. In human imaging applications, increasing M_0 is feasible only through using higher B_0, and fortunately spin density is sufficient in most tissues due to the abundance of water molecules.

1.1.1.2 Excitation

Spin alignment is not sufficient to produce detectable signal; energy is needed to perturb M_0 from its equilibrium state along z-axis. Thus, radio frequency (RF) energy at the Larmor frequency is applied via coils to excite the spins and rotate M_0 toward the transverse plane. This RF signal applied for a brief duration is known as RF pulse and it creates a magnetic field that is called B_1. The RF pulse shape and duration can be tailored to rotate M_0 by a specified angle (called tip or flip angle) (18). After the pulse terminates, magnetization starts the relaxation process toward equilibrium and an RF signal is produced that is detectable using an RF coil. However, the RF coil detects signals from all the excited region and a mechanism to encode the spatial locations of the signals is needed to separate them after receiving.

1.1.1.3 Spatial Encoding

Spatial encoding is achieved using three orthogonal gradient fields ($\vec{G} = (G_x, G_y, , G_z)$ in T/m) that make the frequency of the signals location-dependent: $f(\vec{r}) = f_0 + \gamma\, \vec{G} \cdot \vec{r}$. The gradient fields are applied as pulses whose shape and duration modulate the frequencies of the emitted MR signals (2). For simplicity, here we call encoding along z-axis, y-axis and x-axis as slice encoding, frequency encoding and phase encoding, respectively. The result of applying these gradient fields is that the received signal is spread in the spatial frequency domain (called k-space) and thus can be inverted into the spatial domain using Fourier transformation.

Applied spatial encoding gradients and RF pulses are summarized in a timing diagram known as pulse sequence, which describes the shape, width and timing of the applied pulses and the window in which the MR signal is collected. **Figure 1.1** illustrates two common pulse sequences known as multi-echo gradient-echo (MEGE) and magnetization-prepared rapid gradient-echo (MPRAGE), which are the main sequences used in this thesis. In MPRAGE, a series of single-echo gradient-echo acquisitions are collected after an inversion RF pulse to increase the contrast between gray and white matter regions.

1.1.1.4 Signal Detection

The precession of transverse magnetization generates a changing flux, which induces electromotive force in the receiving coils. This received signal can be expressed as (18):

$$S(\vec{k}) = C \int M(\vec{r})\, e^{-i2\pi \vec{k}\cdot\vec{r}}\, d\vec{r} \qquad (1.3)$$

where $S(\vec{k})$ is the received complex-valued signal at location $\vec{k}$ in k-space, C is a constant, and $M(\vec{r})$ is the complex-valued MR signal at location $\vec{r}$ in image space. The magnitude and phase of the MR signal are conventionally viewed as separate images, and each of them is affected by multiple factors, and thus can be used to probe different tissue properties. Some of these contributing factors are discussed in the following subsection.

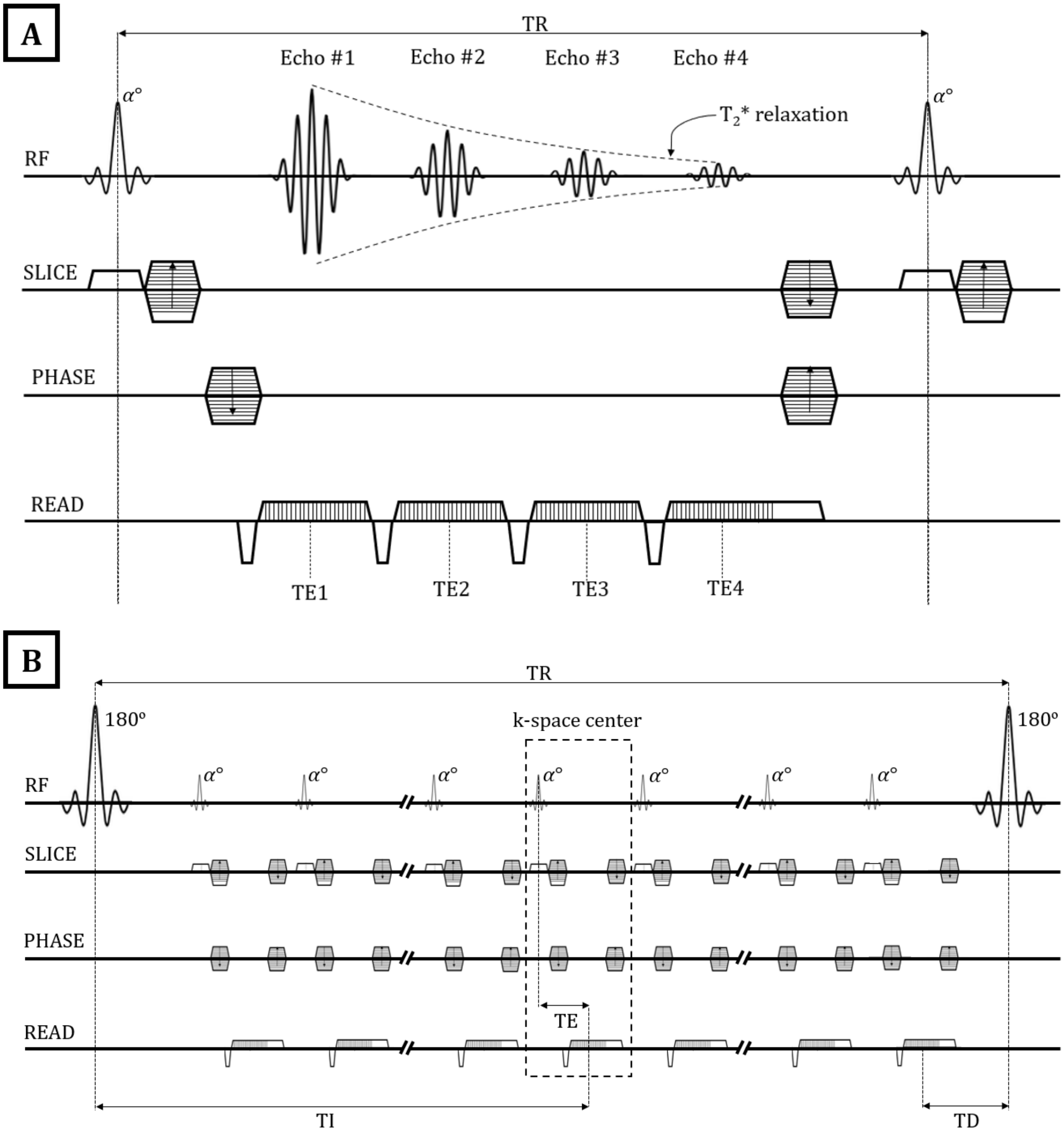

Figure 1.1: *Pulse sequence diagrams are shown for A) 3D multi-echo gradient echo (MEGE), and B) 3D magnetization-prepared rapid gradient-echo (MPRAGE). In the shown MEGE, four echoes are collected using monopolar readouts, and their magnitude signals are weighted by* T_2* *relaxation. α: flip angle, TR: repetition time, TE: echo time, TI: inversion time, TD: delay time.*

1.1.2 **Factors Impacting MR Signal**

Multiple factors can influence the content of the collected MR signal: some of them are intrinsic properties of the tissues, while others are related to the hardware used or the positioning of the imaged object. Here we review some of the main contributors to the MR signal.

1.1.2.1 Relaxation

Relaxation refers to the process in which a produced MR signal is attenuated exponentially with time until vanishing. There are two simultaneous relaxation processes that affect MR signal: 1) a longitudinal relaxation that the magnetization undergoes to recover to its equilibrium state (M_0), which is characterized by a time constant known as T_1 (in s); and 2) a transverse relaxation that happens as the transverse component decays as the magnetization loses its coherence, and it is characterized by another time constant called T_2. Relaxation rate is the inverse of the relaxation time constant (i.e., $R_2 = 1/T_2$ in s^{-1}) and both are used interchangeably to describe and quantify the decay in the collected MR signal.

Both relaxation processes result from spins interacting with each other intra- and inter-molecularly, as each spin acts as a magnetic dipole with its own magnetic field, which affects other spins in its vicinity. The net effect on the surroundings will vary from spin to spin depending on several factors, including the distance and the angle between them, and their relative rates of mobility (18,22). Thus, the relaxation processes are dependent on the spin environment and give insights about the tissue structure. In dense environments (like solids) where spin motion is restricted and slow, individual spin fields fluctuate less frequently and affect the net static field seen by nearby spins, causing them to precess at different frequencies, lose their coherence, and thus accelerate their transverse relaxation (shorter T_2). When spins are more free to move (like in fluids), their individual fields fluctuate more rapidly and the change in the net seen static field is reduced and thus longer T_2 is needed for transverse relaxation. Conversely, the longitudinal relaxation (T_1) is accelerated by the individual spin fields that are perpendicular to the static field and fluctuating near the Larmor frequency, allowing the release of the absorbed RF energy to the lattice of nearby molecules.

Relaxation processes are sensitive also to other factors such as the strength of the static field, the presence of inhomogeneities in the static field, and/or the presence of atoms or molecules with unpaired electrons, which change the net field experienced by spins. These factors are discussed in more detail in the following two subsections.

1.1.2.2 Static Field Strength and Homogeneity

Because Larmor frequency is proportional to the strength of the applied static field (equation (1.1)), a change in the field strength affects the longitudinal relaxation. Tissue spectral density decreases with frequency, thus at higher B_0 fewer perpendicular spin fields would fluctuate at the corresponding Larmor frequency, causing the T_1 to increase (23). By contrast, the transverse relaxation is less affected by the change in field strength, as T_2 is influenced the most by slow, near-zero-frequency fluctuating dipole fields.

Inhomogeneities in the applied static field are expected due to quality limitations in the underlying magnet hardware, as well as due to local perturbation of the field by interfaces between biological tissues (i.e., differences in magnetic susceptibility and/or chemical composition discussed later). These imperfections induce additional dephasing between spins and accelerate the transverse relaxation, increasing the effective transverse relaxation rate (R_2^*):

$$R_2^* = R_2 + R_2' \tag{1.4}$$

where R_2' characterizes the additional relaxation due to the static field inhomogeneities (19). However, since these inhomogeneities do not fluctuate with time, their effect can be reversed using refocusing (180°) RF pulses as in spin-echo based sequences.

In addition to the effects on relaxations, increasing B_0 strength improves the signal-to-noise ratio (SNR) of the received MR signal (as the magnitude of the net magnetization increases, equation (1.2)) and enables exploring higher spatial resolution. Inhomogeneities in the applied field can also affect the encoding of the signal and introduce geometrical distortions in the obtained images.

1.1.2.3 Magnetic Susceptibility:

Different materials become magnetized differently under a static magnetic field depending on their atomic structure. This reaction of materials to the applied external field is characterized and quantified by a property known as magnetic susceptibility (χ). Several mechanisms are involved in the response of a material to the applied B_0 field: some of them result in a negative field that opposes B_0 (called diamagnetism), such as the responses from affected orbital motion of electrons, and affected motion of conduction electrons, while others result in a positive field that adds to B_0

(called paramagnetism), mainly from unpaired electrons and conduction electrons (24). Mathematically, magnetic susceptibility in anisotropic medium can be expressed as:

$$\chi_{ij} = \mu_{ij}\frac{M_i}{B_j} = \mu_0(1+\chi_{ij})\frac{M_i}{B_j} \tag{1.5}$$

where μ_{ij} and μ_0 is the permeability of a given material and vacuum respectively, and $i, j = x, y, z$. Given that the susceptibility range in human tissues is within 10^{-5} (i.e., $|\chi| \ll 1$, see **Figure 1.2**), equation (1.5) can be simplified to:

$$\chi_{ij} = \mu_0\frac{M_i}{B_j} \tag{1.6}$$

Under isotropic assumption, the induced magnetization due to susceptibility aligns with the static field, and equation (1.6) simplifies to: $M = \chi B_0/\mu_0$. Susceptibility can change slightly with temperature and/or frequency, however these changes are negligible in human MR imaging applications (24).

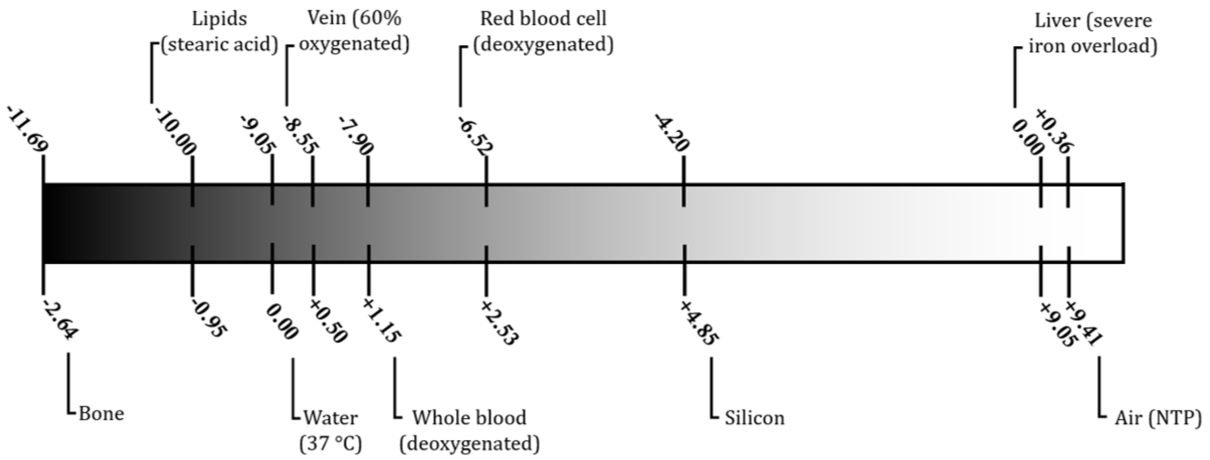

Figure 1.2: *Spectrum of magnetic susceptibility values [in ppm] relevant to biological tissues. The upper scale shows absolute values, while the bottom scale shows relative values referenced to water. Reported values are from* (24,25)*. NTP: Normal temperature and pressure.*

Water at body temperature (37° C) has a diamagnetic susceptibility of -9.05 parts per million (ppm) and most tissues have χ close to water due to the high water content. Lipids and bones are also diamagnetic but slightly more than water (**Figure 1.2**). Transitional metals such as copper, manganese, cobalt and iron are paramagnetic, but need to be highly concentrated to shift tissue susceptibility from water dominance. Out of these, iron is the most abundant and can be found concentrated in specific tissues that allows its effect on susceptibility to be measurable. Iron can be found mainly in blood as hemoglobin, and in basal ganglia, liver and spleen as ferritin and hemosiderin (25). Iron can shift χ by 1.15 ppm in deoxygenated blood, and by several ppm in overloaded tissues. This shift in susceptibility is the main source of contrast in functional MRI (16) and susceptibility weighted imaging (SWI) (13). Myelin change can also cause a measurable shift in susceptibility, as the relative size of the water compartment within myelin wraps to that in interstitial space changes. The levels of iron and myelin change through lifespan (26–28) and with disease progression (29–33), and MRI techniques provide an opportunity to measure these changes noninvasively.

1.1.2.4 Orientation

Molecular movement within some structures is restricted to specific directions such as in white matter fiber bundles (i.e., axons). This anisotropy affects the generated MR signal and causes it to vary depending on the angle between the fibers and the direction of B_0 (**Figure 1.3**). In white matter, both R_2* relaxation and susceptibility are sensitive to the head orientation with respect to B_0 direction (14,34,35).

1.1.2.5 Motion

Subject movement during MR signal acquisition translates into inaccurate measurement of signal within voxels, as spatial encoding assumes a stationary location for each voxel and when a movement occurs the registered signal to a specific voxel might be collected from multiple locations (**Figure 1.4**). This unwanted motion includes eye movement and respiration, and causes artifacts in the obtained MR images. Respiration can also affect the background field due to the changing air volume in the lungs.

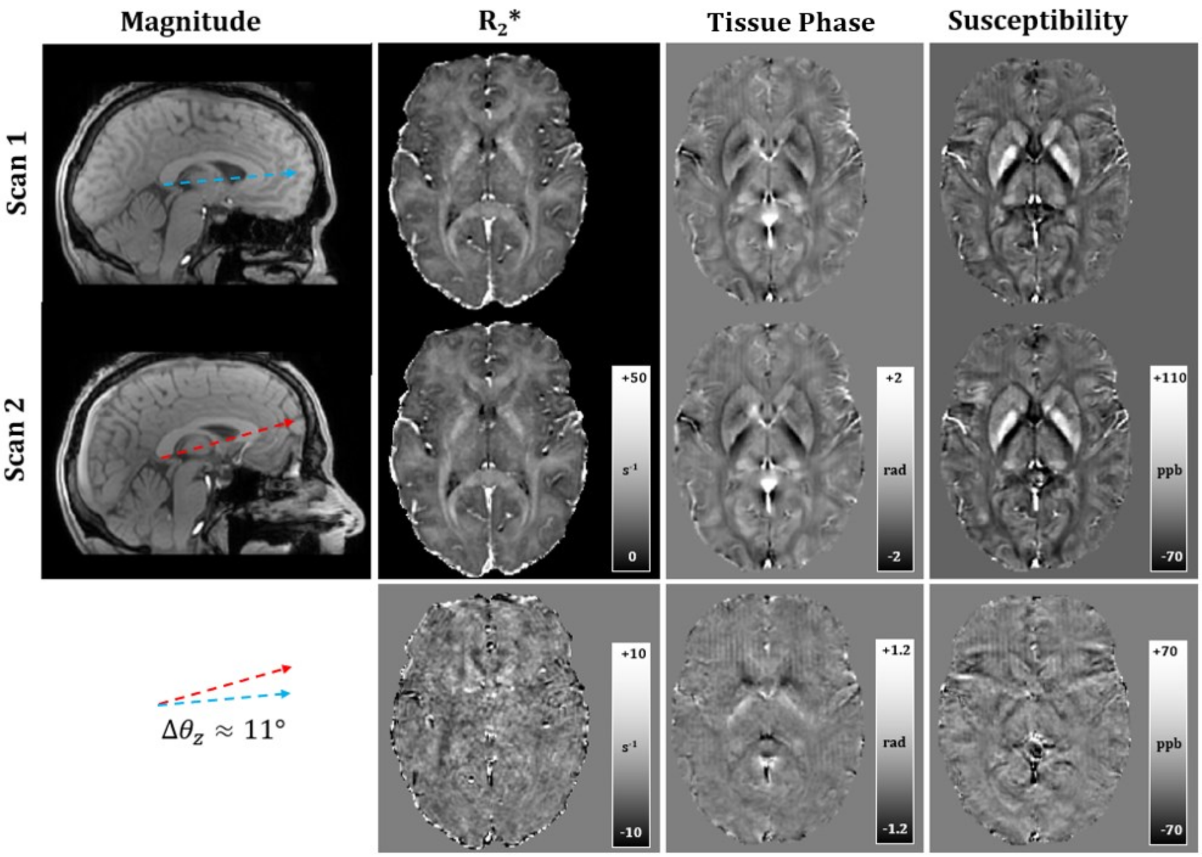

***Figure 1.3:** Orientation effects: A difference in head tilt of 11° with respect to B_0 direction between scans introduces noticeable variations in R_2*, tissue phase shift, and susceptibility maps.*

Advanced techniques can be employed to trace and minimize motion effects, including the use of a navigation echo that tracks the motion in the phase of an additional echo dedicated for tracking and without the need for external hardware (36), or a camera that captures the movement of a marker fixed on the subject (37).

1.2 R_2* RELAXATION MAPPING

R_2* relaxation is one tool to probe iron accumulation in biological tissue. Relying on the iron effect on nearby water molecules, iron concentration can be estimated indirectly by quantifying the change in R_2* relaxation. However, R_2* contains a relaxation component from other mechanisms (i.e., R_2, see equation (1.4)) and thus a change in R_2* might not be merely due to iron. Thus, R_2' is typically sought for better specificity but at the expense of a longer custom data acquisition (38).

In addition, R_2* fails to differentiate between paramagnetic and diamagnetic source-related changes. Also, a change caused by iron on the R_2* map can extend beyond its location, causing what is known as blooming artifacts. Despite limitations, R_2* mapping has demonstrated strong correlation with iron in a postmortem validation (39) and high reproducibility (40–42), and has been used in several aging (26,28,43–47), longitudinal (48,49) and pathological studies (32,33,49–51).

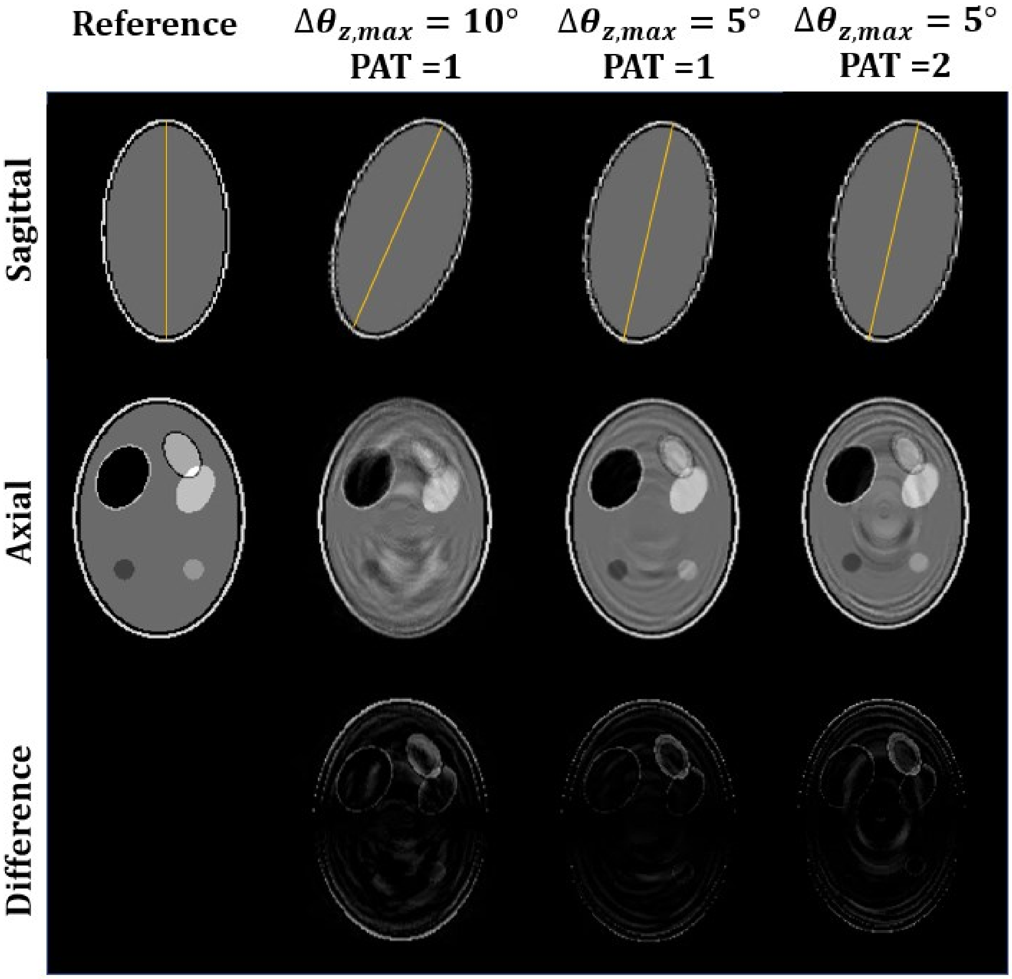

Figure 1.4: *Motion artifacts: A simulation of motion induced artifacts using numerical head phantom. The head is tilted forward and then backward by* $\Delta\theta_{z,max}$ *within each full respiration cycle of 3 seconds. The matrix size is 216×216×88 and TR is 40 ms. Without acceleration (i.e., parallel acquisition technique [PAT] = 1), the total acquisition time is 12.6 mins.*

R_2* relaxation is modelled as a simple mono-exponential (single pool) decay of the MR magnitude:

$$A(TE) = A(0)\exp(-TE \cdot R_2^*) \tag{1.7}$$

With multiple magnitude values acquired at different TE points using MEGE pulse sequence, equation (1.7) can be fitted to retrieve the R_2^* value at each voxel. This model fits sufficiently well most regions in the brain but might deviate in white matter regions due to multi-component relaxation that a single pool model cannot fit.

In the presence of macroscopic field inhomogeneities, magnitude signal might experience additional decay and thus has to be pre-corrected for accurate estimation of R_2^*. The additional decay can be expressed as a sinc term for each direction (52):

$$A(TE) = A(0)\exp(-TE \cdot R_2^*) \cdot sinc\left(\frac{\Delta\omega_{0x}}{2}TE\right) \cdot sinc\left(\frac{\Delta\omega_{0y}}{2}TE\right) \cdot sinc\left(\frac{\Delta\omega_{0z}}{2}TE\right) \tag{1.8}$$

where $\Delta\omega_0$ is computed using the field map (obtained from the phase of the first two echoes) gradient along each direction. These correction terms are typically applied to the magnitude images prior to fitting.

1.3 QUANTITATIVE SUSCEPTIBILITY MAPPING (QSM)

The effect of magnetic susceptibility is more pronounced on the phase of MR signal than on the magnitude part. This improved contrast was exploited in susceptibility weighted imaging (SWI) to enhance veins and iron-related contrast. In SWI, the phase is filtered and mapped into a mask with values ranging between 0 and 1 and then multiplied by the magnitude counterpart (13). However, MR phase captures the dipole effect of the underlying susceptibility sources and thus provides non-localized orientation-dependent information. Quantitative susceptibility mapping (QSM) aims to recover the underlying susceptibility distribution by solving the inverse relation between susceptibility-induced phase shift and susceptibility sources (53–55). Theoretically, QSM requires only the phase information, but practically magnitude information is typically used to define the volume of interest (VOI), estimate regions of low SNR, and as prior knowledge of edge information. QSM is typically obtained from a T_2*-weighted multi-echo sequence such as MEGE, and can be also obtained from single echo sequences such as SWI and single-shot echo-planar imaging (EPI) (56).

Compared to R_2*, QSM is able to visualize local susceptibility sources and specify which of these are paramagnetic or diamagnetic. The forward model that relates the phase shift ($\emptyset$) to the underlying susceptibility (χ) can be expressed as (57,58):

$$\emptyset(\vec{r}) = 2\pi\, \gamma\, B_0\, TE\, (d(\vec{r}) * \chi(\vec{r})) \tag{1.9}$$

where "$*$" refers to the convolution process between the susceptibility source and a unit magnetic dipole response (d) expressed as (59):

$$d(\vec{r}) = FT^{-1}\left\{\frac{1}{3} - \frac{k_p^2}{\vec{k}^2}\right\} = \frac{3\cos^2\theta - 1}{4\pi \cdot |\vec{r}|^3} \tag{1.10}$$

where FT refers to Fourier transform, $\vec{k}$ is the coordinate vector in the k-space, k_p is the projection of $\vec{k}$ into $\overrightarrow{B_0}$, and θ is the angle with respect to $\overrightarrow{B_0}$. The convolution in (1.9) is the reason behind the scattered effect on the phase and it highlights the 3D nature of the relation between the susceptibility and the resultant phase shift. In other words, solving the inverse relation requires extended phase information beyond the region of interest (ROI). Therefore, converting phase shift images into susceptibility maps is not a straightforward process and involves more processing steps, which are discussed in detail in the following subsections. **Figure 1.5** illustrates the main processing steps involved in performing QSM.

1.3.1 Coil Combination

New MRI systems utilize multi-channel receive coils to maximize coverage and SNR. Images from individual coils are then typically combined into a single image of higher SNR. For the magnitude part, a standard "root sum of squares (RSS)" provides sufficient quality. However for the phase part, care must be taken to avoid unresolvable phase wraps called open-ended fringelines. The choice would depend on the availability of a reference scan or multi-echo data (60). In this thesis, adaptive combination (61) was used for Siemens scanner data and sensitivity-based combination (Array coil Spatial Sensitivity Encoding Technique [ASSET]) for GE scanners data.

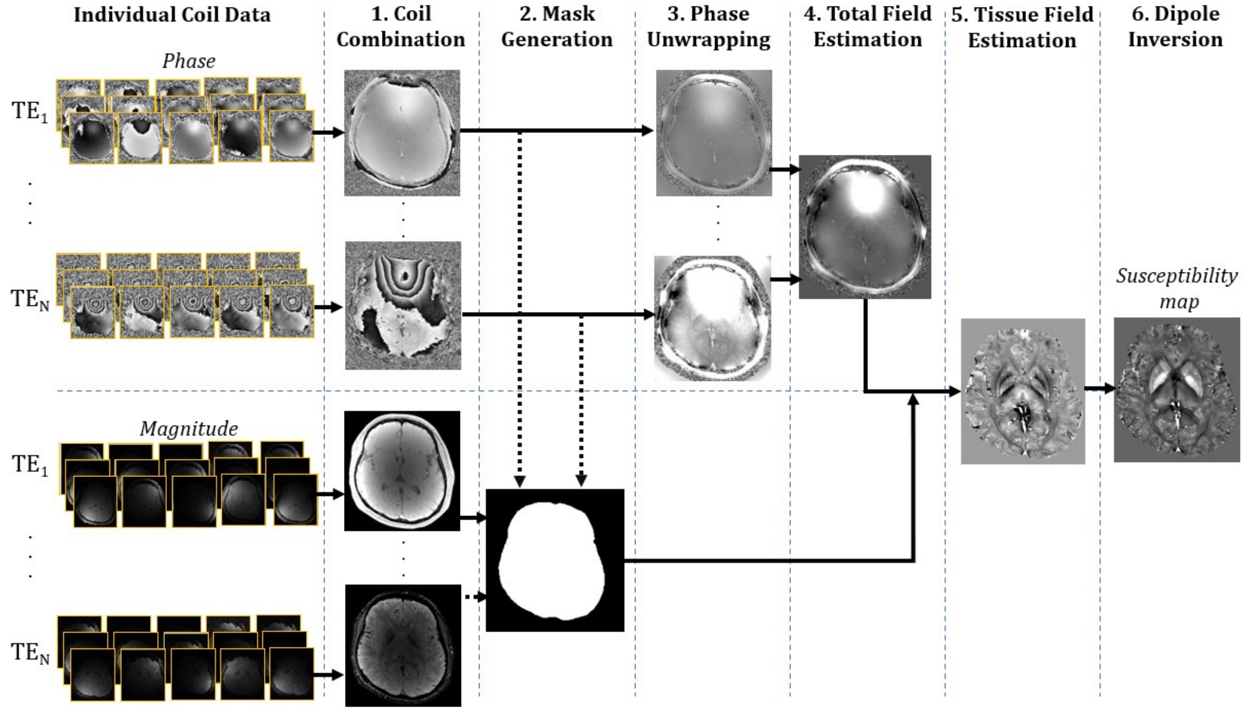

***Figure 1.5:** A flowchart of the standard QSM processing pipeline from the data of individual coils. Arrows with dashed lines represent optional data that might be used to improve the mask creation process by excluding less reliable voxels.*

1.3.2 **Mask Generation**

Since QSM is a 3D inverse convolution problem, mask generation plays a crucial role in defining the boundaries between internal and external susceptibility sources, defining the phase shift voxels involved in the convolution, and removing less reliable voxels of low SNR. Therefore, a small error or change in the mask definition would propagate to the final susceptibility map and affect much bigger volume (**Figure 1.6**). A mask is typically generated from the magnitude of the first echo in MEGE data, and then refined in an additional step to exclude less reliable regions based on magnitude and/or phase information of subsequent echoes (62,63). Alternatively, the magnitude of a later echo can be used to form the mask and remove less reliable regions simultaneously. This becomes useful also if the data contains multiple protocols of different flip angles and TRs, which results in varying and inconsistent magnitude contrast at TE_1. Also, a separate mask for each echo can be generated, based on magnitude and/or phase information.

For brain imaging applications, the mask can be automatically generated using toolboxes such as brain extraction tool (BET) of the FSL package (64), or formed by combining white and gray matter segmentations obtained using segmentation toolboxes such as the statistical parametric mapping (SPM) package (65). Outside the brain, masks are usually formed via thresholding and a series of binary morphological operations that vary depending on the ROI. Overall, automated mask generation works reliably in healthy subjects, but might require tuning and/or manual intervention in the presence of abnormal shape or contrast due to pathological situation (e.g., hemorrhage).

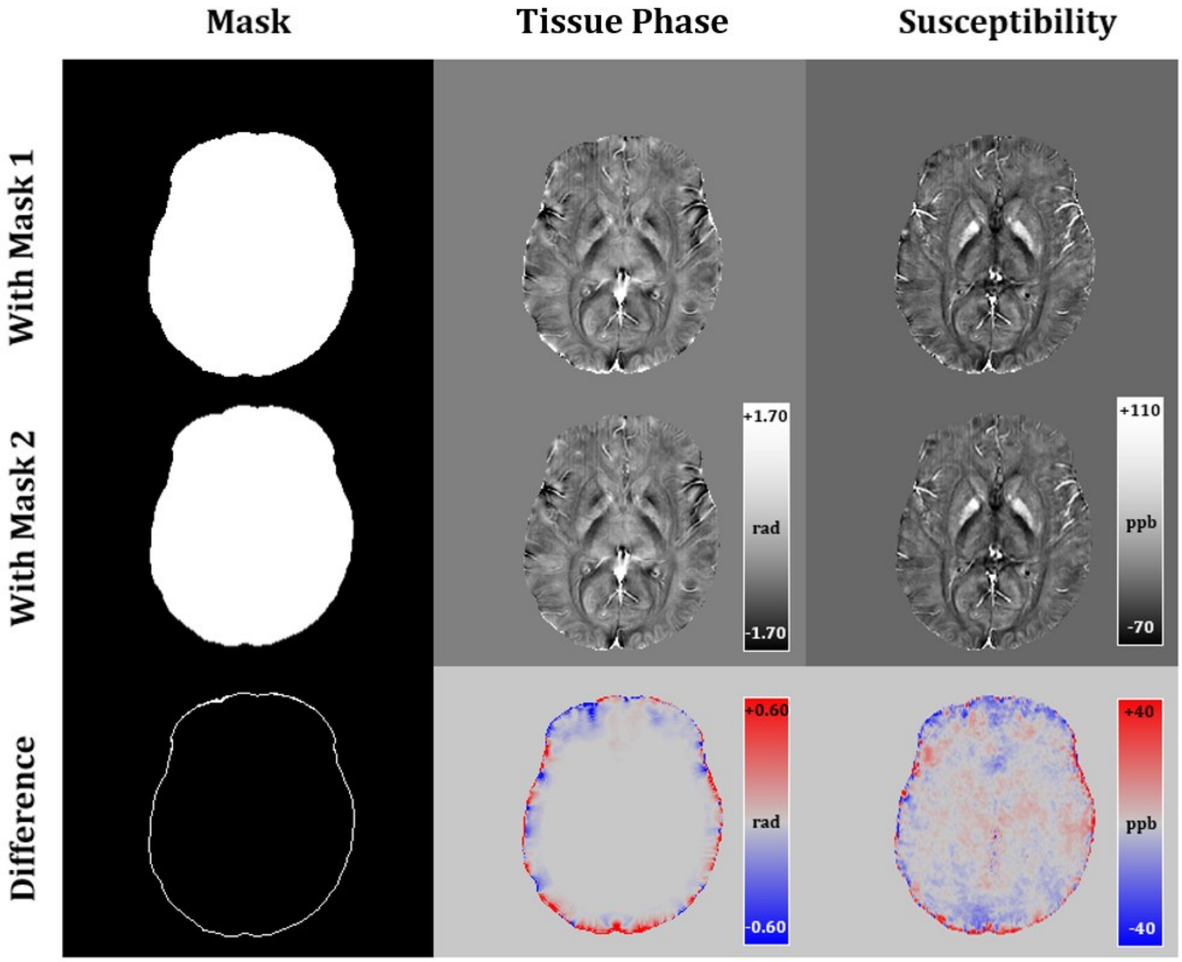

Figure 1.6*: An illustration of the mask effect on obtained tissue phase shift and susceptibility map. Eroding the mask by one voxel would further attenuate the tissue phase near the volume edges but cause no observable difference further away from the edges. However, the effect on the final susceptibility map is more global and distributed over all the volume, and is not confined near the edges.*

1.3.3 **Phase Unwrapping**

When phase information is extracted from the complex MR images, the values are confined in the range [-π, +π] creating phase wraps that should be resolved prior to any further processing. To start the unwrapping process, one or more reference points (called seed points) are required, which can be chosen manually or automatically depending on the used algorithm. Several phase unwrapping algorithms exist in the literature, each with its own merits and demerits. Few of these algorithms are listed in **Table 1.1** for illustration and not as an exclusive list. In terms of accuracy, the PRELUDE algorithm (66) is considered as the gold standard despite its slow performance in high-resolution 3D data when rapid phase changes are present, such as in the late echoes.

Table 1.1*: Some phase unwrapping algorithms and their features.*

Algorithm Year	**Concept**	**Merits**	**Demerits**	**Notes**
PRELUDE (66) 2003	Region partitioning and merging.	Generalizable to any number of dimensions.	Very slow when rapid phase wraps exist.	Useful when time is not limited.
Best path (67) 2007	Follows best path based on edge quality map.	Fast. Does not require a mask.	More prone to error if SNR is low.	Fast and robust in most setups.
Laplacian (68) 2008	Based on Laplacian in Fourier space.	Fast. Eliminates some background field components.	An approximate solution. Fails to recover strong phase jumps.	For qualitative application. Last resort when others fail. Not useful for strong sources.
ROMEO (69) 2021	Follows best path based on spatial and temporal phase coherence and magnitude coherence.	Fast. Does not require a mask.	Temporal coherence may propagate error if the linear phase evolution is violated.	Fast and robust.

A modified version of PRELUDE (called SEGUE) accelerates the processing up to 70 times without a noticeable sacrifice in quality (70). More practical algorithms are known as Best Path (67) and ROMEO (69), which are both fast and robust in MRI applications. Both algorithms use quality maps to decide on the best path to follow for phase unwrapping: the former determines the edge quality based on the second derivative of phase, while the latter uses the magnitude coherence and the spatial and temporal phase coherence as quality metrics. Another common algorithm benefits from Laplacian implementation in Fourier domain to perform fast estimation of the unwrapped phase (68). This algorithm fails to recover rapidly changing phase, particularly near the edge of the volume, and thus should be considered for qualitative applications where knowing the exact phase value is not critical.

1.3.4 **Total Field Estimation**

The term total field refers to the net field induced by the susceptibility distribution within and outside the VOI. It is basically composed of a tissue field introduced by biological tissue within the VOI and a background field from other sources outside the VOI.

In single echo data, the total field estimation is a simple scaling for the phase using the field strength and the echo time. However, this does not remove phase offset from other sources (i.e., coils, eddy current, electrical conductivity, etc.). When multiple echo data is acquired, several options are available to combine these phases into a single total field map. One way is fitting the multiple echo data linearly or nonlinearly to obtain the total field and eliminate phase offset from other sources. However, many coil combination methods already remove the phase offset related to coils (60), and phase unwrapping methods such as ROMEO can implicitly handle the remaining phase offset (69). Thus, multi-echo phase information can be combined by averaging with or without weighting factors and benefits from increased SNR. Here, we briefly review the common ways to estimate total field from multi-echo phase data.

1.3.4.1 Linear Fitting:

The relation between the phase at TE (i.e., $\phi(TE_i, \vec{r})$) and the total field ($b(\vec{r})$, unitless after normalizing by the field strength) can be expressed as (71):

$$\phi(TE_i, \vec{r}) = w_i(TE_i, \vec{r}) \cdot b(\vec{r}) + \phi_0(\vec{r}) \tag{1.11}$$

where w_i is a weighting factor containing the scaling term (i.e., $2\pi\,\gamma\,B_0\,TE_i$). The weighting factor might include also the magnitude information to put more weight on voxels of higher signal. When multiple echo data is available, a system of linear equations can be formed using equation (1.11) and solved for $b(\vec{r})$ and $\phi_0(\vec{r})$.

1.3.4.2 Nonlinear Fitting:

Noisy phase voxels might not be successfully unwrapped and thus introduce errors in the estimated total field that propagate into the final susceptibility map. Therefore, a more robust estimation of the total field can be done using the complex MR signal before performing phase unwrapping via a nonlinear least square fitting (62):

$$argmin_{b(\vec{r}),\phi_0(\vec{r})} \sum_i \| S(TE_i, \vec{r}) - A(TE_i, \vec{r}) \cdot \exp[j2\pi\gamma B_0 \cdot b(\vec{r}) \cdot TE_i + j\phi_0(\vec{r})] \|_2^2 \tag{1.12}$$

where $S(TE_i, \vec{r})$ and $A(TE_i, \vec{r})$ refer to the complex MR image and the magnitude image at TE_i, respectively. After solving (1.12), the obtained total field might contain some wraps that need to be resolved using one of the phase unwrapping algorithms discussed previously.

1.3.4.3 Weighted Average:

Assuming the phase offset is negligible or already removed during the coil combination and phase unwrapping steps, the total field map can be obtained by a weighted averaging of the multiple echo phase data (72):

$$b(\vec{r}) = \frac{1}{2\pi\,\gamma\,B_0\,\sum_i A(TE_i, \vec{r})\,TE_i} \sum_i \phi(TE_i, \vec{r}) \cdot A(TE_i, \vec{r}) \tag{1.13}$$

which effectively uses the SNR (i.e., magnitude) of each echo as a weighting factor. This averaging approach benefits from improved SNR proportional to the number of echoes.

1.3.4.4 Phase Average:

In a multisite data where magnitude contrast varies across different protocols involved in the study, obtaining the total field map by simple averaging of individual echo phase data might be a better approach. Employing non-consistent magnitude contrast in the field estimation could have an adverse effect and might introduce additional variability to the final susceptibility maps. The phase averaging without the magnitude weighting would still improve SNR but with a slight reduction (72):

$$b(\vec{r}) = \frac{1}{2\pi\, \gamma\, B_0\, \sum_i TE_i} \sum_i \phi(TE_i, \vec{r}) \tag{1.14}$$

This approach has also been found useful at 7T to minimize coil-introduced bias and was used to obtain the final susceptibility map from individually processed channel and echo data (73).

1.3.5 Tissue Field Estimation

A critical step in QSM processing pipeline is removing the field contribution from background sources outside the VOI. Explained by the convolution model, sources outside the brain (such as air) contribute to the total field imaged within the brain (i.e., $b(\vec{r}) = b_{bkg}(\vec{r}) + b_{tissue}(\vec{r})$), and these "background" contributions ($b_{bkg}(\vec{r})$) should be separated from the "tissue" field ($b_{tissue}(\vec{r})$) prior to solving the field-to-source inverse problem. The background field is a harmonic field as its sources are not inside the domain. Several background removal methods have been developed, and improving this process is still an active research area (74). Most of these methods rely on two properties of the harmonic field. The first property is based on the harmonic average value theorem, which states that a harmonic function is preserved if convolved with a normalized radially symmetric function (75). Mathematically, this property can be expressed as:

$$b_{bkg}(\vec{r}) * \psi(\vec{r}) = b_{bkg}(\vec{r}) \tag{1.15}$$

where ψ is a normalized spherical kernel of specific radius. The other property of the harmonic field is that it satisfies the Laplace equation within the VOI, as no sources of this field are located within the VOI:

$$\nabla^2 b_{bkg}(\vec{r}) = 0 \quad \text{within VOI} \tag{1.16}$$

In the remaining of this subsection, we review few of these methods and explain their concepts.

1.3.5.1 Sophisticated Harmonic Artifact Reduction for Phase Data (SHARP):

Based on equation (1.15), convolving the total field with a spherical kernel and subtracting the result from the total field eliminates the background field component (55):

$$b(\vec{r}) - b(\vec{r}) * \psi(\vec{r}) = b_{tissue}(\vec{r}) - b_{tissue}(\vec{r}) * \psi(\vec{r}) = b_{tissue}(\vec{r}) * \left(\delta(\vec{r}) - \psi(\vec{r})\right) \quad (1.17)$$

where $\delta(\vec{r})$ is the Dirac delta function. The tissue field can then be obtained by deconvolving the result with $\left(\delta(\vec{r}) - \psi(\vec{r})\right)$. An additional step is usually required to mitigate any remnant background contributions, in which the final tissue field is regularized using truncated singular value decomposition (TSVD). This approach was introduced by Schweser et al. (55), and it is called SHARP. This method calculates the tissue field within spherical kernels with limited extent and thus is less sensitive the definition of the boundaries between tissue and background sources. However, it erodes the VOI by the radius of the used kernel and fails to estimate tissue field accurately near the edges of the VOI. The accuracy of this method can be improved if the total field map is interpolated into higher spatial resolution to minimize digitization error (74).

1.3.5.2 Regularization Enabled SHARP (RESHARP):

Another way to regularize the deconvolution step in SHARP is using Tikhonov regularization and formulating the problem as a least square minimization (76):

$$b_{tissue}(\vec{r}) = argmin_{b_{tissue}} \left\| M\, FT^{-1} C\, FT\left(b(\vec{r}) - b_{tissue}(\vec{r})\right) \right\|_2^2 + \lambda \left\| b_{tissue}(\vec{r}) \right\|_2^2 \quad (1.18)$$

where M is a brain binary mask, FT and FT^{-1} refer to Fourier transform and its inverse, C is the deconvolution kernel in the Fourier domain (i.e., $C = FT[\delta(\vec{r}) - \psi(\vec{r})]$), and λ is a regularization parameter. Compared to the TSVD used in the original SHARP method, the Tikhonov regularization is much smoother and thus minimizes regularization induced artifacts. However, RESHARP like SHARP erodes the final tissue map by the radius of the convolution kernel and thus throws away some useful information from the edge of the volume being processed.

1.3.5.3 Variable radius SHARP (V-SHARP):

To mitigate the issue of excessive erosion in SHARP, Li et al. introduced the use of spherical kernels of variable radius, in which the radius of the used kernel gets smaller towards the edge of the brain (77). This proposed method is known as V-SHARP and it minimizes the required erosion at the volume edge to as small as one voxel, as well as allowing the use of larger radius at the center of the brain and thus better approximating spherical kernels. The kernel radius in SHARP/RESHARP is typically within 3 to 5 mm to limit the amount of eroded cortical voxels, while in V-SHARP the maximum radius can be much larger (e.g., 20 mm). This modified version replaced the original method (i.e., SHARP) and has been widely used in literature. Note that SHARP-based methods do not involve dipole field calculations and thus do not rely on slice orientation information (i.e., slice direction with respect to B_0). Other SHARP-based methods exist in the literature but are not widely adopted, such as E-SHARP that employs Taylor expansion to estimate the tissue field in the eroded region (78), and iRSHARP that uses spatially weighted Gaussian kernels to better handle regions with high susceptibility variations (79).

1.3.5.4 Projection onto dipole fields (PDF):

Another novel way to remove contributions from background sources utilizes the orthogonality between tissue and background fields to solve a least square minimization problem and estimate the background field (80):

$$\chi_{bkg}(\vec{r}) = argmin_{\chi_{bkg}} \left\| w(\vec{r})\{b(\vec{r}) - d(\vec{r}) * \chi_{bkg}(\vec{r})\} \right\|_2^2 \qquad (1.19)$$

where $w(\vec{r})$ is a weighting factor derived from the magnitude information to control the effect of the noise. The background field is then estimated as $b_{bkg}(\vec{r}) = d(\vec{r}) * \chi_{bkg}(\vec{r})$ and subtracted from the total field to obtain the tissue field. This approach is known as projection onto dipole fields (PDF), and it relies on the brain mask to separate between tissue and background susceptibility sources. The PDF also uses slice orientation information to simulate the dipole kernel in the correct orientation with respect to B_0, and this might not be sufficient in oblique slices and could introduce underestimation and some artifacts. One way to overcome this issue is reformatting slices into pure axial orientation prior to the background field removal (81). Furthermore, the orthogonality assumption employed by the PDF is less accurate near the boundaries separating internal and external sources, and thus residual background fields are typically found near the edge of the VOI.

1.3.5.5 Solving Laplacian boundary value (LBV):

Based on equation (1.16), background field contributions can be removed by solving the Laplace equation under the assumption that the tissue field approaches zero at the VOI boundaries (82):

$$\nabla^2 b(\vec{r}) = \nabla^2 b_{tissue}(\vec{r}) \qquad b_{tissue} = 0 \; at \; \partial M \tag{1.20}$$

where ∂M refers to the volume boundaries. This boundary assumption is based on the observation that the background field is stronger by an order of magnitude than the tissue field near the volume edges. However, this assumption can be violated if a strong susceptibility source exists near the volume edges, such as a hemorrhage. This method is known as LBV and it relies on the brain mask to define the boundary between tissue and external sources.

Table 1.2 compares the merits and demerits of the common background removal methods in the literature, and it can be observed that all methods struggle with removing background field near the volume boundary and thus their accuracy reduces toward the VOI edges (74). In addition, recent studies have used artificial intelligence to improve the background removal step (83–85), however their performance has not been widely tested by the community. There are also some efforts to reconstruct susceptibility directly from the total field and completely avoid the background field removal step, which will be discussed later in this section.

***Table 1.2**: Commonly used background removal methods and their features.*

Method	Concept	Merits	Demerits
V-SHARP (77)	Spherical mean kernels of limited extent.	Less sensitive to boundary definition. Insensitive to slice orientation.	Less accurate near volume edges. Sensitive to mismatch in spatial resolution.
PDF (80)	Orthogonality based separation between tissue and external fields.	Insensitive to spatial resolution.	Less accurate near volume edges. Sensitive to boundary definition. Sensitive to slice orientation and might require pre-rotation of total field.
LBV (82)	Solving Laplace equation under zero tissue field assumption at the VOI boundary.	Insensitive to spatial resolution. Insensitive to slice orientation. Fast computation.	Less accurate near volume edges. Sensitive to boundary definition.

1.3.6 **Dipole Inversion**

The final step in the QSM processing pipeline is inverting the tissue field into a susceptibility map. Theoretically, it can be achieved via a deconvolution with magnetic dipole kernel (d), as implied from equation (1.9), which can be performed in Fourier domain via division:

$$b_{tissue}\left(\vec{k}\right) = d\left(\vec{k}\right) \cdot \chi\left(\vec{k}\right) = \left(\frac{1}{3} - \frac{k_p^2}{k^2}\right) \cdot \chi\left(\vec{k}\right) \tag{1.21}$$

However, the magnetic dipole kernel has zero values along the surfaces defined by $k_p^2/k^2 = 1/3$, which makes the inverse problem ill-posed and thus requires special handling. Here, we review the common approaches to solve the field-to-source problem in QSM and discuss their limitations.

1.3.6.1 Calculation of Susceptibility through Multiple Orientation Sampling (COSMOS):

One way to address the ill-posed problem is to collect (at least) two more datasets with two different orientations with the aim to fill the zero-valued surfaces by samples collected in different orientations (86). The result is a system of three equations that can be solved for $\chi\left(\vec{k}\right)$. This approach is known as COSMOS, and although impractical it has been used as the gold standard for comparison with other methods relying on only single acquisition.

1.3.6.2 Truncated k-space Division (TKD):

Another way to tackle this inverse problem without the need to collect additional data and rotating the imaged object twice was suggested by Shmueli et al. In this approach, the dipole kernel is truncated to a specific value whenever its value gets smaller than a predefined threshold (th) (54):

$$d\left(\vec{k}\right) = \begin{cases} \left(\frac{1}{3} - \frac{k_p^2}{k^2}\right) & , \left|d\left(\vec{k}\right)\right| > th \\ th & , otherwise \end{cases} \tag{1.22}$$

However, choosing the optimal threshold is a tradeoff between the accuracy and the introduced streaking artifacts and noise amplification, and thus artifacts are not completely suppressed.

1.3.6.3 Regularized dipole inversion:

To better handle the ill-posed inverse problem along with the associated artifacts, several regularization schemes were proposed in which the inverse problem is reformulated as a minimization problem with fidelity and regularization terms. The most used regularization is based on L1 norm total variation (TV), in which the susceptibility solution is assumed to be generally smooth with limited sharp edges:

$$\chi(\vec{r}) = argmin_{\chi} \; \|w(\vec{r})\{b_{tissue}(\vec{r}) - d(\vec{r}) * \chi(\vec{r})\}\|_2^2 + \lambda \, \|\nabla\chi(\vec{r})\|_1 \qquad (1.23)$$

where w is a weighting factor to prioritize voxels with higher SNR, and $\nabla\chi$ refers to the gradient of the susceptibility solution (87,88). This formulation provides better control on the introduced streaking artifacts as the regularization term will penalize the non-actual edges introduced by the artifacts. Other regularization terms have also been proposed, such as L2 norm (53,89) and total generalized variation (TGV) (90). However, a drawback from imposing regularization is the smoothness of the produced susceptibility maps. Thus, a tradeoff is typically required between the solution smoothness and the acceptable level of remnant streaking artifacts.

Other algorithms utilize magnitude contrast to identify actual edges and further facilitate the regularization process. This family of algorithms is known as morphology-enabled dipole inversion (MEDI), and their base formulation can be expressed as:

$$\chi(\vec{r}) = argmin_{\chi} \; \lambda \left\| W_N(\vec{r}) \left(\mathrm{e}^{\{j \, b_{tissue}(\vec{r})\}} - \mathrm{e}^{\{j \, d(\vec{r}) * \chi(\vec{r})\}} \right) \right\|_2^2 + \|\mathrm{M_G}(\vec{r}) \nabla\chi(\vec{r})\|_1 \qquad (1.24)$$

where $\mathrm{M_G}(\vec{r})$ is a binary mask based on the gradient of the magnitude contrast, which identifies edge information and penalizes non-edge regions (62). Note that MEDI uses different dynamic weighting ($W_N(\vec{r})$) that is updated during the iterations to minimize error propagation. Another MEDI-based algorithm uses additional regularization term to force susceptibility value in CSF to be zero with the aim to minimize CSF-related artifacts and to establish an internal reference value for susceptibility measurements (91). However, edge information on magnitude contrast might not be accurate due to T_2*-related blooming artifacts and thus relying on T_2* magnitude to identify edges might not be the best choice.

Another class of regularized inversion algorithms focuses on minimizing streaking artifacts while preserving the fine details in the reconstructed susceptibility map. These algorithms typically perform two reconstruction passes in which the first reconstruction pass aims to identify the strong susceptibility sources or the unwanted artifacts, and then in the second round the unwanted effects are eliminated. The iLSQR algorithm estimates the artifacts in an initial step by solving a minimization problem restricted to the ill-conditioned portion of the k-space (where $\left|d\left(\vec{k}\right)\right| < th$), and then subtract these artifacts from the total susceptibility obtained using a least square solution (92).

Another algorithm from the same group is called STAR-QSM, which estimates strong susceptibility sources in an initial step using TV-based minimization with strong regularization parameter, then calculates their field contribution using forward modelling (i.e., equation (1.9)) and subtract it from the tissue field. In a second step, the remaining field is inverted into a susceptibility map and then superposed with the susceptibility map produced in the initial step (93). A similar concept was introduced by Sun et al. to deal with hemorrhage patients, in which an initial QSM reconstruction is performed to detect the hemorrhage based on a threshold, and then its contribution to the tissue field is masked out (instead of subtracting contributions estimated by forward-modelling) and a second reconstruction is performed and superposed with the hemorrhage obtained in the initial step (94). Another algorithm that aims to process strong and weak susceptibility sources separately is known as multi-scale dipole inversion (MSDI), which separates field contributions of weak and strong sources using spherical mean filters of different radii, processes them individually and then superpose the final susceptibility solutions (95). In theory, MSDI allows processing the tissue field at several levels and imposing different conditioning and masking at each of these levels, thus providing more control on noise propagation and artifacts reduction. However, the dependency of this method on kernels of different radii makes it vulnerable to additional variability from differences in spatial resolution.

1.3.6.4 Single step inversion:

To avoid the shortcomings of background removal methods, several studies suggested obtaining the susceptibility map directly from the total field without the need for tissue field estimation as an intermediate step. These algorithms aim to solve for the total susceptibility sources, within and outside the VOI, although the focus is mainly on the tissue sources. One of these algorithms benefits from the Laplacian operator in equation (1.16) to implicitly remove background field contributions during the inverse minimization problem (96):

$$\chi(\vec{r}) = argmin_{\chi} \frac{1}{2} \left\| \nabla^2 b(\vec{r}) - (\tfrac{1}{3}\nabla^2(\vec{r}) - \tfrac{\partial^2}{\partial z^2})\chi(\vec{r}) \right\|_2^2 + \lambda \, \|\mathrm{M_G}(\vec{r})\nabla\chi(\vec{r})\|_2^2 \tag{1.25}$$

A drawback of using the Laplace operator is that the final solution is eroded by the radius of the used Laplace kernel. Another total field inversion algorithm is based on MEDI, and it uses an empirical pre-conditioning factor based on R_2* information to accelerate the convergence to a solution (97). Another study accelerated the convergence by including an additional L2 norm regularization in equation (1.23) to guide the algorithm towards the least square solution (98). Despite being available for several years, total field inversion algorithms have not been widely adopted by the community.

1.3.6.5 Deep learning-based inversion:

Recently, several studies introduced artificial intelligence to solve the field-to-source problem. Based on convolutional neural network, an encoder-decoder network is trained to produce a susceptibility map either from the tissue field (99–103) or directly from the total field (104,105). Deep learning-based inversion features fast reconstruction and competing accuracy. Despite their promising potential, the performance of deep learning-based inversion methods came second to the analytical iterative methods (106), highlighting the fact that generalizing the accurate outcome in deep learning is not a trivial task.

1.3.7 **Available QSM Toolboxes**

Most of the QSM literature is centered around brain and neuroscience applications. In response to this demand, several toolboxes were developed for human brain QSM, mostly in the MATLAB environment. The most widely used toolbox was developed by Yi Wang research group at Cornell University and is known as MEDI toolbox (107). The MATLAB-based toolbox has a GUI, takes DICOM files as the input and performs all the necessary processing steps automatically, from mask generation and phase unwrapping to background removal and producing the final susceptibility map. Another fully automated toolbox is known as STI Suite, and it was developed by Chunlei Liu group at the University of California – Berkeley (108). The MATLAB-based toolbox also has a GUI and takes the input as DICOM, mat or nifti files. A newer automated toolbox is known as QSMBox and it was developed by Julio Acosta-Cabronero. This MATLAB toolbox works from the command line and takes the input as nifti files (109). Other toolboxes also exist that aim to combine the distinct features of the above toolboxes and other methods under one umbrella, such as JHU/KKI QSM Toolbox (110) and SEPIA toolbox (111).

All these toolboxes work reliably with healthy subjects data, but might require some tuning for the regularization parameters if the data SNR changes noticeably due to variation in spatial resolution and/or sequence parameters. Moreover, the mask generation might fail or produce sub-optimal results on patient data with abnormal atrophy or iron accumulation, leading to the failure of the subsequent steps.

QSM outside the brain has drawn increasing attention in recent years. However, to the best of our knowledge no dedicated toolbox has been made publicly available. Instead, the above-mentioned toolboxes are typically modified to work on specific regions outside the brain.

1.3.8 **Technical Challenges**

The ability of magnetic susceptibility to probe sub-voxel structures and activities comes with its challenges. A model that fully considers sub-voxel compartments and directional restrictions would be difficult to solve, and a typical single acquisition MEGE data might not be a sufficient input for the model. The majority of MR-based susceptibility imaging studies facilitated QSM based on several simplifications and assumptions, including: 1) measured susceptibility is isotropic, 2) not absolute, and 3) represents the average within a voxel. Also, 4) the obtained phase shift is assumed to be mainly due to the magnetic susceptibility, and 5) it is linearly related to the acquisition echo time. 6) The imaging time is not restricted and thus a dedicated acquisition with sufficiently long echo time to accumulate phase contrast is accessible, and 7) the imaged volume extends well beyond the ROI in all directions. 8) The same imaging protocol is achievable and accessible in any involved imaging center.

Recently, researchers have put efforts to revisit and probe most of these assumptions. The effects of susceptibility anisotropy have been investigated (35), and reconstructing the susceptibility tensor has been reported (14). Studies have also investigated separating voxel susceptibility into two compartments: paramagnetic and diamagnetic, based on MEGE data solely (112,113) or with additional help from R_2 data (114). Moreover, methods to remove phase shift from non-susceptibility components have been proposed (115–117), and the relation between the phase shift and echo-timings has been investigated (118). Possible internal susceptibility references have been investigated (40,41), and automatically setting the CSF as a reference has been proposed (91).

This thesis investigates the last three assumptions listed above, which have not been well studied in the existing literature. Briefly, we investigate the limitations on short echo-time QSM and possible applications in human brain. In addition, we study the difficulties of producing QSM from thin slabs without the need for acquiring full brain coverage, and propose an approach to overcome these difficulties. Furthermore, we investigate multisite QSM reproducibility when local protocol variations are inevitable.

1.3.9 **Clinical Applications**

Magnetic susceptibility plays an important role in determining material compatibility for the MRI environment, both outside and inside the imaging region, such as the instrumentations needed for MR-guided surgeries, orthotics and body implants (24), thanks to its influence on MR positional accuracy, artifacts, and magnetic force hazards. With the emergence of the QSM technique, the unique contrast of susceptibility was found useful in localizing deep gray matter structures for deep brain stimulation (DBS) electrode implantation (119,120), and in segmenting structures that have otherwise weak contrast on other MRI modalities (121–123).

More importantly, the evolved understanding of the magnetic susceptibility mechanisms in human tissue unleashed the potential of using it as a biomarker in many clinical applications. For instance, the ability of the QSM to distinguish between paramagnetic and diamagnetic sources was found useful in tumor characterization by differentiating between hemorrhage and calcification found in malignant and benign tumors in brain, respectively (120). Furthermore, QSM sensitivity to changes in iron and myelin levels has made it attractive to many aging and brain development studies (26–28), to trace these changes and detect any early iron deficiency (124–126) or delayed myelination (127). Monitoring metallic ion deposits and/or demyelination to assess disease progression has become an integral part of various neurological studies, including Alzheimer’s disease (128), amyotrophic lateral sclerosis (129), Huntington's disease (30), multiple sclerosis (130,131), Parkinson's disease (132,133), and Wilson's disease (134).

QSM is also a great tool to monitor and assess traumatic brain injury (135,136), distinguishing between acute and chronic situations (137–139), and reliably evaluating microbleed burden (140,141). Moreover, QSM provides an excellent contrast for deoxygenated blood and thus has been used for vasculature imaging (142) and venous oxygen quantification (143,144).

Although more challenging due to the presence of motion and fat, QSM applications extend beyond the brain to assessing iron load in the liver (145–147), quantifying blood oxygenation in the heart (148,149), and exploring tissue structure in kidneys (150), bones (151) and cartilage (152).

The above discussed applications are only representative and do not cover the full spectrum. More potential applications, limitations and details can be found in (120,153,154).

1.4 **THESIS OVERVIEW**

Quantitative susceptibility mapping is a powerful tool to probe metallic ions and myelination changes at microscopic level. However, its full potential and clinical integration is still hindered by some technical issues. One of these obstacles is that standard QSM requires a dedicated data acquisition, which can be moderately long (for multi-echo data) and thus puts additional time burden on clinical protocols. Successful QSM also requires spatial coverage that extends well beyond the ROI, which impedes scanning time reduction via thin slab imaging. Furthermore, the reproducibility of QSM in the presence of local sequence variations has not been evaluated, a case that would allow aggregating data retrospectively from multiple sites to form datasets of wider demographical and/or pathological coverage.

In this thesis, we investigated these topics and proposed some technical solutions. In Chapter 2, the feasibility of producing QSM from the phase of 3D magnetization-prepared rapid gradient-echo (MPRAGE) was evaluated for the first time. MPRAGE is a standard T_1-weighted imaging that is typically included in brain protocols for providing tissue structural information. Generating a susceptibility map from the MPRAGE phase would avoid the need for additional QSM-related acquisition and thus reduce the time burden for incorporating QSM in clinical studies. In this chapter, MPRAGE-based QSM was evaluated using numerical simulations and in-vivo experiments, and its limitations were explored. Additionally, a possible application for the MPRAGE-QSM to improve deep gray matter segmentation was demonstrated.

In Chapter 3, another application for the MPRAGE-QSM was explored: quantifying cerebral microbleeds without the need for a dedicated QSM acquisition. Microbleed susceptibility and size were quantified using MPRAGE-QSM in patient data and compared to measurements obtained using standard MEGE-based QSM. Additionally, simulations were performed to assess detection sensitivity and quantification accuracy at different microbleed sizes, susceptibility strengths, SNR levels, echo times and spatial locations.

In Chapter 4, the difficulties incurred in performing QSM from thin slabs were discussed. Furthermore, we proposed a hybrid approach to overcome these difficulties and evaluated its performance using synthetic and in-vivo measurements of human brain.

Chapter 5 of this thesis studied the reproducibility of susceptibility and R_2* mapping in non-harmonized multisite data that was investigated using 24 traveling heads. Additionally, this chapter presents possible post-processing techniques to reduce cross-site sequence-induced variability.

In Chapter 6, concluding remarks are presented.

Chapter 2: On the value of QSM from MPRAGE for segmenting and quantifying iron-rich deep gray matter[1]

2.1 **Abstract:**

Purpose: Quantitative susceptibility mapping (QSM) has been employed for both iron evaluation and segmentation of deep gray matter (DGM), but QSM sequences are not typically used in standard brain volumetric studies, which use T_1-weighted magnetization-prepared rapid gradient echo (MPRAGE) with short TE. Here, QSM produced directly from standard MPRAGE phase (QSM_{MPRAGE}) is evaluated for segmentation and quantification of highly iron-rich DGM regions.

Methods: Simulations were used to explore quality and possible limitations. In addition, QSM from a standard multi-echo gradient-echo (QSM_{GRE}) was compared to QSM_{MPRAGE} in 40 healthy adults at 3T. DGM structures with weak contrast on MPRAGE magnitude were evaluated for improving segmentation with QSM_{MPRAGE}, with focus on the iron-rich globus pallidus (GP). Furthermore, susceptibility quantification was assessed on six DGM nuclei and compared to standard QSM_{GRE}.

Results: Limited by TE and signal-to-noise ratio, only iron-rich regions like GP and dentate nucleus produced adequate contrast on QSM_{MPRAGE}, confining applications to such regions. QSM_{MPRAGE} improved GP segmentation with mean Dice scores raised by 9.0%, and mean volumetric differences reduced by 9.7%. Simulations suggested that phase contrast-to-noise ratio (CNR) should be above 3.0 to attain segmentation improvement. For quantification purposes, higher CNR is required, and typical QSM_{MPRAGE} provided comparable estimates to QSM_{GRE} in large iron-rich DGM nuclei.

Conclusion: Despite the short TE of standard MPRAGE, QSM_{MPRAGE} can improve GP segmentation over the use of MPRAGE magnitude alone and roughly quantify high-iron regions in DGM. Thus, reconstructing QSM_{MPRAGE} can be a useful addition to volumetric studies that rarely include standard QSM_{GRE}.

Keywords: deep gray matter, globus pallidus, MPRAGE, QSM, segmentation

---

[1] A version of this chapter has been published: *Naji N, Sun H, Wilman AH. On the value of QSM from MPRAGE for segmenting and quantifying iron-rich deep gray matter. Magn Reson Med. 2020;84:1486–1500.*

2.2 INTRODUCTION

Deep gray matter (DGM) nuclei are receiving increasing attention in neuroscience studies due to their association with various neurological diseases, including multiple sclerosis, Parkinson's disease, and Huntington's disease (132,155–162). Quantitative susceptibility mapping (QSM) has been used to noninvasively probe metallic ion deposits in these nuclei and trace evolution with age and/or pathological condition (27,31,54,130,132,153,161,162). Standard QSM is typically produced from the phase of a multi-echo gradient-echo (GRE) sequence.

In neuroimaging studies, segmentation is a key preprocessing step used to extract specific structures from the whole brain volume for dedicated quantitative analysis, such as voxel-based morphometry and volumetric measurements (163,164). Segmentation of different brain structures is typically performed on T_1-weighted (T_1w) images obtained using a 3D magnetization-prepared rapid gradient-echo (MPRAGE) sequence, relying on the discriminative T_1w contrast between gray matter, white matter, and cerebrospinal fluid (CSF). However, certain DGM nuclei have weak contrast relative to surrounding white matter, which makes their segmentation challenging (165,166). Globus pallidus (GP) in particular, becomes less or nonvisible on MPRAGE magnitude at higher field ($\geq$ 3T) imaging. Within the basal ganglia, GP has the highest iron concentration and plays a crucial role in regulating voluntary movements. However, its segmentation on MPRAGE is much poorer than caudate (CD) and putamen (PT).

QSM studies have been employed for aiding DGM segmentation (27,122,167–175), where improvements have been most significant in the iron-rich structures like GP. However, QSM sequences are not typically used in standard brain volumetric studies, which typically rely on MPRAGE. In this study, we examine the possibility of using MPRAGE phase directly for QSM. Although new multi-echo versions of MP2RAGE are capable of providing multiple contrasts including both T_1 and QSM (176–178), to our knowledge standard MPRAGE used in most volumetric studies has not been used for creating QSM. Here, we evaluate the creation of QSM directly from standard volumetric MPRAGE data to achieve improved segmentation over MPRAGE magnitude and susceptibility quantification of highly iron-rich DGM nuclei. The potential value and the limitations of the method are evaluated in simulation and in vivo with comparison to standard multi-echo QSM.

2.3 METHODS

Numerical simulations of QSM from MPRAGE were used to study the effects of inversion time (TI), echo time (TE), and signal-to-noise ratio (SNR) on QSM results. Anecdotal in-vivo data from three subjects determined the quality of MPRAGE-based QSM for various TEs and its potential for improving segmentation and quantifying susceptibility of iron-rich DGM nuclei. Finally, an in-vivo study of 40 subjects tested QSM from MPRAGE using a standardized protocol with very short TE (2.37 ms) and high resolution ($0.87 \times 0.87 \times 0.85$ mm^3), to determine MPRAGE-QSM capability under severe conditions of limited phase contrast-to-noise ratio (CNR).

2.3.1 Simulations of QSM From MPRAGE

The MPRAGE sequence for volumetric T_1-weighted brain studies differs from a typical QSM sequence in two main ways: inversion recovery is used to enhance T_1 contrast and only a single echo is collected with very short TE. The main consequences for QSM are limited phase CNR and possible phase alterations across the lengthy MPRAGE readout. Therefore, simulations were used to investigate the effects of the evolving longitudinal magnetization (Mz) polarity across the MPRAGE readout and to estimate a minimum requirement for phase CNR to ensure useful MPRAGE-QSM. Simulation code can be found at https://github.com/MRItech/mprage.

A numerical brain phantom from a previous work (179) was modified to match the dimensions and resolution of the in-vivo acquired MPRAGE data (40-subject protocol described later). Maps for proton density, T_1, T_2*, and susceptibility were produced using the values reported in literature at 3T and listed in **Table 2.1** (180–182). The susceptibility-induced tissue magnetic field was produced by convolving the susceptibility map with the magnetic dipole kernel and then scaling to a phase map at 3T. This phase map and the proton density map were combined to form an equilibrium complex-valued Mz map, M_0. Mz evolution during MPRAGE acquisition was simulated using Bloch equations and applied to M_0 in k-space line-by-line along the slice-encoding direction (assuming the slice encoding is the inner loop). In similar steps, GRE data were simulated with identical acquisition parameters used in vivo. MPRAGE and GRE phases were then processed into QSM maps using the same reconstruction pipeline as used for in-vivo data (except skipping the background field removal step). Five imaging parameters affect the Mz evolution (and consequently the portion of readouts collected with negative Mz): TI (time between inversion pulse and k-space center), flip angle, GRE-TR (time between consecutive excitation pulses), delay time

(TD) (the portion of sequence-TR between the last readout and the next inversion pulse), and spatial resolution. We investigated the size of the resultant negative-Mz readouts for the following ranges (TI: 590-1800 ms; flip angle: 1°-25°; TD: 0-2500 ms, isotropic resolution: 0.7-1.0 mm). The GRE-TR was kept at its minimum value for all simulations.

Table 2.1: *Proton density, T_1, T_2*, and susceptibility values used in simulations.*

Tissue	Proton Density	T_1 [ms]	T_2* [ms]	Susceptibility [ppm]
Caudate nucleus	0.802	1280	54.8	+0.03
CSF	1.000	4500	2000	0.00
Globus pallidus	0.744	950	28.8	+0.10
Gray matter	0.807	1390	58.0	−0.01
Putamen	0.797	1150	53.6	+0.04
Substantia nigra	0.750	925	42.0	+0.09
Thalamus	0.756	1150	76.8	0.00
White matter	0.679	910	55.0	−0.04
Others	0.679	910	55.0	−0.04

To study the SNR effect on the quality of reconstructed QSM from MPRAGE phase, a Monte Carlo simulation (10 independent repetitions) was done by adding random complex-valued Gaussian noise to the MPRAGE data in k-space at different SNR levels. In QSM, a susceptibility difference $\Delta\chi$ induces a phase shift of up to $2\pi\cdot\gamma\cdot B_0\cdot 1/3\cdot \Delta\chi\cdot TE$, where γ is the gyromagnetic ratio (in MHz/T) (183). However, phase noise is inversely related to the magnitude SNR (SNR_M) (184). Thus, phase CNR can be defined as $CNR_{\phi} = 2\pi\cdot\gamma\cdot B_0\cdot 1/3\cdot \Delta\chi\cdot TE\cdot SNR_M$ and used to define a threshold for a useful QSM. For in-vivo SNR_M measurement, a DGM region covering GP, PT, and thalamus (TH) on three slices was defined on the magnitude image and used to calculate the mean intensity, and noise SD was estimated on the image background. In simulated datasets, DGM nuclei were segmented from the reconstructed QSM images using Otsu Thresholding (185), and the quality of the recovered DGM boundaries was assessed using Dice score and false positive Dice measures (explained later).

2.3.2 **In-vivo Human Brain Experiments**

Brain imaging was done at 3T (Prisma, Siemens Healthcare, Erlangen, Germany) with a 64-channel head coil. All subjects provided informed consent and studies were approved by the local ethics committee. To explore effects of TE variation, three healthy subjects (males; age: 24, 31, and 42 years) received MPRAGE at three different echo times (TE/sequence-TR 2.43 ms/1830 ms, 3.50 ms/2170 ms, and 4.44 ms/2170 ms) and common spatial resolution of 1 mm isotropic. Other imaging parameters were field of view 256×256×208 mm^3, flip angle 12°, TI 950 ms, GRAPPA acceleration 2, and slice partial Fourier 6/8. Because the MPRAGE sequence forced use of only the minimum TE, echo time was altered by turning on/off echo asymmetry and/or modifying readout bandwidth.

Forty healthy adult subjects (age, 18-70 years; mean ± SD, 36.8 ± 14.3; 11 males) were studied retrospectively for a detailed analysis of segmentation and quantification of QSM with a standardized MPRAGE protocol using very short TE and high resolution. Inclusion criteria were the availability of both MPRAGE and multi-echo GRE sequences with saved raw phase images. MPRAGE parameters included sagittal orientation, 0.87× 0.87×0.85 mm^3 resolution, field of view 250× 250×176.8 mm^3, flip angle 8°, TI 900 ms, sequence-TR 1800 ms, TE 2.37 ms, GRAPPA acceleration 3, acquired in 3.65 minutes. Multi-echo GRE used axial orientation, 0.94×0.94×1.70 mm^3 resolution, field of view 202.6×240×149.6 mm^3, flip angle 13°, TE1 3.82 ms, ΔTE 5.49 ms, 6 echoes, TR 37 ms, GRAPPA acceleration 2, acquired in 5.5 minutes.

2.3.3 **QSM Processing**

The following steps were performed for both MPRAGE and GRE data, unless otherwise stated. Adaptively coil-combined magnitude and phase images were processed using MATLAB R2015b (MathWorks, Sherborn, Massachusetts). Phase images were unwrapped using PRELUDE tool of the FMRIB Software Library (FSL) package (66). For MPRAGE, the frequency shift related to magnetic susceptibility was obtained via phase division by TE. For GRE, the frequency shift was obtained from the phases of different echo times by a voxel-wise least-squares regression. QSM maps were then produced from the frequency shifts of MPRAGE and GRE through background field removal and dipole inversion steps described in the appendix (76). Susceptibility maps obtained from MPRAGE and GRE sequences are referred to as $\mathrm{QSM}_{\mathrm{MPRAGE}}$ and $\mathrm{QSM}_{\mathrm{GRE}}$, respectively. Bias-field in magnitude images of both sequences was removed using N4ITK tool

(186). This bias-corrected brain (skull-stripped) magnitude image is referred to thereafter as the magnitude image. GRE magnitude of first echo was rigidly registered to MPRAGE magnitude using ANTs software (187). The resulting transformation matrix was then used to transform QSM_{GRE} into MPRAGE image space.

2.3.4 **Susceptibility Quantification**

To examine the potential of QSM_{MPRAGE} for susceptibility quantification, we measured mean susceptibility of six iron-rich structures GP, CD, PT, TH, dentate nucleus (DN), and substantia nigra (SN) on both susceptibility maps obtained from MPRAGE and GRE. FSL segmentation of GP, CD, PT, and TH obtained automatically using a hybrid contrast of T_1w and QSM_{GRE} (explained later) were used for susceptibility measurements on both QSM_{GRE} and QSM_{MPRAGE}. Other DGM structures supported by FSL (amygdala, accumbens, and hippocampus) were not considered as their susceptibility values/volumes are too low/small to be accurately quantified at very short TEs. Segmentation masks were first eroded by two voxels to avoid including susceptibility values from surrounding tissues. In addition, susceptibility of DN and SN (not supported by FSL) were measured as the average over manually defined regions on three slices (using QSM_{GRE}). The mean values of susceptibility in the left and the right hemispheres were recorded separately.

2.3.5 **Segmentation Processing**

Incorporating QSM contrast to enhance DGM segmentation can be done in different ways (122,168–175). In this work, we used the Feng et al. approach (122) that first merges T_1w and QSM contrasts into a single hybrid contrast (HC), then segments this HC using FMRIB's Integrated Registration & Segmentation Tool (FIRST) (188). We tested segmentation using three different contrast inputs: standard MPRAGE T_1w contrast, the proposed contrast (HC_{MPRAGE}) made using T_1w and QSM_{MPRAGE}, and a third contrast (HC_{GRE}) made using T_1w and QSM_{GRE}, which was used as a reference to evaluate HC_{MPRAGE} quality. Briefly, HC_{MPRAGE} and HC_{GRE} were obtained as follows:

$$HC_{MPRAGE} = w_{11} \cdot T_1w + w_{12} \cdot QSM_{MPRAGE} \tag{2.1}$$

$$HC_{GRE} = w_{21} \cdot T_1w + w_{22} \cdot QSM_{GRE} \tag{2.2}$$

The weighting coefficients were calculated by equalizing the combined hybrid contrast to that of the FIRST template in two regions in 10 random subjects then taking the average of the 10 calculated weighting coefficients. In this way, a global weighting factor was applied to the whole image term (T_1w or QSM). Two regions are required to solve for the two weighting functions in each case. GP and TH were chosen for the high contrast and the large size, respectively. Before calculation, the T_1w images were first normalized by division to ensure similar mean white matter intensity across all subjects (122). Considering Equation (2.1), the aim is producing HC_{MPRAGE} of similar contrast to the FIRST template, and thus the latter was set as the left-hand-side of Equation (2.1). The two unknowns (w_{11}, w_{12}) are solved for by manually measuring the mean intensities of two structures (GP and TH) on each of the terms (images) in Equation (2.1): the FIRST template, T_1w and QSM_{MPRAGE}. Similarly, (w_{21}, w_{22}) were obtained using Equation (2.2) and measurements on QSM_{GRE}. Average coefficients were found to be w_{11} = 1.38, w_{12} = −78.90, w_{21} = 1.38, and w_{22} = -75.42. Finally, contrast images were fed into the FIRST tool for segmentation with nonlinear (rather than the default linear) registration (122).

2.3.6 **Segmentation Performance Analysis**

Segmentation performance using T_1w and HC_{MPRAGE} were compared to using HC_{GRE} as a reference and also analyzed using a reference-free approach to remove potential bias when assuming HC_{GRE} is the gold standard. Segmentation quality was evaluated quantitatively using four measures, namely Dice score, false negative Dice (FND), false positive Dice (FPD), and percentage absolute volumetric difference (AVD) (189). Dice score measures the spatial overlap between methods. FND assesses the amount of actual structure voxels not segmented (i.e., under segmentation rate), whereas FPD measures how segmentation extends outside the actual structure boundaries, quantifying over segmentation rate. AVD basically describes the relative difference between the volumes of the resultant and the reference segmentations. The ideal score (i.e., perfect match) for Dice is 1.0, whereas for the other three measures is 0.0. For visualization purposes, the latter three measures (FND, FPD, and AVD) were reported in a complementary form (i.e., $\overline{\text{FND}} = 1 - \text{FND}$) such that the ideal score for all the measures becomes 1.0. The scores calculated on the left and the right hemispheres were averaged. Statistical significance of the differences in segmentation was evaluated using a paired, one-tailed t test ($\alpha = 0.05$). In addition, reference-free assessment was used to rank segmentation methods based on statistical inferences (190,191). Briefly, a probabilistic error model is used to relate measurements from different methods to the unknown actual value of interest (here structure volume). Given large number of samples (i.e., measurements), the parameters of the error model can be estimated and used to quantify its precision. We used a quadratic model to express the relation between true and measured volumes, with random multivariate Gaussian error (192). Given the measured volumes of a DGM structure from the obtained segmentations, model parameters were estimated by sampling a posterior distribution of the unknown true volume, using Markov chain Monte Carlo technique implemented in Python (PYMC3 package) (193). The model is then used to predict actual volumes (192). Estimated standard deviation of error (σ_e) was then used to rank the precision of the three segmentation methods, in which smaller σ_e implies higher precision.

2.4 RESULTS

2.4.1 Inversion Pulse and SNR Effects

Collecting the first portion of readouts while Mz of some tissues (e.g., CSF) is still negative (i.e., below the nulling point) introduces inconsistency between high frequency information on both sides of the spectrum and leads to artifacts around the edges of low SNR regions. These artifacts were observed around CSF on simulated MPRAGE phase shown in **Figure 2.1**. However, QSM reconstruction was not significantly affected, especially around GP. The phase images of GRE (first echo) and MPRAGE obtained at the same TE showed similar content and contrast and produced comparable QSMs. The size of the readout portion collected with negative Mz increases with shorter TI, smaller flip angle, longer total sequence-TR (longer TD), and lower spatial resolution. Simulation results showed that a problematic case could occur if some tissues are nulled, or if Mz polarity switching occurs around the center of k-space (i.e., half of the readouts are collected with negative Mz) such that this central region is collected above the nulling point for some tissues (i.e., white matter) and below the nulling point for others (i.e., gray matter and CSF). This case leads to very low SNR and corrupted phase images (**Figure 2.2**) and occurs if a low flip angle (< 8º) is combined with long sequence-TR (3000 ms) and very short TI (~600 ms). However, such a case is not desirable as it results in poor magnitude quality. In the literature, the commonly used values for flip angle, TI and TR at 3T lie in the range 8-15°, 900-1200 ms, and 1950-2530 ms, respectively (194,195).

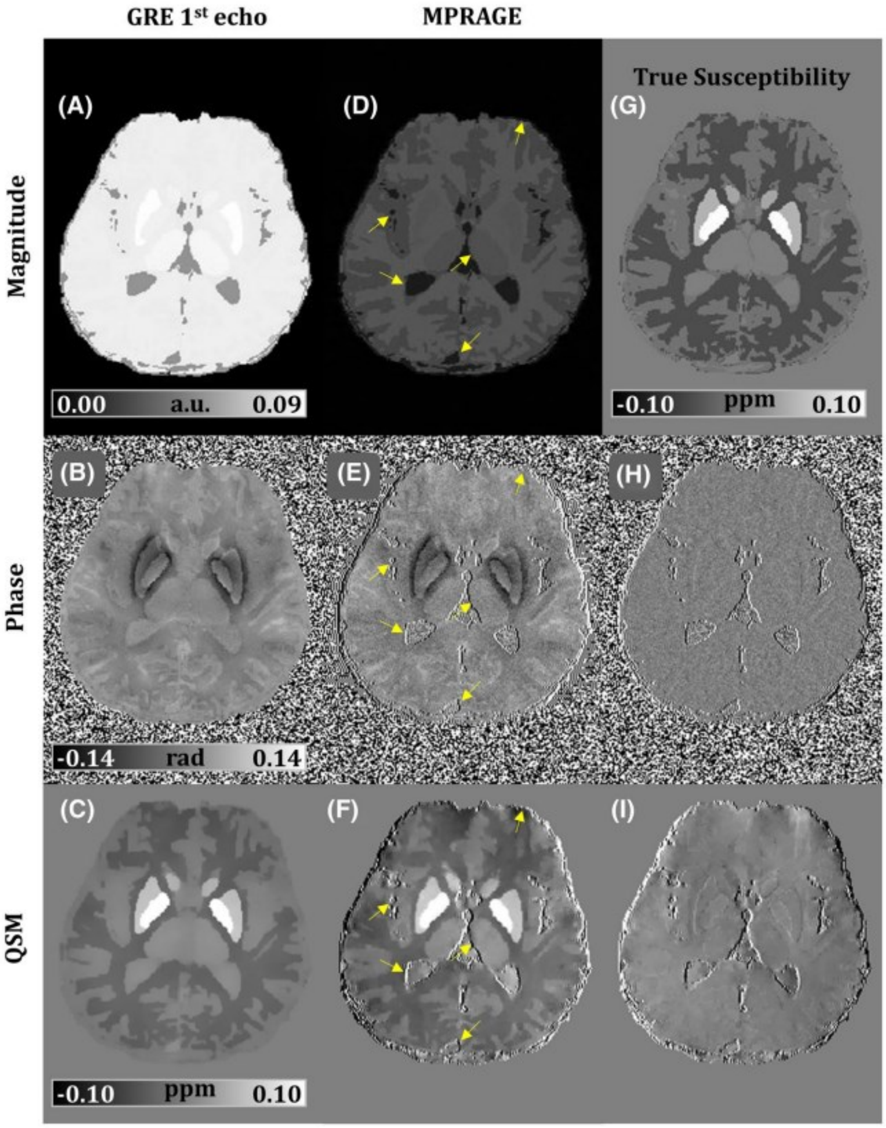

Figure 2.1: *Sample simulated data: Left and middle columns illustrate the simulated gradient-echo (GRE) (A-C) and magnetization-prepared rapid gradient echo (MPRAGE) (D-F) data (magnitude, phase, and quantitative susceptibility mapping [QSM]) at echo time (TE) = 3.82 ms. (G) Ground-truth susceptibility map. (H) Phase difference and (I) QSM difference between GRE and MPRAGE. MPRAGE phase has similar contrast to GRE phase, except at very low SNR regions (yellow arrows) such as cerebrospinal fluid (CSF). Noticeable artifacts appear around sharp edges due to the inconsistency between high frequency components on the left and the right sides of k-space, as a consequence of collecting the first 25% of readouts with negatively polarized Mz.*

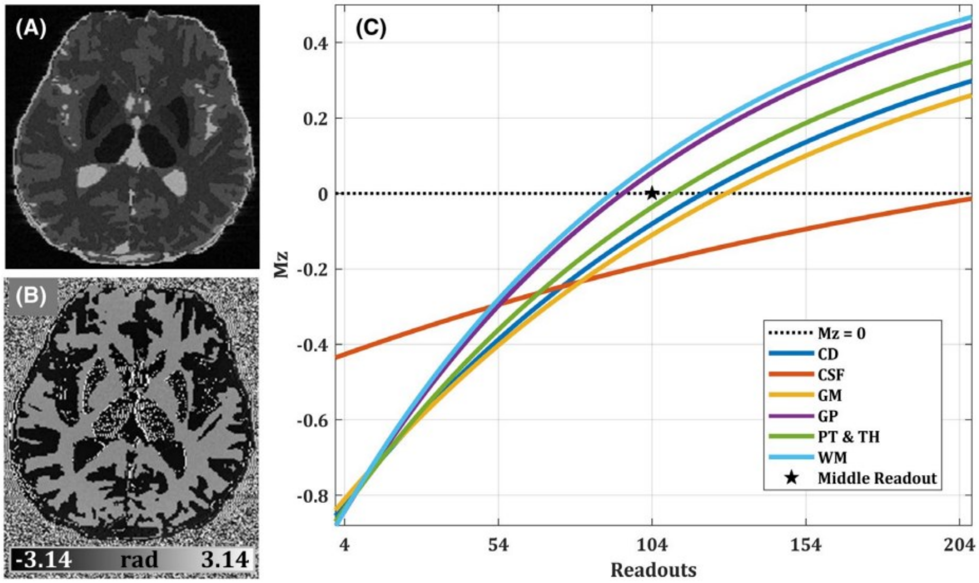

Figure 2.2: *Simulated magnetization-prepared rapid gradient echo (MPRAGE) (A) magnitude and (B) phase images illustrating a problematic case where different tissues have different phase polarity. Imaging parameters included inversion time (TI) 650 ms, echo time (TE) 2.37 ms, sequence-pulse repetition time (TR) 4000 ms, and flip-angle 4°, such that the center of k-space (star) was collected above the nulling point for white matter (WM) and below the nulling point for gray matter (GM) and cerebrospinal fluid (CSF), as demonstrated in (C) Mz evolution during readouts. As a consequence, the phase of WM (and other tissues of similar* T_1*) has different polarity (+) in the phase image (B) than GM and CSF. Contribution of background field was considered in this simulation.*

Figure 2.1 also highlights the lower magnitude SNR of MPRAGE data (compared to GRE) due to several factors. First, MPRAGE used a shorter GRE-TR and a smaller flip angle. In addition, the evolving Mz across readout measurements (compared to steady Mz in GRE) results in lower mean MPRAGE intensity. Magnitude SNR is closely related to $\mathrm{CNR}_{\emptyset}$, which in turn affects the quality of reconstructed QSM. **Figure 2.3A** illustrates the quality of $\mathrm{QSM}_{\mathrm{MPRAGE}}$ reconstructed at different $\mathrm{SNR}_{\mathrm{M}}$ levels. For the same $\mathrm{SNR}_{\mathrm{M}}$ and TE, different DGM structures produce different $\mathrm{CNR}_{\emptyset}$ levels due to the contribution of $\Delta\chi$. When $\mathrm{CNR}_{\emptyset}$ is above 6.2, the error in susceptibility quantification falls below 0.01 ppm in most DGM nuclei including GP (**Figure 2.3B**). However, SN would require higher $\mathrm{CNR}_{\emptyset}$ to achieve the same accuracy. The error reflects underestimation in $\mathrm{QSM}_{\mathrm{MPRAGE}}$ measurements, which elevates as SNR decreases (**Figure 2.4**). Different structures experienced different levels of underestimation, with lower levels being observed in structures of higher total susceptibility (i.e., sum of susceptibility over volume). The higher the total susceptibility, the more phase contrast will be produced and distinguished from the noise floor during (spatially regularized) susceptibility reconstruction.

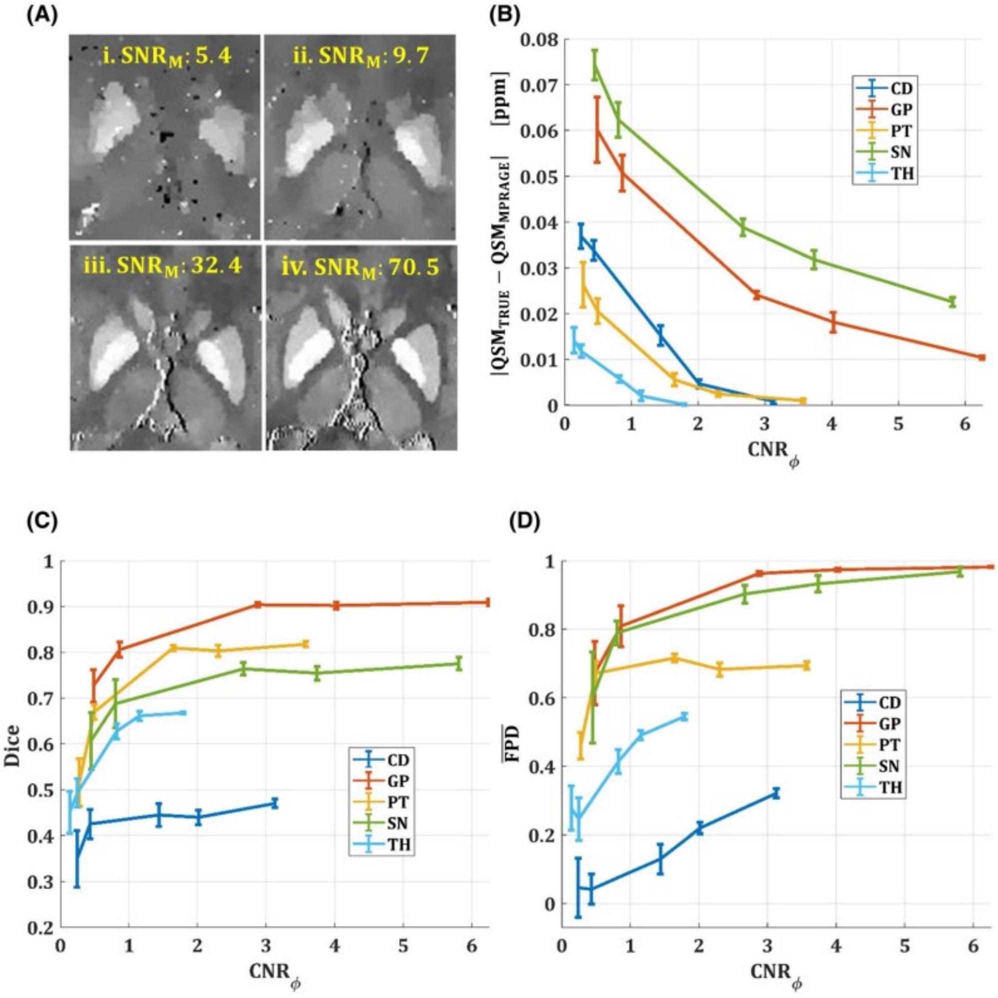

Figure2. 3: *Simulation results of magnetization-prepared rapid gradient echo (MPRAGE)-based quantitative susceptibility mapping (QSM) vs phase contrast-to-noise ratio (*$CNR_{\varnothing}$*). (A) Zoomed QSM windows are given at selected signal-to-noise ratio (SNR) levels to visualize resultant contrast and boundaries of deep gray matter (DGM) nuclei.* SNR_M *refers to the mean magnitude SNR in DGM region. (B) Error in susceptibility quantification vs* $CNR_{\varnothing}$*. Segmentation quality at different* $CNR_{\varnothing}$ *levels are evaluated using (C) Dice and (D) FPD measures. QSMs in (A) i-iv correspond to the first, second, third, and fifth data points in (B-D) plots.*

In addition, DGM nuclei of more distinctive contrast on $\mathrm{QSM_{MPRAGE}}$ resulted in more accurate segmentations. GP, SN, and PT achieved > 0.7 score in both Dice and FPD when $\mathrm{CNR_{\emptyset}}$ was above 3.0 (**Figure 2.3C,D**). With TE of 2.37 ms, this 3.0 $\mathrm{CNR_{\emptyset}}$ corresponds to approximately 34-60 magnitude SNR (for GP, SN, and PT), which is accessible with typical MPRAGE parameters. GP has the highest contrast and achieved 0.9 score in both Dice and FPD at 3.0 $\mathrm{CNR_{\emptyset}}$, and thus $\mathrm{QSM_{MPRAGE}}$ is promising at least for GP segmentation if $\mathrm{CNR_{\emptyset}}$ greater than 3.0 is secured. This $\mathrm{CNR_{\emptyset}}$ gives practical insight into the required $\mathrm{SNR_M}$ and TE levels for $\mathrm{QSM_{MPRAGE}}$ to be useful for GP segmentation.

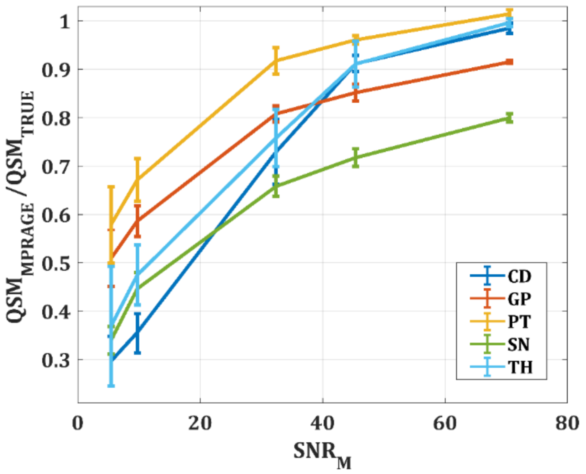

***Figure 2.4**: The ratio of MPRAGE-based QSM to ground-truth QSM simulated at different SNR levels, demonstrating the level of underestimation in MPRAGE-QSM measurements versus SNR.*

2.4.2 In-vivo $\mathrm{QSM_{MPRAGE}}$ Quality and DGM Contrast

Figure 2.5 shows in-vivo images of one subject including standard QSM (A), and QSM from three protocols for MPRAGE (B-D) with increasing TE. On $\mathrm{QSM_{GRE}}$ (**Figure 2.5A**), DGM nuclei have strong contrast, especially iron-rich regions such as GP, DN, SN, and red nucleus (RN). On $\mathrm{QSM_{MPRAGE}}$ however, only GP is adequately observable at the shortest TE of 2.43 ms (**Figure 2.5B**), with clear boundaries depicted from neighboring Internal Capsule. As $\mathrm{CNR_{\emptyset}}$ improves (through longer TE), other iron-rich nuclei achieve better depiction. DN and SN are well depicted in **Figure 2.5C** at TE = 3.50 ms, whereas RN boundaries need longer TE. In the literature, commonly used TEs for MPRAGE at 3T vary between 2.96-4.44 ms (49), where, at least, promising GP contrast on $\mathrm{QSM_{MPRAGE}}$ is expected. Thus, $\mathrm{QSM_{MPRAGE}}$ contrast could be useful for improving GP segmentation. On MPRAGE magnitude, some DGM nuclei such as CD and PT have good T_1w contrast, whereas others with higher iron concentration such as GP, SN, DN, and RN have weak T_1w contrast (**Figure 2.5E**). The hybrid contrast image (**Figure 2.5F**) produced by combining both T_1w and QSM$_{\text{MPRAGE}}$ contrast for TE of 3.5 ms shows improved contrast of GP, SN, and DN while preserving the T_1w contrast of other regions. On QSM$_{\text{MPRAGE}}$, artifacts are observed near low-SNR regions (CSF, brain edges, and around veins), and these artifacts get attenuated as CNR$_{\emptyset}$ improves. On the hybrid contrast, these artifacts fall mainly in and near the low-SNR CSF regions, and thus intensity in these regions deviates from typical values. In simulations, artifacts are more pronounced than in vivo (**Figure 2.12**) as the simulations did not exactly match the in-vivo experiments that had GRAPPA/partial Fourier accelerations, elliptical filtering, background field, partial volume, etc.

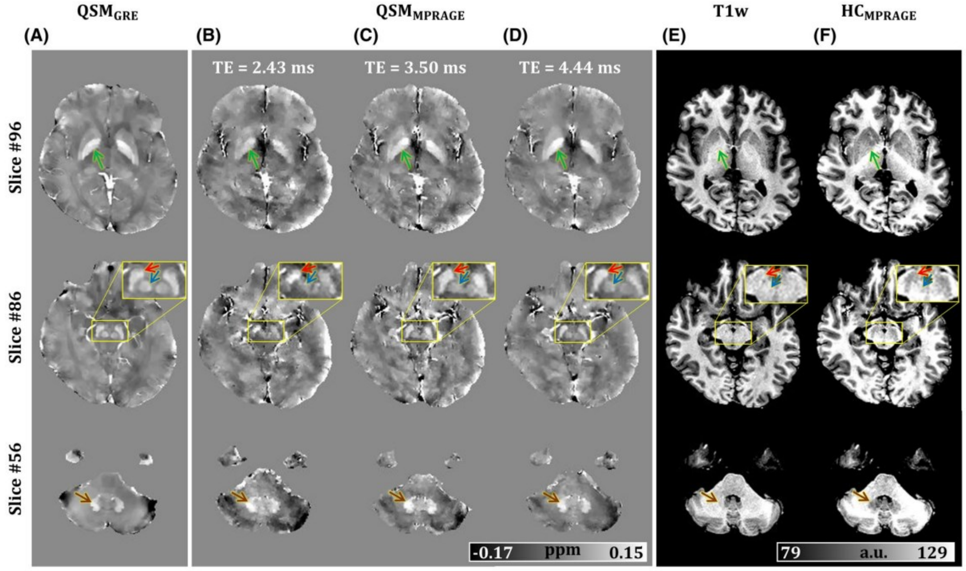

Figure 2.5: *Contrast of deep gray matter (DGM) nuclei on (A) QSM$_{\text{GRE}}$, (B-D) QSM$_{\text{MPRAGE}}$, (E) T_1w and (F) HC$_{\text{MPRAGE}}$. Globus pallidus (GP; green arrow), substantia nigra (SN; red arrow), red nucleus (RN; blue arrow), and dentate nucleus (DN; brown arrow) have higher contrast on quantitative susceptibility mapping (QSM), as shown in (A-D), and their contrast enhances with longer echo time (TE). These nuclei typically have weak contrast on magnetization-prepared rapid gradient echo (MPRAGE) magnitude images (E). Hybrid contrast in (F) was produced by combining T_1w contrast (E) and QSM$_{\text{MPRAGE}}$ with TE = 3.50 ms (C). (B) shows that using TE as short as 2.43 ms could be sufficient to improve GP segmentation. MPRAGE data has 1-mm isotropic resolution.*

2.4.3 **Susceptibility Quantification**

Figure 2.6 illustrates the differences in susceptibility quantification between QSM_{GRE} and QSM_{MPRAGE} for six DGM structures. Note that GRE images have lower spatial resolution (~ × 0.5) in the B_0 direction, which might introduce underestimation in QSM_{GRE} measurements (196). However, scatter plots in **Figure 2.6A**, for the main dataset of 40 subjects, showed consistent underestimation of susceptibility using QSM_{MPRAGE}. This underestimation can be attributed to the low $CNR_{\emptyset}$ of this dataset. GRE data have ~4.9 higher $CNR_{\emptyset}$ (~2 gain from SNR_M and ~$\sqrt{6}$ gain from multiple echoes) than MPRAGE, and this CNR effect seems to be dominant over the effect of the lower resolution in the B_0-direction. The mean susceptibility difference over 40 subjects is below 0.020 ± 0.014 ppm for all structures except SN (**Figure 2.6B**). Although SN is an iron-rich structure, it has the highest difference mainly due to its small size and lower SNR.

The other 3-subject dataset at 1-mm isotropic resolution was used to explore possible improvement in quantification at higher $CNR_{\emptyset}$. **Figure 2.6C** shows a general trend of lower differences with longer TEs. The greatest improvement was observed in GP with mean susceptibility difference being reduced to below 0.008 ± 0.004 ppm and 0.005 ± 0.005 ppm for TE of 3.50 ms and 4.44 ms, respectively. Less improvement was observed in other structures with differences staying around 0.015 ± 0.009 ppm at TE of 4.44 ms. Furthermore, the unexpected increase in differences of some nuclei (CD and TH for instance) at 1-mm resolution compared to 0.87-mm originates from the larger statistical sample (i.e., 40 vs 3) and the wider age spectrum (i.e., higher susceptibility/CNR at older ages) of the 40-subject dataset.

Results reflect that within practically achievable SNR, QSM_{MPRAGE} could give reasonable estimates for only DGM structures of strong susceptibility and large size. Both simulation and experimental results showed a trend of accuracy improvement with higher $CNR_{\emptyset}$. Although simulation results showed that structures like CD, PT, and TH can achieve less than 0.005 ppm error with $CNR_{\emptyset}$ of 2.0, higher error levels were observed in in-vivo measurements. This difference could be attributed to the ideal setup assumed in simulations that uses perfect segmentation masks and does not require background removal nor accounts for coil sensitivity and combination issues.

(A) Scatter plots for 0.87-mm 40-subject dataset

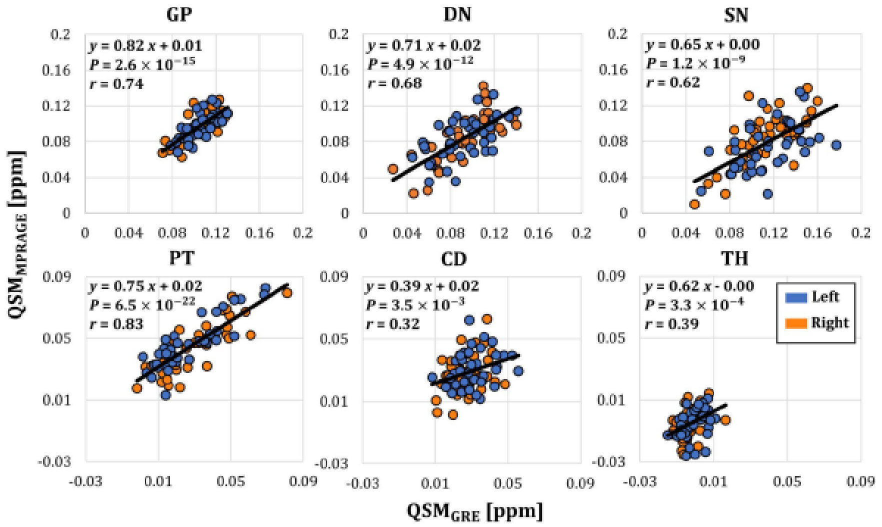

(B) Mean differences for 0.87-mm 40-subject dataset

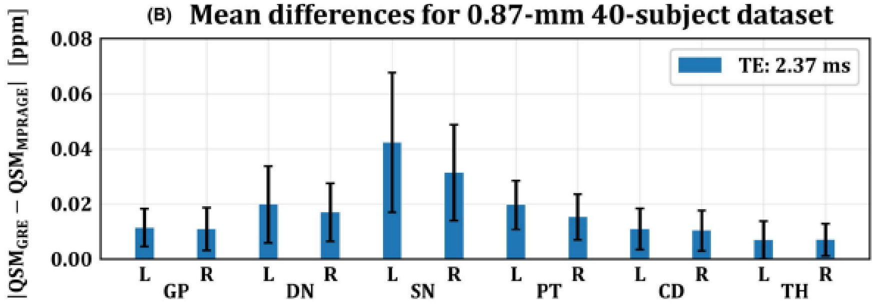

(C) Mean differences for 1-mm 3-subject dataset

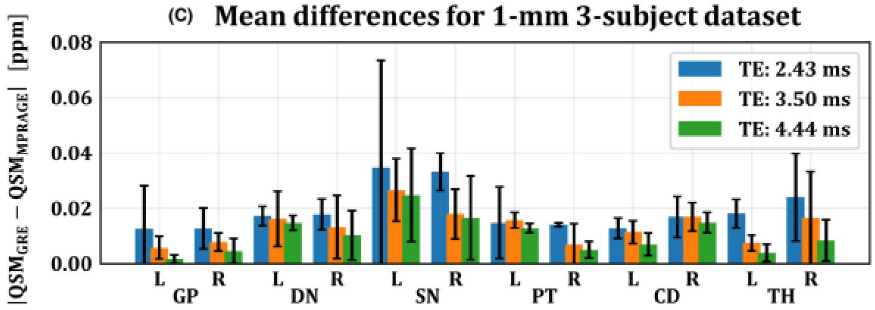

Figure 2.6: *(A) Scatter plots comparing mean susceptibility values (ppm) of six deep gray matter (DGM) structures measured on QSM_{GRE} and QSM_{MPRAGE} of the 40-subject dataset (spatial resolution of 0.87×0.87×0.85 mm^3). Linear regression is represented by a solid line described by the equation, P value, and Pearson correlation coefficient (r) listed on each plot. Plots in the lower row are zoomed in. (B) Mean absolute differences between the measurements in (A). (C) Mean absolute differences at longer echo times (TEs) illustrated using the three-subject dataset of 1.00×1.00×1.00 mm^3 resolution. Measurements on the left (L) and the right (R) hemispheres are reported separately.*

2.4.4 Segmentation Performance

Figure 2.7 illustrates T$_1$w, HC and QSM contrasts of two subjects. Structures like CD and PT already have high contrast on T$_1$w and benefit much less from QSM inclusion. On T$_1$w images, the SNR is as low as 31, due to the very high resolution (0.64 mm^3 voxel volume) and the parallel imaging acceleration (GRAPPA = 3) employed in collecting the MPRAGE data. Combined with a short TE of 2.37 ms, the low CNR$_{\varnothing}$ of this data (~ 0.8-2.7) limits the quality of QSM$_{\text{MPRAGE}}$. At this SNR level, structures other than GP are far below the required CNR$_{\varnothing}$ threshold (i.e., > 3.0) determined by simulation and thus are not visible on QSM$_{\text{MPRAGE}}$. The susceptibility difference between PT and GP is not even enough to sharply depict the boundary between them on QSM$_{\text{MPRAGE}}$. However, the less visible and problematic edge on T$_1$w contrast is the edge between GP and internal capsule that is sufficiently delineated on QSM$_{\text{MPRAGE}}$. Therefore, despite the limited quality, QSM$_{\text{MPRAGE}}$ improves GP visibility on HC$_{\text{MPRAGE}}$ and permits better segmentation for this structure. Thus, in the rest of this section, segmentation performance analysis was focused on GP alone.

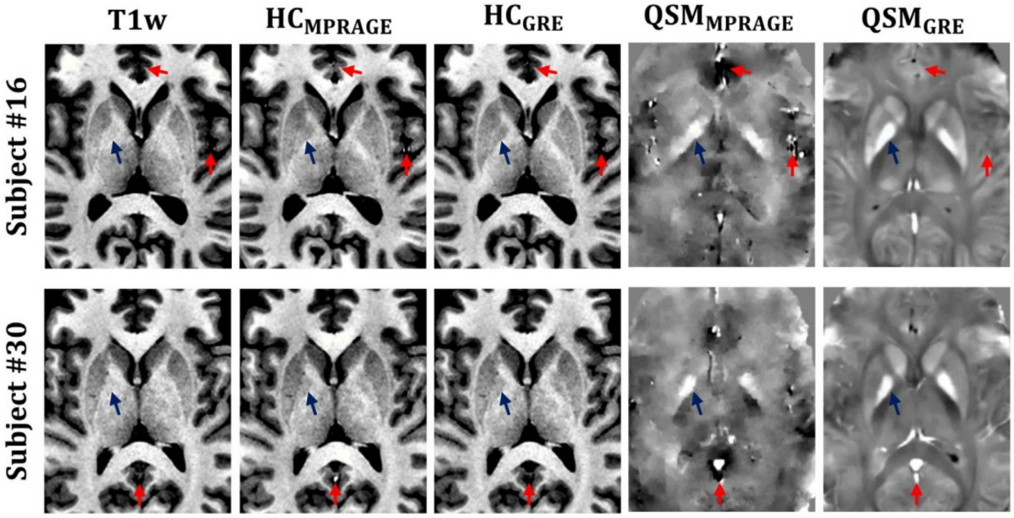

Figure 2.7*: Axial views of T$_1$w, hybrid, and quantitative susceptibility mapping (QSM) contrasts for two subjects. Globus pallidus (GP) visibility was improved on HC$_{MPRAGE}$ images, similar to HC$_{GRE}$. QSM$_{MPRAGE}$ helps emphasize the edge between GP and internal capsule (blue arrows), even though overall quality of QSM$_{MPRAGE}$ is limited. Artifacts near low signal-to-noise ratio (SNR) regions (red arrows) can alter intensity in the corresponding locations on HC$_{MPRAGE}$. Magnetization-prepared rapid gradient echo (MPRAGE) data has 0.87×0.87×0.85 mm^3 resolution and echo time (TE) of 2.37 ms.*

Figure 2.8 demonstrates GP segmentation outputs of the same two subjects. Compared to only using T_1w contrast, incorporating QSM contrast improved GP segmentation (green arrows) in both subjects. Segmentations obtained by employing QSM_{MPRAGE} are comparable to those obtained using QSM_{GRE}. When only magnitude contrast is utilized, GP structures were under-segmented, more severely in subject #16, leading to underestimating the actual GP volume. Red arrows indicate regions that are less accurately segmented even when QSM contrast was utilized.

Segmentation improvements are reported quantitatively in **Figure 2.9A**. With reference to the results obtained using HC_{GRE}, utilizing QSM_{MPRAGE} significantly outperformed T_1w-based segmentation on all measures. Furthermore, deviation in segmentation across all subjects is less pronounced with QSM_{MPRAGE}. The lower scores of T_1w-based segmentations on both FND and AVD indicate under-segmentation of the GP structure and discarding portions of its volume. On FPD, both approaches have > 0.9 scores, with a statistical improvement for HC_{MPRAGE}, reflecting that both approaches tend to not over-segment GP (i.e., to not include many voxels from other neighboring tissues).

Figure 2.9B illustrates that incorporating QSM_{MPRAGE} contrast improved Dice scores of GP segmentation across all subjects. GP volume measurements in **Figure 2.9C** show that both HC_{MPRAGE} and HC_{GRE} give comparable volume estimates (Pearson correlation $(r) = 0.95$), while relying only on magnitude contrast leads to underestimation ($r = 0.71$). The no-reference analysis shown in **Figure 2.10** illustrates the similarity between the predicted GP volumes from the quadratic probabilistic model and the measured volumes, with both HC segmentation methods having substantial improvements over pure T_1w contrast. The latter underestimates predicted GP volumes, as most of the T_1w measurements are below the identity dashed line.

2.5 DISCUSSION

We created QSM_{MPRAGE} from standard MPRAGE phase at 3T and explored two possible applications: susceptibility quantification and segmentation enhancement for iron-rich DGM structures that normally have weak contrast on MPRAGE magnitude. Simulation results revealed that the low phase CNR present in MPRAGE confines the applications of QSM_{MPRAGE} to DGM nuclei of extremely high iron concentration, such as GP. Segmenting GP based on T_1w is problematic and previous studies have proposed incorporating QSM contrast from a GRE sequence in the segmentation pipeline and demonstrated its effectiveness for GP against using T_1w contrast alone (122,167–169). The additional contrast information from QSM can be processed independently or alternatively combined with T_1w magnitude to produce a single contrast-improved image. We used the latter approach in this work and demonstrated a significant improvement at 3T in GP segmentation over using T_1w-only contrast. We showed that comparable improvement in GP segmentation can be achieved using QSM_{MPRAGE} without the need for an additional GRE acquisition, which is normally not included in most brain exams. Generated QSM from MPRAGE phase is intrinsically registered to the MPRAGE magnitude and thus avoids the need for registration and associated translation and interpolation errors. Results showed that relying only on T_1w contrast can lead to misestimation of GP volume. Without enough contrast, the segmentation algorithm tends to outline GP boundaries blindly based on the shape and the size observed in the training datasets. The reference-free analysis also showed that the T_1w-alone method has the highest error with a noticeable tendency to underestimate GP volume.

In addition to being helpful for improving segmentation, QSM_{MPRAGE} contains valuable information by itself as a stand-alone technique for quantifying susceptibility of iron-rich structures. Our results demonstrated that QSM_{MPRAGE} with typical TE range can estimate mean susceptibility of iron-rich DGM nuclei with overall 0.020 ± 0.014 ppm error compared to QSM_{GRE}. The low CNR of QSM_{MPRAGE} introduces underestimation in the susceptibility measurements, with best results in iron-rich structures of large size, such as GP and DN. Utilizing longer TE improves $CNR_{\emptyset}$ and permits better quantification accuracy. However, longer TE generally decreases magnitude SNR and increases T_2* weighting. Nevertheless, this limited quality QSM_{MPRAGE} still provides a susceptibility quantification opportunity for imaging protocols without a standard QSM acquisition.

This work further investigated the effect of the inversion pulse on the quality of MPRAGE phase and QSM. Simulation results revealed limited artifacts around the edges of low SNR regions. These artifacts did not significantly disturb QSM reconstruction. In addition, these artifacts can be further minimized by estimating the inconsistent portion of k-space with techniques like those employed in partial Fourier acquisition (197). Note that the simulation of MPRAGE considered a linear ordering of k-space phase encoding. If centric ordering is used for instance, the k-space inconsistency will be between the low and the high frequency regions, instead of being confined within the high frequency region alone. In this scenario (and others like radial encoding), artifacts and the means to handle them will be different. In 3T experimental data, artifacts were observed around CSF, veins and brain volume edges, and the artifacts were less apparent as $CNR_{\emptyset}$ improved. These artifacts and other intensity variations on QSM_{MPRAGE} propagate into HC_{MPRAGE} and thus could affect the segmentation of structures other than GP. A simple approach to address this issue is segmenting structures that have good contrast based on T_1w image alone and using HC_{MPRAGE} only to segment structures that normally have weak contrast like GP.

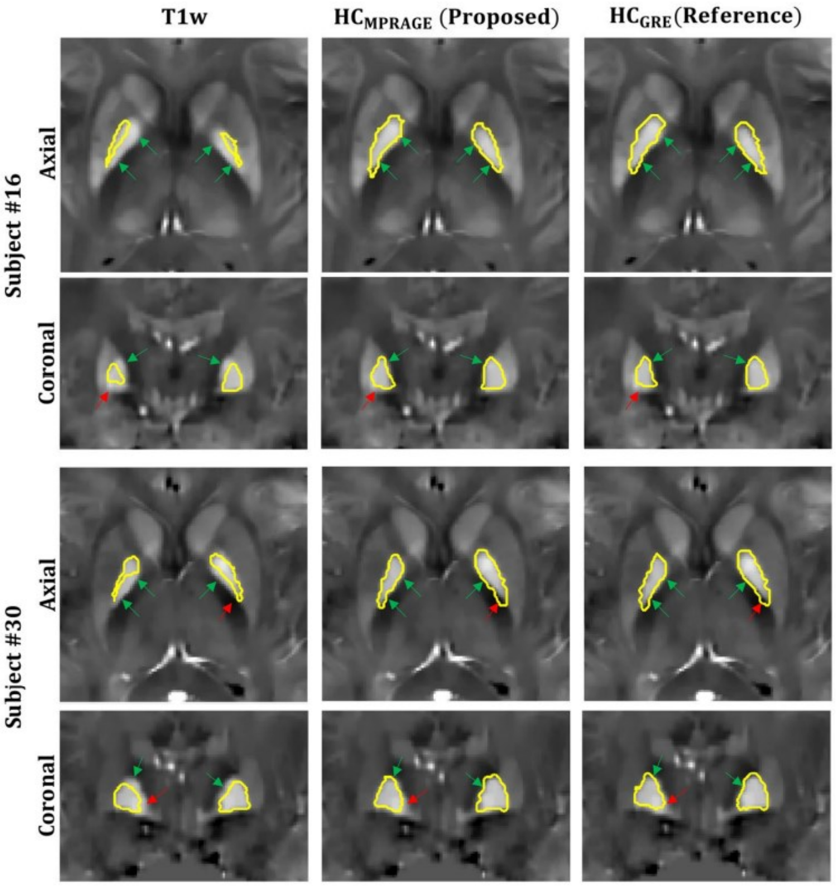

Figure 2.8*: Comparison between FSL segmentation outputs obtained using three different input contrasts. Axial and coronal views of QSM_{GRE} for two subjects are shown with globus pallidus (GP) boundaries (obtained from segmentation) being outlined with yellow color. Segmentations shown in left, middle, and right columns are obtained using standard magnetization-prepared rapid gradient echo (MPRAGE) T_1w contrast, hybrid contrast HC_{MPRAGE}, and hybrid contrast HC_{GRE}, respectively. Employing both T_1w and quantitative susceptibility mapping (QSM) contrasts improved GP segmentation (middle and right columns). Green arrows indicate some regions of improved segmentation, and red arrows point to less improved regions.*

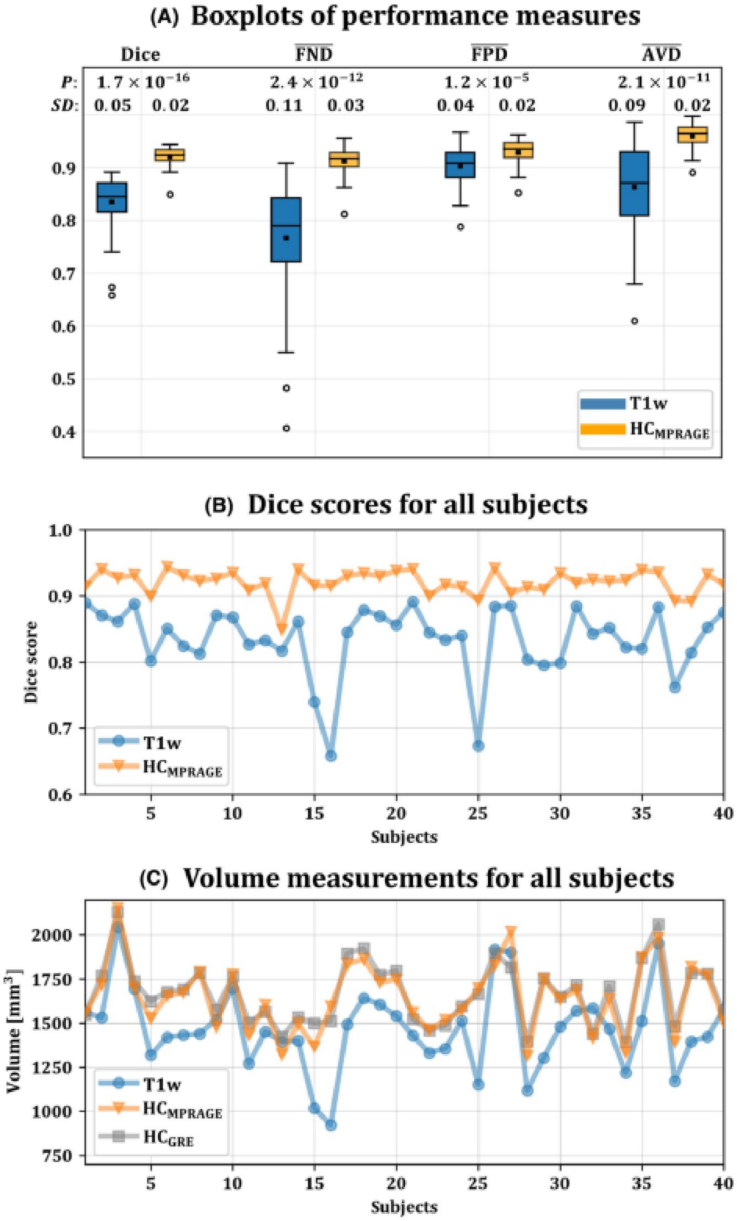

Figure 2.9: *(A) Boxplots of globus pallidus (GP) segmentation performance measures obtained using the 40-subject dataset. Measures are calculated with reference to* HC_{GRE} *segmentation. On all measures, GP segmentations obtained using* HC_{MPRAGE} *are more similar to the reference than those obtained using* T_1w *contrast, with significantly smaller deviations. Standard deviation (SD) and statistical significance (P) values of improvement are listed above boxplots. Squares and circles represent means and outliers, respectively. (B) Dice scores and (C) volume measurements of GP segmentation for all subjects. Segmentation using* T_1w *contrast (blue line) tends to provide smaller volumes.*

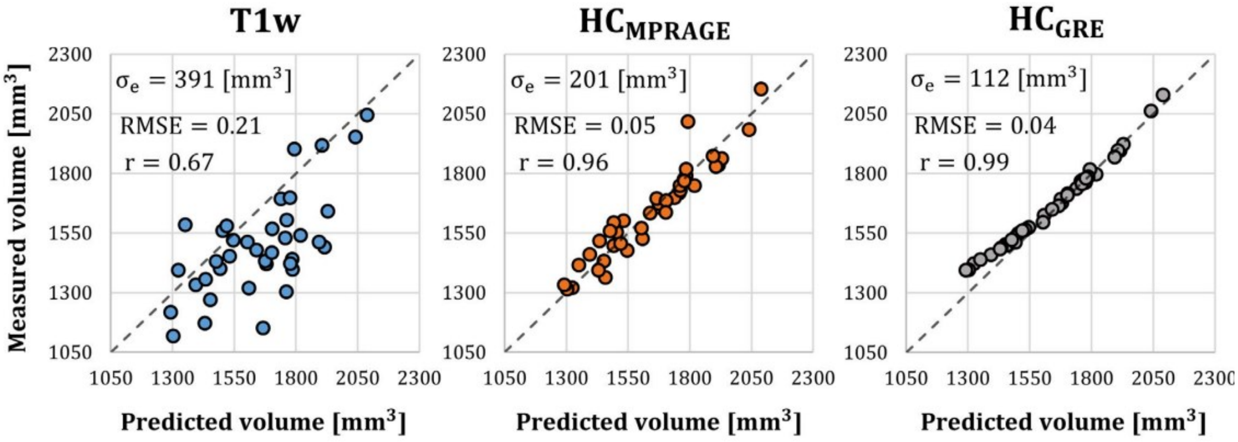

Figure 2.10: *Reference-free performance analysis. Measured globus pallidus (GP) volumes from studied segmentation methods are plotted against predicted volumes from the quadratic probabilistic model. Associated error standard deviation (σ_e), root-mean-square error (RMSE), and Pearson correlation coefficient (r) are given on top of each plot. This analysis demonstrates quantitative susceptibility mapping-based hybrid contrast (HC) methods are more precise than* T_1*w alone.*

We used simulation also to investigate the effect of CNR$_\emptyset$ on the quality of obtained QSM, with the aim to specify a minimum requirement for an acceptable quality. Results showed that segmentation accuracy has dependencies on both the size and the susceptibility strength of the structure. DGM nuclei with smaller size or/and lower iron concentration will require more CNR$_\emptyset$ to achieve adequate segmentation accuracy. Having large size and the highest iron concentration within basal ganglia, GP would require CNR$_\emptyset$ of 3.0 for good segmentation. For the experimental 3T datasets used in the analysis, magnitude SNR around GP was 31.4 and TE was 2.37 ms, making the CNR$_\emptyset$ (~2.7) slightly below 3.0. This dataset was obtained using a fast high-resolution MPRAGE sequence optimized for imaging the cortical layer (with 0.87×0.87×0.85 mm^3 resolution, GRAPPA = 3, acquired in 3.65 min). Nevertheless, the limited-quality QSM obtained from the phase of this low-CNR data contributed significantly to improving GP segmentation, with a better performance being expected at higher CNR levels. Note that QSM contrast is sensitive to the chosen processing setup (198), and thus numeric values given above can deviate depending on the employed processing steps and parameters.

New MPRAGE versions have been proposed recently, known as MP2RAGE (199,200), MPnRAGE (201), and ME-MP2RAGE (176–178), which use two or more inversion times and may collect multiple echoes. For versions such as MP2RAGE, that maintain a single short TE for both optimal SNR and T_1w contrast, the same methods used here could be applied. When multiple echo times are collected including long echo times, a more standard multi-echo QSM reconstruction can be performed. This extended multi-echo MP2RAGE version however requires longer acquisition time for the increased number of echoes sampled along the T_2* decay after each RF pulse and is not standard practice in most brain studies that seek a rapid MPRAGE with strong T_1w contrast without substantial T_2* contamination. For example, acquiring 4 echoes after each RF pulse would quadruple the TR of each encoding, which would limit the number of readouts under the transient conditions of inversion recovery. Furthermore, prolonging encoding TR increases the blurring caused by T_1-recovery modulation.

Limitations of this study include demonstrating segmentation improvement using only a single iron-rich DGM nucleus, GP. This structure was the focus because it is typically poorly visualized and poorly segmented on T_1w images and has been shown to have the greatest benefit from a dual (T_1w+QSM_{GRE}) segmentation approach (168). Furthermore, it has the highest iron concentration of the main basal ganglia structures, making it amenable to short echo-time QSM. Although this work used one scenario to utilize the inherent contrast in MPRAGE phase, better utilization is expected using more sophisticated segmentation algorithms (169). Another limitation is not using manual segmentation as a reference standard because our main goal was to compare segmentation quality to independent acquisitions of (T_1w+QSM_{GRE}) which has previously reported improved results (122,168,169). In addition, (T_1w+QSM_{GRE}) superiority was assessed using reference-free performance ranking.

2.6 CONCLUSION

This study explored QSM produced from MPRAGE phase, thus using a common brain imaging sequence rather than requiring a specialized QSM acquisition. This QSM_{MPRAGE} improved the segmentation of GP that has poor contrast on T_1w images. Results showed that both GP segmentation and volume quantification were significantly improved when both T_1w and QSM_{MPRAGE} contrasts from MPRAGE are employed. In addition, QSM_{MPRAGE} provides access, though limited, to explore and quantify susceptibility of iron-rich regions in clinical protocols that do not include multi-echo GRE acquisition.

2.7 Acknowledgements

This work was supported by the Canadian Institutes of Health Research (grant number MOP 102582), the Natural Sciences and Engineering Research Council of Canada (grant number RGPIN-2017-04006), and the University of Alberta Hospital Foundation and the Women & Children's Health Research Institute for the Alberta 300 study. We thank Peter Seres for assistance in data selection and reconstruction. Some plots in this work were produced using Matplotlib (202).

2.8 Appendix

2.8.1 Background Field Removal

Tissue frequency shift due to tissue-induced field was extracted using RESHARP (Regularization Enabled Sophisticated Harmonic Artifact Reduction for Phase) (76). For both MPRAGE and GRE, a kernel radius of 3 mm was used. Tikhonov regularization parameter was 1×10^{-3} for GRE, and 5×10^{-4} for MPRAGE data.

2.8.2 Susceptibility Reconstruction

Susceptibility maps were reconstructed using the iterative total variation inversion algorithm in the spatial domain. Regularization parameter (λ) for GRE data was set to 5×10^{-4}. However, MPRAGE data has lower SNR and thus higher regularization was required (see **Figure 2.11**). Regularization parameters of 2×10^{-3} and 6×10^{-3} were used for the MPRAGE data of resolution $1.00\times1.00\times1.00$-mm^3 and $0.87\times0.87\times0.85$-mm^3 respectively. The code files for background field removal and susceptibility reconstruction can be found at https://github.com/sunhongfu/QSM/tree/master/Siemens_3T.

2.8.3 Artifacts in Simulation versus In-vivo

Figure 2.12 shows that the low-SNR artifacts observed in simulations are also found in tissue field maps acquired in-vivo. However, these artifacts are less pronounced (smoother) in-vivo mainly because simulations did not exactly match the experimental setup, which included further processing such as GRAPPA, partial Fourier, elliptical and spatial filtering. Also, the simulation phantom has sharp transitions between tissues and did not consider partial volume effects nor background field effects. Moreover, relaxation effects (both T_1 and T_2*) were applied readout-by-readout (instead of real-world point-by-point) to simplify simulations (i.e., number of FFTs/IFFTs). Nevertheless, the simulations clarify the problematic issues. These low-SNR artifacts are further reduced in the final susceptibility map due to the use of spatial regularization (see **Figure 2.11**).

In addition, the in-vivo tissue field map has artifacts near brain boundaries arising from unsuccessful removal of background field. These artifacts can be minimized by proper masking and selection of kernel radius during the background field removal step.

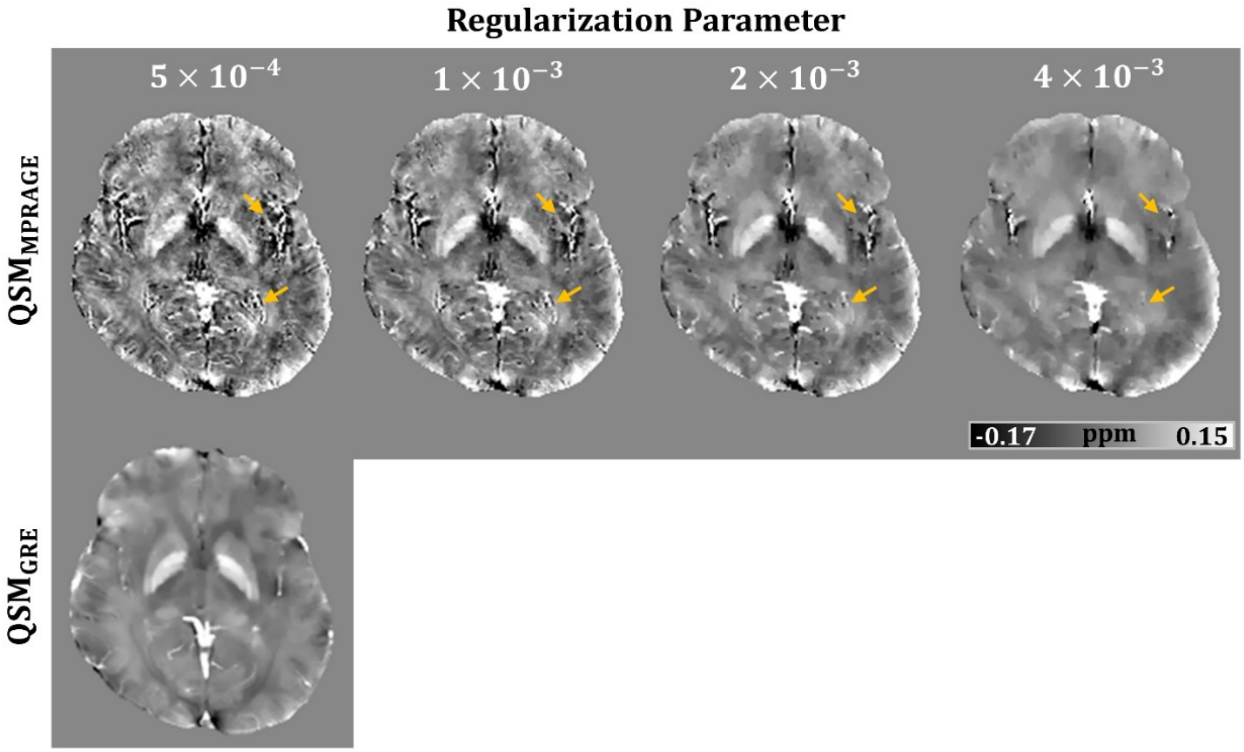

Figure 2.11: *Illustration of regularization parameter (λ) effect on reconstructed QSM.* QSM_{MPRAGE} *has lower SNR/CNR than* QSM_{GRE} *and requires a higher level of regularization. Higher* λ *values reduced artifacts found in* QSM_{MPRAGE} *around low-SNR regions such CSF and veins (orange arrows). MPRAGE data has 1-mm isotropic resolution and TE of 3.50 ms.*

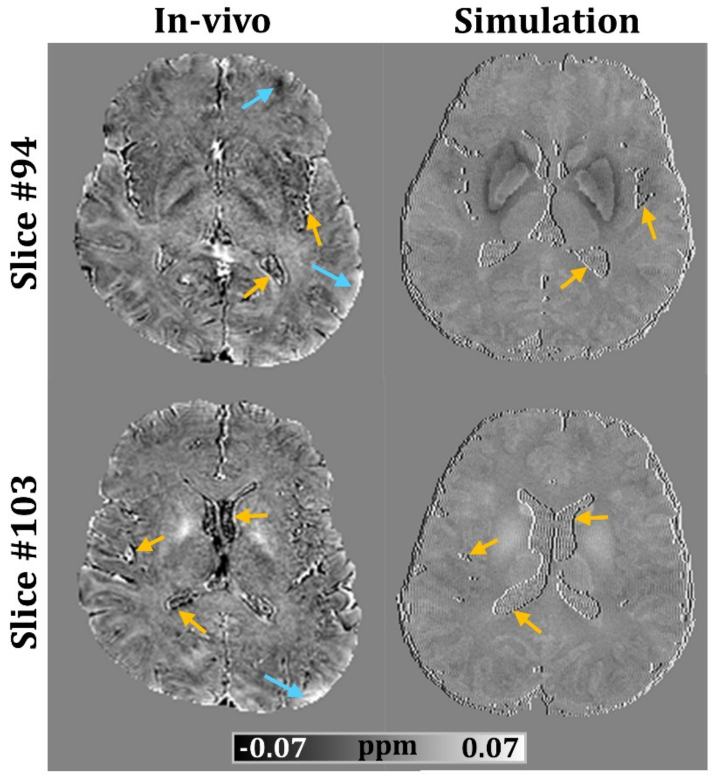

Figure 2.12*: Comparison between artifacts found in-vivo and simulation. tissue field maps of both cases show artifacts around low-SNR regions (orange arrows). Additionally, the in-vivo tissue field map has artifacts near brain edges (blue arrows) originating from remnant background field. In-vivo MPRAGE data has 1-mm isotropic resolution and TE of 3.50 ms.*

Chapter 3: Quantifying cerebral microbleeds using MPRAGE-QSM[1]

3.1 Abstract:

Purpose: T1-weighted magnetization-prepared rapid gradient-echo (MPRAGE) is commonly included in brain studies for structural imaging using magnitude images; however, its phase images can provide an opportunity to assess microbleed burden using QSM. This potential application for MPRAGE-based QSM was evaluated using in-vivo and simulated measurements. Possible factors affecting image quality were also explored.

Methods: Detection sensitivity was evaluated against standard multi-echo gradient-echo (MEGE) QSM using 3T in-vivo data of 14 subjects with 106 confirmed microbleeds. The two methods were compared based on the microbleed size and susceptibility measurements. In addition, simulations explored detection sensitivity of MPRAGE-QSM at different representative field strengths, echo times, and voxel aspect ratios using microbleeds of different size, susceptibility, and location.

Results: In-vivo, microbleeds appeared to be smaller (×0.54) and of higher mean susceptibility (×1.8) on MPRAGE-QSM than on MEGE-QSM, but total susceptibility estimates were in closer agreement (slope:0.97, r^2:0.94) and detection sensitivity was comparable. In simulations, QSM at 1.5T had low contrast-to-noise ratio that obscured the detection of many microbleeds. SNR levels at 3T and above resulted in better contrast and increased detection. The detection rates for microbleeds of minimum 1-voxel diameter and 0.4 ppm susceptibility were 0.55, 0.80, and 0.88 at SNR levels of 1.5T, 3T, and 7T respectively. Size and total susceptibility estimates were more consistent than mean susceptibility estimates, which showed size-dependent underestimation.

Conclusion: MPRAGE-QSM provides an opportunity to detect and quantify the size and susceptibility of microbleeds of at least 1-voxel diameter at $B_0 \geq 3T$ with no additional cost, when standard T_2*-weighted images are not available. The total susceptibility measure is more robust against sequence variations and might allow combining data from different protocols.

Keywords: Microbleed, QSM, MPRAGE, 3T.

---

[1] A portion of this chapter was presented as an abstract in: *Naji N, Gee M, Jickling GC, Camicioli R, and Wilman AH. Quantifying Cerebral Microbleeds using MPRAGE-based QSM. ISMRM 28th Annual Meeting & Exhibition, online, 2020: abstract #1760.*

3.2 INTRODUCTION

Cerebral microbleeds (CMBs) are chronic, tiny blood leakages associated with several neurological diseases including Alzheimer's disease, cerebral amyloid angiopathy (CAA) and vascular dementia (203–205). CMBs prevalence increases with age and can be found in healthy elderly populations (206–209). Their shape is typically defined to be round or ovoid with size up to 10 mm on T_2*-sensitive imaging (204). The CMB distribution in the brain varies from disease to disease, with predominance in deep regions in hypertension related diseases and in lobar regions in Alzheimer's disease and CAA (206,210). Therefore, localizing CMBs and quantifying their size and iron content can help in characterizing, assessing the severity and monitoring the progression of the underlying illness. Furthermore, knowing the CMB burden can help in assessing the safety of antithrombotic medications and in therapeutic management (211).

CMBs are mainly hemosiderin deposits that appear as homogeneous hypointense foci on T_2*-weighted images, owing to their paramagnetic susceptibility property that accelerates spin dephasing and reduces the effective transverse relaxation time (T_2*). Thus, T_2*/susceptibility sensitive MRI techniques are used to detect CMBs and quantify their size; using the magnitude of gradient recalled echo (GRE) images for instance, or incorporating phase information from susceptibility weighted imaging (SWI) to improve contrast and to differentiate between CMBs and diamagnetic mimics (212). However, the detection and the size of CMBs on GRE and SWI images are affected by several acquisition parameters, including: field strength, echo time, spatial resolution and the gap width between slices. As both signal-to-noise ratio (SNR) and susceptibility effects enhance with field strength, the detection sensitivity for CMBs increases significantly at higher field strengths (212–216). Longer echo times permit more spin dephasing and thus intensify the signal loss caused by CMBs on magnitude images; known as the blooming effect. However, the dependence of the CMB size on echo time complicates burden assessment and comparison between different studies. Furthermore, spatial resolution is directly related to partial volume effects and digitization error, consequently the contrast of small CMBs might be missed by averaging in relatively large voxels or by large inter-slice gaps. For this reason, 3D GRE imaging markedly improves the detection sensitivity compared to 2D, by allowing smaller slice thickness (217).

In addition to the dependency on acquisition parameters, quantifying CMB size directly on magnitude or phase images suffers from overestimation as both provide non-localized information caused by magnetic dipole effects. On the other hand, quantitative susceptibility mapping (QSM) is another technique derived from the phase of the T_2*-weighted images that retrieves the underlying susceptibility distribution rather than showing its dipole blooming effects (55,218). QSM is typically derived from multi-echo gradient-echo (MEGE) data and has been employed for assessing the burden of CMBs, providing higher contrast and improved localization accuracy over magnitude-based approaches (140,219,220). Despite increasing interest in QSM, its time-consuming 3D T_2*-based imaging sequence is not nearly as common in brain studies as other MRI modalities such as T1-weighted used for structural imaging.

3D magnetization-prepared rapid gradient-echo (MPRAGE) is a T1-based imaging sequence commonly found in brain studies for volumetry and segmentation purposes, benefiting from the high contrast between gray matter (GM), white matter (WM) and cerebrospinal fluid (CSF) on its magnitude image. MPRAGE phase is an integral part of the sequence that is available at no additional acquisition time, and it can be converted into a susceptibility map. Recently, it was shown that a susceptibility map derived from the phase of the MPRAGE sequence (referred to thereafter as MPRAGE-QSM) can provide sufficient contrast for regions of extreme iron concentration, such as the globus pallidus (221). Employing MPRAGE phase to quantify microbleed load can help in reducing total exam time, as well as allowing microbleed assessment in studies that do not already include T_2*-sensitive sequences. In particular, the predominance of MPRAGE structural imaging in brain studies might open windows for MPRAGE-QSM to further microbleed quantification in larger populations undergoing this standard scan.

We evaluate the potential of MPRAGE-QSM for assessing the burden of CMBs in comparison to the standard MEGE-QSM at 3T, and we use simulations to explore limitations and possible effects of field strength, echo time, resolution and microbleed location on MPRAGE-QSM results.

3.3 METHODS

In-vivo data of subjects with microbleeds were used to evaluate the accuracy of CMB detection and quantification using MPRAGE-QSM in comparison to the standard MEGE-QSM. Additionally, numerical simulations were used to study the ability of MPRAGE-QSM to detect and quantify CMBs of different sizes and susceptibility levels at different field strengths, echo times, voxel aspect ratios, and locations.

3.3.1 In-vivo Study

Fourteen subjects (age 53-89 years, mean ± SD: 69 ± 10 years, 5 females) were studied retrospectively based on the inclusion criteria of having CMBs (identified by an experienced radiologist Dr. Feryal Saad) and the availability of both MEGE and MPRAGE sequences with saved raw phase images. Subjects were recruited from prospective research studies which studied either aging, vascular dementia, or CAA (222,223). All subjects provided informed consent and studies were approved by the local ethics committee. Brain imaging was done at 3T (Prisma, Siemens Healthcare, Erlangen, Germany) with a 20- or 64-channel head coil.

Sagittal MPRAGE images used 0.87×0.87×0.85 mm^3 resolution, FOV 250×250×176.8 mm^3, flip-angle 8°, TR 1800 ms, TI 900 ms, TE 2.37 ms, GRAPPA factor 3, and acquired in 3.65 minutes. Axial MEGE images were all acquired using TE1 3.82 ms, ΔTE 5.5 ms, 240-mm frequency FOV, 0.94×0.94 mm^2 in-plane resolution and GRAPPA factor of 2. Other MEGE parameters had slight variations between two protocols: slice thickness (1.7 vs 2.0 mm), number of slices (88 vs 80), number of echoes (6 vs 7), flip angle (13° vs 17°), TR (37 vs 45 ms), phase FOV (202.5 vs 217.5 mm), and acquisition time (5.50 vs 5.65 minutes). The two sequences (MPRAGE and MEGE) were not always acquired in the same session (43% acquired on same week). The median interval between the two scans was 17 days (range: same day to 3.4 months).

To explore the achievable contrast improvement at a longer echo time, one subject (male, 73 years old) received one additional MPRAGE with TE 4.44 ms and common spatial resolution of 1 mm isotropic acquired in 5.57 minutes. Other imaging parameters were FOV: 256×256×208 mm^3, flip angle: 12°, TI: 950 ms, TR 2170 ms, GRAPPA acceleration: 2, and slice partial Fourier: 6/8.

3.3.2 Numerical Simulation Study

In brain volumetric studies, the MPRAGE sequence collects a single echo at a very short echo time, which limits the achievable SNR and phase contrast. In MPRAGE, the shortest possible TE is typically used, depending upon factors such as the receiver bandwidth, acquisition matrix and fractional echo percentage, as well as RF pulse length, gradient strength and slew rate, with typical TE of 3 ms (range: 2.37 to 4.44 ms) (194,195,224,225). To explore the consequences of the resultant limited phase contrast on CMB detectability, numerical simulations were performed using a brain phantom with typical sequence parameters.

A realistic numerical brain phantom was created based on a 0.33-mm isotropic in-vivo susceptibility map from a healthy subject (226), which was further interpolated into 0.10 mm isotropic spatial resolution. To simulate background field contributions, air regions were added to the susceptibility map in the sinuses and outside the skull. Spherical CMBs of different radii (a in mm: 0.15, 0.25, 0.45, 0.85, 1.75, and 3.45) and susceptibility levels ($\Delta\chi$ in ppm: 0.10, 0.20, 0.40, 0.70, 1.00, 1.50, and 2.00) were added to the susceptibility map in groups of maximum 20 CMBs per experiment. The total volume susceptibility for each susceptibility and radius pair (computed as $4\pi a^3\Delta\chi/3$) is given in **Table 3.1**. The added CMBs were distributed over the whole brain in deep and cortical regions, such that each CMB is tested both near and far from the brain edge. The susceptibility phantom was then used to simulate a field shift map at different echo times (TE in ms: 2.37, 3, 3.5, and 4.44) and field strengths (B_0 in T: 1.5, 3, and 7).

Table 3.1: *Total volume susceptibility [ppm.mm^3] of simulated microbleeds.*

a[mm] / **Δχ [ppm]**	**0.15**	**0.25**	**0.45**	**0.85**	**1.75**	**3.45**
0.10	0.001	0.006	0.038	0.257	2.24	17.2
0.20	0.003	0.013	0.076	0.514	4.49	34.4
0.40	0.006	0.026	0.153	1.029	8.98	68.8
0.70	0.010	0.046	0.267	1.801	15.71	120.4
1.00	0.014	0.065	0.382	2.572	22.45	172.0
1.50	0.021	0.098	0.572	3.859	33.67	258.0
2.00	0.028	0.131	0.763	5.144	44.90	344.0

The resultant data were then down sampled to 0.85 mm isotropic resolution to simulate sub-voxel CMBs and partial volume effects. At this spatial resolution, the diameters of the smallest and the largest CMBs would be equivalent to 1/3 voxel and 8 voxels, respectively. The down sampled data were then used to produce MPRAGE phase and magnitude (**Figure 3.1**) with the following sequence parameters: 8º flip-angle, 208 turbo factor, 208 sagittal slices, 180×249 mm^2 FOV and

212×294×208 matrix size. The inversion time (TI) and repetition time (TR) were adjusted for different field strength based on literature values: TI/TR of 1000/2400 ms at 1.5T, 900/1800 ms at 3T, 1000/3000 ms at 7T (224,225). To investigate the effect of the voxel shape, two through-plane resolutions were tested: 0.85 mm (1:1:1 aspect ratio) and 1.70 mm (1:1:2 aspect ratio). In MPRAGE simulation, a proton density map was synthetically constructed using segmentations of GM, WM and CSF with the following values: 0.807, 0.679 and 1.0 for GM, WM, and CSF respectively. Tissue segmentations were obtained based on the T$_1$w image using the 'fast' tool of the FSL package (227). The proton density map was used as the initial magnetization and exposed to T$_1$ relaxation based on the field strength. T$_1$ values used for different tissues were (GM/WM/CSF) 1200/650/4300 ms at 1.5T, 1600/840/4300 ms at 3T, and 1940/1130/4300 ms at 7T (23,228). The effect of the CMBs on the MPRAGE magnitude was simulated via R$_2$* relaxation, which was approximated as $R_2^* = 127|\Delta\chi| + 23$ at 3T (26), and scaled linearly to other field strengths.

To include noise effects, each setup was repeated 10 times with complex white noise being added to the MPRAGE data in k-space at a specified SNR level. Measured SNR level from in-vivo data at 3T was set as a reference and then adjusted in each run based on the field strength and the voxel size. QSM was then obtained from the MPRAGE phase using the processing pipeline described in Section 3.3.3.

The magnetic field induced by a sphere of $\Delta\chi$ susceptibility and a radius can be calculated at distance r from the center of the sphere using the following analytical expression (24):

$$\Delta B_{sphere}(r) = \frac{1}{3} B_0\, \Delta\chi \left(\frac{a}{r}\right)^3 (3\cos^2\theta - 1) \qquad , r \geq a \tag{3.1}$$

To estimate lower limits on the susceptibility value of a CMB of a given diameter for successful detection, equation (3.1) can be used to calculate the phase shift ($\Delta\emptyset$) introduced by a spherical susceptibility source along the main field direction ($\theta = 0°$):

$$\Delta\emptyset = 2\pi\gamma\, TE\, \Delta B_{sphere}(r) = 2\pi\gamma\, TE \frac{2}{3} B_0\, \Delta\chi \left(\frac{a}{r}\right)^3 \qquad , r \geq a \tag{3.2}$$

Additionally, the introduced phase contrast should be sufficiently above the noise level to be distinguishable from background noise, which can be quantified using phase contrast-to-noise ratio (CNR_ϕ). From equation (3.1), a spherical susceptibility source can induce a phase shift of up to

$2\pi\gamma\ TE\,\frac{2}{3}B_0\ \Delta\chi$ and $2\pi\gamma\ TE\,\frac{1}{3}B_0\ \Delta\chi$ along the directions parallel ($\theta = 0°$) and perpendicular ($\theta = 90°$) to the main field, respectively. The latter can be used in CNR_{ϕ} calculation to ensure that phase contrast is above the noise level in both directions. Given that phase noise is inversely related to the magnitude SNR (SNR_M) (184), CNR_{ϕ} can be expressed as:

$$CNR_{\phi} = 2\pi\gamma\ TE\,\frac{1}{3}B_0\ \Delta\chi \cdot SNR_M \tag{3.3}$$

Simulation results will be used to determine lower bounds for microbleed susceptibility and CNR_{ϕ} that yield successful detection, using equations (3.2-3). Successful detection of a particular CMB is defined as detecting it with a rate ≥ 90% (i.e., detected at least 18 times out of the 20 repetitions).

3.3.3 **QSM Processing**

The following processing steps were used for all simulated and in-vivo data (both MEGE and MPRAGE) unless otherwise stated. A brain mask was obtained from the magnitude of the first echo using brain extraction tool (BET) of the FSL package (64) with 0.4 threshold and 2.0 smoothness factor. ROMEO was used to resolve aliasing in phase images of both sequences (69), which considers both spatial and temporal (if available) phase evolution to unfold phase wraps. For the MEGE data, the average phase of the first five echoes was used in the subsequent steps. Phase contributions from background field were removed using the variable-radius sophisticated harmonic artifact reduction for phase (V-SHARP) data algorithm with a maximum kernel of 12 mm (55,77), and susceptibility maps were produced using total variation dipole inversion (229) with a regularization parameter optimized using the curvature of the L-curve method (230).

3.3.4 **Registration and Measurement**

The in-vivo MEGE-QSM data was transformed into MPRAGE space by rigidly registering the magnitude of the MEGE first echo to the MPRAGE magnitude using the advanced normalization tools (ANTs) package (187), and then applying the resultant transformation coefficients to the MEGE susceptibility map.

For simulated data, measurements were done automatically using spherical masks representing the CMBs. The radius of these masks was expanded to capture any partial volumes and then voxels with values lower than 20% of the maximum susceptibility within the mask were excluded. Area measurement was done on the slice of the highest susceptibility within the 3D mask.

For in-vivo data, each microbleed was manually circumferenced with a spherical mask using ITK-SNAP software v. 3.4.0 (231), and then the mask was refined using the same susceptibility threshold mentioned above. The produced measurement masks were also checked manually and adjusted when needed.

Agreement between measurements was evaluated using linear regression. All processing (except brain extraction, registration, and segmentation), simulations, analyses, and plots were performed using MATLAB (version R2020a; MathWorks, MA, USA).

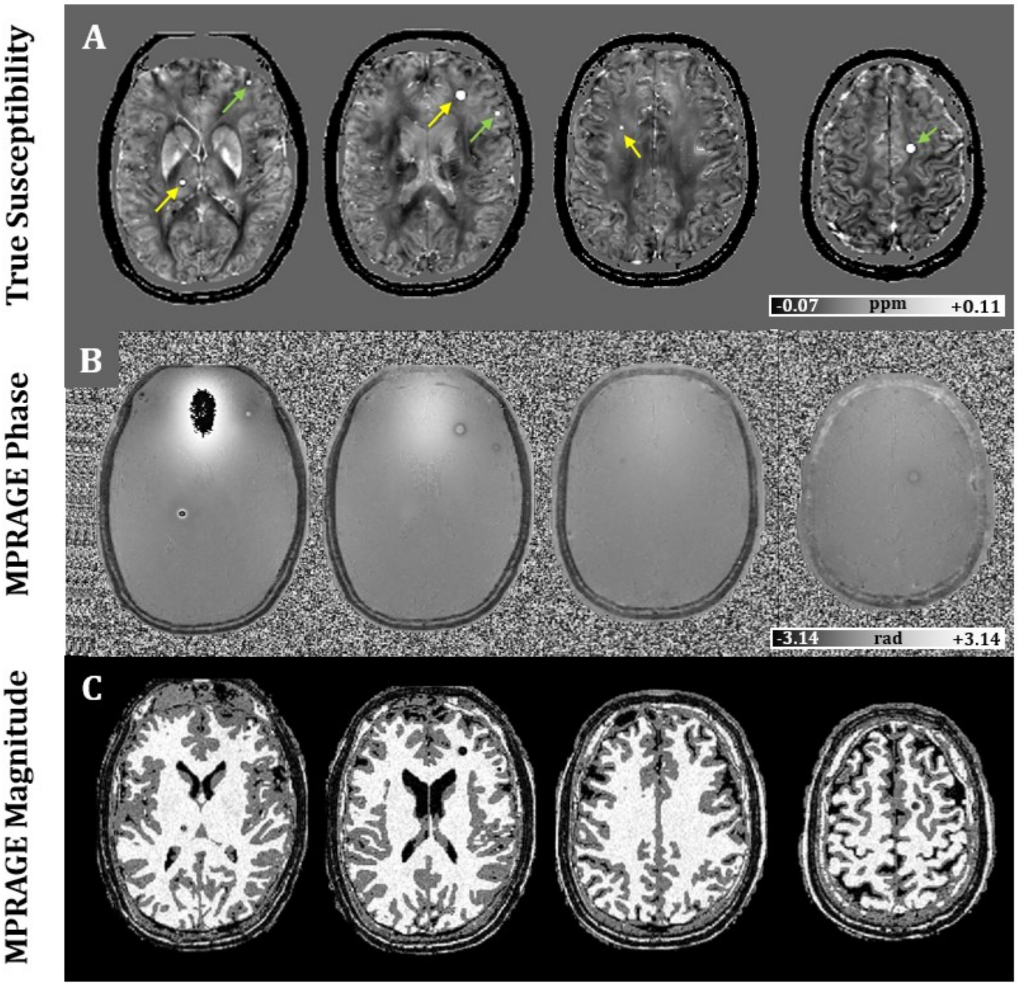

***Figure 3.1**: An illustration of simulated microbleeds of different radii and susceptibility levels shown on multiple axial slices of A) susceptibility map, B) MPRAGE phase and C) MPRAGE magnitude. MPRAGE was simulated at 3T with TI of 900 ms, TE of 4.44 ms, TR of 1800 ms, and 0.85 mm isotropic resolution. Green and yellow arrows indicate microbleed locations in cortical and subcortical regions, respectively.*

3.4 RESULTS

3.4.1 In-vivo Measurements

A total of 106 microbleeds were identified across all subjects using the MEGE magnitude of the fourth echo and confirmed using the corresponding susceptibility map. All these microbleeds were visible on both MEGE- and MPRAGE-based susceptibility maps. Five tiny microbleeds had weak contrast on the MEGE-QSM ($\Delta\chi \sim 0.03$ ppm) and were more visible on the MPRAGE-QSM, while another three tiny microbleeds were less visible on the MPRAGE-QSM ($\Delta\chi \sim 0.07$ - 0.1 ppm) compared to the MEGE-QSM. In general, microbleeds had stronger susceptibility value and smaller size on the MPRAGE-QSM compared to the MEGE-QSM.

Figure 3.2 illustrates the appearance of microbleeds on susceptibility maps obtained from the MEGE and the MPRAGE phase images versus other MRI techniques typically found in neuroimaging protocols. Strong susceptibility sources such as CMBs introduce sufficient phase shift to be depicted clearly on QSM. On the susceptibility maps, microbleeds introduced much higher contrast difference with respect to their vicinity and thus can be easily detected, particularly those of the smallest size that span only few voxels.

In general, the MPRAGE-QSM has lower contrast when compared to the standard multi-echo QSM, and regions of low susceptibility contrast were less visible and missing their sharp edges, more notably in subcortical regions. Nevertheless, the microbleeds size and contrast on MPRAGE-QSM were comparable to the multi-echo QSM and their boundaries were recognizable, as shown in **Figure 3.3**. **Figure 3.4** demonstrates that using longer TE (4.44 ms) and slightly lower resolution (e.g., 1-mm isotropic) at 3T can improve the SNR and boost the contrast of the MPRAGE-QSM remarkably. Quantitatively, microbleeds on MPRAGE-QSM have almost half the size (volume slope of 0.54) as on MEGE-QSM, and nearly twice the mean susceptibility (slope of 1.8), as shown in **Figure 3.5**. However, both methods resulted in comparable total susceptibility estimates (slope of 0.97), which are also the most correlated measurements (r^2 of 0.94). Overall, estimating the microbleed size and susceptibility over the whole volume rather than over a cross-sectional slice resulted in better correlated measurements (e.g., r^2 of 0.91 vs 0.71).

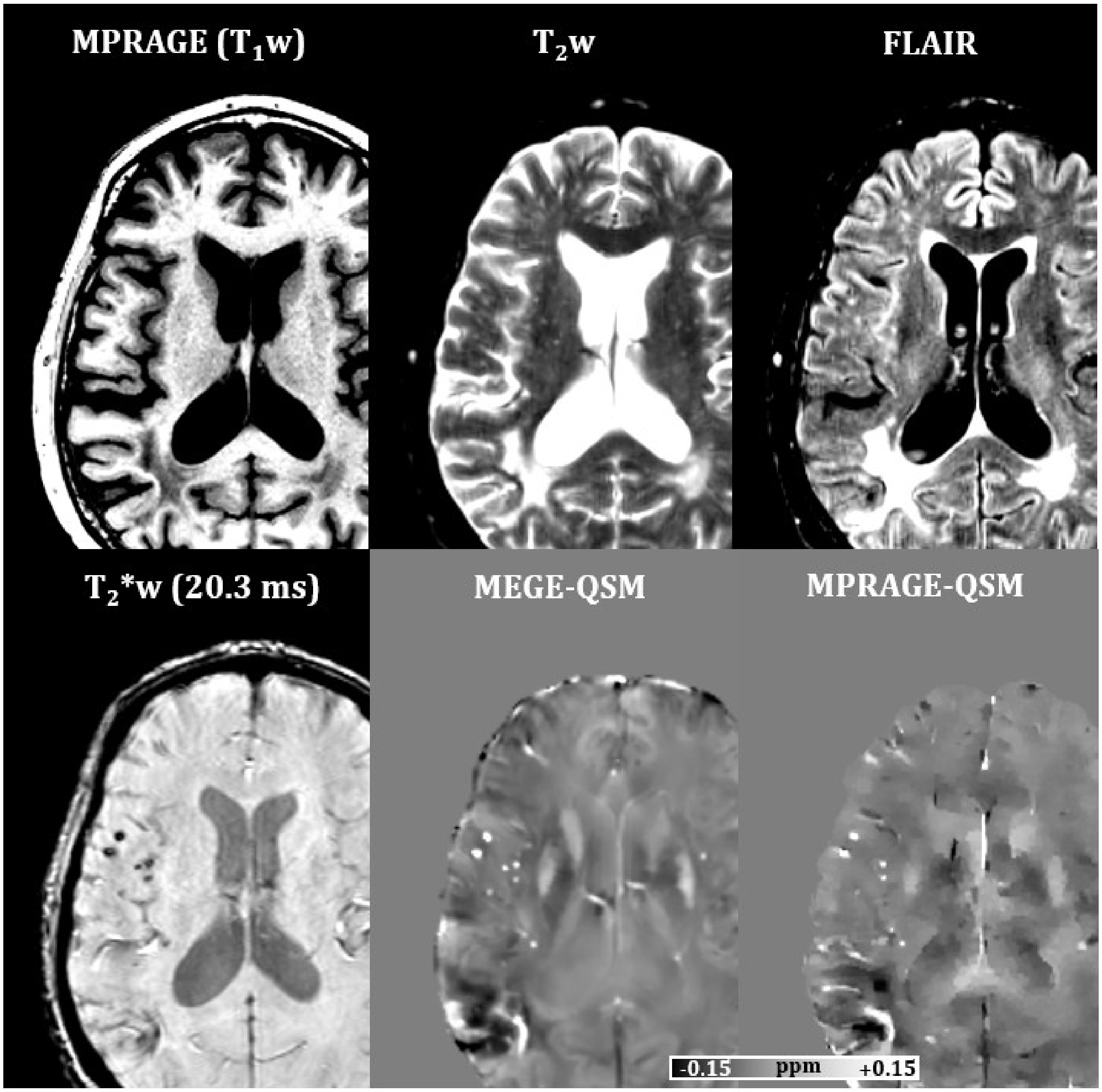

Figure 3.2: *A demonstration of microbleed visibility (60-year-old male) on common MRI modalities (*T_1*w,* T_2*w, FLAIR, and* T_2^**w) versus QSM from MEGE and MPRAGE. Microbleeds are more visible on the susceptibility maps with high contrast to surrounding tissue. Despite the short TE and low SNR, microbleeds of different sizes are well depicted on the MPRAGE-QSM, which required no additional acquisition. Other brain features are better depicted on the standard MEGE-QSM. Due to differences in slice thickness, a few microbleeds that appear on the shown slice of MEGE-QSM are seen on the adjacent slices on the MPRAGE-QSM. The spatial resolution of the MPRAGE is 0.85×0.87×0.87* mm^3*, of the MEGE is 0.94×0.94×2.0* mm^3*, and of* T_2*w and FLAIR is 0.94×0.94×3.0* mm^3*. FLAIR: fluid attenuated inversion recovery.*

3.4.2 Numerical Simulations

Depending on their size and susceptibility, CMBs introduced different levels of phase shift in the MPRAGE phase images, as shown in **Figure 3.1**. The introduced phase shift depends also on the imaging field strength, the echo time, and the spatial resolution of the acquisition. **Figure 3.6** illustrates reconstructed QSM from simulated MPRAGE at different field strengths and echo times and compares it to the ground truth susceptibility map. As the field strength and/or echo time increases, more CMBs are detected and distinguished from the surrounding tissue. At 1.5T SNR levels and with short TE, CNRø in MPRAGE phase is low and reconstructed susceptibility maps are noisy. Nevertheless, CMBs with 1.7 mm diameter (i.e., two-voxel width at 0.85 mm resolution) and 1.0 ppm susceptibility were observable on these images (by visual inspection, after widening the gray scale to distinguish them from noise).

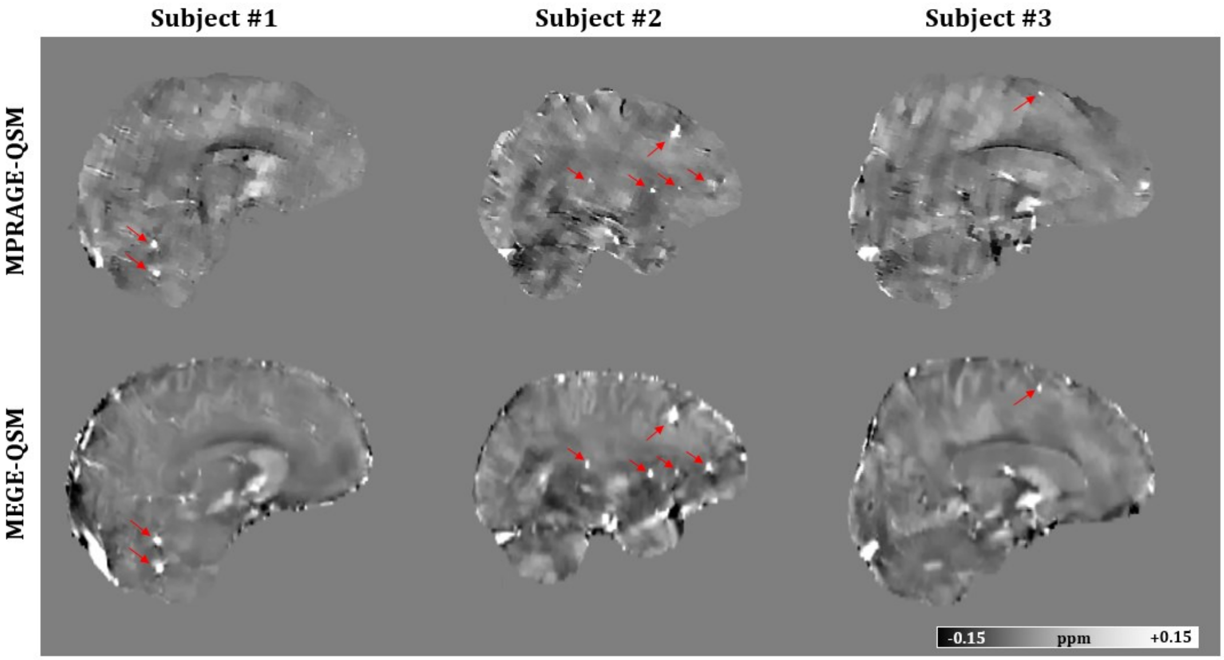

***Figure 3.3**: Sagittal views from three subjects comparing microbleed appearance (indicated by red arrows) in MPRAGE-QSM versus MEGE-QSM. MEGE-QSM images were registered and transformed into the MPRAGE space. On the MPRAGE-QSM, microbleeds have smaller dimensions, more notably in the superior- inferior direction. The brain in each QSM was extracted by a mask from the corresponding sequence, causing some shape differences. The time interval between the two scans was 1 hour, 23 days, and 103 days for subject #1, #2, and #3, respectively.*

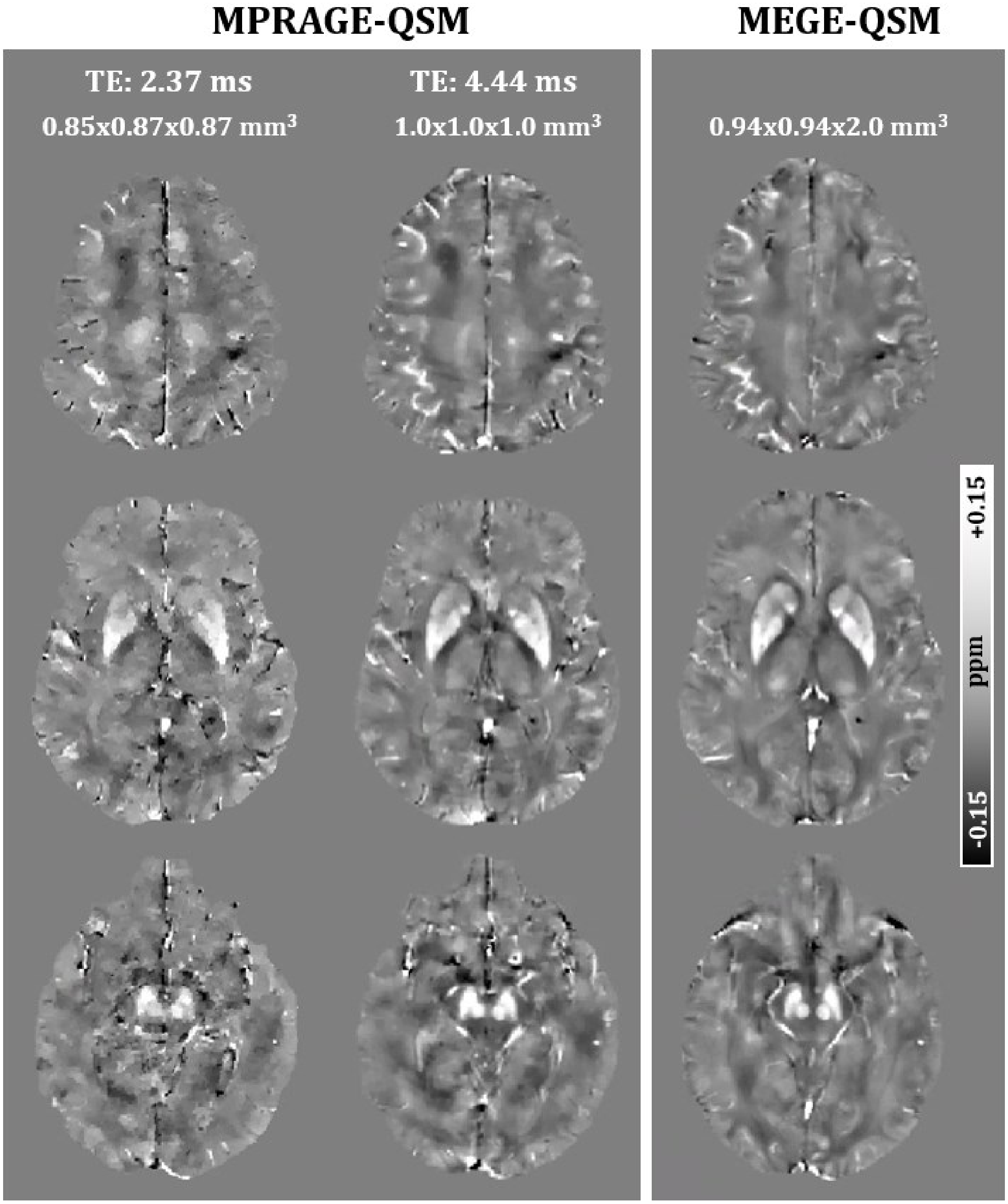

Figure 3.4: *A demonstration of improved MPRAGE-QSM contrast at 3T when the echo time is prolonged to 4.44 ms and the spatial resolution is relaxed to 1-mm isotropic. With very short TE (2.37 ms), MPRAGE-QSM still have good contrast for strong susceptibility sources, however edges are less sharp due to elevated noise level, more notably in the deep regions. Both MPRAGE scans were acquired in the same session in 3.65 and 5.57 minutes respectively. The MEGE scan was acquired in 5.65 minutes, 34 days earlier. Subject is 73-year-old male.*

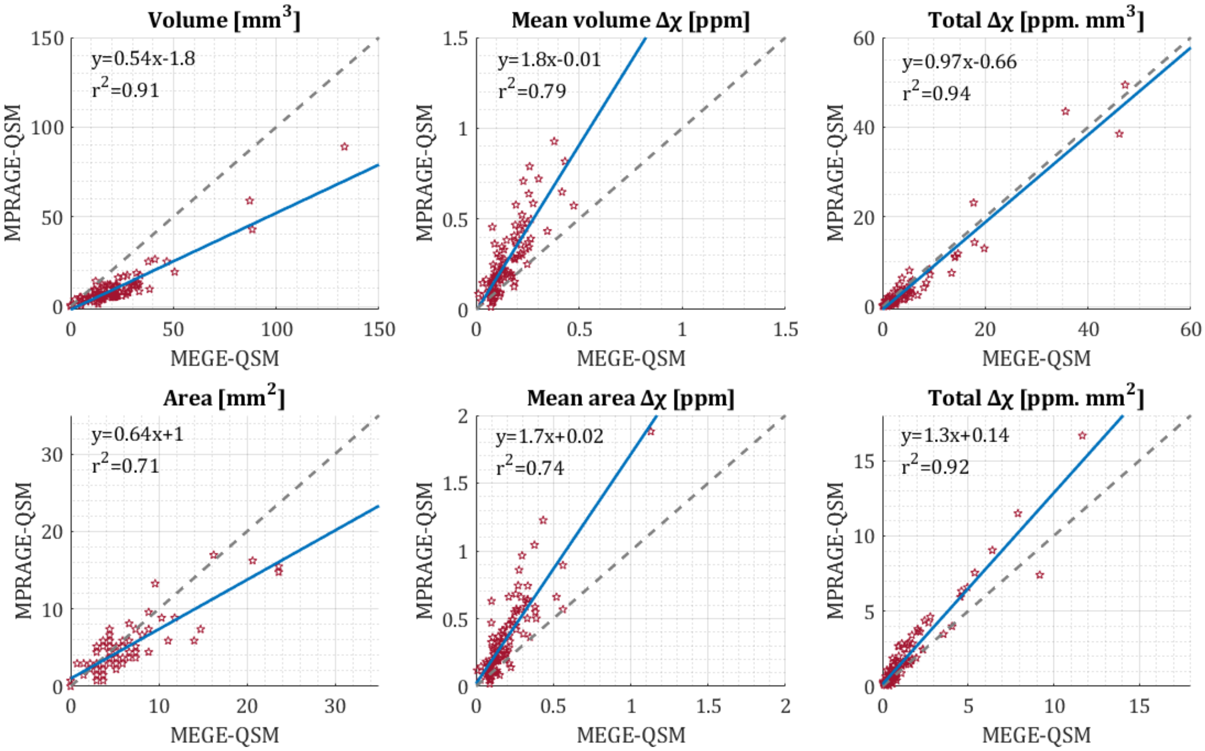

Figure 3.5: *Quantitative comparison of MPRAGE-based and MEGE-based microbleed size, mean and total susceptibility estimates obtained from in-vivo data at 3T. The top row used volume measures, while the bottom row used only a central slice through each microbleed. Microbleeds on MPRAGE-QSM are smaller in size and stronger in susceptibility. Total susceptibility measurements have the highest correlation coefficient and the closest slope to unity. Measurements over microbleed volume were better correlated than measurements over a single cross-sectional slice.*

3.4.2.1 Microbleed detectability

No sub-voxel CMB (i.e., diameter of 0.3 and 0.5 mm) was detected in the range of simulated susceptibility and SNR levels. Overall in simulated CMBs of one-voxel diameter and above, the percentage of detection was 51% at 1.5T, 74% at 3T, and 81% at 7T. With minimum susceptibility of 0.4 ppm, the detection percentages rose to 55%, 80%, and 88% at 1.5T, 3T, and 7T respectively.

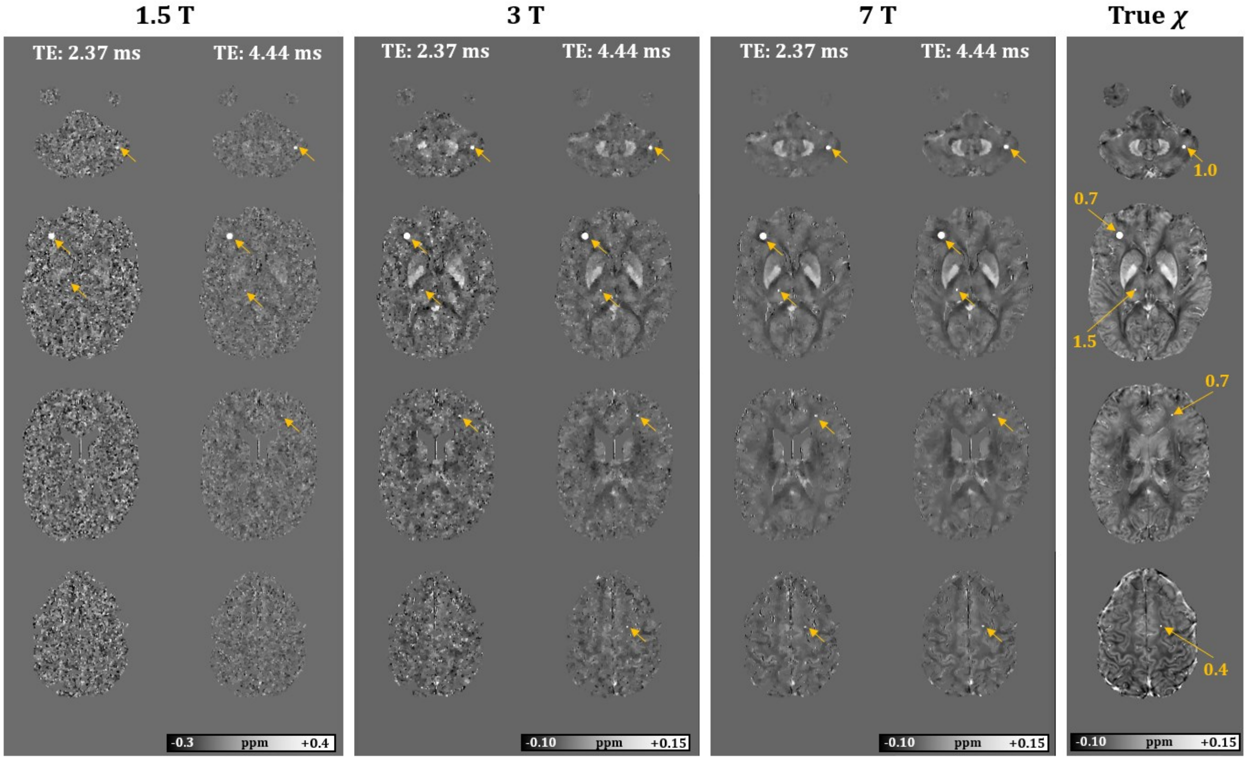

***Figure 3.6**: An illustration of reconstructed susceptibility maps from simulated MPRAGE phase data at different field strengths and echo times. Susceptibility of CMBs varied between 0.4 to 1.5 ppm as indicated on the right column. More CMBs are observable at higher field strengths and longer echo times, however none of the sub-voxel CMBs (diameter of 0.3 to 0.5 mm) were detected. The smallest detected CMB in this example has 0.9 mm diameter and 1 ppm susceptibility, and it was observable at 7T SNR levels. A wider gray scale was used in 1.5T images to distinguish small CMBs from noise.*

CMBs were successfully detected (i.e., with rate ≥ 90%) at 1.5T, 3T and 7T SNR levels when total volume susceptibility (i.e., $4/3 \cdot \pi \cdot a^3 \Delta\chi$) reached 2.57, 1.03 and 0.57 ppm·mm^3, respectively. Using these values and equation (3.2), the susceptibility-introduced phase shift can be estimated at any distance from the center of the CMB. It was found that the above-mentioned values for successful detection resulted in approximately similar phase shift levels, which reached ~ 0.005 rad at distance of 5 voxels (i.e., 4.25 mm). Using this observation as a threshold (i.e., 0.005 rad at fifth voxel), it is possible to estimate the minimum required $\Delta\chi$ for each CMB radius that can introduce sufficient phase for successful detection. These estimated $\Delta\chi$ levels are illustrated in

Figure 3.7, which shows a nonlinear relation that increases the required $\Delta\chi$ rapidly as the CMB diameter deceases below one voxel. For instance, a CMB of 0.5-mm diameter (i.e., 0.29-voxel radius) would be detected at the presented SNR levels of 1.5T, 3T and 7T if its $\Delta\chi$ is at least 38.7, 19.4 and 8.3 ppm, respectively. These extreme values indicate that detecting sub-voxel CMBs is not feasible at the expected MPRAGE phase contrast. For a CMB of 1.7-mm diameter (one-voxel radius), detection would require only $\Delta\chi$ of 0.99, 0.49, 0.21 ppm at 1.5T, 3T and 7T, respectively.

Regarding CNR_{ϕ}, microbleeds were not distinguishable from noise when the CNR_{ϕ} dropped below 1.5, even if the phase shift requirement was satisfied. Those cases are associated with the low SNR at 1.5T, where noise level in the obtained susceptibility map exceeded 100 ppb (SD: 82 ppb).

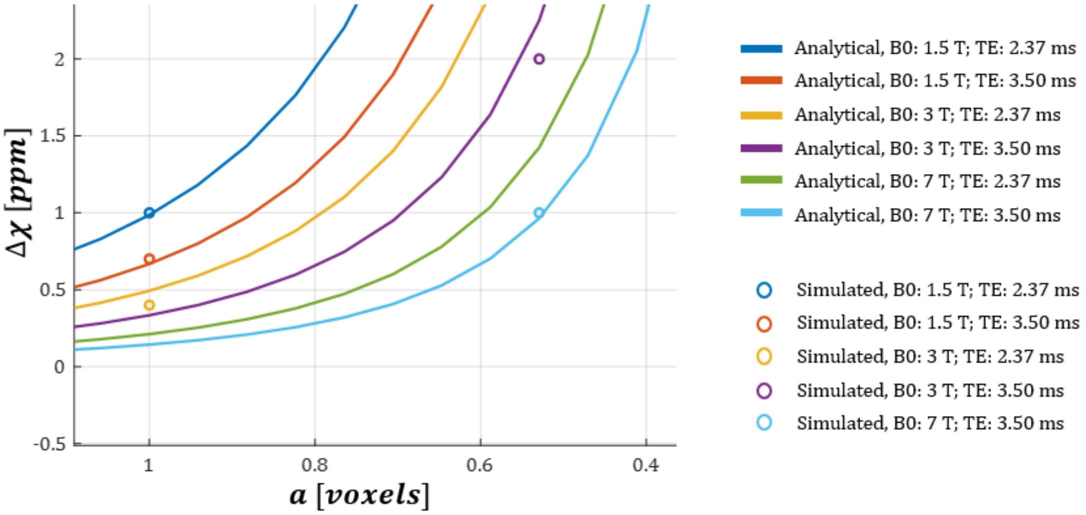

Figure 3.7: *Analytically obtained minimum required susceptibility $\Delta\chi$ for successful detection versus CMB radius (in voxels). As the CMB radius decreases, the required $\Delta\chi$ increases exponentially. Circles represent susceptibility and radius pairs obtained from simulations.*

3.4.2.2 Microbleed radius estimation

For microbleed radius estimation, volume-based measurements were slightly better than area-based measurements (**Table 3.2**). In general, the error in radius estimation gets smaller as the microbleed radius and/or SNR level increases. Actual versus estimated measurements were highly correlated ($r^2 \geq 0.93$), although the slope was slightly below unity (range of 0.85-0.93) mainly due to overestimation of small radii (**Figure 3.8**). In microbleeds with diameter larger than 4 voxels (i.e., radius ≥1.75 mm), the error in estimated radii based on volume measurements was less than 16% and 11% at 3T and 7T respectively. When area measurements were used, the error in radius estimation was less than 21% and 14% at 3T and 7T respectively. However, the error might exceed 100% in microbleeds of one-voxel diameter at 3T due to size overestimation for such small CMBs.

***Table 3.2**: Root mean square error of estimated microbleed radius using volume and area measurements expressed as a percentage of actual radius (%). Slope and correlation coefficient (r^2) of estimated versus actual microbleed radii are given in the last two rows.*

	Volume-based measurements			**Area-based measurements**		
Radius (mm)	**1.5T**	**3T**	**7T**	**1.5T**	**3T**	**7T**
0.45	205.29	105.79	94.62	216.87	130.98	94.74
0.85	96.99	37.91	49.77	94.84	42.38	57.42
1.75	27.92	15.66	10.85	35.00	20.42	13.11
3.45	13.46	5.62	9.79	17.35	6.56	12.21
Slope	*0.87*	*0.93*	*0.90*	*0.85*	*0.92*	*0.88*
r^2	*0.95*	*0.96*	*0.96*	*0.93*	*0.94*	*0.95*

Figure 3.8 illustrates the actual and estimated radii for different detected microbleeds at different simulated susceptibility levels and field strengths. The radius was estimated based on microbleed volume measurements. Out of all simulated susceptibility levels, estimated CMB radii at $\Delta\chi$ of 0.1 ppm (lowest level, gray colored in **Figure 3.8**) had the worst accuracy and varied widely between different repetitions. Other susceptibility levels resulted in good estimation with less than 0.5 mm variability between repetitions.

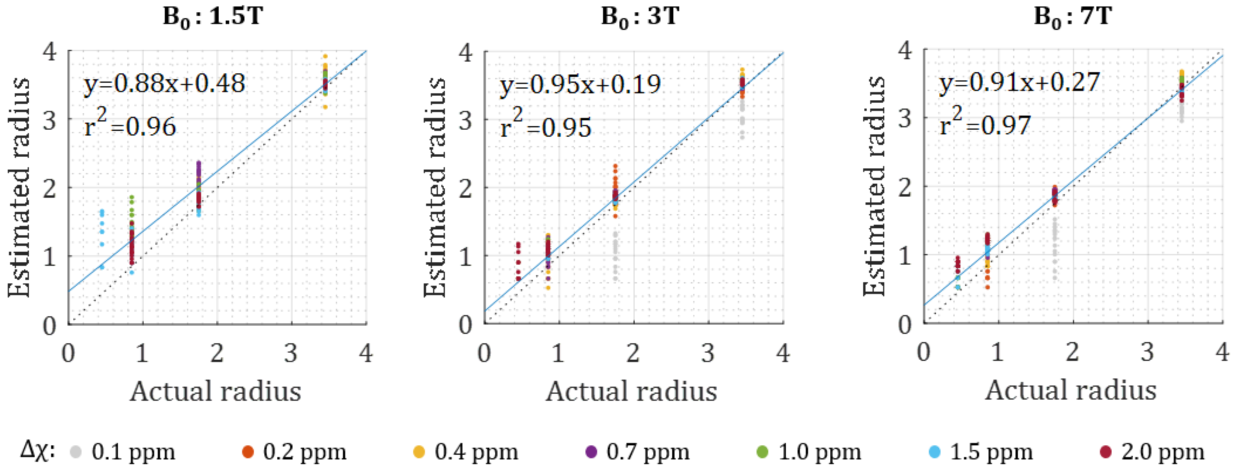

Figure 3.8*: Correlation plots of microbleed actual versus estimated radii [in mm] based on volume measurements at different simulated susceptibility levels and field strengths. MPRAGE was simulated at TE of 3 ms. The blue solid line represents the linear fit of the measurements, and the black dashed line represents the case of exact match (i.e., slope of 1.0 and zero intercept). None of the sub-voxel (i.e., radii: 0.15 and 0.25 mm) CMBs was detected. The deviation of slopes from unity is mainly due to size overestimation of smaller microbleeds with radius ≤ 1 mm.*

3.4.2.3 Susceptibility quantification

When comparing mean susceptibility measurements of CMBs on MPRAGE-based QSM versus the actual values on the simulated high-resolution susceptibility map, a clear systematic underestimation was observed that depends on the size of the microbleed: more underestimation as the microbleed size gets smaller, as illustrated in **Figure 3.9A** and **Table 3.3**. To check if this is originating from resolution and partial volume effects, these mean susceptibility values were compared to those obtained from a down-sampled version (to the same resolution of 0.85-mm isotropic voxels) of the true susceptibility map, which were found to be highly correlated ($r^2 \geq 0.91$) and in more agreement (slope of 0.90 to 1.0), as illustrated in **Figure 3.9B**. In addition, the slope deviation from 1.0 between the measurements on the reconstructed and the high-resolution ground truth maps was found to be reduced when the total susceptibility within the volume is reported instead of the mean susceptibility (**Table 3.3**), although underestimation is still present.

Similar trends were observed also when area measurements were used for calculating the mean and the total susceptibility values. Mean susceptibility values were lower than those obtained from the high-resolution ground truth, but in agreement with the measurements obtained from the low-resolution ground truth. Also, total susceptibility measurements were highly correlated with those obtained from the high-resolution ground truth. Unlike radius estimation, area-based susceptibility estimation resulted in slightly better slopes (than volume-based, e.g., 0.88 vs 0.85) in both mean susceptibility and total susceptibility measurements (not shown).

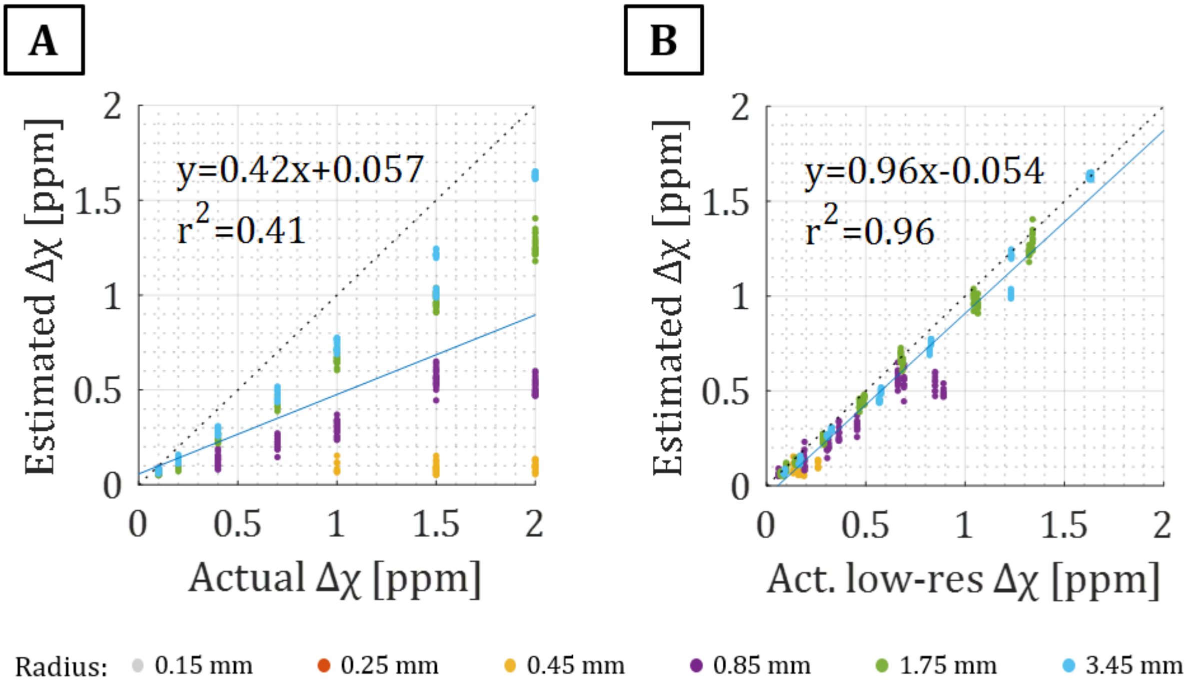

Figure 3.9*: Comparison of estimated microbleed mean susceptibility versus values measured on the true susceptibility map A) at the initial high spatial resolution of 0.10-mm isotropic voxels, and B) after down-sampled into 0.85-mm isotropic voxels. Susceptibility measurements in A) show size-dependent underestimation, which was reduced notably when the ground truth susceptibility was down-sampled into the same resolution (B). Simulation used TE of 4.44 ms and* B_0 *of 3T.*

Table 3.3*: Slope and correlation coefficient (r^2) of estimated mean susceptibility and total susceptibility versus measurements on high resolution ground truth at different microbleed sizes. The underlined slope values illustrate an example of the size-dependent underestimation in the mean susceptibility measurements which is less observed in the total susceptibility measurements.*

Radius (mm)		**Mean volume susceptibility [ppm]**			**Total volume susceptibility [ppm·mm^3]**		
		1.5T	**3T**	**7T**	**1.5T**	**3T**	**7T**
0.45	***Slope***	0.09	0.02	0.04	0	0.67	0.79
	r^2	0	0.09	0.55	0	0.24	0.77
0.85	***Slope***	0.32	0.3	0.24	0.46	0.85	0.91
	r^2	0.68	0.86	0.92	0.27	0.92	0.98
1.75	***Slope***	0.67	0.67	0.61	0.78	0.91	0.79
	r^2	0.97	0.99	0.99	0.95	0.99	0.99
3.45	***Slope***	0.74	0.78	0.89	0.8	0.88	0.83
	r^2	0.97	0.98	0.98	0.96	0.98	0.98

3.4.2.4 Location effect on estimates

Each microbleed configuration (i.e., specific size and susceptibility) were simulated at two locations: in the cortical region of the brain and in the subcortical region. **Table 3.4** summarizes the comparisons of microbleed size and susceptibility estimates when it is placed in these two regions, which indicates that the location of the microbleed did not have a clear and consistent effect on the radius and susceptibility estimates. It shows also that the variation between cortical and subcortical estimates gets reduced as the phase CNR improves.

3.4.2.5 Voxel aspect ratio effect

Simulated anisotropic voxels with twice the slice thickness resulted in lower estimates for both CMB radius (slope of 0.86 to 0.95) and mean susceptibility (slope of 0.88 to 0.95) when compared to isotropic voxels, as shown in **Figure 3.10**. However, measurements were highly correlated for radius estimation when CMB susceptibility was ≥ 0.2 ppm, and for susceptibility estimation when CMB radius was at least equal to slice thickness (i.e., ~1.75 mm). CMB detection was also impacted when the slice thickness was doubled (not shown). In general, reliable detection was achievable only when CMB diameter is at least of the slice thickness width, although 85% (i.e., 17 out of 20) of the CMBs that had 0.9-mm diameter and 2.0-ppm susceptibility were detected at 7T and 4.44 ms echo time. Predicting the minimum $\Delta\chi$ needed for successful detection at a given CMB radius was achievable using equation (3.2) and the same threshold mentioned earlier but with field measurements 6.3 voxels away.

Table 3.4*: Slope and correlation coefficient (r^2) of estimated microbleed radius and mean susceptibility when it is located in cortical versus subcortical regions.*

TE (ms)		**Radius [mm]**			**Mean susceptibility [ppm]**		
		1.5T	**3T**	**7T**	**1.5T**	**3T**	**7T**
2.37	***Slope***	1.0	1.0	1.0	0.99	1.0	1.0
	r^2	0.94	0.96	0.99	0.9	0.97	0.98
3	***Slope***	1.0	1.0	1.0	1.0	1.0	1.0
	r^2	0.97	0.98	0.99	0.91	0.98	0.98
3.5	***Slope***	1.0	1.0	1.0	1.0	1.1	0.95
	r^2	0.94	0.98	0.99	0.93	0.98	0.98
4.44	***Slope***	1.0	1.0	1.0	1.1	1.0	0.93
	r^2	0.92	0.99	0.99	0.96	0.98	0.98

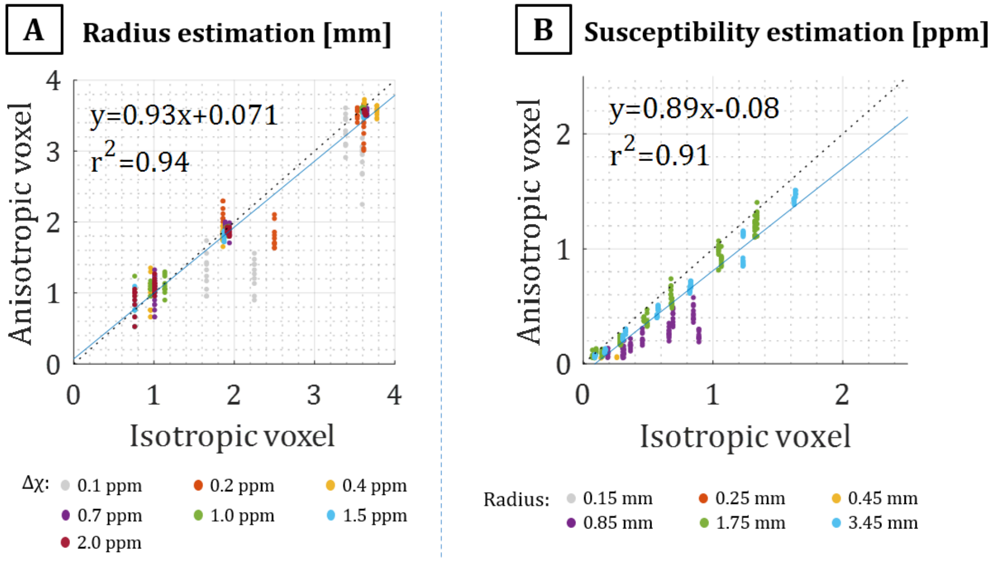

Figure 3.10*: Linear regression of microbleed A) radius[mm], and B) mean susceptibility [ppm] estimates in simulations with isotropic (0.85×0.85×0.85 mm^3) versus anisotropic (0.85×0.85×1.70 mm^3) voxels, at 3T and TE of 2.37 ms. Increasing slice thickness resulted in lower estimates more notably at lower susceptibility levels and smaller radii in microbleed radius and susceptibility estimation, respectively.*

3.5 DISCUSSION

This work studied the feasibility of quantifying the size and susceptibility of cerebral microbleeds using a susceptibility map derived from the phase of MPRAGE data, which is typically an integral part of neuroimaging protocols. This reduces the burden of acquiring additional T_2*-weighted data for QSM, and also allows assessment of CMBs via QSM from studies that do not include T_2*-weighted images.

Comparing in-vivo measurements of MPRAGE- and MEGE-QSM revealed that the two methods have comparable CMB detection sensitivity. However, susceptibility contrast in MPRAGE-QSM is generally weaker, and only iron-rich regions have adequate contrast. The MPRAGE sequence is used mainly for structural imaging with prerequisites of using high spatial resolution and very short echo time to preserve fine details and T1-weighted contrast, respectively. Both of these requirements reduce the CNR of the MPRAGE phase and thus put a limit on the retrievable susceptibility information. Using simulations, a lower limit on the CMB size and susceptibility was empirically determined for successful detection at practical SNR levels for the MPRAGE phase. The lower limit was defined based on the susceptibility-introduced phase shift five voxels away from the microbleed center. This distance for the phase shift measurement was chosen to cover the radius of the largest CMB used in the simulation (of 4 voxel radius) and can be adjusted as needed. In addition, it was defined based on voxels to keep it general and resolution independent. Using the defined lower limit and assuming an upper limit of 2 ppm for the mean CMB susceptibility, it can be predicted for instance that the smallest detectable CMB at a common 1-mm isotropic resolution and a TE of 3 ms is of 0.9 – 1.5 mm diameter, depending on the field strength (i.e., 1.5 mm, 1.2 mm and 0.9 mm at 1.5T, 3T and 7T, respectively). Conversely, for an average-sized CMB of 3-mm diameter the lowest detectable $\Delta\chi$ is expected to be 0.05 ppm at 7T and 0.11 ppm at 3T. At 1.5T however, it is expected to be 0.3 ppm, limited by the phase contrast-to-noise ratio threshold.

Overall, the achievable phase contrast at 1.5T is weak compared to the noise and thus only microbleeds of large size and/or strong susceptibility were detectable with MPRAGE-QSM. Although applying stronger regularization can reduce the noise level in the susceptibility map, it can also lead to a false detection of left-over noise as tiny CMBs. Moreover, high error is expected in quantifying detectable CMBs at these low CNR_{ϕ} levels. For these reasons, the MPRAGE-based

QSM at 1.5T is not promising with typically used sequence parameters. On the other hand, the achievable contrast of the MPRAGE phase at field strength ≥ 3T seems to be adequate for detecting CMBs of at least one-voxel diameter. Quantification however is promising for CMBs of at least two-voxel diameter and susceptibility above 0.2 ppm. At 1.5T and 3T expected SNR levels, increasing TE generally resulted in an improved correlation and less variability due to noise. However at 7T, the best correlation coefficients were observed with 3.0-ms echo time, and increasing the TE further weakened the correlation between measurements, mainly due to higher phase wraps at strong susceptibility levels that are not completely resolved.

A previous study reported that the optimal echo time for quantifying a CMB of one-voxel diameter is 14 ms at 1.5T, 7 ms at 3T, and 3 ms at 7T (212). For 7T, the reported optimal TE of 3 ms is within the typical range used in MPRAGE and coincides with our findings. However, the reported optimal echo times for 1.5T and 3T are longer than the typical values used in MPRAGE sequence imaging, particularly a TE of 14 ms at 1.5T is three times longer than practically allowed values. Despite that the allowable TEs in the MPRAGE are 34-63% smaller than the reported optimal TE at 3T, we found them useful for CMB detection, although very short TE such as 2.37 ms limited the quality of other tissues of lower susceptibility. In-vivo MPRAGE data used in this work had lower SNR than the MEGE due to the higher resolution, higher acceleration factor, lower flip-angle, single-echo measurement, and the T1 recovery during acquisition readouts. Altogether with the short echo time (2.37 ms), QSM produced from the MPRAGE phase had weak contrast for most structures, other than strong sources like CMBs or highly iron-rich regions (221). In addition, deep regions suffered from higher noise levels, being further from receiving coils. However, typically used TE in MPRAGE is around 3 ms, and if extending it to 4.4 ms is tolerable, the susceptibility contrast can improve notably. The use of 4.4-ms TE was reported in an optimized MPRAGE protocol to maximize brain tissue contrast at 3T (194). Furthermore, higher phase CNR is expected at 1-mm isotropic resolution, which is commonly used in MPRAGE.

Simulations also suggested that detecting sub-voxel microbleeds using MPRAGE-based QSM is not feasible in the range of allowable echo times. In contrary, a previous work showed using simulation that CMBs with diameter as small as 1/4 voxel and susceptibility of 1.5 ppm was detectable at 3T and 5-ms echo time (212). Possible reasons for the inability to detect sub-voxel microbleeds here includes that the simulations were more realistic with CMBs being placed within tissues and not against a zero-background, and that field contributions from outside brain tissue were assumed and thus tissue field estimation was required before susceptibility inversion. Furthermore, the simulation included the inversion-recovery modulation effect of the MPRAGE sequence on the phase information, which further complicates and lowers the phase SNR distribution.

Microbleed size measurement is typically performed manually over a single slice image by expert radiologists, allowing size quantification over thin slabs and requiring less labor than a full volume measure. However, we found that measurements over volume (rather than cross-section) resulted in more consistent estimations, notably with in-vivo measurements, benefiting from reduced digitization error and further noise averaging. The required effort to perform volume measurements might be minimized by using automatic or semi-automatic detection techniques (232–234) followed by manual adjustment.

Spatial resolution of the images has a clear impact on the accuracy of both CMB radius and susceptibility estimation. Digitization error due to the finite grid imposed by the limited resolution impacts the volume/radius quantification, more notably in CMBs with 1 to 2 voxels diameter. However, the error (RMSE) drops to below 16% when the CMB diameter reaches 4 voxels. The resolution effect is more pronounced in susceptibility estimation where quantification is impacted by the partial volume effect, which leads to CMB size-dependent underestimation that exacerbates as the diameter gets smaller. Previous studies have reported that mean susceptibility is underestimated in QSM of coarser spatial resolution (196,198) due to phase contrast reduction. It is also reported that at longer echo times microbleeds appear larger on QSM (140,182) and their susceptibility is more underestimated (182,212). Owing to their small size and extreme iron concentration, microbleeds can introduce phase shifts larger than π rapidly within spatial and temporal scales smaller than the resolution used in the acquisition, and thus these phase jumps might not be successfully detected and resolved by the phase unwrapping algorithms (182).

These factors might explain the observed differences between in-vivo measurements of MPRAGE- and MEGE-based susceptibility maps, in which detected microbleeds appeared smaller (0.54 slope) and of higher mean susceptibility (1.8 slope) on MPRAGE-QSM. Compared to the MEGE, voxels in the MPRAGE data are smaller by a factor of 2.3 to 2.7 (depending on the MEGE slice thickness), and the used echo time (2.37 ms) is at least three-fold shorter (average TE in the MEGE is 14.8 ms). When measurements were compared between QSM produced from MPRAGE (TE 2.37 ms) or the first echo of the MEGE (TE of 3.8 ms) in a post-hoc analysis, the MPRAGE-QSM slopes were closer to 1 by ~ 19% (volume slope of 0.64 and mean susceptibility slope of 1.4), indicating a role for echo-timing in the observed differences between MPRAGE-QSM and MEGE-QSM. To overcome these spatial and temporal resolution dependencies, it has been suggested to quantify microbleed load using total susceptibility (140); a measure that accounts for both CMB volume and susceptibility and has demonstrated reduced variation with echo time (140,212). This measure is proportionally related to the magnetic dipole moment which can be expressed for a spherical source as: $4\pi a^3 \Delta\chi/3\ (B_0/\mu_0)$, with μ_0 being the vacuum magnetic permeability (18). In other words, the total volume susceptibility is an estimate of the magnetic moment normalized by the field strength. We observed that the total susceptibility measurements from MPRAGE-QSM and MEGE-QSM were more consistent and correlated, both in simulated and in-vivo measurements, and thus looked more attractive for CMB burden quantification. In addition, the total susceptibility measure seems to offer an opportunity to retrospectively combine and analyze data acquired using different protocols. This conclusion, however, necessitates further rigorous evaluation using variety of acquisition protocols that is beyond the scope of this study.

Cerebral microbleeds are more associated with the cortical region of the brain, where QSM measurements might be less reliable due to a degraded background removal performance towards the surface of the brain (74) and an expected susceptibility underestimation when tissue field information is truncated (196,235). However, we did not observe any consistent effect in CMB radius and susceptibility quantification due to its location being closer to the brain surface, most probably due to its small size that does not require extended tissue field information for the dipole inversion.

A limitation of this work is that the in-vivo validation of quantifying microbleeds using MPRAGE-based QSM was limited to a single set of field strength and echo-time combination. However, more practical combinations of B_0 and TE were explored using simulations, which gave an idea of the expected quality and accuracy at different phase SNR levels. Another limitation is that the time interval between the MPRAGE and the MEGE scans was long for few subjects, though no significant change in microbleeds is expected within a few months (236).

3.6 CONCLUSION

The MPRAGE sequence is commonly included in brain studies, and its phase can provide opportunity to assess microbleed burden. The quality of MPRAGE-QSM is limited by the short TE and the low SNR at field strength $\leq$ 3T, but can still be useful for detecting and quantifying microbleeds when a dedicated T_2*- sensitive sequence is not performed. In-vivo results showed that the MPRAGE-QSM has a comparable detection sensitivity to the MEGE-QSM at 3T, its contrast can be improved notably by using echo time in order of 4.4 ms, and that the total susceptibility measure is less susceptible to sequence variations.

3.7 Acknowledgements

Funding from Canadian Institutes of Health Research is acknowledged.

Chapter 4: Quantitative susceptibility mapping from thin slabs: Challenges and possible solutions[1]

4.1 **Abstract:**

Susceptibility maps reconstructed from thin slabs may suffer underestimation due to background-field removal imperfections near slab boundaries and the increased difficulty of solving a 3D-inversion problem with reduced-support, particularly in the direction of the main magnetic field. Reliable QSM reconstruction from thin slabs would enable focal acquisitions in a much-reduced scan time.

This work proposed using additional rapid low-resolution data of extended spatial coverage, that serves as prior knowledge, to improve background-field estimation and regularize the inversion-to-susceptibility process for high resolution, thin slab data. The new method was tested using simulated and in-vivo brain data of high resolution (0.33×0.33×0.33 mm^3 and 0.54×0.54×0.65 mm^3, respectively), and compared to the standard large volume approach. Simulation results showed that the proposed method produced more consistent measurements from slabs of at least 8 slices. Reducing the mean ROI error to 5% required the supporting data to cover ~ 60 mm in the direction of the main field, have at least 2-mm isotropic resolution that is not coarser than the high-resolution data by more than 4-fold in any direction. Using the proposed method, in-vivo high-resolution QSM at 3T was obtained from slabs of width as small as 10.4 mm, aided by a lower-resolution dataset of 24 times coarser voxels.

Applying the proposed QSM method in imaging applications dealing with regions of limited extent, like deep gray nuclei, has the potential of reducing the acquisition time for QSM by a factor up to seven, which could make QSM useful for rapid, focal acquisitions at sub-millimeter resolution.

Keywords: QSM, 3T, thin slab, focal acquisition.

---

[1] A portion of this chapter has been presented as an abstract in: *Naji N and Wilman AH.* Towards fast single-slice QSM: Challenges and possible solutions. *ISMRM 31st Annual Meeting & Exhibition, London, UK, 2022: abstract #3559.*

4.2 INTRODUCTION

Quantitative Susceptibility mapping (QSM) is a post-processing technique developed to visualize and measure tissue magnetic susceptibility to the applied MR static field, using the phase of T_2*-weighted images (53–55). QSM retrieves localized information about the underlying susceptibility sources and thus provides the opportunity to monitor changes in iron deposits and myelination, both of which are associated with several neurodegenerative diseases (15,153,154).

QSM is typically reconstructed from a whole brain three-dimensional (3D) phase volume acquired via a multi-echo gradient-echo (MEGE) sequence. Obtaining QSM from single-echo phase is also possible as long as the data is collected using a T_2*-sensitive pulse sequence, such as echo planar imaging (EPI) and susceptibility-weighted imaging (SWI)(13,56). The necessity of collecting large 3D spatial coverage arises mainly from the underlying 3D physical model relating the MR phase to the tissue susceptibility via convolution with a magnetic dipole, which is not a voxel-to-voxel relation. Thus, reconstructing susceptibility accurately requires extended phase information in the vicinity of the region of interest (ROI), particularly along the direction of the static field (B_0, conventionally along z-direction). Previous studies have reported elevated underestimation in QSM when the volume of interest (VOI) is reduced, more noticeably in iron-rich regions (196,235,237). These studies suggested extending the coverage based on the ROI size to minimize susceptibility underestimation. For instance, Elkady et al. suggested a minimum slab width of 560% the GP physical size for reliable measurement with less than 5% error (235), which is about 64-mm after post-processing erosion. Karsa et al. further extended the analysis to more ROIs and concluded that the minimum required coverage is linearly related to the ROI susceptibility, making the necessary coverage between 120% to 580% the ROI size (196). They also reported a significant decrease in QSM contrast when the coverage along B_0 dropped below 40 mm. In a recent study, Zhu et al. showed that their deep learning-based reconstruction minimized the susceptibility underestimation and allowed for less than 5% error with as small as 150% coverage (48 mm slab) for deep gray matter (DGM) structures (237).

The requirement of acquiring 3D extended coverage adds a burden on studies focused on a specific region that can be covered otherwise using a few slices. Examples could include thin slab imaging of the hippocampus, as has been done in diffusion imaging (238), or focused acquisitions of iron-rich DGM rather than more typical whole brain studies that often only focus on iron-rich DGM

(132,239,240). In particular, if high resolution data is required, limiting the coverage to the region-of-interest can save substantial time that may make the scan time feasible, unlike whole brain collection. Furthermore, reduced scan times may limit motion artifacts and increase patient comfort. Although collecting a fast large volume for QSM is achievable using advanced parallel imaging techniques (241,242) and/or fast pulse sequences (56,90,243), image quality is typically compromised. Producing QSM from thin slabs would further accelerate the acquisition, allow higher resolution imaging, and potentially accelerate clinical adoption.

This study proposes and validates improved reconstruction of thin-slab QSM with the aid of additional rapid low-resolution data. The challenges incurred in reduced-VOI QSM applications are also discussed.

4.3 THEORY

QSM reconstruction involves challenges as it consists of multiple processing steps in which the performance and accuracy of each step is influenced by those preceding it (**Figure 4.1A**). In addition, three of these processing steps (phase unwrapping, background field removal [BFR] and dipole inversion) rely on non-local spatial information to determine the value of each voxel. Consequently, an error in one voxel might propagate and affect other surrounding voxels. Similarly, voxel omission affects other adjacent voxels and increases the difficulty of solving the background removal and the dipole inversion steps.

Background-field removal methods are known for increasing inaccuracy toward the VOI edges (74), and as the VOI shrinks the error in the resultant tissue field elevates substantially and propagates to the final susceptibility map. Previous studies have showed that the background removal step is an important factor in the underestimation problem of thin-slab QSM (196,237). Furthermore, the field-into-susceptibility inversion process aims to solve equation (4.1) for χ:

$$f_{tissue}(\vec{k}) = d(\vec{k}) \cdot \chi(\vec{k}) \quad \text{or} \quad f_{tissue}(\vec{r}) = d(\vec{r}) * \chi(\vec{r}) \tag{4.1}$$

where $f_{tissue}(\vec{k})$ is the tissue frequency shift (or tissue field, used interchangeably) induced by the susceptibility distribution $\chi(\vec{k})$, $d(\vec{k})$ is the magnetic dipole kernel, and $\vec{k}$ and $\vec{r}$ refer to the coordinates vector in frequency and spatial domains respectively (57,58).

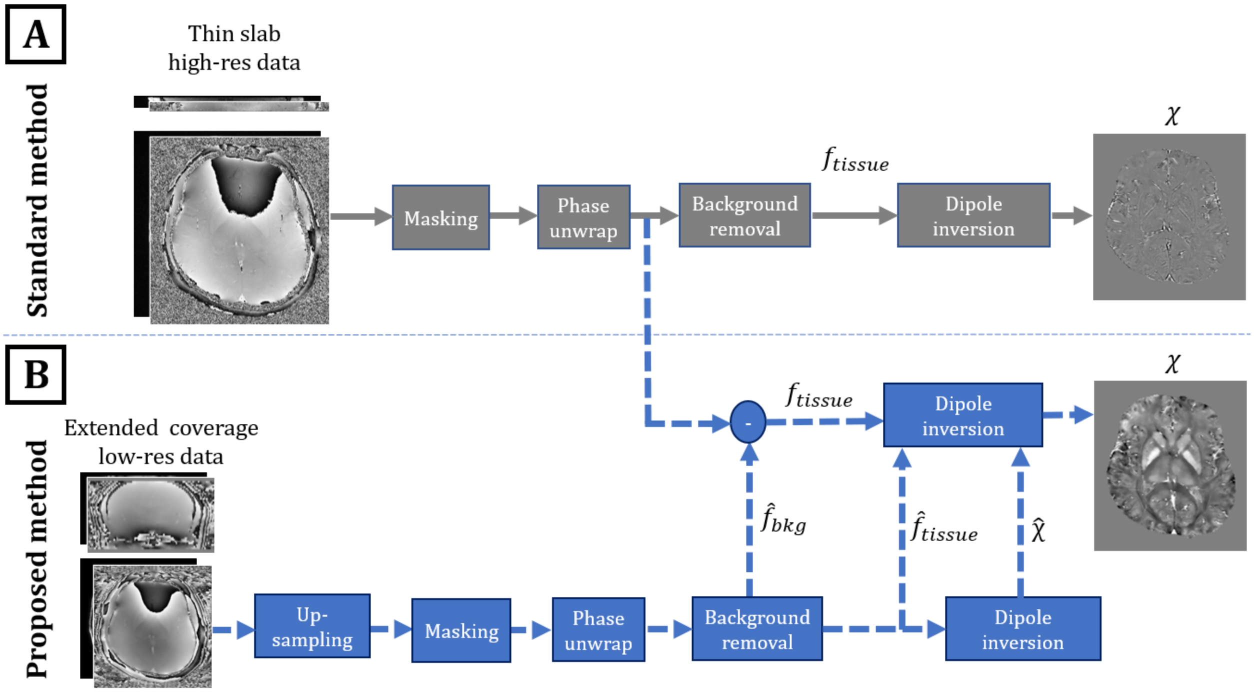

***Figure 4.1**: Flowcharts of A) the standard QSM processing pipeline and B) the proposed pipeline. In the proposed method, the tissue field (f_{tissue}) is obtained by subtracting the background field ($\hat{f}_{bkg}$) estimated from the low-resolution data. Low-resolution tissue field ($\hat{f}_{tissue}$) and/or susceptibility ($\hat{\chi}$) are also used to regularize the reconstruction of the high-resolution susceptibility.*

Equation (4.1) represents an ill-conditioned 3D problem due to the existence of zeros in the frequency-domain representation of the magnetic dipole kernel, $d(\vec{k})$, and thus is typically solved via minimization approaches in the spatial domain with some help from prior knowledge about $\chi(\vec{r})$ (62,89,244). However, truncating the support region of $f_{tissue}(\vec{r})$ further complicates the process of finding a global solution for the minimization problem as more than one solution can produce the same tissue frequency shift (for instance, see **Figure 4.2**). Moreover, solving this inversion problem yields a zero-mean solution within the VOI, and thus the obtained QSM from thin slab would be normalized by a shifted mean value that depends on the slab contents and width. The shift in the mean value is typically small in healthy subjects, but it could be significant if the imaged thin slab contains lesions of strong susceptibility such as hemorrhage.

To overcome the above-mentioned deficiencies associated with the reduced-VOI QSM, we propose using a rapid low-resolution acquisition of extended brain coverage to assist the background removal and dipole inversion steps, as illustrated in **Figure 4.1B**. Since the frequency shift due to background sources, $f_{bkg}(\vec{r})$, is slowly varying carrying low-frequency contents, we hypothesize that it can be estimated from an extra full-coverage acquisition of a lower spatial resolution (thereafter referred to as the **low-res** data). The low-res background frequency shift, $\hat{f}_{bkg}(\vec{r})$, then can be subtracted from the high-resolution total frequency shift to yield the required $f_{tissue}(\vec{r})$. This way, the resultant high-res tissue frequency shift should be more accurate near the slab edges despite the narrowed width, as the background contribution is calculated based on an extended brain coverage.

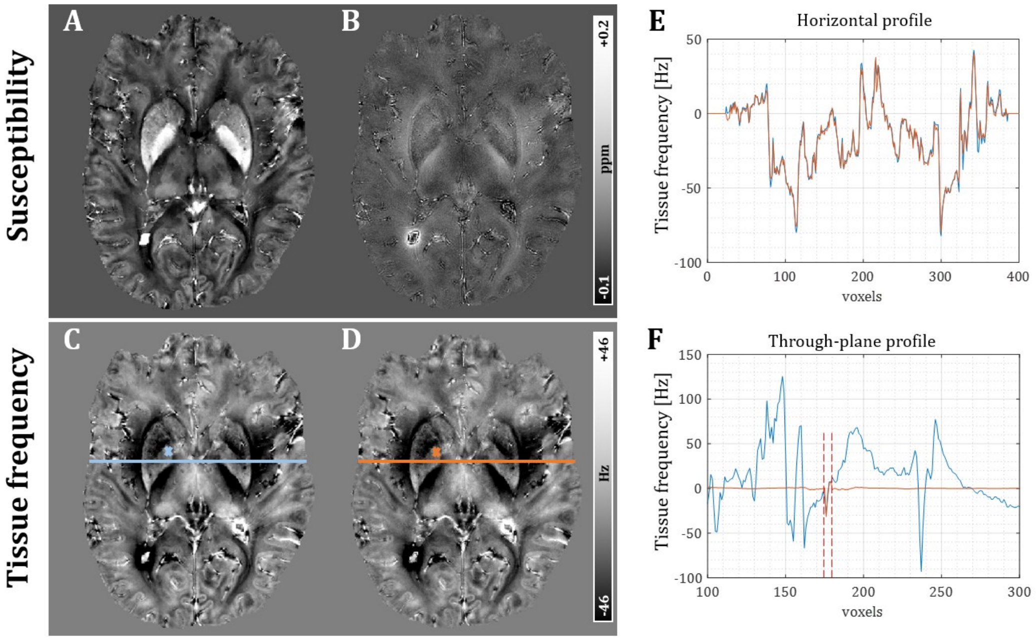

Figure 4.2: *Demonstration of dipole inversion ambiguity when slab thickness is too small. Two different susceptibility distributions (A and B) can produce similar tissue frequency maps (C and D) if the slab thickness is limited to 4 slices. E) Horizontal and F) through-plane profiles from the tissue frequency maps illustrating the similarity between (C) and (D). The locations of plotted profiles on tissue frequency maps are visualized by solid lines and cross symbols, respectively. Profile plots illustrate that both tissue frequency maps have similar in-plane distribution (E), but through-plane similarity is confined to 4 slices (dashed-red lines in F). Panel F) shows that wider slab thickness would help in distinguishing between (C) and (D) and thus aiding the inversion algorithm in recovering the correct susceptibility distribution.*

In addition, the low-res data can help the dipole inversion process by giving the algorithm some prior knowledge of the susceptibility distribution outside the imaged slab. This can be achieved by adding another regularization term to the minimization formulation, as expressed in equation (4.2):

$$\chi^{*}(r) = \arg\min_{\chi(r)} \left\| W(r)\big(d(r) * \chi(r) \; - \; f_{tissue}(r)\big) \right\|_2^2 + \lambda_1 \left\| M_G(r) \nabla \chi(r) \right\|_1 + \lambda_2 \, R(\chi) \qquad (4.2)$$

with λ_1 and λ_2 being regularization parameters, and $W(r)$ and $M_G(r)$ being weighting coefficients computed based on estimated noise and magnitude gradient, respectively. The first two terms in equation (4.2) represent a widely used QSM inversion algorithm known as morphology-enabled dipole inversion (MEDI), which iteratively finds the susceptibility distribution $\chi(r)$ that yields the minimum norms (62). The third term, $R(\chi)$, can be used to enforce additional knowledge about the solution. We tested two possible forms based on the low-res data; the first one uses the low-res tissue frequency shift $\hat{f}_{tissue}(\vec{r})$, while the other one uses the reconstructed low-res susceptibility $\hat{\chi}(r)$:

$$R_1(\chi) = \left\| M_{out}(r) \, \widehat{W}(r) \, \Big(L\{d(r) * \chi(r)\} - \hat{f}_{tissue}(r) \Big) \right\|_2^2 \qquad (4.3)$$

$$R_2(\chi) = \left\| M_{out}(r) \, \widehat{W}(r) \, \big(L\{\chi(r)\} - \hat{\chi}(r) \big) \right\|_2^2 \qquad (4.4)$$

where $L\{\cdot\}$ is a gaussian low-pass filter that makes the resolution of the solution similar to the supporting data, and $M_{out}(r)$ is a mask that contains zeros within the imaged slab and ones otherwise, to force the regularization only outside the slab (i.e., consider the added knowledge for the non-imaged portion of the brain in the high-res data).

4.4 **METHODS**

Simulations were used to test the proposed approach, explore possible limitations and determine a lower bound for the spatial resolution of the additional low-res data. In-vivo data at 3T was then used to validate the proposed method in human brain.

4.4.1 **Simulation**

A numerical brain phantom of realistic features was constructed based on an actual high-resolution healthy human brain data of 0.33-mm isotropic resolution, 165.8×200 mm^2 FOV, and 448 slices (226). To facilitate comparison with previous studies, the susceptibility map of the phantom was linearly scaled such that the mean susceptibility of globus pallidus (GP) is 0.2 ppm. In addition, two lesions of strong susceptibility (each of them extends ~6.5 mm in all three dimensions) were added to the susceptibility with mean ± SD susceptibility of 0.8±0.1 ppm and -0.4±0.1 ppm, representing a hemorrhage and a calcification respectively (see **Figure 4.3A**). To simulate background field contributions, skull susceptibility was assumed to be -2.0 ppm and air susceptibility (i.e., +9.0 ppm) was added to the sinuses. The resultant susceptibility map was then used to produce a total field map via convolution with the magnetic dipole. The total field was then scaled to an MR phase at 3T for six different echo times (TE1:4.6 ms, ΔTE: 7.1 ms). This phase together with the raw magnitude of the healthy subject were used to simulate a reference high-resolution MEGE data (thereafter called the reference high-res).

In this reference high-res data, the brain is fully covered with 386 slices (127 mm). Additional volumes of smaller slab coverage were produced by limiting the number of slices to 180, 90, 44, 22, 8, 4 and 2, centered on putamen in the DGM. Focusing on the DGM structures, note that covering caudate, putamen and GP requires ~90 axial slices (29.7 mm). Thus, the above-mentioned slab widths represent a DGM coverage of 428% (386 slices), 200% (180 slices), 100% (90 slices), 49% (44 slices), 24% (22 slices), 8.8% (8 slices), 4.4% (4 slices) and 2.2% (2 slices), as illustrated in **Figure 4.3B**. The added two lesions are also centered within the DGM region and are fully covered with 20 slices; thus the tested slab widths represent a coverage of 1930%, 900%, 450%, 220%, 110%, 40%, 20%, and 10%, respectively. Another two iron-rich structures of interest, red nucleus (RN) and substantia nigra (SN), are located lower in the brain and thus were covered separately with the same slab widths mentioned-above and the slab center passing through these two structures.

The high-res reference (of full brain coverage) was also used to generate the low-res data (required for the dual reconstruction approach) by down-sampling in k-space. To determine a lower bound for the resolution that can be used, the lower-res data was produced using different combinations of down-sampling factors (2, 4, 6 and 8) applied to the three dimensions (x: phase, y: readout, and z: slice). Prior to any QSM pipeline processing, low-res data was up-sampled via k-space zero-padding (ZP) to the original resolution.

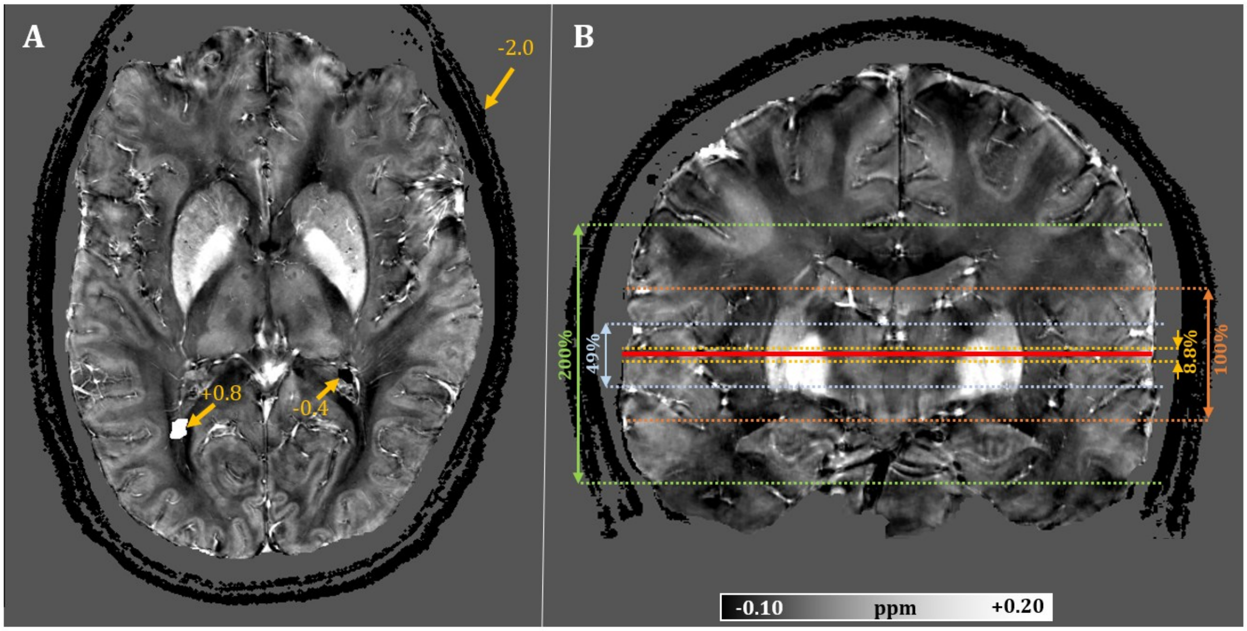

***Figure 4.3**: An illustration of the brain susceptibility distribution used in simulations. A) The first axial slice used for measurements, which shows iron-rich deep gray matter structures and the two added lesions. B) A coronal view demonstrating the location of the measurement slice (solid red line) and some of the tested slab widths (indicated by dashed lines).*

4.4.2 **In-vivo Imaging Protocol**

Brain images from three healthy adults (males, aged 25 to 34 years) were collected at 3T (Prisma, Siemens Healthcare, Erlangen, Germany) with a 64-channel head coil after giving written informed consent and under the approval of the local ethics committee. The imaging protocol included two sets of axial MEGE, 3D and 2D, with seven echoes and different spatial resolutions. The 3D MEGE set had high-resolution of 0.54×0.54 mm^2 (matrix of 324×384), 0.65-mm slice thickness, and through-plane coverage of 78 mm (120 slices acquired in 16.28 minutes), 19.5 mm (30 slices, 4 minutes) and 14.3 mm (22 slices, 3 minutes) centered on putamen. Additional high-resolution 3D MEGE volumes with smaller coverage were produced from the first data by limiting the number of slices to 50, 16, 8, 4 and 2. The second 3D MEGE acquisition had brain coverage of 80 mm (40 slices, 1.68 minutes), and its resolution was lowered by a factor of 4:2:3 (2.18×1.09×2.0 mm^3). All 3D acquisitions used FOV of 178×210 mm^2, TE/ΔTE/TR of 4.14/6.13/47 ms, and flip angle of 17º.

The 2D MEGE set consisted of two high-resolution (0.49×0.49 mm^2, 432×512 matrix, 1.0-mm slice thickness) small coverage acquisitions (16 mm, 16 slices in 2.8 minutes) centered on putamen and RN, and one low-resolution (1.95×0.98 mm^2, 108×256 matrix, 2.0-mm slice thickness) acquisition of wider through-plane coverage (80 mm, 40 slices in 2 minutes). Additional high-resolution 2D acquisition of smaller coverage was produced by limiting the number of slices to 8. The 2D high-/low-resolution acquisitions used TR of 736/1810 ms, flip angle of 59º/79º, TE of 4.28 ms, ΔTE of 6.05 ms, and FOV of 211×250 mm^2. Other common parameters for all acquisitions included: 2 GRAPPA acceleration with 24 reference lines and BW of 270 Hz/pixel.

4.4.3 **QSM Reconstruction**

The following procedures were used to process the data in simulation and in-vivo, unless otherwise stated. The proposed approach employed the additional low-res data to improve the reconstruction in two steps, as shown in **Figure 4.1B** (blue blocks and arrows). First, tissue field was estimated by subtracting the low-res background field. Residual background field was removed by a second order polynomial fitting and the Laplacian boundary value method (82). Then, the low-res tissue field or susceptibility was used as prior knowledge to regularize the field-to-source inversion process according to equations (4.2-4).

In-vivo data from individual coils were combined using the scanner built-in adaptive method, and prior to any processing for the 3D high-res data, the outer 6 slices were excluded due to aliasing and poor SNR at the edge of the imaged slab. Bias in magnitude images was removed using ANTs tool (187). Brain mask from magnitude images was obtained using the brain extraction tool (BET) from FSL package (64) with active "-Z" option (i.e., small brain coverage in Z direction) and threshold ranging between 0.12 -0.5 adjusted based on the data. Phase unwrapping was performed using ROMEO (69) with enabled offset correction. To eliminate unreliable voxels and maximize coverage near air-tissue interfaces, a brain mask was obtained for each echo time and used to define reliable phase regions. The total field was then obtained via magnitude-weighted average of the masked phase information (72). The background field was removed using the variable-radius sophisticated harmonic artifact reduction for phase (V-SHARP) data algorithm with maximum 20-mm kernel radius (55,77). Finally, the susceptibility map was reconstructed using a modified version (according to equation [4.2]) of the MEDI algorithm (62), with λ_1 and λ_2 set to 10^4 and 2000 respectively. When the slab width is reduced, the dipole inversion step was tested with and without zero-padding to the original full brain coverage.

4.4.4 Segmentation and Measurement

Registering the in-vivo low-res data to the high-res was done by forming a sum-of-squares magnitude image (produced from all echoes) for each data and then registering them rigidly using ANTs tool (187). Obtained transformation matrix was then used to map the files of the low-res data to the space of the high-res counterpart.

Seven deep gray matter ROIs were segmented manually over few slices using ITK-SNAP (231): caudate, putamen, thalamus, GP, RN, SN, and internal capsule (IC). For the simulation phantom, the masks for the synthetic lesions were produced by thresholding.

Measurements were performed using 2D ROIs (extracted from the segmentation masks) separately on two slices covering all the structures of interest: one slice covering caudate, putamen, thalamus, GP, and the two lesions (in the simulation part); and the other slice covering RN and SN. All measurements were referenced to the IC mean susceptibility and compared in susceptibility maps obtained from different slab widths.

All processing (except brain extraction, registration, and segmentation), analyses, and plots were performed using MATLAB (version R2020a; MathWorks, MA, USA).

4.5 RESULTS

4.5.1 Simulation Results

Figure 4.4 shows the top 98% frequency coefficients of the tissue and background field in the healthy brain used for simulation, demonstrating the lower frequency content of the background field which spans around 8-time smaller k-space spectrum (compared to tissue field) in the phase encoding (k_x) and slice encoding (k_z) directions. This implies that the background field could be estimated at a lower resolution, at least in two encoding directions. The results of estimating the background field at different levels of down-sampling are illustrated in **Figure 4.5**, in which the obtained high-res tissue field through low-res background field subtraction is shown at two axial locations, along with the difference from the high-res reference. It can be seen that with down-sampling up to 6 in each direction (i.e., ~ 2-mm isotropic resolution), the tissue field can be estimated with minimal difference. With much lower resolution, artifacts and residuals in the resultant tissue field became notable mainly near air-tissue interfaces. When the resolution of the high-res reference was assumed 0.66-mm isotropic, the highest down-sampling factor before observing notable artifacts was 3 in each direction (results not shown), indicating that estimating background field with minimal error requires at least 2-mm resolution.

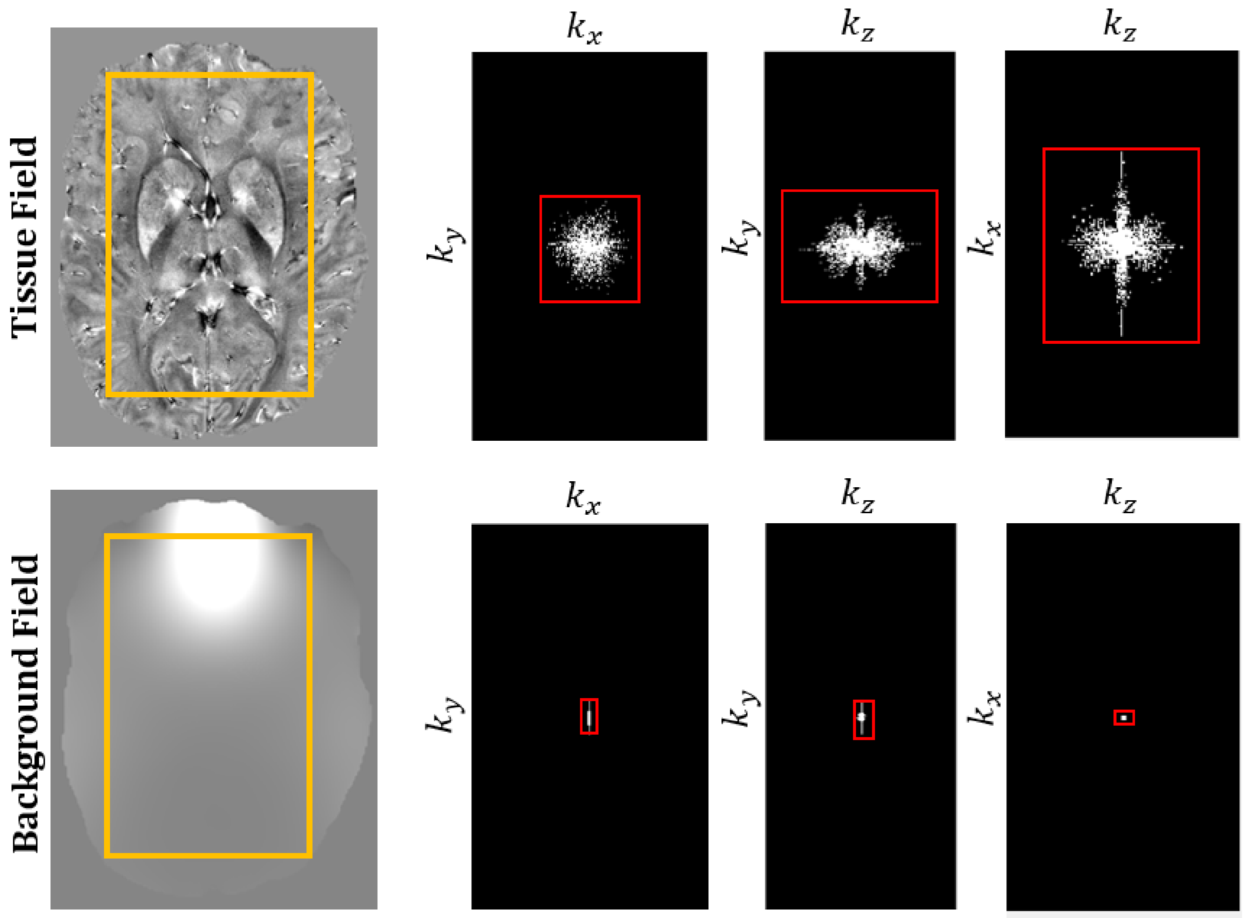

***Figure 4.4**: Comparison of frequency content in tissue field (top row) versus background field (bottom row). The volumes within the orange boxes (shown in the first column) were transformed into frequency domain. Columns two to four show orthogonal views of the corresponding frequency domain signals after removing the lowest 2%. Background field has much lower frequency content and thus can be estimated with lower spatial resolution. The data had 0.33-mm isotropic voxels.*

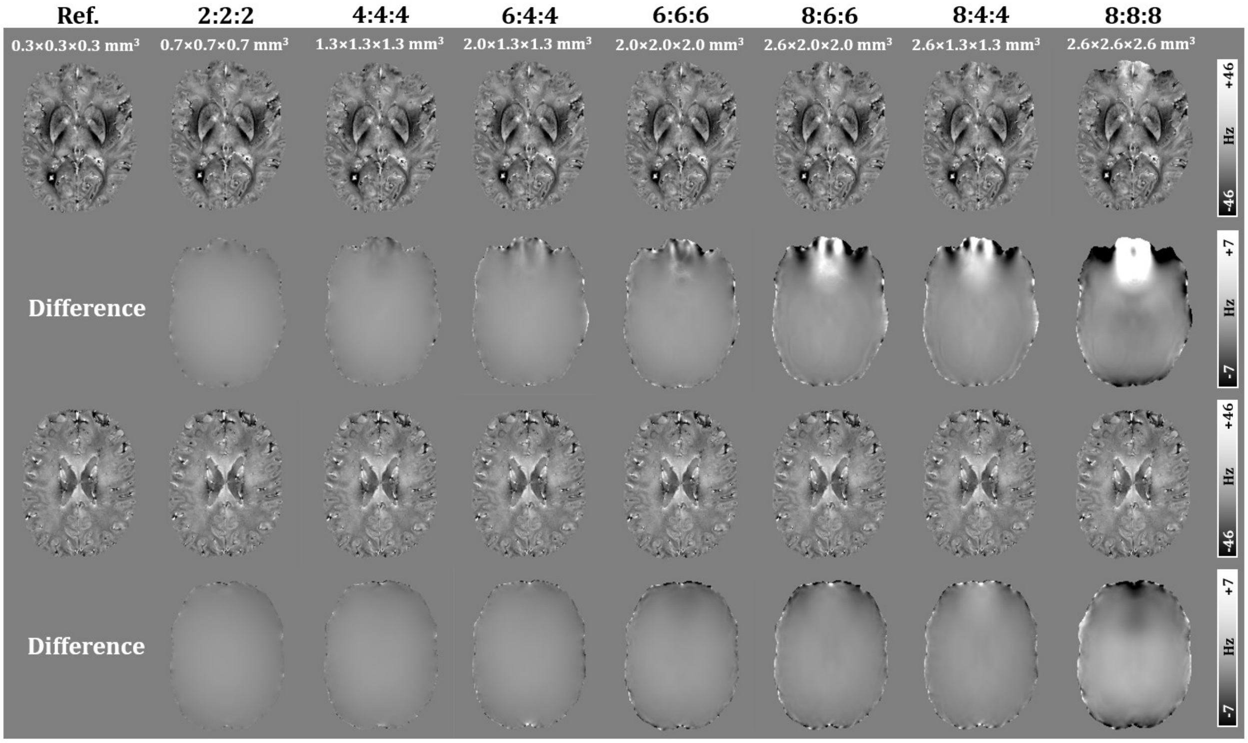

Figure 4.5: *Demonstration of resolution effect on background removal using subtraction. Tissue frequency map obtained by subtracting background frequency estimated from simulated low-resolution version at different down-sampling factors (phase encoding: frequency encoding: slice encoding). Difference images show that background contribution can be removed using a down-sampled data by a factor up to 6 without introducing significant error. The reference resolution is 0.33-mm isotropic.*

Recoverable susceptibility distribution details at different levels of spatial resolution are illustrated in **Figure 4.6(A, C-E).** It also shows (in panel **B**) how the contrast would significantly fade if QSM is reconstructed from a thin slab of 2.64-mm width (8 slices) using the standard method. In contrast, most of the susceptibility contrast and details were preserved using the proposed method with help from additional low-res data. However, artifacts were notable when the resolution of the supporting data was six-times lower than the reference. **Figure 4.6E** demonstrates one possible scenario to minimize the artifacts and maximize the saving in acquisition time, in which the resolution is lowered the most (×6) in the phase encoding direction, but relaxed (×4) in the slice direction, and kept moderately high (×2) in the readout direction, yielding a possible 24-fold reduction in acquisition time.

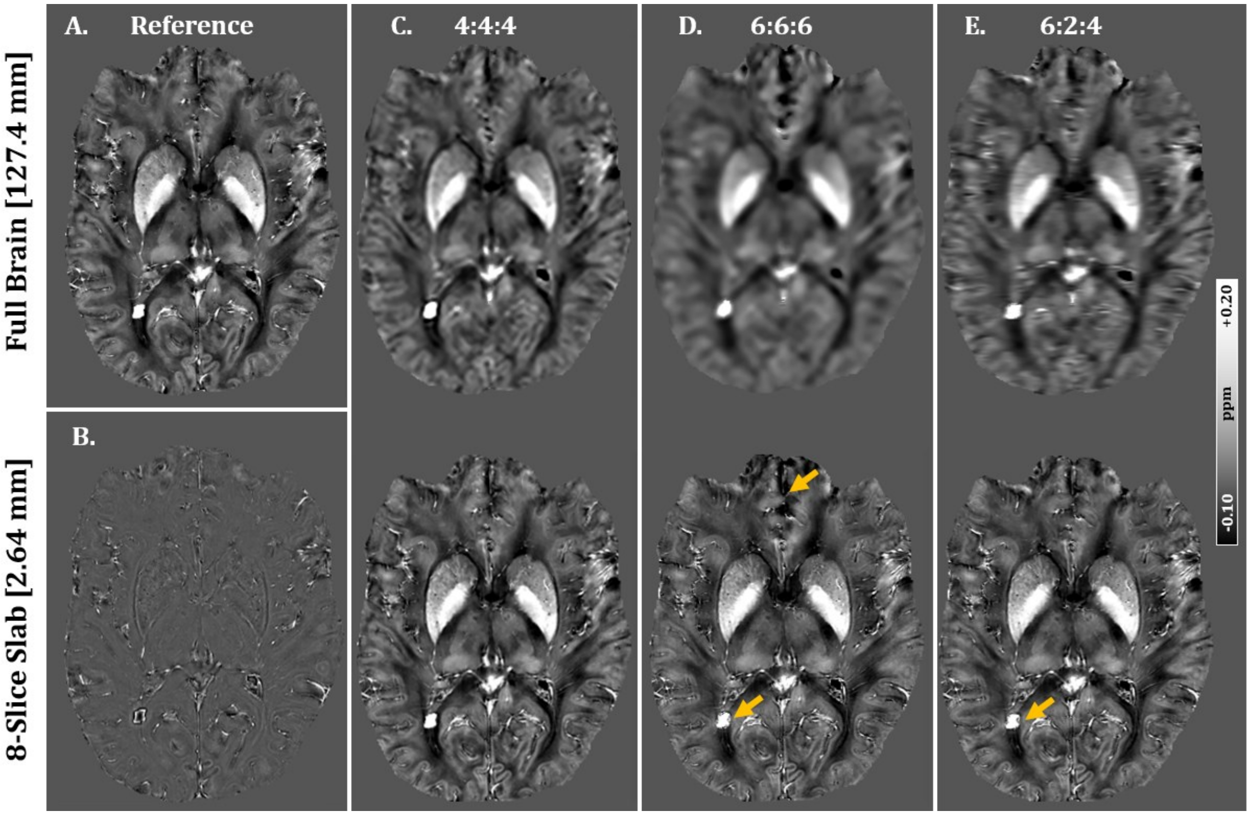

Figure 4.6: *QSM simulation results showing one slice from A) the reference full brain coverage, and B) the reconstructed from a 2.64-mm slab (8 slices) using the standard method. The remaining three columns show the reconstructed QSM (bottom row) from the same 2.64-mm slab using the proposed hybrid method with aid from a low-res full coverage data (top row) down sampled by a factor of C) 4:4:4, D) 6:6:6, and E) 6:2:4 along phase, readout, and slice encoding directions, respectively. QSM produced using the standard method lost most of the contrast due to the limited phase information in the thin imaged slab. On the other hand, the proposed method perceived most of the original contrast, although some artifacts appear as the down-sampling factor exceeds 4. Arrows point to some notable artifacts.*

ROI measurements of susceptibility obtained using the standard versus proposed method for varying imaged slab width are given in **Figure 4.7**. Using the standard method, three scenarios were tested: the imaged slab is processed i) with and ii) without zero-padding (ZP) to the full brain depth, and iii) reducing the slab width after removing background field to exclude its effect. Of these three, the least susceptibility underestimation was obtained when slab width reduction was performed after the BFR step, highlighting that the BFR process has a significant role in the underestimation problem. In addition, zero-padding in the through-plane direction slightly improved the measurements. However, the accuracy dropped in both cases (i.e., with and without ZP) in many ROIs as the slab width reduced below 60 mm (~ 180 slices). In contrast, the proposed method provided more consistent measurements with slab width as small as 2.64-mm (8 slices), with the tissue field-based regularization (i.e., $R_1(\chi)$) outperforming the susceptibility-based one. Therefore, the standard method with ZP and the proposed method with $R_1(\chi)$ were used in the rest of this work.

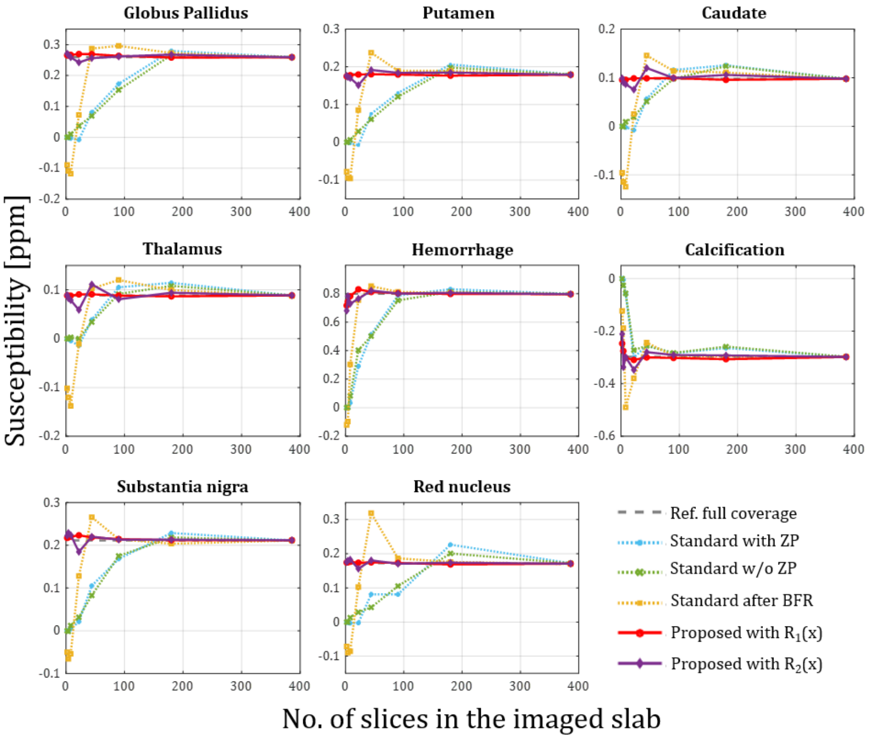

Figure 4.7: *Simulation results of 2D susceptibility measurements using different processing approaches at different slab widths (i.e., number of slices). All measurements are referenced to the mean value of internal capsule. The measurement at full brain coverage is indicated using a dashed gray line. The low-res data used in the proposed method was produced with a down-sampling factor of 4:4:4. The proposed method with* $R_1(\chi)$ *regularization (red solid line) provided the closest measurements to the reference with slab width ≥ 8 slices (i.e., 2.64 mm). Measurements of the standard method started deviating from the reference as the slab width drops below 60 mm (i.e., 180 slices). The yellow line illustrates the case if the slab width is reduced after the BFR step (i.e., neglecting the effect of inaccurate background removal). ZP: zero padding, BFR: background frequency shift removal.*

Figure 4.8 shows the effect of utilizing supporting data at different levels of resolution in the proposed method. Using a down-sampled data by 4 in all directions and with slab reduction down to 8 slices, the difference in measurements was within 4 ppb in putamen, caudate, thalamus and RN, 10 ppb in GP, 12 ppb in the calcification and SN, and 31 ppb in the hemorrhage; all of which is within 4% of the ROI mean value, except in SN where the difference represents 5.6% of its mean value. When much lower resolution is used, the measurements difference further increased. This Figure also shows that resolution reduction in phase encoding introduced less difference in measurements compared to reduction in the direction parallel to the main magnetic field, B_0. In **Figure 4.9**, the error at different slab widths is visualized in the DGM region for the standard method and the proposed method, in which the latter produced more consistent contrast. When the high-to-low resolution ratio is 4:4:4, no remarkable difference is observed as the slab width decreases until 8 slices. With the low-to-high ratio of 6:2:4 however, the differences became notable at a 22-slice width and below.

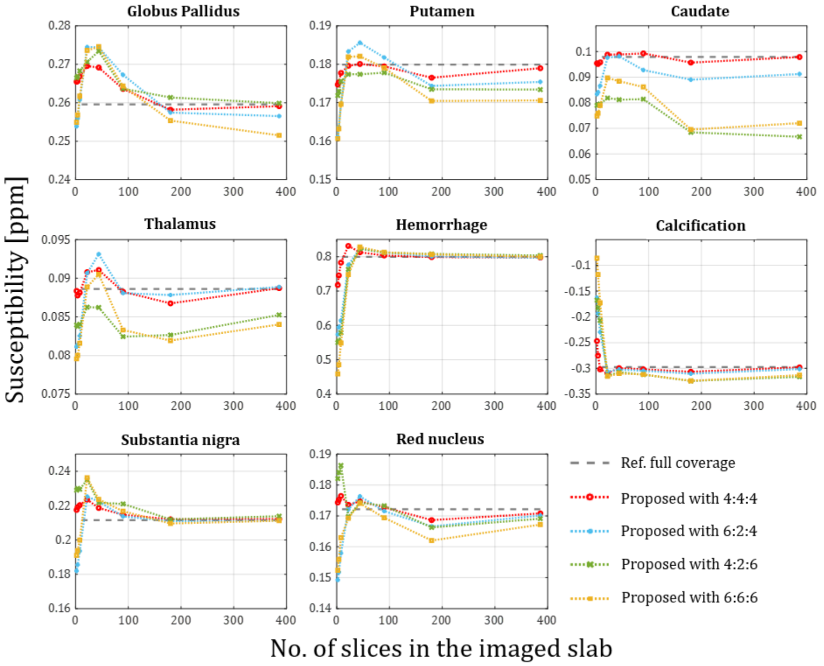

***Figure 4.8**: Simulation results of susceptibility 2D measurements using the proposed hybrid method at different down-sampling factors (phase:readout:slice) for the low-res data. Measurements deviate further from the reference full-coverage values with higher down-sampling factor. Resolution reduction in phase-encoding direction caused less error than in through-plane (i.e., slice) direction.*

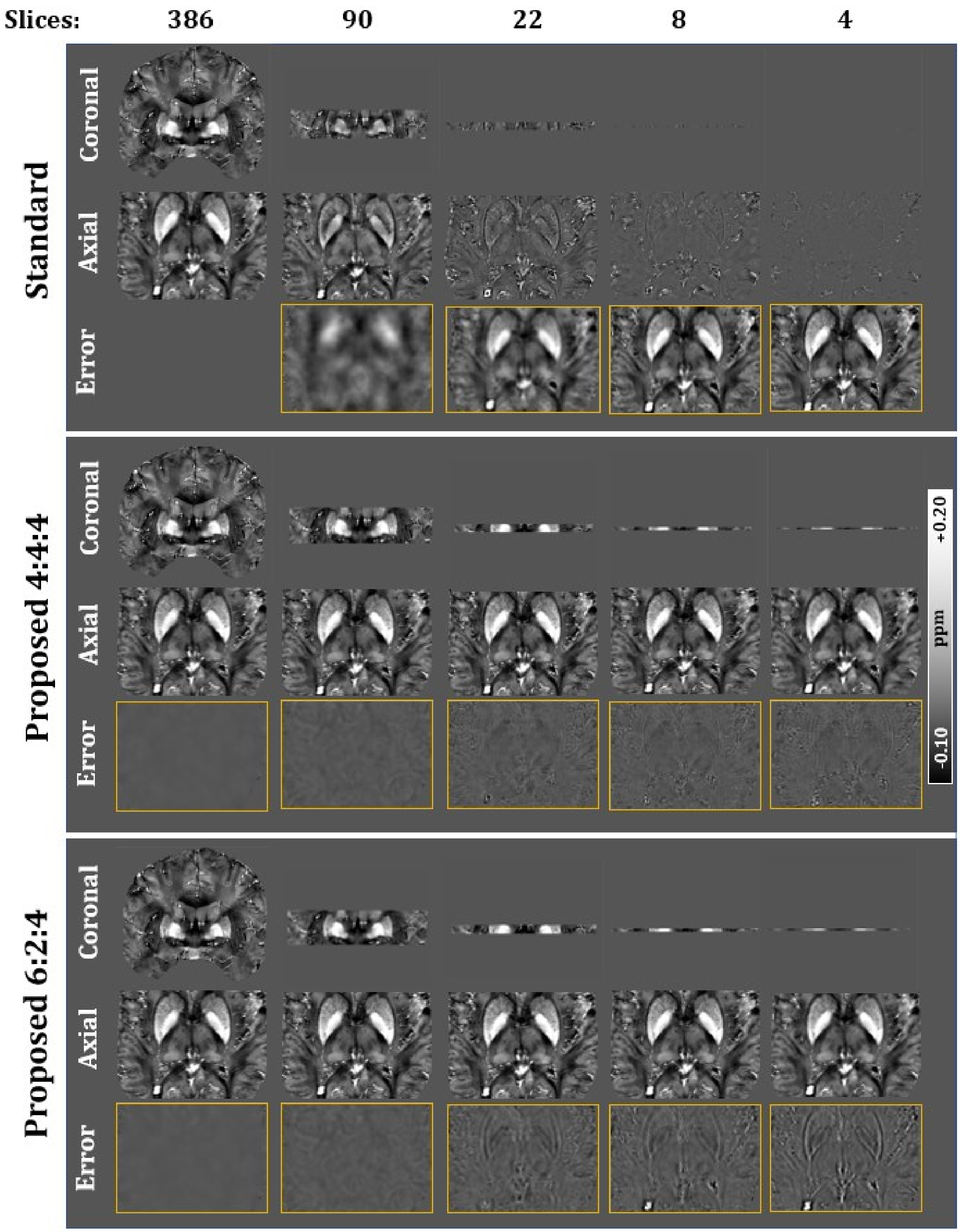

Figure 4.9*: Visualization of the obtained QSM results from simulation at different slab widths using the standard method (top), and the proposed method with 4:4:4 (middle) and 6:2:4 (bottom) down-sampling factors. For each method, coronal and zoomed-in axial views are shown, as well as the difference with respect to the reference full-coverage susceptibility map.*

4.5.2 **In-vivo Experiments**

Similar to simulations, in-vivo measurements presented in **Figure 4.10** demonstrate that reducing the slab width caused an increased underestimation in the produced QSM using the standard method, while the proposed method resulted in a more consistent measurements with around 5% error in most ROIs down to 8 slices (**Figure 4.10B**). **Table 4.1** shows that with an 8-slice slab the mean difference with respect to the 78-mm width slab stayed within 10 ppb for most measurements. **Figure 4.10** also shows that measurements obtained with actual thin slab acquisitions (indicated by star and tringle markers) are comparable with those obtained from the artificially reduced slab post acquisition.

In **Figure 4.11A**, example QSM images obtained from in-vivo 78-mm slab are visualized: the high-res and the two supporting low-res acquisitions. In panels **B** and **C** of the same Figure, QSM obtained from in-vivo thin-slab acquisitions (3D and 2D) using the studied methods are illustrated. The proposed method better preserved both contrast and fine details from an actual 14.3-mm slab (10.4-mm effective width excluding aliased slices) acquisition, as well as 5.2-mm slab (8 slices) virtually produced at post-processing stage. However, acquiring such a thin slab at 3T is challenging (without compromising scanning time) due to SNR issues.

Table 4.1*: ROI measurements (mean ± SD in ppb) from 8-slice slab of three subjects using the proposed method compared to the full slab width measurements of the 3D acquisition (referred to as Ref.). Mean differences above 10 ppb are highlighted using bold italic font.*

			GP	**Putamen**	**Caudate**	**Thalamus**	**RN**	**SN**
Subject	**1**	**Ref.**	155.1±21.3	86.9±28.7	85.2±22.2	64.0±30.2	154.8±27.0	181.1±30.5
		Proposed	149.0±24.0	82.1±27.2	79.8±25.7	60.5±28.8	149.8±20.6	***156.3±35.7***
	2	**Ref.**	168.2±28.1	95.0±24.7	95.2±20.1	79.5±32.7	167.9±23.9	143.5±30.1
		Proposed	176.8±29.4	104 ±19.4	91.8±22.6	78.7±36.5	178.0±29.9	146.0±28.7
	3	**Ref.**	193.4±28	75.5±19.5	79.9±21.4	63.1±17.5	191.3±23.8	176.6±28.1
		Proposed	***207.8±26.9***	***87.3±18.7***	74.9±23.9	65.4±19.9	197.1±28.9	176.0±27.2

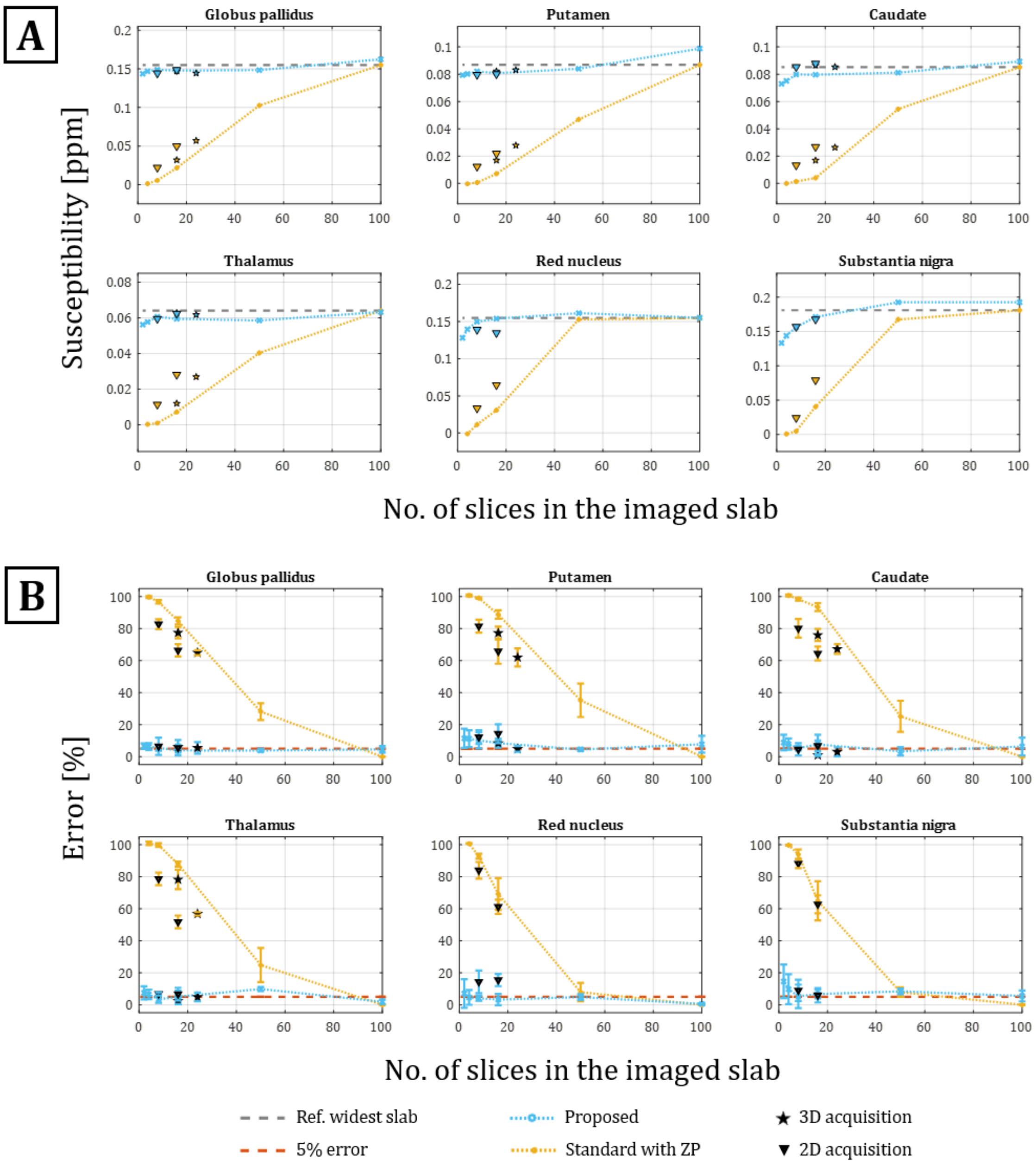

***Figure 4.10**: In-vivo measurements of QSM obtained using the standard and the proposed methods at different slab widths. A) Mean susceptibility measurements of one subject referenced to the mean value of internal capsule. The measurement at the full width of the imaged slab is indicated using a dashed gray line. B) Mean ± SD percentage error (with respect to the full width measurements) in three subjects indicates that the proposed method improved the measurements notably with ~5% error in most ROIs from slab width as small as 8 slices. ZP: zero-padding.*

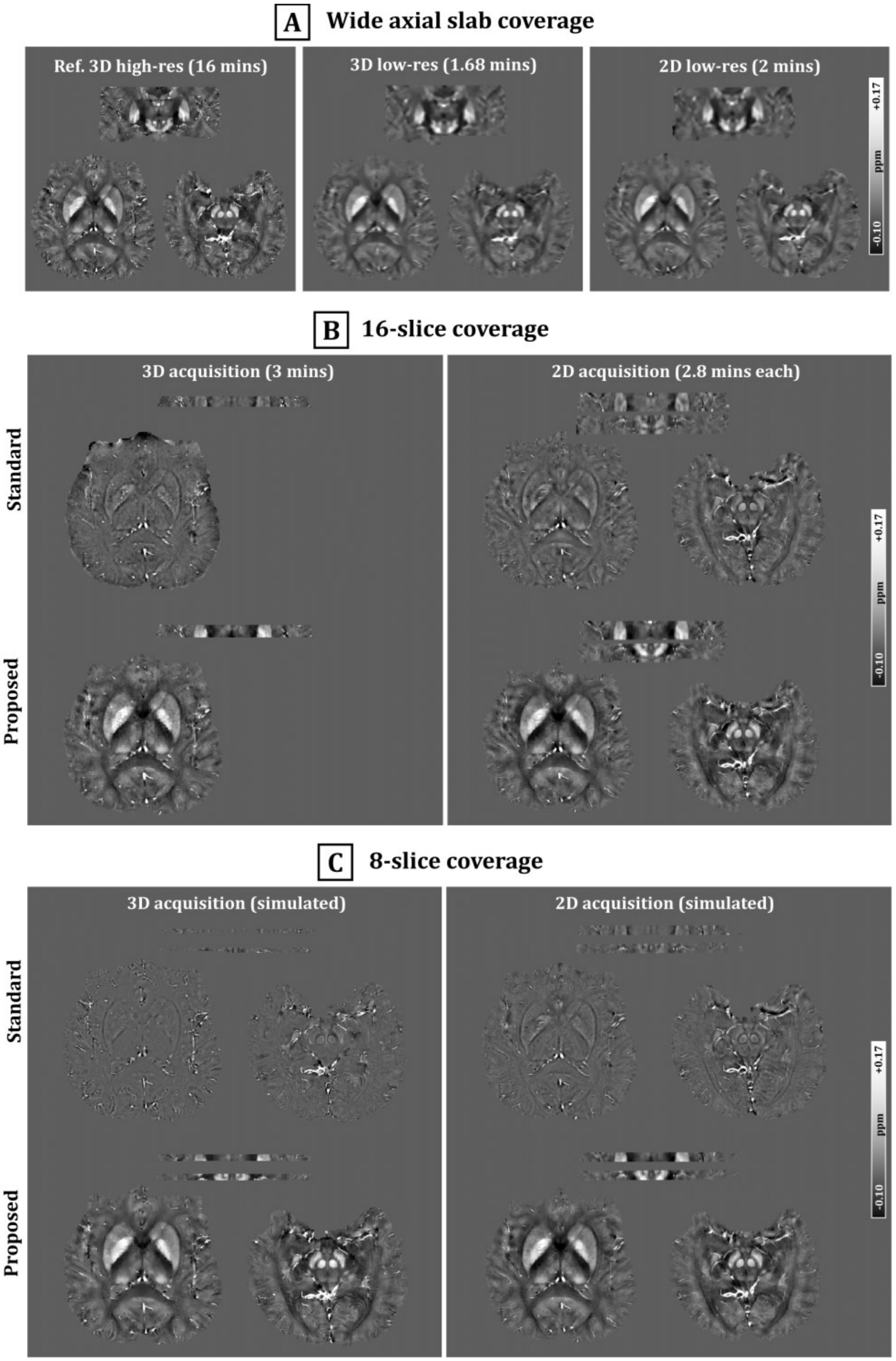

Figure 4.11*: In-vivo QSM images of one subject shown in A) are from the wide-slab coverage high-resolution reference and the supporting low-resolution data (3D and 2D), B) the acquired high-resolution thin-slab of 16 slices (after excluding aliased slices in 3D), and C) 8 slices obtained using the standard and the proposed methods. Slabs in C) were produced by reducing the number of slices after acquisition.*

4.6 DISCUSSION

Imaging thin slabs instead of full brain further reduces scanning time, thus improving the scanner efficiency and minimizing motion artifacts. The saved time can also be exploited to explore higher resolution (up to hardware/SNR limits) or improve the signal quality. However, accurate reconstruction of QSM from restricted spatial coverage is challenging due to deficiencies in the background removal and the dipole inversion processes. We proposed using additional rapid low-res data to overcome those deficiencies and stabilize the reconstruction solution, which enabled thin slab QSM acquisition with minimal artifacts in simulated and in-vivo datasets.

Previous studies reported that limiting the error due to the reduced coverage to 5% in the DGM region would require a slab width in the range 44 to 64 mm (196,235,237), depending on the actual physical dimension of the ROI, which agrees with the 60-mm width requirement for the standard method found in this study. Using the proposed method however, similar accuracy was achievable with only an 8-slice slab width (i.e., 2.64-mm slab at 0.33-mm slice thickness and 5.2-mm slab at 0.65-mm thickness). The achieved reduction in the required coverage represents a remarkable improvement over the standard method (e.g., ×11 smaller slab at 0.65-mm slice thickness).

This improvement was attained with support from additional rapid low-res data that serves two purposes: improving the background field removal process and guiding the dipole inversion algorithm. Simulation results suggested that accurate estimation of the background field would require the spatial resolution of the supporting data to be at least 2-mm isotropic. Below this resolution, voxels near air-tissue interfaces accumulate large amounts of phase at long echo times that destroys the magnitude signal and renders the signal in these regions unreliable, causing phase errors and challenging the unwrapping process. This eventually affects the accuracy of reconstructed susceptibility in nearby regions, which was notable both in simulated and in-vivo measurements. Moreover, other processing steps in the pipeline become more problematic and challenging when the voxel size exceeds 2^3 mm^3, including the brain extraction and the registration to the higher-res data.

Results also suggested the low-to-high resolution ratio should not exceed 4 for acceptable accuracy of 5% error in iron-rich regions. Assuming the lower bound mentioned above of 2-mm low-res data, this means that the resolution of the high-res data should be at most 0.5-mm in any direction. If the high-res data has voxels smaller than this, the resolution of the low-res data has to be improved proportionately. In addition, the low-res data should have extended coverage that is sufficient for the standard reconstruction method (i.e., 60-mm for iron-rich DGM).

To illustrate the potential saving in the acquisition time using the proposed method in light of the above discussed requirements, we consider two cases at the lower and upper bounds. For a high-res data of 1-mm isotropic voxels and a low-res data of 2-mm isotropic voxels; if the standard method would take 3.75 minutes to achieve the required accuracy at the middle of the slab (imaging a minimum of 60-mm slab), the proposed method would need about 1.44 minutes with a potential saving of 60%. If the high-res data has 0.5-mm voxels and the standard method takes about 15 minutes, the proposed method with the same low-res data (i.e., 2-mm isotropic) would need about 1.94 minutes with a potential saving of 87%. In these calculations, the time reduction is based on reducing the number of samples in the phase encoding and the slice encoding directions. In practice, time saving through reducing readouts is not encouraged for several reasons. First, it is recommended to keep the echo-timings of both the high- and the low-res data comparable, as previous studies have suggested matching echo times between different acquisition to minimize variations in the obtained tissue frequency shift (42,245). Second, keeping the resolution in the readout direction relatively high helps in facilitating the registration of the low-res to the high-res images. Third, it helps in reducing excessive phase accumulation near air-tissue regions and thus enhancing signal reliability in those voxels. Another practical consideration when using 3D sequence acquisition is that more than 60-mm coverage is typically required to compensate for the aliasing and low SNR at the slab edges. Here, the acquisition time for the high-res 78-mm slab obtained in-vivo was 16.29 minutes. Using the proposed method, comparable accuracy from a 14-mm thin slab (22 slices) required 4.68 minutes (~ ×3.5-fold time reduction). Further reduction in acquisition time by imaging only 8 slices (at this high-res) was hindered by the resultant low SNR at 3T. Although the proposed method was only tested using MEGE acquisition, it might be used with other sequences like EPI as long as sufficient SNR is attainable.

The concept of using a supporting rapid scan is common in several MRI applications, including correcting geometric distortions in echo planar imaging using a field map (246,247), and compensating surface coil sensitivity using a pre-scan (248,249). This work aimed to introduce the idea of the hybrid (high-res low-res) QSM reconstruction that uses a coarser version of the data with extended coverage to overcome the challenges encountered in reduced FOV scenarios. For the background removal step, the low-res data was used to estimate the slowly varying background field, which was then subtracted from the high-res data to yield the tissue field information. This way, the tissue field information in a thin imaged slab is preserved from the being attenuated by standard methods that are inefficient closer to the slab edges (74). In simulations, background subtraction was sufficient to obtain the tissue field without further processing. For in-vivo data, residual background field was observed after subtraction, which was minimized by a second order polynomial fitting and LBV. A possible reason for this difference is that in-vivo phase information undergoes more processing steps that might alter the phase and introduce a shift between the low-res and the high-res images. These additional steps include parallel imaging acceleration, coil combination, and phase offset estimation, which might have resolution-dependent processing (e.g., filtering). The difference might be reduced if interpolating the low-res images is performed from the raw measurements prior to coil combination, however at the cost of increasing the required computation and storage capacity.

For the dipole inversion step, two implementations were tested that utilize the low-res tissue field and susceptibility respectively. Using the tissue field distribution for regularization was found to produce more consistent measurements at very thin slabs, compared to using the susceptibility distribution. The improved performance is mostly because information in the tissue field is less processed, whereas the susceptibility information underwent more processing and can be affected by more involved parameters. Note that the added regularization term can shift the obtained susceptibility distribution from having zero-mean, which can be compensated by referencing the susceptibility values to a specific ROI within the brain. In general, obtained susceptibility values are relative and thus are typically referenced to facilitate comparison with other studies (40). Measurements in this study was referenced to the mean value of the IC, similar to other related literature (196,235).

With the current implementation of the proposed method, it was observed that the accuracy decreases as echo-timings get longer, due to the increased phase accumulation in the low-res data near air-tissue interfaces discussed above. We tested typical TEs used at 3T of range up to 40 ms and found that some phase unwrapping errors can be seen in the later echoes of the low-res images near sinuses, which affect the reliability in their vicinity. To eliminate unreliable regions while maximizing coverage near sinuses, we masked the phase information at each echo time using the corresponding magnitude mask prior to computing the total field map. Alternatively, one might try to estimate the unreliable regions iteratively using forward dipole field modelling (250). In general, QSM is sensitive to the definition of the VOI boundaries (i.e., brain mask) and thus an inherent variation is expected in the proposed method due to masking differences between the low- and high-res volumes. Minimizing the difference between the masks of the two data sets would further improve the accuracy and thus investigating better masking approaches is warranted, including deep learning-based segmentation (251,252).

Imaging thin slabs using 3D sequences suffers from aliasing artifacts and low SNR near the edge of the slab due to slab-selective profile imperfections (253). Those affected slices are discarded and thus the effective slab width becomes smaller, requiring the coverage to be extended further beyond the actual required width. The exact amount of slice oversampling would depend on the characteristics of the used RF pulse. This issue is avoided when 2D sequence acquisition is used, however at the cost of reducing the maximum achievable through-plane resolution (i.e., slice thickness). Another limitation for the minimum width of the acquired slab is SNR, which depends on the used spatial resolution and the imaging field strength. In 3D acquisitions, thinner slab means fewer data points are collected and thus less noise averaging. Although increasing the number of signal averages can improve the achievable SNR, it lengthens the acquisition time which for 3D sequences can be used instead to acquire more slices and gain the same SNR. Similarly, reducing the acquisition time in 2D sequences by collecting fewer slices necessitates reducing the repetition time (and flip-angle), which leads to a lower SNR.

Limitations of this study include the absence of the introduced method validation on in-vivo patient data with abnormal iron accumulation. However, the performance in the presence of strong iron sources was tested using simulated data with a hemorrhagic lesion, which was accurately reconstructed using few slices. Another limitation is that the measurements were mainly focused on the iron-rich regions because these are the most affected by reducing the VOI. Also, the study focused only on reduced VOI along the dimension parallel to the main magnetic field, which is reported to be impacted the most (e.g., accurate estimation of globus pallidus susceptibility required spatial coverage that is ×1.3, ×3.3, and ×5.6 the ROI size along left–right, anterior–posterior, and superior–inferior directions, respectively) (235). However, it is expected that the introduced method is generalizable to any dimension as indicated by simulations. Moreover, the method was tested only at a single field strength of 3T, two sequence variations, and a few pairs of resolution. Further testing of the new method is warranted to confirm its efficiency.

4.7 CONCLUSION

A new method was introduced to improve the accuracy of QSM obtained from thin slabs with aid from a lower-resolution acquisition with extended coverage. This could help in reducing the acquisition time burden of QSM in applications focusing on imaging specific regions of limited extent. The new method was tested using simulated and in-vivo data, in which more consistent QSM measurements were achievable in-vivo at 3T with spatial coverage as small as 10.4 mm, with aid from a dataset of ×24 coarser resolution.

4.8 Acknowledgements

This work was supported by the Natural Sciences and Engineering Research Council of Canada.

Chapter 5: Multisite reproducibility of quantitative susceptibility mapping and effective transverse relaxation rate in deep gray matter at 3 T using locally optimized sequences in 24 traveling heads[1]

5.1 **Abstract:**

Iron concentration in the human brain plays a crucial role in several neurodegenerative diseases and can be monitored noninvasively using quantitative susceptibility mapping (QSM) and effective transverse relaxation rate (R_2*) mapping from multi-echo T_2*-weighted images. Large population studies enable better understanding of pathologies and can benefit from pooling multisite data. However, reproducibility may be compromised between sites and studies using different hardware and sequence protocols.

This work investigates QSM and R_2* reproducibility at 3 T using locally optimized sequences from three centers and two vendors, and investigates possible reduction of cross-site variability through post-processing approaches. Twenty-four healthy subjects traveled between three sites and were scanned twice at each site. Scan-rescan measurements from seven deep gray matter regions were used for assessing within-site and cross-site reproducibility using intraclass correlation coefficient (ICC) and within-subject standard deviation (SDw) measures. In addition, multiple QSM and R_2* post-processing options were investigated with the aim to minimize cross-site sequence-related variations, including: mask generation approach, echo-timing selection, harmonizing spatial resolution, field map estimation, susceptibility inversion method, and linear field correction for magnitude images.

The same-subject cross-site region of interest measurements for QSM and R_2* were highly correlated ($R^2 \geq 0.94$) and reproducible (mean ICC of 0.89 and 0.82 for QSM and R_2*, respectively). The mean cross-site SDw was 4.16 parts per billion (ppb) for QSM and 1.27 s^{-1} for R_2*. For within-site measurements of QSM and R_2*, the mean ICC was 0.97 and 0.87 and mean SDw was 2.36 ppb and 0.97 s^{-1}, respectively. The precision level is regionally dependent and is reduced in the frontal lobe, near brain edges, and in white matter regions. Cross-site QSM variability (mean SDw) was reduced up to 46% through post-processing approaches, such as

---

[1] A version of this chapter has been published*: Naji N, Lauzon ML, Seres P, et al. Multisite reproducibility of quantitative susceptibility mapping and effective transverse relaxation rate in deep gray matter at 3 T using locally optimized sequences in 24 traveling heads. NMR in Biomedicine. 2022; 35(11): e4788.*

masking out less reliable regions, matching available echo timings and spatial resolution, avoiding the use of the non-consistent magnitude contrast between scans in field estimation, and minimizing streaking artifacts.

Keywords: multisite, QSM, R_2* mapping, reproducibility, 3 T

5.2 INTRODUCTION

The effective transverse relaxation rate (R_2*) and quantitative susceptibility mapping (QSM) offer non-invasive ways to estimate metallic ion deposits in brain tissue, with additional sensitivities to myelin, calcium, and water content. Both are typically calculated from multi-echo gradient echo (MEGE) data and are widely used to estimate iron concentrations in known iron-rich regions indirectly via its effect on the local magnetic field (15,52,54,254,255). However, R_2* lacks the ability to differentiate between paramagnetic and diamagnetic sources, and suffers from blooming artifacts. On the other hand, QSM overcomes these issues by solving the field-to-source model and estimating the bulk susceptibility in each voxel. Susceptibility can also be mapped from single-echo T_2*-sensitive sequences. QSM and R_2* have shown strong correlation with postmortem iron measurements (39,256–258) and have been used in several iron-related longitudinal (31,48,259), lifespan (26–28,260), and pathological studies (128,131,133,261). Many QSM and R_2* studies have focused on deep gray matter regions, including the basal ganglia and thalamus, as these structures play key roles in motor control and sensory perception, whereby iron accumulation in these regions has been associated with several neurodegenerative diseases including Alzheimer's disease, Huntington's disease, multiple sclerosis, and Parkinson's disease (30,131,158,262).

Large population studies to examine wider pathologic and demographic variations can benefit from pooling studies from multiple sites. However, this requires methods to be highly reproducible and minimally sensitive to hardware and/or sequence differences among sites. Previous studies have reported high QSM and R_2* repeatability in brain (40,41,263), as well as high reproducibility across different sites (two to 10 sites) (41,264–267), vendors (up to three) (41,266), and field strengths (1.5, 3, and 7 T) (245,268,269). These studies excluded sequence-related variability by using almost the same protocol in all the repeated scans. However, it is also beneficial to be able to pool multisite data acquired without the same standardized protocol retrospectively to form larger datasets of wider pathological and/or demographical coverage, such as maximizing age/demographical coverage in lifespan studies, or increasing the statistical power of specific under-represented cohorts of a disorder, effect, or demographic. Data would then typically contain local sequence variations, which influence reconstructed R_2* and susceptibility maps (196,270,271). Moreover, although previous large-scale multisite studies included up to 10 sites, the number of subjects to test reproducibility (traveling heads) was only one or two healthy subjects (265–267). The largest previous study with respect to the number of traveling heads included 10 subjects scanned in five sites at 7 T (41).

This study aimed to 1) assess QSM and R_2* reproducibility in 24 traveling heads at three sites (all at 3 T) with two vendors (and three scanner models) using locally optimized non-harmonized data from the same 24 subjects collected using three independently optimized sequences, and 2) investigate possible reduction of cross-site variability induced by sequence variations through post-processing approaches.

5.3 METHODS

5.3.1 Subjects and Imaging Setup

Twenty-four healthy subjects (11 males and 13 females, aged 20 to 49 years) were imaged at three sites (**Table 5.1**) at 3 T under the approval of the local ethics committee. Each subject gave written informed consent prior to imaging and was imaged twice at each site in different sessions (leaving the scanner in between). The mean interval between within-site sessions was 8.5 days (79% of sessions occurred within 48 h, with three sessions experiencing longer delays between 2.4 to 3.6 months), and all six sessions were completed within 18 to 110 days. Imaging protocols were optimized independently by each site and included a whole brain 3D MEGE with at least six echoes for R_2* and QSM measurements (**Table 5.1**). While the acquisitions were similar, there were substantial differences in echo and repetition times (TE and TR, respectively), flip angle, spatial resolution, slice orientation, and parallel imaging approach between sites based on local optimization. Each study also included a 3D inversion recovery T_1-weighted imaging sequence for registration and tissue segmentation purposes. To minimize variability from segmentation, only the 3D T_1-weighted acquisition from the first scan of Site 3 was used with the following parameters: 250×250 mm^2 FOV, 208 sagittal slices, 0.87×0.87×0.85 mm^3 voxel size, 8° flip angle, and TI/TE/TR of 900/2.37/1800 ms acquired in 3 min 39 s. After a manual quality check of the MEGE data, three subjects were found to have motion artifact in one or more examinations, leading to exclusion of those scans. Additionally, one subject did not complete their protocol at

Site 1. Therefore, analyzed data included full data (two scans at each of three sites) in 20 subjects and at least one scan from two sites in the remaining four subjects (subject #3: five scans, subject #9: three scans, subject #13: three scans, subject #14: three scans), giving a total of 134 scans.

5.3.2 QSM and R_2* Processing

For QSM, 3D MEGE phase images were processed with standard methods for coil combination, phase unwrapping, and background field removal. Other processing steps were tested with multiple options to reduce sequence variations, as described in the following section. Coil combination for complex data was performed using the default method in each system: Siemens used an adaptive approach (61), while GE scanners used a sensitivity-based combination (Array coil Spatial Sensitivity Encoding Technique [ASSET], GE Medical Systems). Phase images were unwrapped using a best path approach (67). A tissue field map was extracted using a variable-radius sophisticated harmonic artifact reduction for phase (V-SHARP) data algorithm with a maximum kernel of 12 mm (77). For R_2* map reconstruction, a voxel-wise mono-exponential fitting for the magnitude images was performed using the autoregression on linear operation (ARLO) method (272).

5.3.3 Post-processing Options to Minimize Sequence Variations

To minimize the effect of sequence variations on the quantitative maps, multiple post-processing options were tested, including:

a. Volume of interest (VOI) mask: VOI mask extraction was tested using the MEGE magnitude of (i) the first TE and (ii) the longest comparable TE between protocols (TE ~ 26 ms), via FMRIB Software Library (FSL) (v. 5.0.8)'s brain extraction tool (64) with 0.4 threshold and 2.0 smoothness factor.

b. TE selection: Because the imaging protocols utilized different ranges of echo times, two TE selection scenarios were examined: processing data from (i) all the echo times, and (ii) only from the five comparable TEs found in the three protocols (TE times underlined in **Table 5.1**).

c. Total field map: Three common approaches (based on three publicly available QSM toolboxes: STI Suite v. 3.0 (108), QSM reconstruction (229), and the morphology-enabled dipole inversion [MEDI] Toolbox [6 November 2017 release] (107)) were tested for computing the total field map from MEGE phase images, namely (i) taking the average over selected TEs (108), (ii) doing a magnitude-weighted average (229), and (iii) via complex signal nonlinear fitting (62,107).

d. Input field map resolution: The process of background field removal using V-SHARP involves computing a moving average using approximated sphere-shaped kernels of radii as small as 1 mm. This causes digitization error and might introduce variability when resolution is not consistent in all exams. To test the effect of matching spatial resolution before extracting the tissue field map, the background field was removed using (i) the raw resolution, and (ii) after interpolation to the highest reconstructed resolution (Site 2, isotropic 1 mm^3 voxels).

e. Field-to-source inversion: Three inversion algorithms were tested to produce the final susceptibility map: (i) the iterative least square method (iLSQR), which does not rely on magnitude information and minimizes streaking artifacts (92,108); (ii) total variation dipole inversion (TVDI), which solves a magnitude-weighted linear model with total variation regularization (56,229); and (iii) MEDI, which solves the magnitude-weighted nonlinear model and also uses magnitude contrast for regularization (62,107). The regularization parameters were set to 5×10^{-4} and 2500 (average optimized values over a subset of the data using the curvature of the L-curve method (230)) in the TVDI and MEDI algorithms, respectively. Other parameters used the default values given in the official code packages (107,108,229).

f. Linear field correction for R_2*: R_2* maps were fitted (i) with and (ii) without applying a linear field correction to MEGE magnitudes (52). The linear field correction was achieved as follows: a field map was estimated from the difference of the first two echoes phase information. Then MEGE magnitudes were corrected through division by $sinc(\Delta\omega_{0x}/2t)\cdot sinc(\Delta\omega_{0y}/2t)\cdot sinc(\Delta\omega_{0z}/2t)$ (52), where t refers to echo time, and $\Delta\omega_{0x}$, $\Delta\omega_{0y}$ and $\Delta\omega_{0z}$ are computed using the field map gradient along x, y and z, respectively.

Multiple combinations of the above-mentioned options were evaluated. For demonstration purposes, we present eight processing pipelines (combinations of processing steps) for QSM (Sx1 to Sx8) and three for R_2* (Rx1 to Rx3), in which only one processing step was changed in each pipeline. The summary of these pipelines and their labels used thereafter are listed in **Table 5.2**.

Table 5.1: *MR systems and imaging parameters of all sites.*

	Site 1	**Site 2**	**Site 3**
Site Name	Alberta Children's Hospital	Foothills Medical Centre	Peter S. Allen MR Research Centre
Location	Calgary, AB, Canada	Calgary, AB, Canada	Edmonton, AB, Canada
Vendor	GE Healthcare	GE Healthcare	Siemens
Scanner model	Discovery MR750w	Discovery MR750	Prisma
Software version	DV25	DV25	Syngo VE11C
Field strength (T)	3.001	3.002	2.895
Head coil	32 channels	16 channels	64 channels
FOV (mm^3)	192×240×174.8	204.8×256×148	202.5×240×149.6
Slice orientation	Axial	Axial	Axial oblique
Acquired voxel size (mm^3)	0.94×0.94×1.90	1.33×1.33×2.00	1.14×0.94×1.70
Reconstructed voxel size (mm^3)	0.94×0.94×1.90	1.00×1.00×1.00	0.94×0.94×1.70
Acquired matrix size	204×256×92	154×192×74	177×256×88
Flip angle (deg)	10	20	13
TR (ms)	56.8	29.5	37
TEs (ms)[a]	4.5, 9.8, 15.1, 20.4, 25.7, 31.0, 36.3, 41.6, 46.9, 52.2	3.0, 6.3, 9.6, 13.0, 16.3, 19.6, 23.0, 26.3	3.8, 9.3, 14.8, 20.3, 25.8, 31.3
Readout mode	monopolar	monopolar	monopolar
Acceleration factor	2.5 (ASSET)	1 (ASSET)	2 (GRAPPA)
Slice partial Fourier	0.7	0.7	1
Flow compensation	On	On	Off
Scan time (min:sec)	5:14	4:10	5:30

[a] Comparable echo times (min TE, and approximately ~10 ms, ~15 ms, ~20 ms and ~26 ms) are underlined.

Table 5.2*: Summary of different processing pipelines tested to minimize sequence-induced variations. Change in each setup is highlighted in bold text.*

	Setup	Mask	TEs Selection	Field Mapping	Field Map Resolution	Susceptibility Inversion	Linear Field Correction
QSM	**Sx1**	Last comparable TE	Comparable TEs	Average	Matched	iLSQR	N/A
	Sx2	**First TE**	Comparable TEs	Average	Matched	iLSQR	N/A
	Sx3	Last comparable TE	**All TEs**	Average	Matched	iLSQR	N/A
	Sx4	Last comparable TE	Comparable TEs	**Magnitude weighted average**	Matched	iLSQR	N/A
	Sx5	Last comparable TE	Comparable TEs	[a] **Nonlinear fitting**	Matched	iLSQR	N/A
	Sx6	Last comparable TE	Comparable TEs	Average	**Raw**	iLSQR	N/A
	Sx7	Last comparable TE	Comparable TEs	Average	Matched	**TVDI**	N/A
	Sx8	Last comparable TE	Comparable TEs	Average	Matched	**MEDI**	N/A
R_2*	**Rx1**	Last comparable TE	All TEs	N/A	N/A	N/A	On
	Rx2	Last comparable TE	All TEs	N/A	N/A	N/A	**Off**
	Rx3	Last comparable TE	**Comparable TEs**	N/A	N/A	N/A	Off

[a] Nonlinear fitting of total field in Site 2 data was done using 8 echoes (i.e., up to the last comparable TE) to avoid uneven echo spacing.

5.3.4 Registration and Measurements

The performance measures of the different processing pipelines were compared voxel-wise and region of interest (ROI)-wise. Seven deep gray matter ROIs were delineated for measurement and comparison with previous studies: caudate, putamen, thalamus, globus pallidus (GP), substantia nigra (SN), red nucleus (RN), and dentate nucleus (DN). Four of these (caudate, putamen, thalamus, and GP) were automatically segmented using the VolBrain online tool (273) from T_1-weighted images, after which the obtained segmentation masks were eroded by one voxel to minimize inclusion of nearby tissues. The other three structures (SN, RN, and DN) are not supported by VolBrain and were manually segmented (by N.N. and were verified by two additional MRI scientists: A.W. and P.S.) on all slices using ITK-SNAP software (v. 3.4.0) (231). Transformation matrices into the measurement (i.e., segmentation) space were obtained by rigidly registering the first echo MEGE magnitude (i.e., at TE1) of each scan to the T_1-weighted volume of the reference scan (i.e., first scan of Site 3), using the advanced normalization tools (ANTs) package (187). These matrices were then used to linearly map quantitative susceptibility and R_2^* images into the measurement space. Measurements of structure mean value were recorded by pooling over both hemispheres. For QSM, all values were referenced to the brain average, which has been reported among the best options and/or used in the recent literature involving healthy subjects, including scan-rescan studies (40,41) and lifespan studies (27,28). For voxel-wise analysis, the T_1-weighted volumes were nonlinearly registered into the FSL MNI152 T_1-weighted average structural template using the "fsl_anat" tool of the FSL package (227). The transformation warp fields obtained were then used to map QSM and R_2^* images from the measurement space into the MNI152 template space.

5.3.5 Statistical Analysis

Scan-rescan reproducibility (within-site and cross-site separately) was statistically assessed using the intraclass correlation coefficient (ICC) as a relative reliability index, and the within-subject standard deviation (SDw) as a measure of absolute variability. The ICC estimates the ratio of between-subject variance (SDb^2) to the total variance (i.e., $ICC \sim SDb^2 / [SDb^2 + SDw^2]$), which was calculated based on a single-rating, absolute agreement, two-way mixed-effects model (274). Within-site ICC/SDw values were calculated in each site separately and the average of the three sites was reported. Similarly, cross-site values were calculated in Scan 1 and 2 separately and the average of the two scans was reported. Additionally, the group average value was calculated by averaging the values of all scans and subjects to detect any global shift in susceptibility and R_2* contrast due to post-processing steps. Statistical significance among different processing setups was tested using one-way analysis of variance (ANOVA; with the significance level set at 0.05), followed by multiple comparisons using Tukey's test.

Within-site and cross-site measurements were statistically analyzed using a linear mixed effects model (LME) (275) in order to use all data, including those from incomplete datasets. The tissues (i.e., ROIs) and the subjects acted as random effects, while the fixed effect was the repeated scan and the scanner site in the within-site model and the cross-site model, respectively. Pair-wise comparisons between different scans were statistically analyzed using Student's paired t-test for means (two-sided with the significance level set at 0.05 and zero difference null hypothesis), and visualized using correlation and Bland–Altman plots (276). In correlation and Bland–Altman plots, all possible combinations of cross-site scans were included (i.e., four points per subject between any two sites).

All processing (except brain extraction, registration, and segmentation), analyses, and plots were performed using MATLAB (version R2020a; MathWorks, MA, USA). QSM and R_2* processing code files are publicly available via the links in the cited references. The processed maps, measurements, and analysis scripts of this study are available from the corresponding author upon request. Participant MRI images are not publicly available due to ethical considerations.

5.4 RESULTS

Figure 5.1 demonstrates sample scan-rescan images of one subject at the level of the deep gray matter nuclei. The contrast of MEGE magnitude varies widely between different sites as a consequence of differences in flip angles and repetition times. This was also observed in analytical calculations (not shown) using nominal values for proton density and T_2* (i.e., gray matter > white matter, gray matter < white matter, and gray matter ~ white matter in Site 1, 2, and 3, respectively). Quantitative maps however are more consistent, showing few differences near regions of high susceptibility gradient, such as veins and air–tissue interfaces.

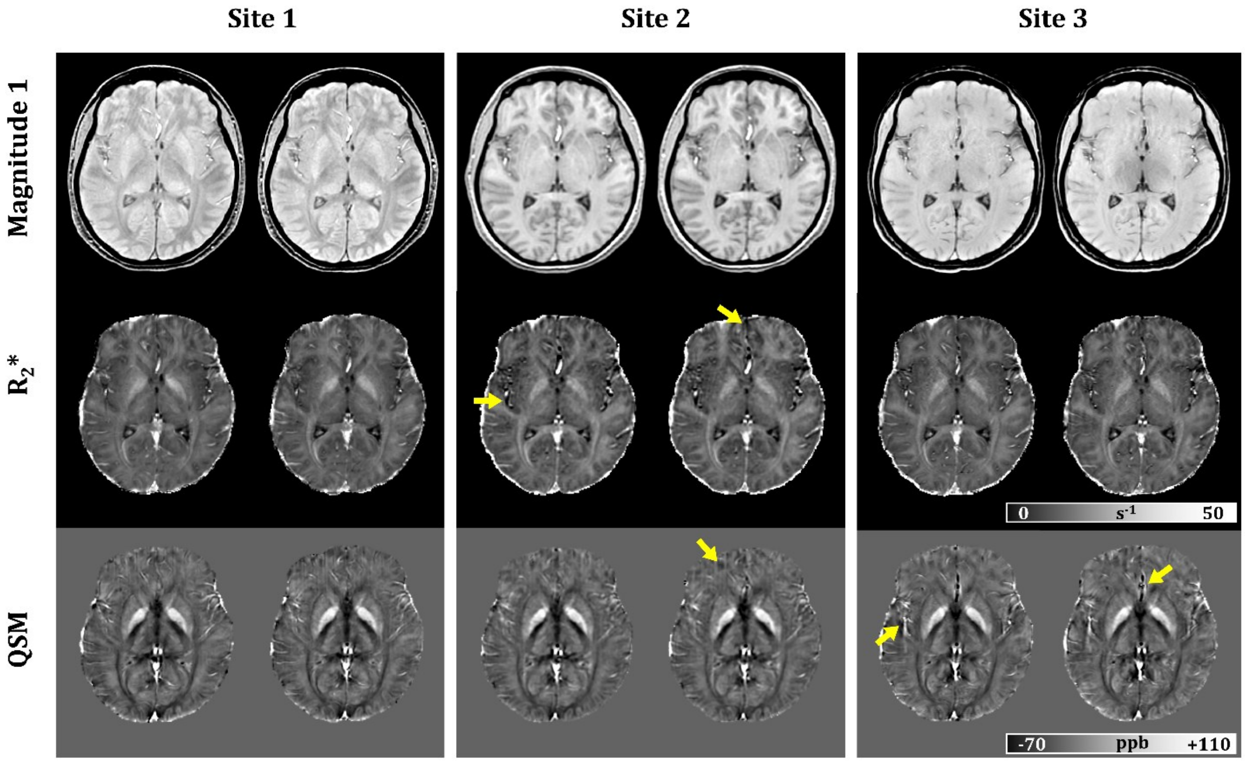

Figure 5.1: *Scan-rescan demonstration of one slice (at the level of deep gray matter nuclei) in one subject of first echo MEGE magnitude (which shows different T_1 weightings due to variation in acquisition parameters), effective transverse relaxation rate (R_2*), and quantitative susceptibility mapping (QSM). Small differences between quantitative maps are noticeable around strong susceptibility gradient regions (arrows) such as near veins and air–tissue interfaces. R_2* and susceptibility maps were obtained using the Rx1 and Sx1 processing pipelines (see Table 5.2), respectively. MEGE, multi-echo gradient echo.*

5.4.1 Post-processing Options

A demonstration of postprocessing-related within-site and cross-site variability is shown in **Figure 5.2** with voxel-wise metric maps. In general, the lowest reliability in QSM was observed in the frontal lobe and the cortical regions. In R_2*, white matter regions have the lowest reliability. Overall, the highest variability was observed near high susceptibility gradients (e.g., veins) and near the edges of the brain. For QSM, setup Sx1 showed the lowest overall variability. Generating the brain mask using the magnitude of the first TE (i.e., setup Sx2) induced variability in the frontal lobe and in regions near the sinus–tissue interface. Similarly, processing data of all TEs without matching (i.e., setup Sx3) and including magnitude contrast in the field estimation step (i.e., setups

Sx4 and Sx5) elevated the level of variability in the regions where the TE/magnitude information differ. Moreover, matching spatial resolution before removing background field (setup Sx1 vs. Sx6) further reduced overall variability (-8% in mean SDw). Reconstructed QSM images using the iLSQR have higher reliability and lower variability when compared with TVDI (Sx7) and MEDI (Sx8) based reconstructions, with differences more pronounced in cortical regions. In the case of R_2*, processing all TEs without matching (setups Rx1 and Rx2 vs. Rx3) appears to slightly reduce variability in the frontal lobe but increases variability in white matter regions. Furthermore, applying linear field correction before fitting (setup Rx1 vs. Rx2) slightly reduced sinus artifacts in the frontal lobe (not shown) but introduced variability in cortical regions.

ROI-wise comparisons of different post-processing setups are shown in **Figure 5.3**. In QSM, maps produced using Sx2 had lower average values (**Figure 5.3A**). Other processing setups resulted in comparable measurements in most ROIs, although GP average value was lower (~ -9%) in QSM reconstructed using the iLSQR (i.e., Sx1 to Sx6) compared with TVDI and MEDI methods (i.e., Sx7 and Sx8). The iLSQR, however, was better at reducing scan-rescan differences and artifacts, notably when head orientation (with respect to B_0) varied between scans (**Figure 5.4**). For R_2* measurements, all processing setups produced comparable average values in all ROIs (**Figure 5.3A**), although Rx1 measurements were slightly lower (0.2% to 2%). For reproducibility measures (**Figure 5.3B,C**), higher reliability (and less variability) was observed in within-site measurements compared with cross-site in both QSM and R_2*, regardless of the processing setup. The lowest ICC values were found in thalamus, and the highest cross-site variability was observed in SN and DN for QSM and R_2* values, respectively. For QSM, better overall performance was achieved using setup Sx1 with ICC for within-site/cross-site $\geq 0.90/0.58$ (0.97/0.90 excluding the thalamus) and SDw below 3.79/7.14 parts per billion (ppb). Improvement in SDw values using Sx1 was statistically significant compared with most other processing setups. Therefore, susceptibility maps obtained using setup Sx1 were used in the remaining analyses. For R_2*, processing all TEs (setups Rx1 and Rx2) improved thalamus reliability (+13% in ICC). In addition, applying a linear field correction prior to fitting (setup Rx1 vs. Rx2) slightly improved cross-site caudate and putamen measures (+7% and +2% in ICC, respectively), but increased cross-site SDw in DN, SN, and RN (~ +3% to +6%). However, these changes in SDw values were not statistically significant. For simplicity, the R_2* maps obtained using setup Rx1 were used throughout.

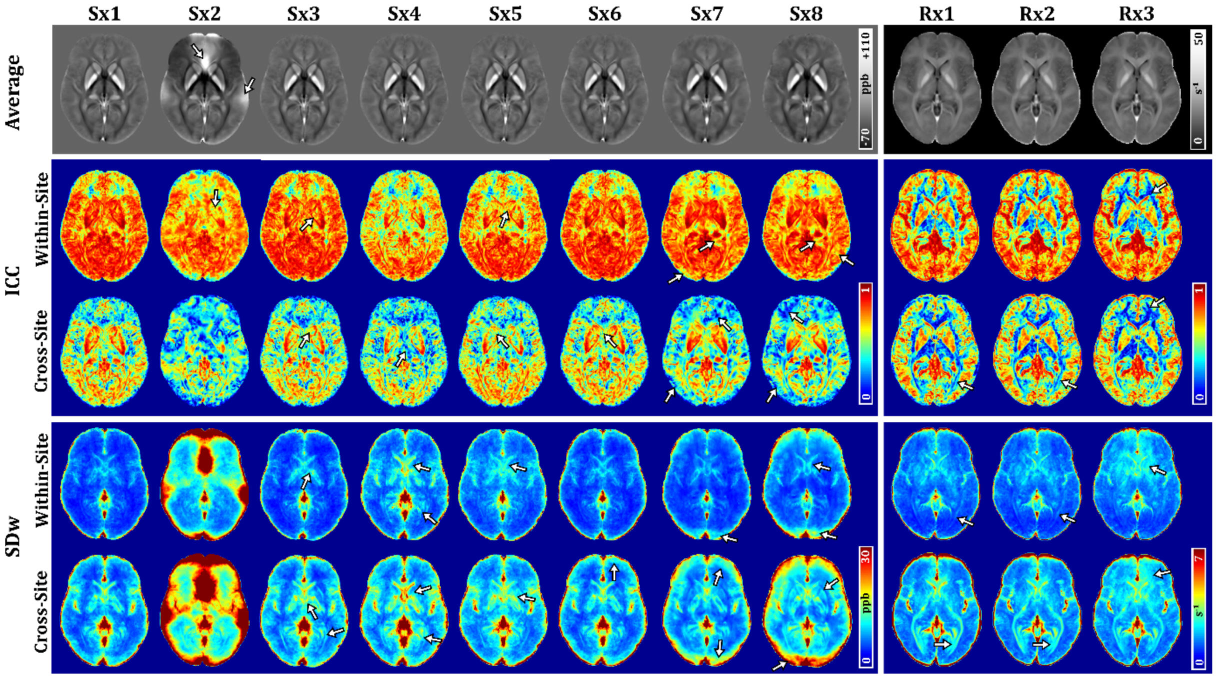

Figure 5.2: *Voxel-wise maps of average value, intraclass correlation coefficient (ICC), and within-subject SD (SDw) measures (obtained by nonlinearly registering QSM and R_2* images of all subjects to the same T_1-weighted average structural template) demonstrating post-processing variability for all the processing pipelines in Table 5.2. Arrows indicate some regions of increased variability. Overall, the highest and the lowest cross-site reliability was observed in the iron-rich regions, and in the frontal lobe and cortical layer, respectively. Higher variability was observed in the regions of high susceptibility gradient, such as around veins and air–tissue interfaces. When TEs were not matched, higher cross-site variability was observed in white matter regions in both QSM and R_2* (setup Sx3 in QSM, and setups Rx1 and Rx2 in R_2*). Using magnitude contrast in QSM processing introduced variability mostly in regions where magnitude information varied (setups Sx4 and Sx5). In R_2*, the lowest cross-site reliability was observed in the white matter and the frontal lobe. Minimal differences were observed when linear field correction was applied in R_2* processing (Rx1 vs. Rx2). Fitting R_2* over all TEs without matching reduced the variability in the frontal lobe (Rx1 and Rx2 vs. Rx3).*

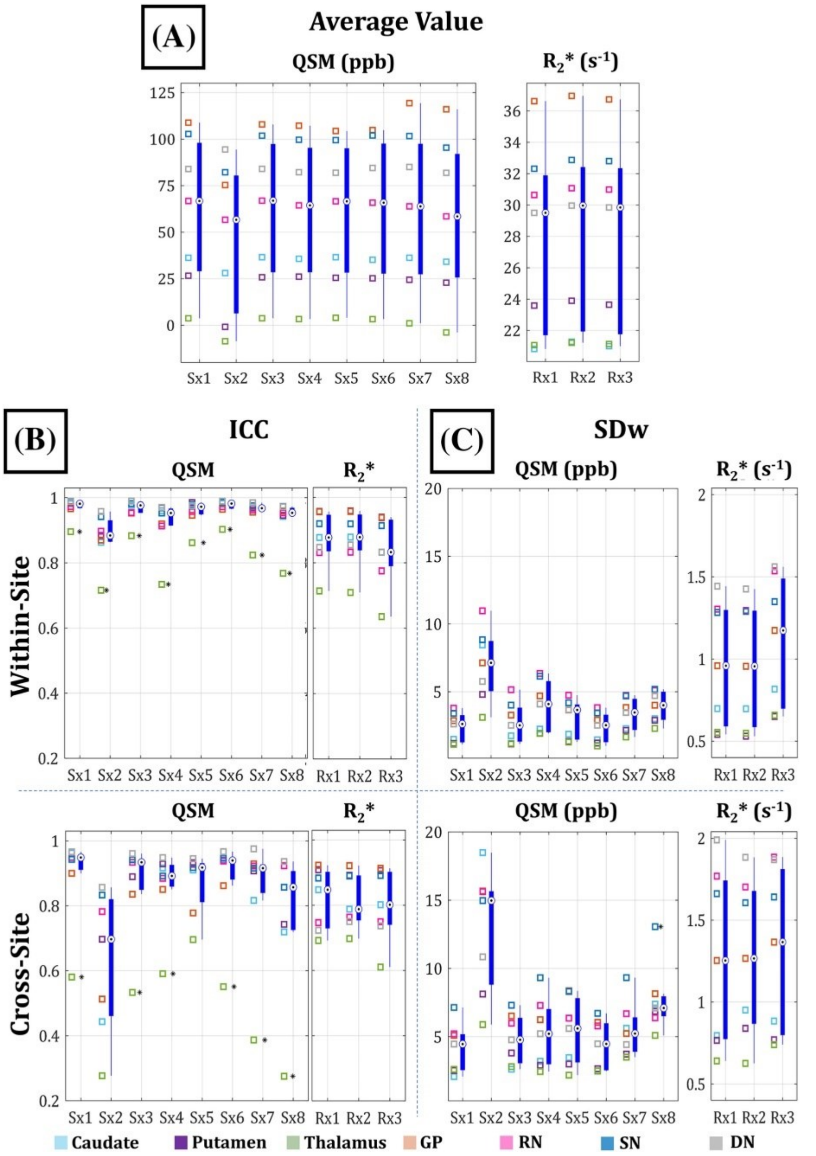

***Figure 5.3**: Boxplots of (A) Group average value, (B) ICC, and (C) SDw measures for all ROI measurements in QSM and R_2*. Values of each ROI are shown with squares. Median values and outliers are indicated by black dots within white circles and by black asterisks, respectively. Average QSM values are comparable in most processing setups (except Sx2). When the iLSQR reconstruction was used (i.e., Sx1 to Sx6), lower susceptibility values were obtained in GP, compared with TVDI and MEDI reconstruction algorithms. In R_2*, Rx1 measurements have slightly lower average values. Higher ICC and lower SDw indicate better reproducibility. For QSM, setup Sx1 demonstrated the best overall performance. For R_2*, minimal difference was observed between different processing pipelines, although setups Rx1 and Rx2 improved the reproducibility of measurements in the thalamus.*

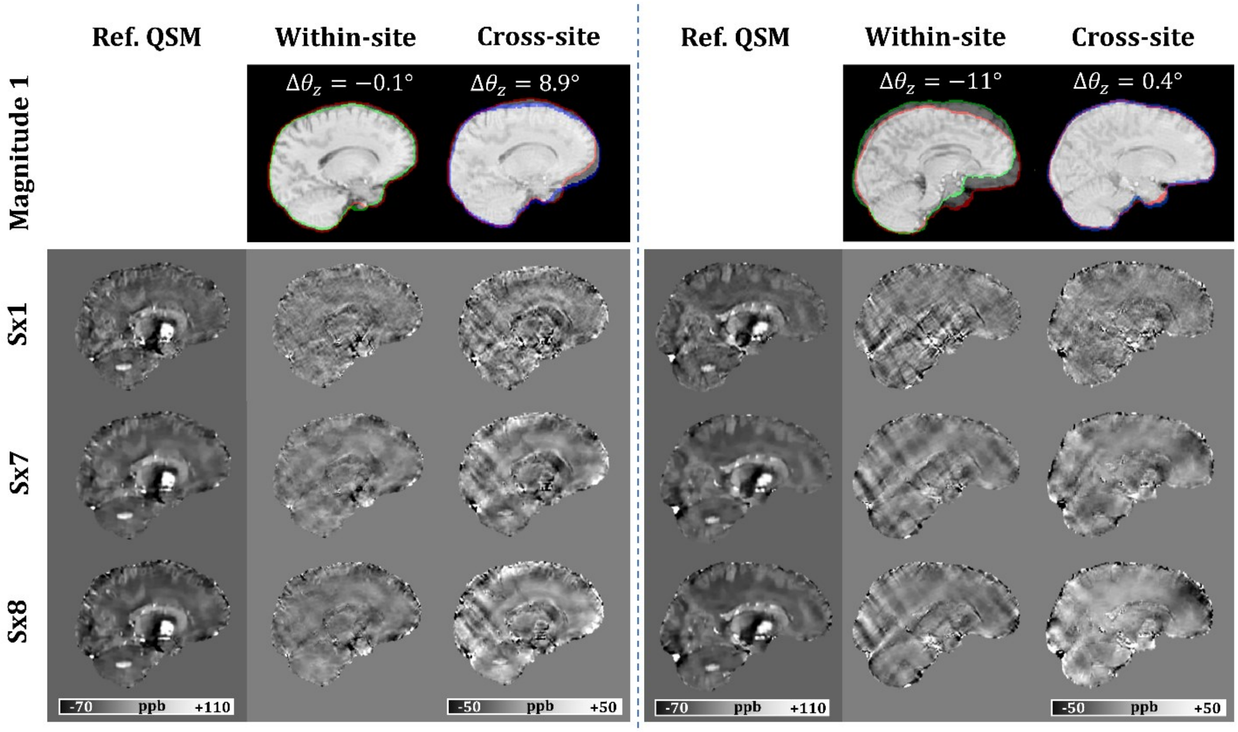

Figure 5.4: *A demonstration of scan-rescan differences in two subjects for different susceptibility inversion algorithms. Images show sagittal slices passing through the left globus pallidus (GP) and dentate nucleus (DN). The first row illustrates the variation in head orientation between scans. The brain in the MEGE first magnitude of Scan 1 (reference) is outlined by a solid red line, while in the second scan, within-site and cross-site are outlined using green and blue colored lines, respectively. Δθz refers to the angular difference between head orientations with respect to the B_0 direction. In the first and fourth columns, QSM of the reference scan is shown. The within-site/cross-site susceptibility differences are shown in the second/third and fifth/sixth columns, for subject 1 and 2, respectively. Noticeable artifacts can be seen in the difference maps when head orientation changed between scans. As evident by visual inspection, these artifacts are less severe in the QSM maps reconstructed by the iLSQR algorithm (i.e., Sx1).*

5.4.2 Reproducibility Analysis

The LME model of the within-site measurements uses Scan 1 as a reference (intercept) and estimates whether changing the scan (to Scan 2) would cause a significant change in the model prediction. Using the model residuals, four outlier measurements (of SN) in QSM and one (of DN) in R_2* were identified and excluded in the remaining analyses. The results of the model showed that the effect of changing the scan is not statistically significant ($p > 0.05$). The same observations were found in a post-hoc analysis using Student's paired t-test for means (Scan 2 – Scan 1) when the data from all sites were combined, in which no statistically significant difference was found between repeated scans. Furthermore, no significant difference was found between repeated measurements of any individual ROI in any individual site except in a few cases: QSM of RN in Site 2 ($p = 0.04$, mean difference [CI] = -1.89 [-3.78, -0.01] ppb) and caudate in Site 3 ($p < 0.01$, mean difference [CI] = 1.42 [0.75, 2.09] ppb), and R_2* of DN in Site 1 ($p = 0.048$, mean difference [CI] = 1.09 [0.01, 2.17] s^{-1}).

For the cross-site case, the model uses Site 1 as a reference (i.e., intercept) and estimates whether changing the site (to Site 2 or 3) would change the model prediction. Results showed that changing the site has a statistically significant effect ($p << 0.05$), and the estimated change is within 7% and 3% for QSM and R_2*, respectively.

Figure 5 visualizes the correlations (**Figure 5.5A**) and the differences (**Figure 5.5B**) between the scan-rescan measurements for both QSM and R_2*. Correlation plots demonstrated high correlations between all setups: within-site, cross-site, and cross-vendor, for both QSM and R_2*, with $R^2 \geq 0.94$. Slopes are within 4% and 8% from 1.0 (with standard error ≤ 0.01) in QSM and R_2*, respectively. In QSM, the highest slope deviation (4%) is associated with Site 1, demonstrating that QSM measurements are slightly lower in Site 1 when compared with Site 2. In R_2*, however, the highest slope deviation (8%) is found between different vendors, reflecting that R_2* measurements in Site 3 are slightly lower compared with other sites. The scan-rescan differences are emphasized in the Bland–Altman plots of **Figure 5.5**. The absolute bias between any two scans was within 4.1 ppb and 0.94 s^{-1} in QSM and R_2*, respectively. The SD of scan-rescan differences was within 5.3 ppb and 1.7 s^{-1} in QSM and R_2*, respectively. Overall, within-site biases and differences were smaller than for cross-site measurements. The distribution of within-site scan-rescan differences is almost symmetric around the mean in all structures, for both

QSM and R_2*. However, in cross-site measurements, some structures exhibit different patterns. In QSM for instance, distribution asymmetries were observed in the Site 1-related measurements. GP and DN measurements for instance deviate downward from the mean difference, reflecting that Site 1 measurements of GP and DN values were lower when compared with other sites. In the R_2* case, larger values, such as those observed in GP and SN, deviate further upward from the mean difference in Site 3-related measurements; this shows that deviation in Site 3 measurements is more pronounced in regions of higher magnitude. Furthermore, higher cross-site variability was observed in small structures such as SN and RN.

The key findings of the reproducibility analysis in this work can be summarized as follows: within-site QSM ROI measurements were correlated with R^2 of 0.99 and slope of 1.00, and were repeatable with a mean ICC of 0.97 and mean SDw of 2.36 ppb. For R_2* measurements, R^2 was 0.95, slope was 0.99, with mean ICC of 0.87 and mean SDw of 0.97 s^{-1}. On the other hand, cross-site QSM measurements were correlated with $R^2 \geq 0.98$ and mean slope of 0.99 (0.96 to 1.02), and reproducible with a mean ICC of 0.89 and mean SDw of 4.16 ppb. R_2* measurements were correlated with an R^2 of 0.94 and mean slope of 1.02 (0.93 to 1.08), and reproducible with a mean ICC of 0.82 and mean SDw of 1.27 s^{-1}. No significant bias was found between within-site measurements. For cross-site variability, the absolute bias was ≤ 4.1 ppb and ≤ 0.94 s^{-1} for QSM and R_2*, respectively. These results were achieved using the Sx1 and Rx1 processing pipelines for susceptibility and R_2* mapping, respectively.

5.5 DISCUSSION

The reproducibility of QSM and R_2* in the subcortical brain regions was assessed in a multisite dataset acquired at 3 T with non-harmonized MEGE sequences optimized separately by each site. This represents a realistic scenario for retrospective combination of multicenter data enabling larger datasets of wider pathological and/or demographical coverage. To the best of our knowledge, this is the first work that presents reproducibility analysis for QSM and R_2* data collected using non-harmonized protocols, and in a large number of traveling heads (N = 24).

Previous multisite reproducibility studies focused on harmonized acquisition protocols and reported promising results at 3 and 7 T, for QSM and R_2* (41,264–266,277). Different studies used different statistical measures to assess reproducibility, with SDw and SD of differences (SD_d) being the most common measures. At 3 T for these harmonized studies, the reported average QSM cross-site SDw, (absolute) bias and SD_d were in the ranges of 7.7 to 13.9, 1.22 to 4.5, and 7.3 to 10.4 ppb, respectively (264,266,277). The average reported regression slope and R^2 were in the ranges of 0.96 to 1.02 and 0.92 to 0.98, respectively. The differences among the reported values can be attributed to the variations in hardware, processing, and/or statistical sampling power. Although our data include additional variability from protocol differences, our cross-site QSM reproducibility results were in agreement with literature values from harmonized studies (mean SDw: 4.16 ppb, absolute bias ≤ 4.1 ppb, SD_d < 5.3 ppb, slope: 0.99 ± 0.03, R^2: 0.99) (264,266,277). Cross-site R_2* reproducibility at 3 T was reported previously to be below 8% coefficient of variation (265), which agrees with our results of 6.2%. Furthermore, our within-site repeatability measures for QSM and R_2* agree with the 3-T literature values reported (R^2: 0.93 to 0.99, slope: 0.94 to 1.01, absolute bias: 0.2 to 3.0 ppb, mean ICC: 0.91 to 0.95, mean SDw: 3.2 to 4.96 ppb (40,268,269,277) and mean ICC: 0.72 to 0.92, mean SDw: 0.84 to 1.58 s^{-1} (40,263), respectively). Cross-site values reported in our study are also comparable with those reported in a recent 7-T study where SDw values were reported to be within 5 ppb and 1.5 s^{-1} for QSM and R_2*, respectively (41).

In addition to thermal noise, several other sources are involved in the variation between repeated measurements of QSM and R_2*, namely those that are related to either magnetic field differences (strength and homogeneity), subject-specific differences (positioning, head tilt, and motion) or sequence differences. Dealing first with magnetic field differences, a striking difference between R_2* and QSM is the strong dependence of R_2* on field strength, which typically increases linearly with B_0. Despite all three systems in our study being nominally 3 T, there were small field strength differences (3.6% absolute variation) between scanners, which could partially explain the differences in R_2* cross-vendor regression slopes. In a post-hoc analysis, normalizing R_2* maps into exactly 3.0 T slightly improved the regression slopes of Site 3-related measurements (e.g., 1.04 slope instead of 1.08 vs. Site 2). In QSM, however, the effect of B_0 differences is canceled during the phase-to-field scaling step. A second variation source related to the main field is the field inhomogeneity, which is affected by the shimming process used by each system. Furthermore, field homogeneity is sensitive to magnetic susceptibility and gets distorted to some degree in regions of high susceptibility gradients such as air–tissue and vein–tissue interfaces. Differences in the shimming quality between scans translate into geometrical distortions in regions of high susceptibility gradients affecting both QSM and R_2*. We observed higher variability in these regions. Rua et al. recently reported that registering repeated scans nonlinearly, rather than rigidly, reduced variation in these regions (reduced median cross-site SDw in R_2* from 0.86 to 0.66 s^{-1}, at 7 T) (41).

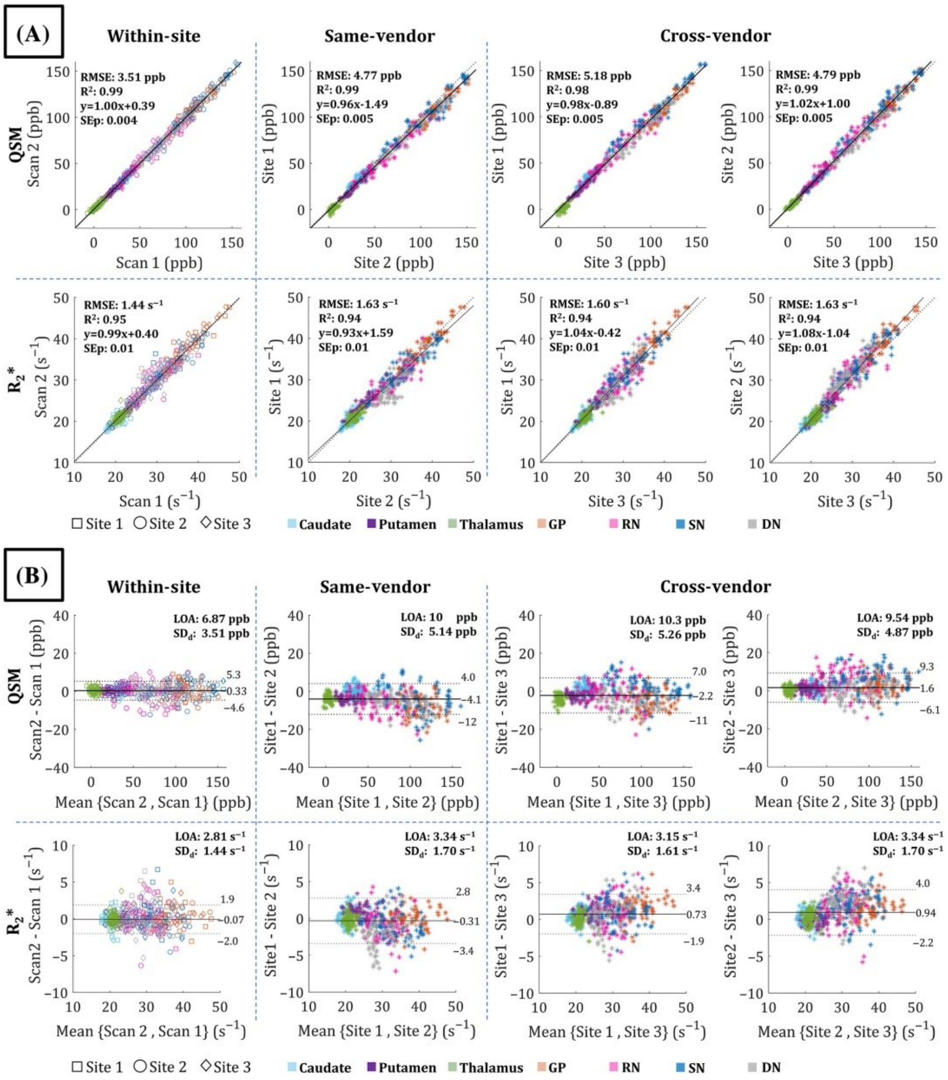

Figure 5.5*: Scan-rescan quantitative comparisons using region of interest measurements. (A) Correlation plots show that both quantitative techniques have strong correlation between repeated measurements with slope 1.00 ± 0.05 and $R^2 \geq 0.94$. (B) Bland–Altman plots compare the scan-rescan difference to the mean of both scans. The standard deviation of differences (SD_d) was within 5.3 ppb and 1.7 s^{-1} for QSM and R_2*, respectively. The solid and dashed horizontal lines indicate the mean difference and the limits of agreement (LOA), respectively. DN, dentate nucleus; GP, globus pallidus; RMSE, root mean square error; RN, red nucleus; SEp, estimated standard error of the slope; SN, substantia nigra.*

With regards to subject-specific variations, differences in head orientation between repeated scans can add variation in several ways. The angle between the B_0 direction and white matter tracts affects estimation of both QSM and R_2* in white matter regions due to fiber anisotropy (14,34,35). Rua et al. have shown recently that scan-rescan variability can be reduced by correcting QSM values using head angle information (41). Moreover, scan-rescan differences in head orientation can introduce variability in QSM due to inherited post-processing deficiencies that results in angle-dependent streaking artifacts. If not properly minimized, these artifacts contaminate nearby tissues and may produce variation between repeated scans. In addition, QSM reconstruction requires removing contributions from background fields, a process known as being increasingly prone to error towards brain edges (74). Combined with the geometrical distortion near air–tissue interfaces, the background field-removal process deficiency can cause angle-dependent inconsistencies between repeated scans. In this work, QSM measurements from Site 1 were found to be slightly lower (slope: 0.96 to 0.98) compared with other sites. A post-hoc analysis of head orientation revealed that the heads were generally more forward-tilted at Site 1, with a mean inclination angle difference of 7.4° (range: -3.3° to 19.9°, $p < 0.001$). Therefore, the lower QSM measurements in Site 1 could be originating from head orientation differences. Another subject-related source of variation is motion during image acquisition, which translates into inaccurate measurements of voxel signal. Choi et al. showed that correcting respiratory motion-related effects (using a navigator echo) improved repeatability at 3 T by up to 12% and 23% in QSM and R_2*, respectively (36).

Imaging sequence parameters can be tuned to minimize the variability from the above-discussed sources, although a tradeoff is usually required, but it can also add to the variability if not applied consistently in all repeated scans. For instance, long echo times help improve phase contrast, but could magnify distortions in high susceptibility gradient regions. Increasing spatial resolution improves accuracy and minimizes both geometrical distortions and partial volume effects, but it sacrifices signal-to-noise ratio (SNR) and makes images more prone to motion artifacts due to prolonging acquisition time. Flip angles and repetition times also modulate contrast and SNR. Acceleration techniques reduce scanning time at the cost of lowering SNR and altering k-space content. Flow compensation and gradient-warp correction techniques minimize flow-related and gradient nonlinearity artifacts, respectively. However, these techniques could be a source of variability if not applied in all repeated scans (271,278). Furthermore, differences between vendor implementations of hardware and sequences are additional possible sources of scan-rescan variation; here we aimed to quantify the collective effect of sequence variations on the reproducibility of susceptibility and R_2* maps. By comparing our results with previous harmonized cross-site reproducibility studies, the contribution of sequence variations to the total cross-site variability seems secondary compared with magnetic field and subject-related contributions, if managed properly during post-processing steps. However, in quantifying small structures (such as SN and RN), resolution and slice orientation can cause substantial variability due to irreversible partial volume effects. Differences in slice orientation can also affect other regions if not properly handled during QSM post-processing, as some background removal and susceptibility inversion methods have been shown to be sensitive to variation in slice orientation, and thus pre-aligning slices might be required (81). The methods applied in this study (i.e., V-SHARP background removal and iterative total variation-based inversions) are not susceptible to variation in slice orientation.

The above-discussed variability sources imply that QSM and R_2* reproducibility has some regional dependency. Higher variability is expected in small structures (e.g., RN and SN) and regions near brain edge and air cavities (e.g., RN, SN, and DN). Furthermore, the reliability of measurements is reduced in regions where changes observed with age and/or pathology are not larger than scan-rescan variability by an order of magnitude, such as in the thalamus, where the between-subject change was not large enough compared with SDw, leading to a good reliability rather than excellent as in other ROIs.

We investigated and identified some possible post-processing steps that can improve cross-site reproducibility whenever sequence variations are inevitable. Excluding unreliable field regions in QSM using a mask produced from the MEGE magnitude of the last comparable TE reduced variability. This also reduced mask variations between scans of different flip angles/TRs without the need for tuning mask extraction parameters for each protocol. Alternatively, more advanced techniques can be applied to exclude unreliable regions in each echo by utilizing both magnitude and phase information in the masking process and performing two-pass susceptibility inversion (63). In addition, restricting QSM reconstruction to comparable echo times found in all scans reduced variability further (mean SDw reduced from 4.83 to 4.16 ppb), which is consistent with findings in previous work (245). This ensures similar field content within the VOI, including regions of high susceptibility gradients. Note that reducing variability between scans acquired at different field strengths would require careful selection of echo times considering the ratio between the different field strengths (245). Furthermore, background field estimation was performed after matching spatial resolution to minimize digitization error incurred during spherical mean value calculations. Note that there are other background removal methods that do not involve kernel-based spherical mean calculations (80,82), and thus matching resolution might not be required. However, the V-SHARP method was used here for being slice-orientation independent and producing susceptibility maps with fewer artifacts at minimal VOI erosion (**Figure 5.6**), as it estimates the tissue field in each voxel based on kernels of limited coverage, and relies on neither the definition of the boundaries between local and background sources nor slice orientation information. Matching spatial resolution can also be applied to the raw complex signal prior to any processing, however, at the cost of increasing the required computation time and capacity (i.e., all processing steps must be performed at higher spatial resolution) (279). Moreover, no magnitude-based weighting was used in field estimation, as MEGE magnitude varied widely between different sites and contrast variation could propagate into the final susceptibility map. Note that employing magnitude information in the field-to-source inversion step is helpful if the contrast is consistent between different scans, as previous studies have illustrated (106,244). To understand the effect of the varying magnitude contrast on the susceptibility inversion step, a post-hoc analysis was performed, in which TVDI and MEDI algorithms were tested with and without employing magnitude information (**Figures 5.7 and 5.8**). For TVDI, no clear change in reproducibility was observed when magnitude usage was avoided. For MEDI, not using magnitude in the regularization term reduced variability without a clear improvement in reliability. However, not employing a noise map (estimated from magnitude) in the fidelity term further increased the variability. Therefore, using the varying magnitude contrast as a weighting factor in the inversion step did not have a clear negative impact on the reproducibility, mostly due to the ability of the weighting mechanism used in these algorithms to absorb the variability in the magnitude contrast. On the other hand, the improved performance of the iLSQR algorithm seems to be mainly benefiting from minimizing streaking artifacts in the reconstructed susceptibility maps (92). However, we observed that this algorithm produced lower susceptibility levels in GP (compared with other reconstruction methods), which coincides with a previous study that reported lower estimation of venous susceptibility using the iLSQR (280). This may originate from the concept the iLSQR employs to suppress streaking artifacts that involves estimating and subtracting the artifacts from an initial susceptibility map, which may alter the contrast of strong susceptibility sources (92). Thus, the iLSQR might not be the best choice for applications that involve estimating strong susceptibility sources, and other methods could be considered.

Applying the above-mentioned steps improved mean ICC by 17% and reduced mean SDw by 46%. Regarding R_2* mapping, fitting data from all TEs improved the reproducibility of thalamus measurements; however, increased variability was visually observed in white matter regions. This difference in white matter contrast between sites can be attributed to the head orientation variation and fiber anisotropy discussed above, which are emphasized further when echo timings are not matched. Unlike QSM, including all echoes was beneficial for R_2* mapping, mainly due to the simpler 1D (exponential decay) model being solved that does not rely on spatial information. By contrast, QSM solves a 3D convolution model whose support is sensitive to multiple TE-dependent steps including mask generation, phase unwrapping, and field estimation. In addition, linear field correction for MEGE magnitude before R_2* fitting slightly improved reproducibility measures of caudate and putamen, but adversely affected other iron-rich regions such as SN, RN, and DN. This could be attributed to the correction method that relies on the phase information to suppress regions of extreme susceptibility, which may invariably affect iron-rich structures as well. Therefore, selecting TEs and applying field correction in R_2* mapping could be tailored based on the application and the ROIs.

The limitations of this work include the lack of sequence harmonized data, which could facilitate distinguishing sequence-related variability from hardware/subject variability. However, comparisons with previous harmonized studies have helped in drawing some insights in this regard. Another limitation is that the presented data were collected from a single field strength and a limited number of sites and vendors, so this does not fully represent the widest spectrum of variations encountered in multisite studies. Nevertheless, the observed high reproducibility results are promising and should encourage further expansion of similar studies. Another limitation is that measurements are focused on deep gray matter nuclei. These iron-rich regions have a crucial role in cognitive and motor functions and focusing on them facilitates comparison with many previous studies of these regions. However, the voxel-wise analysis gives a general idea of the reproducibility in the regions outside deep gray matter.

In conclusion, we investigated the reproducibility of quantitative susceptibility and R_2^* maps at 3T in the presence of local sequence variations across multiple sites and vendors in deep gray matter. Both techniques demonstrated high reproducibility in within-site and cross-site measurements. QSM variability originating from site and sequence differences can be minimized through post-processing steps, including exclusion of unreliable regions, not relying on magnitude contrast in field estimation if significantly varying between scans, matching echo timings and spatial resolution, and minimizing streaking artifacts.

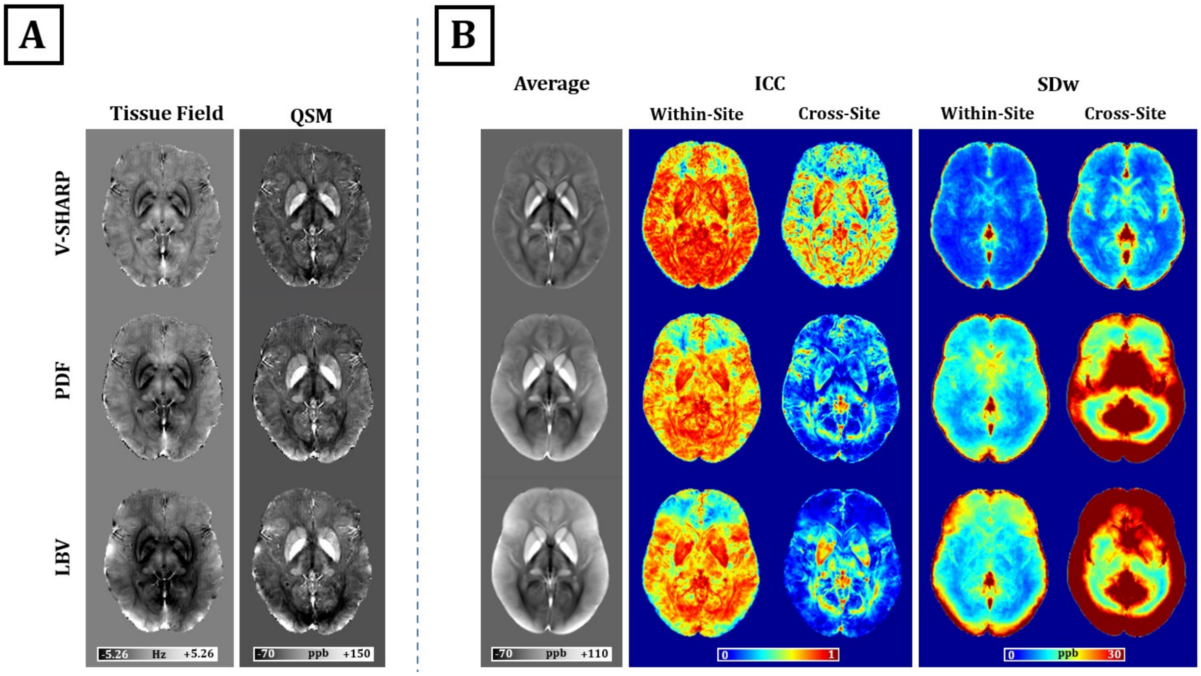

Figure 5.6: *Demonstration of the effect of three background removal methods on the final susceptibility map in A) one example subject, and B) voxel-wise group metric maps. Overall, the V-SHARP method produced less edge artifacts, higher ICC values and lower SDw values. Group maps were produced by nonlinearly registering all scans into MNI152 1-mm T_1w template. The inputs of the PDF and the LBV methods were eroded by one voxel to produce tissue fields of the same VOI as V-SHARP. Oblique slices were processed in their native orientation without rotation.*

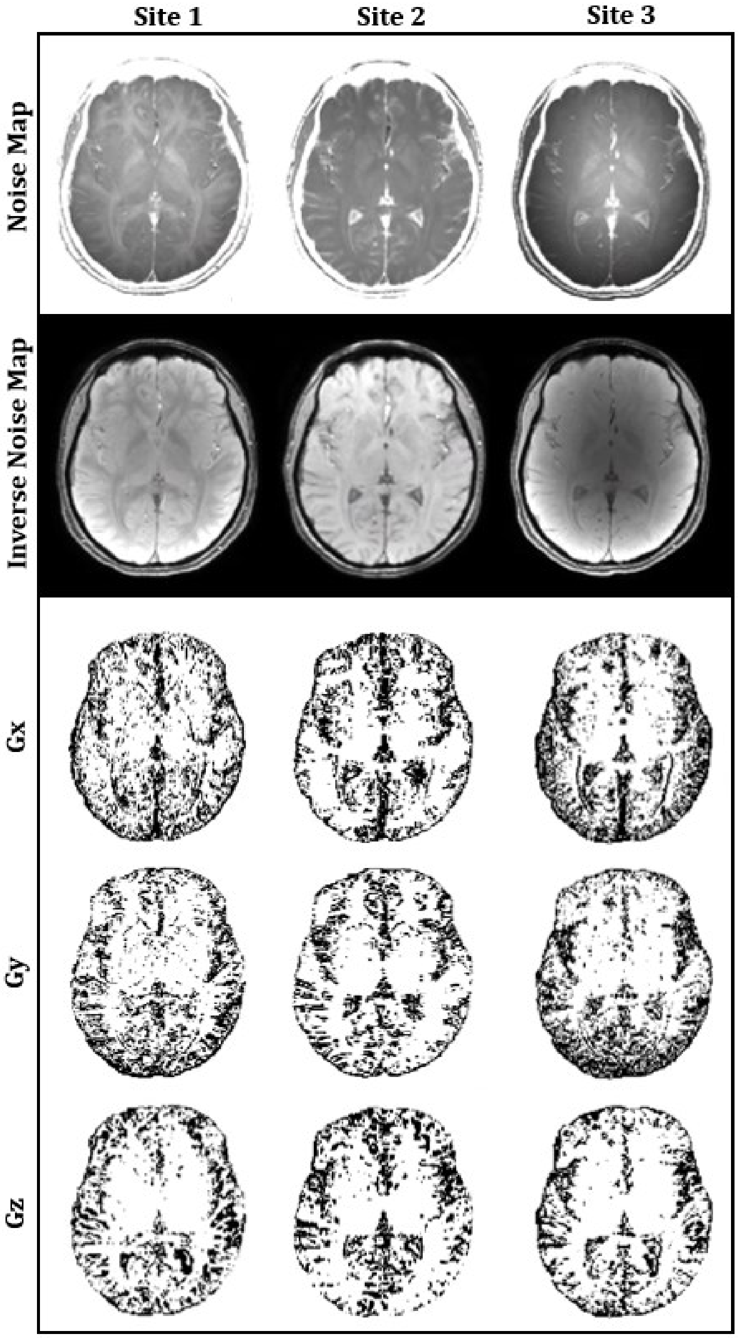

Figure 5.7: *An illustration of the magnitude contrast variation effect on the weighting factors used in MEDI susceptibility inversion algorithm. The inverse noise map is used as a weighting factor in the fidelity term of MEDI formulation, while magnitude gradients (Gx, Gy and Gz) are used in the regularization term as prior knowledge of edge information.*

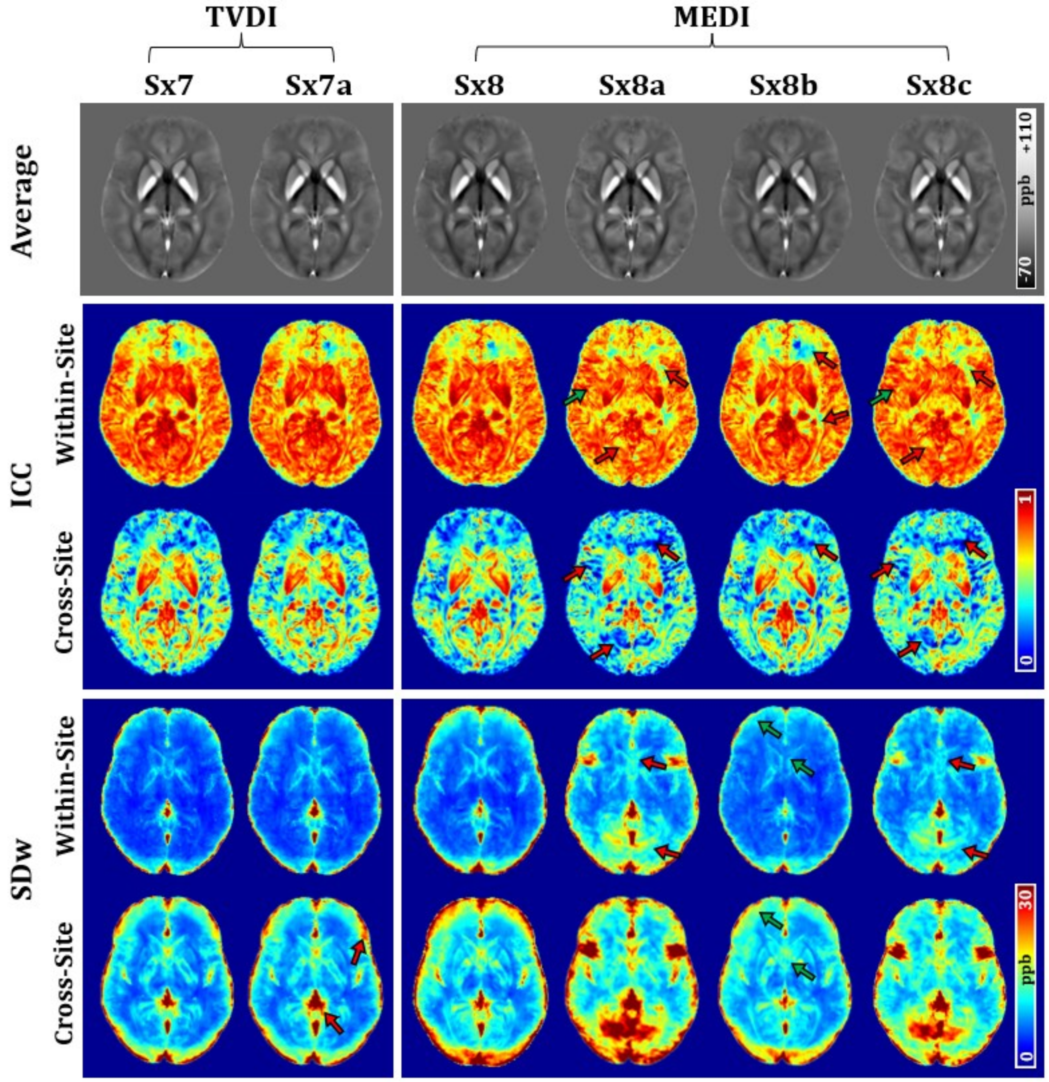

Figure 5.8: *The effect of the magnitude contrast on QSM inversion: Voxel-wise comparisons (average value, ICC and SDw) of TVDI and MEDI produced susceptibility maps. Sx7: TVDI with magnitude weighting, Sx7a: TVDI without magnitude weighting, Sx8: conventional MEDI with inverse noise map weighting and magnitude gradients regularization, Sx8a: MEDI without inverse noise map weighting, Sx8b: MEDI without magnitude gradients regularization, Sx8c: MEDI without inverse noise map weighting and without magnitude gradients regularization. In TVDI, magnitude weighting slightly reduced variability without clear improvement in reliability. In MEDI, keeping the inverse noise map weighting but switching off magnitude gradients information (Sx8b) reduced variability noticeably in cortical regions. However, no improvement in reliability is evident. Green and red arrows refer to regions of gain and loss in reliability (compared to Sx7/Sx8), respectively.*

5.6 Acknowledgements

This work was supported by the Canadian Institutes of Health Research (CIHR), Women's and Children's Health Research Institute (WCHRI) and the University of Alberta Hospital Foundation (UHF). Salary support (authors CL and CB) was provided by the Canada Research Chairs program.

Chapter 6: Conclusions

In its core, this thesis aimed at reducing the technical challenges of adopting QSM in brain clinical studies by developing technical methods to minimize the acquisition burden of QSM measurements, as well as its inter-site and inter-sequence variability.

Obtaining high-resolution QSM is relatively slow, typically adding six minutes or more (whole brain at 1-mm isotropic) to the total acquisition time when included in imaging protocols. Several acceleration techniques exist with a trade-off in image quality. The complete acquisition cost can be avoided when QSM is obtained from the phase of a sequence that already exists in the imaging protocol such as the MPRAGE sequence, which is widely included for tissue segmentation and volumetric purposes. In Chapter 2, producing QSM from the phase of the MPRAGE sequence was proposed and tested using simulations and measurements on healthy subjects. Imposed by the short echo time typically used in the sequence, the susceptibility contrast driven from the MPRAGE phase was sufficient only in iron-rich regions, restricting the applications to such regions. One feasible application that was validated in-vivo is improving the segmentation of the globus pallidus using the phase of MPRAGE sequence itself without additional acquisition cost, even though normally it has weak contrast on the MPRAGE magnitude. In addition, QSM derived from the MPRAGE phase can be used to roughly quantify iron-rich regions (221).

Furthermore, MPRAGE-based QSM has the potential to be used for examining microbleed load in brain, as these blood leakages contain high concentration of iron which produces strong susceptibility contrast with only a few milliseconds of echo time. In Chapter 3, we validated this application using in-vivo 3T measurements and compared the performance with QSM obtained from a standard multi-echo sequence. The detection sensitivity was comparable in both methods, although microbleeds had smaller size and stronger susceptibility on the MPRAGE-QSM, benefiting from the higher-resolution and the shorter echo time. Simulations were also used to explore possible limitations, in which using the MPRAGE-QSM for detecting microbleeds as small as one-voxel was promising at the SNR levels of 3T and above. The limited quality of MPRAGE-QSM at 3T can be boosted remarkably by extending the echo time to 4.4 ms at commonly used spatial resolution of 1 mm isotropic.

Another aspect of minimizing the acquisition burden of QSM data is reducing the imaged volume beyond the ROI. This however is challenged by the non-local relation between the susceptibility distribution and the MR phase, requiring extended coverage for accurate reconstruction. In Chapter 4, we proposed a hybrid model to overcome this issue, in which a rapid lower-resolution version with extended coverage is used as prior knowledge to assist the reconstruction process. The feasibility of the new method was tested using simulations and human brain experiments at 3T, which showed the potential of the introduced method to produce more accurate measurements than the standard method from thin slabs of 8 slices, promoting up to seven-fold reduction in the imaging time for small ROI-focused applications.

The final pillar of this thesis is rooted in investigating the reproducibility of QSM and R_2* when there are inter-site variations in the imaging sequence parameters, and exploring post-processing techniques to minimize the effects of these variations. This aspect has been often overlooked under the assumption that matching the sequence parameters is achievable. However, this assumption restricts tailoring the sequence for local needs and aggregating data from wide geographical coverage for large studies. The study in Chapter 5 included 24 healthy subjects who travelled between three 3T sites from two vendors. Cross-site QSM (and R_2^*) measurements were highly correlated and reproducible despite the variations in sequence parameters. Matching echo times and spatial resolution, minimizing less reliable regions and streaking artifacts, and avoiding the use of magnitude in field estimation helped in improving cross-site QSM reproducibility (42).

6.1 LIMITATIONS

As detailed in **Section 1.3.8**, the current implementations of QSM use several assumptions to simplify a rather difficult to solve complex model that noninvasively probes sub-voxel interactions. Thus, the full potential of QSM has yet to be achieved and several shortcomings are still present to be addressed. At the top of these is that producing QSM involves multiple cascading steps and each of them has many different approaches with multiple user-defined parameters, along with the absence of an optimal or consensus processing pipeline. Inherited from phase imaging, QSM accuracy is sensitive to magnitude SNR, as well as several phase preprocessing steps, including combining signals for different coils and echo times (60,62,182), defining reliable phase regions (63,64), and unfolding phase wraps (60,66–70). Furthermore, extracting tissue-induced phase (74) and inverting it into a susceptibility distribution (237) are complex mathematical problems in which existing methods to solve them require compromising accuracy (106,244). In addition, the relative nature of QSM measurements necessitates normalizing them by an internal reference, which is still an open question. Several regions have been used as a reference point for brain QSM, including whole brain (28,41,42), CSF(91), internal capsule (56,196,235), other white matter regions (27,281,282), and cortical gray matter (40); each seems to work for specific applications, but the best is still a topic of debate. Moreover, several acquisition parameters can influence the QSM output, particularly echo-timings (182,245), spatial resolution (196,198), and spatial coverage (196,235). Altogether, this variety of processing options makes comparing QSM results from different studies of different setups challenging and limits its quantitative utility. Nevertheless, QSM has been utilized in many pathological studies and has provided insightful information about the underlying disease and its progression (120,153). In addition to the quantitative value, it has been found useful in other applications such as improving localization of structures (119) and lesions (140,261), and improving their segmentation (167,221).

In addition to the limitations of the QSM technique itself, there are some limitations to the applied methods and the performed experiments in this thesis. Overall, the in-vivo data was limited to one field strength (i.e., 3T), and sometimes one set of echo time(s) and/or spatial resolution, which might limit the generality of the conclusions, especially for the reproducibility study. However, simulations were used where appropriate to explore the expected quality and accuracy at other field strengths, echo-timings and resolution, such as in the MPRAGE-based microbleeds quantification and the thin-slab QSM studies. In the MPRAGE-based QSM study, the utility of using QSM for improving segmentation was demonstrated in only one iron-rich structure of the basal ganglia (globus pallidus), because it is typically poorly segmented based on the contrast of the MPRAGE magnitude alone. Also, the segmentation performance was not compared to a manually obtained reference, but rather to a hybrid method that uses a combination of the T_1w magnitude and the standard MEGE-QSM, as the goal was to show that a similar improved performance is achievable using QSM derived from the MPRAGE sequence itself without the need for the extra MEGE acquisition. In the thin-slab QSM study, the method was tested only on in-vivo data of healthy subjects, and thus it is yet to be validated in patients. However, the performance in the presence of strong susceptibility sources was evaluated using simulated lesions. Another limitation is that the in-vivo data was obtained using one set of echo timings and two resolution sets, and thus further testing is still needed. In the reproducibility study, there were no inter-site measurements obtained using a sequence with matched parameters. If available, it could have helped differentiate the variability introduced by sequence variations from the variability caused by changes in hardware or subject positioning. However, the obtained results were compared to previous studies that used matched sequences, which was useful in drawing some insights in this regard.

6.2 FUTURE DIRECTIONS

Given the complexity of the physical model relating the MR phase to the tissue susceptibility, there is room for improvement in each block of the QSM processing pipeline, more importantly in the steps of extracting the tissue-related field and mapping this field information into a susceptibility distribution. For instance, existing tissue field estimation methods perform less accurately near the boundaries of the imaged volume (74), which limits the reliability of the QSM measurements in the cortical layer of the brain. Also, most dipole inversion algorithms make trade-offs between suppressing artifacts and retaining fine details.

Focusing on the technical methods introduced in this thesis, the current implementations of both the MPRAGE- and the thin-slab QSM aimed generally to prove the concept and demonstrate the benefits. The processing pipelines need further optimization to be robust against variations in the acquired data, notably in magnitude contrast, echo-timings and resolution. For example, brain extraction is currently achieved using the BET toolbox of the FSL package (64), which generally works well with healthy subject images of sufficient contrast and resolution. However, the performance decreases at lower resolution and/or SNR, and in the presence of structural abnormality. Possible alternatives include incorporating deep learning techniques to bypass the brain extraction step and accelerate the reconstruction time (283). Furthermore, the scan-rescan reliability of both introduced methods should be evaluated within and across sites.

For the reduced-FOV QSM, one implementation was introduced which utilizes the low-resolution data to regularize the minimization formula by informing the algorithm of the expected susceptibility distribution outside the imaged slab. Better utilization of this information might improve the performance further, potentially allowing accurate QSM reconstruction from a single slice. Currently, estimating the tissue field via subtraction permits dipole inversion from single slice acquisition, as no erosion is involved in the process. However, the dipole inversion step fails to converge to the right solution, possibly by stopping earlier at a local minimum. This issue requires further investigation to understand the cause of the failure.

Another future direction for this study is exploring the idea of utilizing the phase of already existing sequences in the imaging protocol to serve the purpose of the low-resolution data. This way, the additional cost of acquiring the low-resolution version can be avoided. Possible candidates include the phase of the B_0 field mapping and the MPRAGE sequences. The other option is minimizing the acquisition cost of the low-resolution by using a fast sequence such as EPI, which can provide a full brain coverage acquisition of isotropic 2-mm voxels within 10 seconds (56).

Thin-slab QSM has potential applications outside the brain, where shortening the acquisition time is critical to minimize respiratory-induced motion artifacts. Examples include QSM of liver (146,147,284) and kidney (150), where data acquisition is performed during a breath-hold of 15 to 33 seconds, which limits the achievable spatial resolution. Moreover, holding breath for such a long period might not be feasible for patients or elderly participants. Obtaining QSM from fewer slices could allow exploring higher resolution, or further reducing the required time for imaging.

Another potential application, yet more challenging, is cardiac QSM to measure blood oxygen saturation, which includes additional complexity from cardiac motion. Data then would be typically acquired using a 2D multi-slice MEGE sequence with breath-hold and cardiac synchronization using electrocardiographic gating (149), or a 3D MEGE with free breathing and diaphragmatic navigator gating (148). Both acquisition techniques would normally take five minutes with a through-plane resolution of 5-mm. The 2D multi-slice acquisition is prone to slice mis-registration, as slices are acquired over several breath-holds which might not lead to consistent slice positioning. Such misalignment of the slices distorts the continuity of the tissue field and causes strong artifacts. This is avoided in the 3D sequence by automatically tracking the diaphragm motion and triggering the acquisition window at more consistent positions. Thin-slab imaging could potentially provide the opportunity to improve the resolution of cardiac QSM within reasonable acquisition time.

In conclusion, future work could focus on improving the robustness of the introduced techniques as well as exploring more potential applications, both of which contribute to enhancing the utility of QSM.

Bibliography

1. Rabi II, Zacharias JR, Millman S, Kusch P. A new method of measuring nuclear magnetic moment. Physical Review. 1938;53(4):318.
2. Vlaardingerbroek MT, Boer JA. Magnetic Resonance Imaging: Theory and Practice. Springer Berlin Heidelberg; 2003.
3. Filler AG, Filler A. The history, development and impact of computed imaging in neurological diagnosis and neurosurgery: CT, MRI, and DTI. Nature Precedings . 2009;1.
4. Grover VPB, Tognarelli JM, Crossey MME, Cox IJ, Taylor-Robinson SD, McPhail MJW. Magnetic resonance imaging: Principles and techniques: Lessons for clinicians. J Clin Exp Hepatol. 2015;5(3):246–55.
5. Brateman L. Chemical shift imaging: A review. American Journal of Roentgenology. 1986;146(5):971–80.
6. Zhu H, Barker PB. MR spectroscopy and spectroscopic imaging of the brain. Methods in Molecular Biology. 2010;711:203–26.
7. Baliyan V, Das CJ, Sharma R, Gupta AK. Diffusion weighted imaging: Technique and applications. World J Radiol. 2016;8(9):785–98.
8. Alexander AL, Lee JE, Lazar M, Field AS. Diffusion tensor imaging of the brain. Neurotherapeutics. 2007;4(3):316–29.
9. Grossman RI, Gomori JM, Ramer KN, Lexa FJ, Schnall MD. Magnetization transfer: Theory and clinical applications in neuroradiology. RadioGraphics. 1994;14(2):279–90.
10. Göksu C, Hanson LG, Siebner HR, Ehses P, Scheffler K, Thielscher A. Human in-vivo brain magnetic resonance current density imaging (MRCDI). Neuroimage. 2018;171:26–39.
11. Woo EJ, Seo JK. Magnetic resonance electrical impedance tomography (MREIT) for high-resolution conductivity imaging. Physiol Meas. 2008;29(10):R1.

12. Katscher U, Kim DH, Seo JK. Recent progress and future challenges in MR electric properties tomography. Comput Math Methods Med. 2013;2013:e546562.

13. Haacke EM, Mittal S, Wu Z, Neelavalli J, Cheng YCN. Susceptibility-Weighted Imaging: Technical Aspects and Clinical Applications, Part 1. American Journal of Neuroradiology. 2009;30(1):19–30.

14. Li W, Liu C, Duong TQ, van Zijl PCM, Li X. Susceptibility tensor imaging (STI) of the brain. NMR Biomed. 2017;30(4):e3540.

15. Liu C, Wei H, Gong NJ, Cronin M, Dibb R, Decker K. Quantitative Susceptibility Mapping: Contrast Mechanisms and Clinical Applications. Tomography. 2015;1(1):3–17.

16. Glover GH. Overview of Functional Magnetic Resonance Imaging. Neurosurg Clin N Am. 2011;22(2):133–9.

17. Petrella JR, Provenzale JM. MR Perfusion Imaging of the Brain: Techniques and Applications. American Journal of Roentgenology. 2000;175(1):207–19.

18. Brown RW, Cheng YCN, Haacke EM, Thompson MR, Venkatesan R. Magnetic Resonance Imaging: Physical Principles and Sequence Design: Second Edition. Wiley Blackwell; 2014.

19. Bernstein MA, King KF, Zhou XJ. Handbook of MRI Pulse Sequences. Elsevier Inc.; 2004.

20. Liang ZP, Lauterbur PC. Principles of Magnetic Resonance Imaging: A Signal Processing Perspective. SPIE Optical Engineering Press; 2000.

21. Callaghan PT. Principles Of Nuclear Magnetic Resonance Microscopy. Clarendon Press; 1991.

22. Bloembergen N, Purcell EM, Pound R. Relaxation effects in nuclear magnetic resonance absorption. Physical Review. 1948;73(7):679.

23. Rooney WD, Johnson G, Li X, Cohen ER, Kim SG, Ugurbil K, et al. Magnetic field and tissue dependencies of human brain longitudinal 1H2O relaxation in vivo. Magn Reson Med. 2007;57(2):308–18.

24. Schenck JF. The role of magnetic susceptibility in magnetic resonance imaging: MRI magnetic compatibility of the first and second kinds. Med Phys. 1996;23(6):815–50.

25. Duyn JH, Schenck J. Contributions to magnetic susceptibility of brain tissue. NMR Biomed. 2017;30(4):e3546.

26. Li W, Wu B, Batrachenko A, Bancroft-Wu V, Morey RA, Shashi V, et al. Differential developmental trajectories of magnetic susceptibility in human brain gray and white matter over the lifespan. Hum Brain Mapp. 2014;35(6):2698–713.

27. Acosta-Cabronero J, Betts MJ, Cardenas-Blanco A, Yang S, Nestor PJ. In vivo MRI mapping of brain iron deposition across the adult lifespan. Journal of Neuroscience. 2016;36(2):364–74.

28. Treit S, Naji N, Seres P, Rickard J, Stolz E, Wilman AH, et al. R2* and quantitative susceptibility mapping in deep gray matter of 498 healthy controls from 5 to 90 years. Hum Brain Mapp. 2021;42(14):4597–610.

29. Kruer MC. The neuropathology of neurodegeneration with brain iron accumulation. Int Rev Neurobiol. 2013;110:165–94.

30. van Bergen JMG, Hua J, Unschuld PG, Lim IAL, Jones CK, Margolis RL, et al. Quantitative susceptibility mapping suggests altered brain iron in premanifest Huntington disease. AJNR Am J Neuroradiol. 2016;37(5):789–96.

31. Elkady AM, Cobzas D, Sun H, Seres P, Blevins G, Wilman AH. Five year iron changes in relapsing-remitting multiple sclerosis deep gray matter compared to healthy controls. Mult Scler Relat Disord. 2019;33:107–15.

32. Damulina A, Pirpamer L, Soellradl M, Sackl M, Tinauer C, Hofer E, et al. Cross-sectional and longitudinal assessment of brain iron level in Alzheimer disease using 3-T MRI. Radiology. 2020;296(3):619–26.

33. Johnson EB, Parker CS, Scahill RI, Gregory S, Papoutsi M, Zeun P, et al. Altered iron and myelin in premanifest Huntington's Disease more than 20 years before clinical onset: Evidence from the cross-sectional HD young adult study. EBioMedicine. 2021;65:103266.

34. Bender B, Klose U. The in vivo influence of white matter fiber orientation towards B0 on T2* in the human brain. NMR Biomed. 2010;23(9):1071–6.

35. Lancione M, Tosetti M, Donatelli G, Cosottini M, Costagli M. The impact of white matter fiber orientation in single-acquisition quantitative susceptibility mapping. NMR Biomed. 2017;30(11):e3798.

36. Choi JY, Lee J, Nam Y, Lee J, Oh SH. Improvement of reproducibility in quantitative susceptibility mapping (QSM) and transverse relaxation rates (R2*) after physiological noise correction. Journal of Magnetic Resonance Imaging. 2019;49(6):1769–76.

37. Maclaren J, Armstrong BSR, Barrows RT, Danishad KA, Ernst T, Foster CL, et al. Measurement and correction of microscopic head motion during magnetic resonance imaging of the brain. PLoS One. 2012;7(11):e48088.

38. Ordidge RJ, Gorell JM, Deniau JC, Knight RA, Helpern JA. Assessment of relative brain iron concentrations using T2-weighted and T2*-weighted MRI at 3 Tesla. Magn Reson Med. 1994;32(3):335–41.

39. Langkammer C, Krebs N, Goessler W, Scheurer E, Ebner F, Yen K, et al. Quantitative MR imaging of brain iron: A postmortem validation study. Radiology. 2010;257(2):455–62.

40. Feng X, Deistung A, Reichenbach JR. Quantitative susceptibility mapping (QSM) and R2* in the human brain at 3T: Evaluation of intra-scanner repeatability. Z Med Phys. 2018;28(1):36–48.

41. Rua C, Clarke WT, Driver ID, Mougin O, Morgan AT, Clare S, et al. Multi-centre, multi-vendor reproducibility of 7T QSM and R2* in the human brain: Results from the UK7T study. Neuroimage. 2020;223:117358.

42. Naji N, Lauzon ML, Seres P, Stolz E, Frayne R, Lebel C, et al. Multisite reproducibility of quantitative susceptibility mapping and effective transverse relaxation rate in deep gray matter at 3 T using locally optimized sequences in 24 traveling heads. NMR Biomed. 2022;e4788.

43. Ghadery C, Pirpamer L, Hofer E, Langkammer C, Petrovic K, Loitfelder M, et al. R2* mapping for brain iron: Associations with cognition in normal aging. Neurobiol Aging. 2015;36(2):925–32.

44. Haacke EM, Miao Y, Liu M, Habib CA, Katkuri Y, Liu T, et al. Correlation of putative iron content as represented by changes in R2* and phase with age in deep gray matter of healthy adults. Journal of Magnetic Resonance Imaging. 2010;32(3):561–76.

45. Hect JL, Daugherty AM, Hermez KM, Thomason ME. Developmental variation in regional brain iron and its relation to cognitive functions in childhood. Dev Cogn Neurosci. 2018;34:18–26.

46. Pirpamer L, Hofer E, Gesierich B, de Guio F, Freudenberger P, Seiler S, et al. Determinants of iron accumulation in the normal aging brain. Neurobiol Aging. 2016;43:149–55.

47. Aquino D, Bizzi A, Grisoli M, Garavaglia B, Bruzzone MG, Nardocci N, et al. Age-related iron deposition in the basal ganglia: Quantitative analysis in healthy subjects. Radiology. 2009;252(1):165–72.

48. Larsen B, Bourque J, Moore XTM, Adebimpe A, Calkins ME, Elliott MA, et al. Longitudinal development of brain iron is linked to cognition in youth. Journal of Neuroscience. 2020;40(9):1810–8.

49. Ulla M, Bonny JM, Ouchchane L, Rieu I, Claise B, Durif F. Is R2* a new MRI biomarker for the progression of Parkinson’s disease? A longitudinal follow-up. PLoS One. 2013;8(3):e57904.

50. Bagnato F, Hametner S, Boyd E, Endmayr V, Shi Y, Ikonomidou V, et al. Untangling the R2* contrast in multiple sclerosis: A combined MRI-histology study at 7.0 Tesla. PLoS One. 2018;13(3):e0193839.

51. Wood JC, Enriquez C, Ghugre N, Tyzka JM, Carson S, Nelson MD, et al. MRI R2 and R2* mapping accurately estimates hepatic iron concentration in transfusion-dependent thalassemia and sickle cell disease patients. Blood. 2005;106(4):1460–5.

52. Sedlacik J, Boelmans K, Löbel U, Holst B, Siemonsen S, Fiehler J. Reversible, irreversible and effective transverse relaxation rates in normal aging brain at 3 T. Neuroimage. 2014;84:1032–41.

53. de Rochefort L, Liu T, Kressler B, Liu J, Spincemaille P, Lebon V, et al. Quantitative susceptibility map reconstruction from MR phase data using bayesian regularization: Validation and application to brain imaging. Magn Reson Med. 2010;63(1):194–206.

54. Shmueli K, de Zwart JA, van Gelderen P, Li TQ, Dodd SJ, Duyn JH. Magnetic susceptibility mapping of brain tissue in vivo using MRI phase data. Magn Reson Med. 2009;62(6):1510–22.

55. Schweser F, Deistung A, Lehr BW, Reichenbach JR. Quantitative imaging of intrinsic magnetic tissue properties using MRI signal phase: An approach to in vivo brain iron metabolism? Neuroimage. 2011;54(4):2789–807.

56. Sun H, Wilman AH. Quantitative susceptibility mapping using single-shot echo-planar imaging. Magn Reson Med. 2015;73(5):1932–8.

57. Salomir R, de Senneville BD, Moonen CTW. A fast calculation method for magnetic field inhomogeneity due to an arbitrary distribution of bulk susceptibility. Concepts Magn Reson Part B Magn Reson Eng. 2003;19B(1):26–34.

58. Marques JP, Bowtell R. Application of a Fourier-based method for rapid calculation of field inhomogeneity due to spatial variation of magnetic susceptibility. Concepts Magn Reson Part B Magn Reson Eng. 2005;25B(1):65–78.

59. de Rochefort L, Brown R, Prince MR, Wang Y. Quantitative MR susceptibility mapping using piece-wise constant regularized inversion of the magnetic field. Magn Reson Med. 2008;60(4):1003–9.

60. Robinson SD, Bredies K, Khabipova D, Dymerska B, Marques JP, Schweser F. An illustrated comparison of processing methods for MR phase imaging and QSM: Combining array coil signals and phase unwrapping. NMR Biomed. 2017;30(4):e3601.

61. Walsh DO, Gmitro AF, Marcellin MW. Adaptive reconstruction of phased array MR imagery. Magn Reson Med. 2000;43(5):682–90.

62. Liu T, Wisnieff C, Lou M, Chen W, Spincemaille P, Wang Y. Nonlinear formulation of the magnetic field to source relationship for robust quantitative susceptibility mapping. Magn Reson Med. 2013;69(2):467–76.

63. Stewart AW, Robinson SD, O'Brien K, Jin J, Widhalm G, Hangel G, et al. QSMxT: Robust masking and artifact reduction for quantitative susceptibility mapping. Magn Reson Med. 2022;87(3):1289–300.

64. Smith SM. Fast robust automated brain extraction. Hum Brain Mapp. 2002;17(3):143–55.

65. Ashburner J, Friston KJ. Unified segmentation. Neuroimage. 2005;26(3):839–51.

66. Jenkinson M. Fast, automated, N-dimensional phase-unwrapping algorithm. Magn Reson Med. 2003;49(1):193–7.

67. Abdul-Rahman HS, Gdeisat MA, Burton DR, Lalor MJ, Lilley F, Moore CJ. Fast and robust three-dimensional best path phase unwrapping algorithm. Appl Opt. 2007;46(26):6623.

68. Bagher-Ebadian H, Jiang Q, Ewing JR. A modified fourier-based phase unwrapping algorithm with an application to MRI venography. Journal of Magnetic Resonance Imaging. 2008;27(3):649–52.

69. Dymerska B, Eckstein K, Bachrata B, Siow B, Trattnig S, Shmueli K, et al. Phase unwrapping with a rapid opensource minimum spanning tree algorithm (ROMEO). Magn Reson Med. 2021;85(4):2294–308.

70. Karsa A, Shmueli K. SEGUE: A speedy region-growing algorithm for unwrapping estimated phase. IEEE Trans Med Imaging. 2019;38(6):1347–57.

71. Gilbert G, Savard G, Bard C, Beaudoin G. Quantitative comparison between a multiecho sequence and a single-echo sequence for susceptibility-weighted phase imaging. Magn Reson Imaging. 2012;30(5):722–30.

72. Wu B, Li W, Avram AV, Gho SM, Liu C. Fast and tissue-optimized mapping of magnetic susceptibility and T2* with multi-echo and multi-shot spirals. Neuroimage. 2012;59(1):297–305.

73. Bollmann S, Robinson SD, O'Brien K, Vegh V, Janke A, Marstaller L, et al. The challenge of bias-free coil combination for quantitative susceptibility mapping at ultra-high field. Magn Reson Med. 2018;79(1):97–107.

74. Schweser F, Robinson SD, de Rochefort L, Li W, Bredies K. An illustrated comparison of processing methods for phase MRI and QSM: Removal of background field contributions from sources outside the region of interest. NMR Biomed. 2017;30(4):e3604.

75. Kim J, Wong MW. Invariant mean value property and harmonic functions. Complex Variables, Theory and Application: An International Journal . 2005;50(14):1049–59.

76. Sun H, Wilman AH. Background field removal using spherical mean value filtering and Tikhonov regularization. Magn Reson Med. 2014;71(3):1151–7.

77. Li W, Wu B, Liu C. Quantitative susceptibility mapping of human brain reflects spatial variation in tissue composition. Neuroimage. 2011;55(4):1645–56.

78. Topfer R, Schweser F, Deistung A, Reichenbach JR, Wilman AH. SHARP edges: Recovering cortical phase contrast through harmonic extension. Magn Reson Med. 2015;73(2):851–6.

79. Fang J, Bao L, Li X, van Zijl PCM, Chen Z. Background field removal for susceptibility mapping of human brain with large susceptibility variations. Magn Reson Med. 2019;81(3):2025–37.

80. Liu T, Khalidov I, de Rochefort L, Spincemaille P, Liu J, Tsiouris AJ, et al. A novel background field removal method for MRI using projection onto dipole fields (PDF). NMR Biomed. 2011;24(9):1129–36.

81. Kiersnowski OC, Karsa A, Wastling SJ, Thornton JS, Shmueli K. Investigating the effect of oblique image acquisition on the accuracy of QSM and a robust tilt correction method. Magn Reson Med. 2022;e29550.

82. Zhou D, Liu T, Spincemaille P, Wang Y. Background field removal by solving the Laplacian boundary value problem. NMR Biomed. 2014;27(3):312–9.

83. Bollmann S, Kristensen MH, Larsen MS, Olsen MV, Pedersen MJ, Østergaard LR, et al. SHARQnet – Sophisticated harmonic artifact reduction in quantitative susceptibility mapping using a deep convolutional neural network. Z Med Phys. 2019;29(2):139–49.

84. Liu J, Koch KM. Deep gated convolutional neural network for QSM background field removal. In: Medical Image Computing and Computer Assisted Intervention – MICCAI 2019. Springer Science and Business Media Deutschland GmbH; 2019. p. 83–91.

85. Zhu X, Gao Y, Liu F, Crozier S, Sun H. BFRnet: A deep learning-based MR background field removal method for QSM of the brain containing significant pathological susceptibility sources. Z Med Phys. Forthcoming 2022.

86. Liu T, Spincemaille P, de Rochefort L, Kressler B, Wang Y. Calculation of susceptibility through multiple orientation sampling (COSMOS): A method for conditioning the inverse problem from measured magnetic field map to susceptibility source image in MRI. Magn Reson Med. 2009;61(1):196–204.

87. Kressler B, de Rochefort L, Liu T, Spincemaille P, Jiang Q, Wang Y. Nonlinear regularization for per voxel estimation of magnetic susceptibility distributions from MRI field maps. IEEE Trans Med Imaging. 2010;29(2):273–81.

88. Wu B, Li W, Guidon A, Liu C. Whole brain susceptibility mapping using compressed sensing. Magn Reson Med. 2012;67(1):137–47.

89. Bilgic B, Chatnuntawech I, Fan AP, Setsompop K, Cauley SF, Wald LL, et al. Fast image reconstruction with L2-regularization. Journal of Magnetic Resonance Imaging. 2014;40(1):181–91.

90. Langkammer C, Bredies K, Poser BA, Barth M, Reishofer G, Fan AP, et al. Fast quantitative susceptibility mapping using 3D EPI and total generalized variation. Neuroimage. 2015;111:622–30.

91. Liu Z, Spincemaille P, Yao Y, Zhang Y, Wang Y. MEDI+0: Morphology enabled dipole inversion with automatic uniform cerebrospinal fluid zero reference for quantitative susceptibility mapping. Magn Reson Med. 2018;79(5):2795–803.

92. Li W, Wang N, Yu F, Han H, Cao W, Romero R, et al. A method for estimating and removing streaking artifacts in quantitative susceptibility mapping. Neuroimage. 2015;108:111–22.

93. Wei H, Dibb R, Zhou Y, Sun Y, Xu J, Wang N, et al. Streaking artifact reduction for quantitative susceptibility mapping of sources with large dynamic range. NMR Biomed. 2015;28(10):1294–303.

94. Sun H, Kate M, Gioia LC, Emery DJ, Butcher K, Wilman AH. Quantitative susceptibility mapping using a superposed dipole inversion method: Application to intracranial hemorrhage. Magn Reson Med. 2016;76(3):781–91.

95. Acosta-Cabronero J, Milovic C, Mattern H, Tejos C, Speck O, Callaghan MF. A robust multi-scale approach to quantitative susceptibility mapping. Neuroimage. 2018;183:7–24.

96. Bilgic B, Langkammer C, Wald L, Setsompop K. Single-step QSM with fast reconstruction. In: In Proceedings of the 3rd International Workshop on MRI Phase Contrast & Quantitative Susceptibility Mapping. Durham, North Carolina, USA; 2014. p. 3321.

97. Liu Z, Kee Y, Zhou D, Wang Y, Spincemaille P. Preconditioned total field inversion (TFI) method for quantitative susceptibility mapping. Magn Reson Med. 2017;78(1):303–15.

98. Sun H, Ma Y, MacDonald ME, Pike GB. Whole head quantitative susceptibility mapping using a least-norm direct dipole inversion method. Neuroimage. 2018;179:166–75.

99. Yoon J, Gong E, Chatnuntawech I, Bilgic B, Lee J, Jung W, et al. Quantitative susceptibility mapping using deep neural network: QSMnet. Neuroimage. 2018;179:199–206.

100. Bollmann S, Rasmussen KGB, Kristensen M, Blendal RG, Østergaard LR, Plocharski M, et al. DeepQSM - using deep learning to solve the dipole inversion for quantitative susceptibility mapping. Neuroimage. 2019;195:373–83.

101. Jung W, Yoon J, Ji S, Choi JY, Kim JM, Nam Y, et al. Exploring linearity of deep neural network trained QSM: QSMnet+. Neuroimage. 2020;211:116619.

102. Gao Y, Zhu X, Moffat BA, Glarin R, Wilman AH, Pike GB, et al. xQSM: Quantitative susceptibility mapping with octave convolutional and noise-regularized neural networks. NMR Biomed. 2021;34(3):e4461.

103. Liu J, Koch KM. Non-locally encoder-decoder convolutional network for whole brain QSM inversion. arXiv:1904.05493v1 [Preprint]. 2019.

104. Wei H, Cao S, Zhang Y, Guan X, Yan F, Yeom KW, et al. Learning-based single-step quantitative susceptibility mapping reconstruction without brain extraction. Neuroimage. 2019;202:116064.

105. Gao Y, Xiong Z, Fazlollahi A, Nestor PJ, Vegh V, Nasrallah F, et al. Instant tissue field and magnetic susceptibility mapping from MRI raw phase using Laplacian enhanced deep neural networks. Neuroimage. 2022;259:119410.

106. Bilgic B, Langkammer C, Marques JP, Meineke J, Milovic C, Schweser F. QSM reconstruction challenge 2.0: Design and report of results. Magn Reson Med. 2021;86(3):1241–55.

107. Cornell MRI Research Lab. MEDI Toolbox (Jan 15 2020 update). Cornell University. 2020.

108. Liu C. STI Suite V3. UC Berkeley. 2017.

109. Acosta-Cabronero J. QSMbox · GitLab. 2021.

110. Fang J, Bao L, Li X, van Zijl P, Chen Z. JHU/KKI QSM Toolbox v3.0. 2019.

111. Chan KS. SEPIA: Matlab GUI pipeline application for quantitative susceptibility mapping. GitHub. 2022.

112. Emmerich J, Bachert P, Ladd ME, Straub S. On the separation of susceptibility sources in quantitative susceptibility mapping: Theory and phantom validation with an in vivo application to multiple sclerosis lesions of different age. Journal of Magnetic Resonance. 2021;330:107033.

113. Dimov A v., Nguyen TD, Gillen KM, Marcille M, Spincemaille P, Pitt D, et al. Susceptibility source separation from gradient echo data using magnitude decay modeling. Journal of Neuroimaging. 2022;32(5):852–9.

114. Shin HG, Lee J, Yun YH, Yoo SH, Jang J, Oh SH, et al. χ-separation: Magnetic susceptibility source separation toward iron and myelin mapping in the brain. Neuroimage. 2021;240:118371.

115. Lin H, Wei H, He N, Fu C, Cheng S, Shen J, et al. Quantitative susceptibility mapping in combination with water-fat separation for simultaneous liver iron and fat fraction quantification. European Radiology 2018 28:8. 2018;28(8):3494–504.

116. Schweser F, Zivadinov R. Quantitative susceptibility mapping (QSM) with an extended physical model for MRI frequency contrast in the brain: a proof-of-concept of quantitative susceptibility and residual (QUASAR) mapping. NMR Biomed. 2018;31(12):e3999.

117. Bachrata B, Trattnig S, Robinson SD. Quantitative susceptibility mapping of the head-and-neck using SMURF fat-water imaging with chemical shift and relaxation rate corrections. Magn Reson Med. 2022;87(3):1461–79.

118. Sood S, Urriola J, Reutens D, O'Brien K, Bollmann S, Barth M, et al. Echo time-dependent quantitative susceptibility mapping contains information on tissue properties. Magn Reson Med. 2017;77(5):1946–58.

119. Rasouli J, Ramdhani R, Panov FE, Dimov A, Zhang Y, Cho C, et al. Utilization of quantitative susceptibility mapping for direct targeting of the subthalamic nucleus during deep brain stimulation surgery. Operative Neurosurgery. 2018;14(4):412–9.

120. Bandt SK, de Rochefort L, Chen W, Dimov A v., Spincemaille P, Kopell BH, et al. Clinical integration of quantitative susceptibility mapping magnetic resonance imaging into neurosurgical practice. World Neurosurg. 2019;122:e10–9.

121. Liu T, Eskreis-Winkler S, Schweitzer AD, Chen W, Kaplitt MG, Tsiouris AJ, et al. Improved subthalamic nucleus depiction with quantitative susceptibility mapping. Radiology. 2013;269(1):216–23.

122. Feng X, Deistung A, Dwyer MG, Hagemeier J, Polak P, Lebenberg J, et al. An improved FSL-FIRST pipeline for subcortical gray matter segmentation to study abnormal brain anatomy using quantitative susceptibility mapping (QSM). Magn Reson Imaging. 2017;39:110–22.

123. Basukala D, Mukundan R, Lim A, Hurrell MA, Keenan RJ, Dalrymple-Alford JC, et al. Automated segmentation of substantia nigra and red nucleus using quantitative susceptibility mapping images: Application to Parkinson's disease. Computers & Electrical Engineering. 2021;91:107091.

124. Tang S, Zhang G, Ran Q, Nie L, Liu X, Pan Z, et al. Quantitative susceptibility mapping shows lower brain iron content in children with attention-deficit hyperactivity disorder. Hum Brain Mapp. 2022;43(8):2495–502.

125. Chen Y, Su S, Dai Y, Zou M, Lin L, Qian L, et al. Quantitative susceptibility mapping reveals brain iron deficiency in children with attention-deficit/hyperactivity disorder: a whole-brain analysis. Eur Radiol. 2022;32(6):3726–33.

126. Tang S, Xu Y, Liu X, Chen Z, Zhou Y, Nie L, et al. Quantitative susceptibility mapping shows lower brain iron content in children with autism. Eur Radiol. 2020;31(4):2073–83.

127. Nikparast F, Ganji Z, Danesh Doust M, Faraji R, Zare H. Brain pathological changes during neurodegenerative diseases and their identification methods: How does QSM perform in detecting this process? Insights Imaging. 2022;13(1):1–20.

128. Acosta-Cabronero J, Williams GB, Cardenas-Blanco A, Arnold RJ, Lupson V, Nestor PJ. In vivo quantitative susceptibility mapping (QSM) in Alzheimer's disease. PLoS One. 2013;8(11):e81093.

129. Acosta-Cabronero J, Machts J, Schreiber S, Abdulla S, Kollewe K, Petri S, et al. Quantitative susceptibility MRI to detect brain iron in Amyotrophic Lateral Sclerosis. Radiology. 2018;289(1):195–203.

130. Langkammer C, Liu T, Khalil M, Enzinger C, Jehna M, Fuchs S, et al. Quantitative susceptibility mapping in multiple sclerosis. Radiology. 2013;267(2):551–9.

131. Li X, Harrison DM, Liu H, Jones CK, Oh J, Calabresi PA, et al. Magnetic susceptibility contrast variations in multiple sclerosis lesions. Journal of Magnetic Resonance Imaging. 2016;43(2):463–73.

132. Lotfipour AK, Wharton S, Schwarz ST, Gontu V, Schäfer A, Peters AM, et al. High resolution magnetic susceptibility mapping of the substantia nigra in Parkinson’s disease. Journal of Magnetic Resonance Imaging. 2012;35(1):48–55.

133. Barbosa JHO, Santos AC, Tumas V, Liu M, Zheng W, Haacke EM, et al. Quantifying brain iron deposition in patients with Parkinson’s disease using quantitative susceptibility mapping, R2 and R2*. Magn Reson Imaging. 2015;33(5):559–65.

134. Li G, Wu R, Tong R, Bo B, Zhao Y, Gillen KM, et al. Quantitative measurement of metal accumulation in brain of patients with Wilson’s disease. Movement Disorders. 2020;35(10):1787–95.

135. Wang S, Lou M, Liu T, Cui D, Chen X, Wang Y. Hematoma volume measurement in gradient echo MRI using quantitative susceptibility mapping. Stroke. 2013;44(8):2315–7.

136. De A, Sun H, Emery DJ, Butcher KS, Wilman AH. Rapid quantitative susceptibility mapping of intracerebral hemorrhage. Journal of Magnetic Resonance Imaging. 2020;51(3):712–8.

137. Chang S, Zhang J, Liu T, Tsiouris AJ, Shou J, Nguyen T, et al. Quantitative susceptibility mapping of intracerebral Hemorrhages at various stages. Journal of Magnetic Resonance Imaging. 2016;44(2):420–5.

138. Zhang Y, Wei H, Sun Y, Cronin MJ, He N, Xu J, et al. Quantitative susceptibility mapping (QSM) as a means to monitor cerebral hematoma treatment. Journal of Magnetic Resonance Imaging. 2018;48(4):907–15.

139. Sun H, Klahr AC, Kate M, Gioia LC, Emery DJ, Butcher KS, et al. Quantitative susceptibility mapping for following intracranial hemorrhage. Radiology. 2018;288(3):830–9.

140. Liu T, Surapaneni K, Lou M, Cheng L, Spincemaille P, Wang Y. Cerebral Microbleeds: Burden assessment by using quantitative susceptibility mapping. Radiology. 2012;262(1):269–78.

141. Nakagawa D, Kudo K, Awe O, Zanaty M, Nagahama Y, Cushing C, et al. Detection of microbleeds associated with sentinel headache using MRI quantitative susceptibility mapping: Pilot study. J Neurosurg. 2018;130(4):1391–7.

142. Liu S, Brisset JC, Hu J, Haacke EM, Ge Y. Susceptibility weighted imaging and quantitative susceptibility mapping of the cerebral vasculature using Ferumoxytol. J Magn Reson Imaging. 2018;47(3):621–33.

143. Xu B, Liu T, Spincemaille P, Prince M, Wang Y. Flow compensated quantitative susceptibility mapping for venous oxygenation imaging. Magn Reson Med. 2014;72(2):438–45.

144. Fan AP, Bilgic B, Gagnon L, Witzel T, Bhat H, Rosen BR, et al. Quantitative oxygenation venography from MRI phase. Magn Reson Med. 2014;72(1):149–59.

145. Li J, Lin H, Liu T, Zhang Z, Prince MR, Gillen K, et al. Quantitative susceptibility mapping (QSM) minimizes interference from cellular pathology in R2* estimation of liver iron concentration. Journal of Magnetic Resonance Imaging. 2018;48(4):1069–79.

146. Jafari R, Sheth S, Spincemaille P, Nguyen TD, Prince MR, Wen Y, et al. Rapid automated liver quantitative susceptibility mapping. Journal of Magnetic Resonance Imaging. 2019;50(3):725–32.

147. Qu Z, Yang S, Xing F, Tong R, Yang C, Guo R, et al. Magnetic resonance quantitative susceptibility mapping in the evaluation of hepatic fibrosis in chronic liver disease: A feasibility study. Quant Imaging Med Surg. 2021;11(4):1170–83.

148. Wen Y, Weinsaft JW, Nguyen TD, Liu Z, Horn EM, Singh H, et al. Free breathing three-dimensional cardiac quantitative susceptibility mapping for differential cardiac chamber blood oxygenation - Initial validation in patients with cardiovascular disease inclusive of direct comparison to invasive catheterization. Journal of Cardiovascular Magnetic Resonance. 2019;21(1):1–13.

149. Wen Y, Nguyen TD, Liu Z, Spincemaille P, Zhou D, Dimov A, et al. Cardiac quantitative susceptibility mapping (QSM) for heart chamber oxygenation. Magn Reson Med. 2018;79(3):1545–52.

150. Bechler E, Stabinska J, Thiel T, Jasse J, Zukovs R, Valentin B, et al. Feasibility of quantitative susceptibility mapping (QSM) of the human kidney. Magnetic Resonance Materials in Physics, Biology and Medicine. 2021;34(3):389–97.

151. Diefenbach MN, Meineke J, Ruschke S, Baum T, Gersing A, Karampinos DC. On the sensitivity of quantitative susceptibility mapping for measuring trabecular bone density. Magn Reson Med. 2019;81(3):1739–54.

152. Zhang M, Li Z, Wang H, Chen T, Lu Y, Yan F, et al. Simultaneous quantitative susceptibility mapping of articular cartilage and cortical bone of human knee joint using ultrashort echo time sequences. Front Endocrinol (Lausanne). 2022;13:221.

153. Wang Y, Spincemaille P, Liu Z, Dimov A, Deh K, Li J, et al. Clinical quantitative susceptibility mapping (QSM): Biometal imaging and its emerging roles in patient care. Journal of Magnetic Resonance Imaging. 2017;46(4):951–71.

154. Vinayagamani S, Sheelakumari R, Sabarish S, Senthilvelan S, Ros R, Thomas B, et al. Quantitative susceptibility mapping: Technical considerations and clinical applications in neuroimaging. Journal of Magnetic Resonance Imaging. 2021;53(1):23–37.

155. Obeso JA, Rodriguez-Oroz MC, Stamelou M, Bhatia KP, Burn DJ. The expanding universe of disorders of the basal ganglia. The Lancet. 2014;384(9942):523–31.

156. Roccatagliata L, Vuolo L, Bonzano L, Pichiecchio A, Mancardi GL. Multiple Sclerosis: Hyperintense dentate nucleus on unenhanced T1-weighted MR images is associated with the secondary progressive subtype. Radiology. 2009;251(2):503–10.

157. Eshaghi A, Prados F, Brownlee WJ, Altmann DR, Tur C, Cardoso MJ, et al. Deep gray matter volume loss drives disability worsening in multiple sclerosis. Ann Neurol. 2018;83(2):210–22.

158. Martin WRW, Wieler M, Gee M. Midbrain iron content in early Parkinson disease: A potential biomarker of disease status. Neurology. 2008;70(16 PART 2):1411–7.

159. Huddleston DE, Langley J, Dusek P, He N, Faraco CC, Crosson B, et al. Imaging Parkinsonian pathology in substantia nigra with MRI. Curr Radiol Rep. 2018;6(4):15.

160. Aylward EH, Liu D, Nopoulos PC, Ross CA, Pierson RK, Mills JA, et al. Striatal volume contributes to the prediction of onset of Huntington disease in incident cases. Biol Psychiatry. 2012;71(9):822–8.

161. Domínguez D JF, Ng ACL, Poudel G, Stout JC, Churchyard A, Chua P, et al. Iron accumulation in the basal ganglia in Huntington's disease: Cross-sectional data from the IMAGE-HD study. J Neurol Neurosurg Psychiatry. 2016;87(5):545–9.

162. Chen L, Hua J, Ross CA, Cai S, van Zijl PCM, Li X. Altered brain iron content and deposition rate in Huntington's disease as indicated by quantitative susceptibility MRI. J Neurosci Res. 2019;97(4):467–79.

163. Ashburner J, Friston KJ. Voxel-based morphometry-The methods. Neuroimage. 2000;11(6):805–21.

164. Wyciszkiewicz A, Pawlak MA. Basal Ganglia volumes: MR-Derived reference ranges and lateralization indices for children and young adults. Neuroradiology Journal. 2014;27(5):595–612.

165. Derakhshan M, Caramanos Z, Giacomini PS, Narayanan S, Maranzano J, Francis SJ, et al. Evaluation of automated techniques for the quantification of grey matter atrophy in patients with multiple sclerosis. Neuroimage. 2010;52(4):1261–7.

166. Helms G, Draganski B, Frackowiak R, Ashburner J, Weiskopf N. Improved segmentation of deep brain grey matter structures using magnetization transfer (MT) parameter maps. Neuroimage. 2009;47(1):194–8.

167. Schweser F, Feng X, Batlle RM, Güllmar D, Deistung A, Dwyer MG, et al. Improved deep gray matter segmentation using anatomical information from quantitative susceptibility maps. In: Proc Intl Soc Mag Reson Med. 2014. p. 1787.

168. Cobzas D, Sun H, Walsh AJ, Lebel RM, Blevins G, Wilman AH. Subcortical gray matter segmentation and voxel-based analysis using transverse relaxation and quantitative susceptibility mapping with application to multiple sclerosis. Journal of Magnetic Resonance Imaging. 2015;42(6):1601–10.

169. Visser E, Keuken MC, Douaud G, Gaura V, Bachoud-Levi AC, Remy P, et al. Automatic segmentation of the striatum and globus pallidus using MIST: Multimodal Image Segmentation Tool. Neuroimage. 2016;125:479–97.

170. Garzón B, Sitnikov R, Bäckman L, Kalpouzos G. Automated segmentation of midbrain structures with high iron content. Neuroimage. 2018;170:199–209.

171. Lim IAL, Faria A v., Li X, Hsu JTC, Airan RD, Mori S, et al. Human brain atlas for automated region of interest selection in quantitative susceptibility mapping: Application to determine iron content in deep gray matter structures. Neuroimage. 2013;82:449–69.

172. Visser E, Keuken MC, Forstmann BU, Jenkinson M. Automated segmentation of the substantia nigra, subthalamic nucleus and red nucleus in 7 T data at young and old age. Neuroimage. 2016;139:324–36.

173. Hanspach J, Dwyer MG, Bergsland NP, Feng X, Hagemeier J, Bertolino N, et al. Methods for the computation of templates from quantitative magnetic susceptibility maps (QSM): Toward improved atlas- and voxel-based analyses (VBA). Journal of Magnetic Resonance Imaging. 2017;46(5):1474–84.

174. Zhang Y, Wei H, Cronin MJ, He N, Yan F, Liu C. Longitudinal atlas for normative human brain development and aging over the lifespan using quantitative susceptibility mapping. Neuroimage. 2018;171:176–89.

175. Li X, Chen L, Kutten K, Li Y, Kang N, Hsu JT, et al. Multi-atlas tool for automated segmentation of brain gray matter nuclei and quantification of their magnetic susceptibility. Neuroimage. 2019;191:337–49.

176. Caan M, Bazin PL, Marques J, de Hollander G, Dumoulin S, Zwaag W van der. MP2RAGEME: T1, T2* and QSM mapping in one sequence at 7 Tesla. Hum Brain Mapp. 2018;40(6):1786–98.

177. Metere R, Kober T, Möller HE, Schäfer A. Simultaneous quantitative MRI mapping of T1, T2∗ and magnetic susceptibility with Multi-Echo MP2RAGE. PLoS One. 2017;12(1):1–28.

178. Sun H, Cleary JO, Glarin R, Kolbe SC, Ordidge RJ, Moffat BA, et al. Extracting more for less: Multi-echo MP2RAGE for simultaneous T1-weighted imaging, T1 mapping, R2*

mapping, SWI, and QSM from a single acquisition. Magn Reson Med. 2020;83(4):1178–91.

179. Milovic C, Bilgic B, Zhao B, Acosta-Cabronero J, Tejos C. FAst Nonlinear Susceptibility Inversion (FANSI Toolbox for QSM). In: 34th ESMRMB Annual Scientific Meeting. Barcelona, Spain; 2017. p. 727.

180. Gracien RM, Jurcoane A, Wagner M, Reitz SC, Mayer C, Volz S, et al. The relationship between gray matter quantitative MRI and disability in secondary progressive multiple sclerosis. PLoS One. 2016;11(8):161036.

181. Granziera C, Daducci A, Donati A, Bonnier G, Romascano D, Roche A, et al. A multi-contrast MRI study of microstructural brain damage in patients with mild cognitive impairment. Neuroimage Clin. 2015;8:631–9.

182. Cronin MJ, Wang N, Decker KS, Wei H, Zhu WZ, Liu C. Exploring the origins of echo-time-dependent quantitative susceptibility mapping (QSM) measurements in healthy tissue and cerebral microbleeds. Neuroimage. 2017;149:98–113.

183. Duyn JH, van Gelderen P, Li TQ, de Zwart JA, Koretsky AP, Fukunaga M. High-field MRI of brain cortical substructure based on signal phase. Proceedings of the National Academy of Sciences of the USA. 2007;104(28):11796–801.

184. Conturo TE, Smith GD. Signal-to-Noise in phase angle reconstruction: Dynamic range extension using phase reference offsets. Magn Reson Med. 1990;15:420–37.

185. Otsu N. A threshold selection method from gray-level histograms. IEEE Trans Syst Man Cybern. 1979;9(1):62–6.

186. Tustison NJ, Avants BB, Cook PA, Zheng Y, Egan A, Yushkevich PA, et al. N4ITK: Improved N3 bias correction. IEEE Trans Med Imaging. 2010;29(6):1310–20.

187. Avants BB, Tustison N, Song G. Advanced Normalization Tools: V1.0. Insight journal. 2009;2:1–35.

188. Patenaude B, Smith SM, Kennedy DN, Jenkinson M. A Bayesian model of shape and appearance for subcortical brain segmentation. Neuroimage. 2011;56:907–22.

189. Babalola KO, Patenaude B, Aljabar P, Schnabel J, Kennedy D, Crum W, et al. An evaluation of four automatic methods of segmenting the subcortical structures in the brain. Neuroimage. 2009;47(4):1435–47.

190. Lebenberg J, Buvat I, Lalande A, Clarysse P, Casta C, Cochet A, et al. Nonsupervised ranking of different segmentation approaches: Application to the estimation of the left ventricular ejection fraction from cardiac cine MRI sequences. IEEE Trans Med Imaging. 2012;31(8):1651–60.

191. Jha AK, Mena E, Caffo B, Ashrafinia S, Rahmim A, Frey E, et al. Practical no-gold-standard evaluation framework for quantitative imaging methods: application to lesion segmentation in positron emission tomography. Journal of Medical Imaging. 2017;4(1):011011.

192. Madan H, Pernuš F, Spiclin Z. Reference-free error estimation for multiple measurement methods. Stat Methods Med Res. 2018;0(0):1–14.

193. Salvatier J, Wiecki T v., Fonnesbeck C. Probabilistic programming in Python using PyMC3. PeerJ Comput Sci. 2016;2:e55.

194. Wang J, He L, Zheng H, Lu ZL. Optimizing the magnetization-prepared rapid gradient-echo (MP-RAGE) sequence. PLoS One. 2014;9(5):e96899.

195. Ellingson BM, Bendszus M, Boxerman J, Barboriak D, Erickson BJ, Smits M, et al. Consensus recommendations for a standardized brain tumor imaging protocol in clinical trials. Neuro Oncol. 2015;17(9):1188–98.

196. Karsa A, Punwani S, Shmueli K. The effect of low resolution and coverage on the accuracy of susceptibility mapping. Magn Reson Med. 2019;81(3):1833–48.

197. Foo TK, Polzin JA, Derbyshire JA. Method for phase contrast reconstruction for partial Fourier acquisitions. In: Proc Intl Sot Mag Reson Med 8. Colorado, USA; 2000. p. 1718.

198. Zhou D, Cho J, Zhang J, Spincemaille P, Wang Y. Susceptibility underestimation in a high-susceptibility phantom: Dependence on imaging resolution, magnitude contrast, and other parameters. Magn Reson Med. 2017;78:1080–6.

199. Marques JP, Kober T, Krueger G, van der Zwaag W, van de Moortele PF, Gruetter R. MP2RAGE, a self bias-field corrected sequence for improved segmentation and T1-mapping at high field. Neuroimage. 2010;49(2):1271–81.

200. de Moortele PF, Auerbach EJ, Olman C, Yacoub E, Uğurbil K, Moeller S. T1 weighted brain images at 7 Tesla unbiased for Proton Density, T2* contrast and RF coil receive B1 sensitivity with simultaneous vessel visualization. Neuroimage. 2009;46:432–46.

201. Kecskemeti S, Samsonov A, Hurley SA, Dean DC, Field A, Alexander AL. MPnRAGE: A technique to simultaneously acquire hundreds of differently contrasted MPRAGE images with applications to quantitative T1mapping. Magn Reson Med. 2016;75(3):1040–53.

202. Hunter JD. Matplotlib: A 2D graphics environment. Comput Sci Eng. 2007;9(3):90–5.

203. Cordonnier C, Al-Shahi Salman R, Wardlaw J. Spontaneous brain microbleeds: systematic review, subgroup analyses and standards for study design and reporting. Brain. 2007;130(8):1988–2003.

204. Greenberg SM, Vernooij MW, Cordonnier C, Viswanathan A, Al-Shahi Salman R, Warach S, et al. Cerebral microbleeds: a guide to detection and interpretation. Lancet Neurol. 2009;8(2):165–74.

205. McAuley G, Schrag M, Barnes S, Obenaus A, Dickson A, Holshouser B, et al. Iron quantification of microbleeds in postmortem brain. Magn Reson Med. 2011;65(6):1592–601.

206. Pettersen JA, Sathiyamoorthy G, Gao FQ, Szilagyi G, Nadkarni NK, st. George-Hyslop P, et al. Microbleed topography, Leukoaraiosis, and cognition in probable Alzheimer Disease from the Sunnybrook dementia study. Arch Neurol. 2008;65(6):790–5.

207. Goos JDC, Henneman WJP, Sluimer JD, Vrenken H, Sluimer IC, Barkhof F, et al. Incidence of cerebral microbleeds: A longitudinal study in a memory clinic population. Neurology. 2010;74(24):1954–60.

208. Poels MMF, Ikram MA, van der Lugt A, Hofman A, Krestin GP, Breteler MMB, et al. Incidence of cerebral microbleeds in the general population. Stroke. 2011;42(3):656–61.

209. Ding J, Sigurdsson S, Garcia M, Phillips CL, Eiriksdottir G, Gudnason V, et al. Risk factors associated with incident cerebral microbleeds according to location in older people: The age, gene/environment susceptibility (AGES)–Reykjavik study. JAMA Neurol. 2015;72(6):682–8.

210. Werring DJ. Cerebral Microbleeds: Pathophysiology to Clinical Practice. Cambridge University Press; 2011.

211. Charidimou A, Jäger HR, Werring DJ. Cerebral microbleed detection and mapping: Principles, methodological aspects and rationale in vascular dementia. Exp Gerontol. 2012;47(11):843–52.

212. Buch S, Cheng YCN, Hu J, Liu S, Beaver J, Rajagovindan R, et al. Determination of detection sensitivity for cerebral microbleeds using susceptibility-weighted imaging. NMR Biomed. 2017;30(4):e3551.

213. Nandigam RNK, Viswanathan A, Delgado P, Skehan ME, Smith EE, Rosand J, et al. MR imaging detection of cerebral microbleeds: Effect of susceptibility-weighted imaging, section thickness, and field strength. American Journal of Neuroradiology. 2009;30(2):338–43.

214. Stehling C, Wersching H, Kloska SP, Kirchhof P, Ring J, Nassenstein I, et al. Detection of asymptomatic cerebral microbleeds. A comparative study at 1.5 and 3.0 T. Acad Radiol. 2008;15(7):895–900.

215. Bian W, Hess CP, Chang SM, Nelson SJ, Lupo JM. Susceptibility-weighted MR imaging of radiation therapy-induced cerebral microbleeds in patients with glioma: a comparison between 3T and 7T. Neuroradiology 2013 56:2. 2013;56(2):91–6.

216. Conijn MMA, Geerlings MI, Biessels GJ, Takahara T, Witkamp TD, Zwanenburg JJM, et al. Cerebral Microbleeds on MR imaging: Comparison between 1.5 and 7T. American Journal of Neuroradiology. 2011;32(6):1043–9.

217. Vernooij MW, Ikram MA, Wielopolski PA, Krestin GP, Breteler MMB, van der Lugt A. Cerebral Microbleeds: Accelerated 3D T2*-weighted GRE MR imaging versus

conventional 2D T2*-weighted GRE MR imaging for detection. Radiology. 2008;248(1):272–7.

218. Wang Y, Liu T. Quantitative susceptibility mapping (QSM): Decoding MRI data for a tissue magnetic biomarker. Magn Reson Med. 2015;73(1):82–101.

219. Klohs J, Deistung A, Schweser F, Grandjean J, Dominietto M, Waschkies C, et al. Detection of cerebral microbleeds with quantitative susceptibility mapping in the ArcAbeta mouse model of cerebral amyloidosis. Journal of Cerebral Blood Flow and Metabolism. 2011;31(12):2282–92.

220. Najafabadi PB. Quantitative Susceptibility Mapping in Ischemic Stroke: Cerebral Veins, Tissue, and Microbleeds. Master thesis, Edmonton (CA): University of Alberta; 2019.

221. Naji N, Sun H, Wilman AH. On the value of QSM from MPRAGE for segmenting and quantifying iron-rich deep gray matter. Magn Reson Med. 2020;84(3):1486–500.

222. Peca S, McCreary CR, Donaldson E, Kumarpillai G, Shobha N, Sanchez K, et al. Neurovascular decoupling is associated with severity of cerebral amyloid angiopathy. Neurology. 2013;81(19):1659–65.

223. Sharma M, Hart RG, Smith EE, Bosch J, Eikelboom JW, Connolly SJ, et al. Rivaroxaban for prevention of covert brain infarcts and cognitive decline: The COMPASS MRI substudy. Stroke. 2020;2901–9.

224. Jack CR, Bernstein MA, Fox NC, Thompson P, Alexander G, Harvey D, et al. The Alzheimer's disease neuroimaging initiative (ADNI): MRI methods. Journal of Magnetic Resonance Imaging. 2008;27(4):685–91.

225. Oliveira ÍAF, Roos T, Dumoulin SO, Siero JCW, van der Zwaag W. Can 7T MPRAGE match MP2RAGE for gray-white matter contrast? Neuroimage. 2021;240:118384.

226. Lüsebrink F, Mattern H, Yakupov R, Acosta-Cabronero J, Ashtarayeh M, Oeltze-Jafra S, et al. Comprehensive ultrahigh resolution whole brain in vivo MRI dataset as a human phantom. Sci Data. 2021;8(1):1–13.

227. Jenkinson M, Beckmann CF, Behrens TEJ, Woolrich MW, Smith SM. FSL. Neuroimage. 2012;62(2):782–90.

228. Wright PJ, Mougin OE, Totman JJ, Peters AM, Brookes MJ, Coxon R, et al. Water proton T1 measurements in brain tissue at 7, 3, and 1.5T using IR-EPI, IR-TSE, and MPRAGE: Results and optimization. Magnetic Resonance Materials in Physics, Biology and Medicine. 2008;21(1):121–30.

229. Sun H. Hongfu Sun's MATLAB codes for QSM. GitHub. 2018.

230. Bilgic B, Fan AP, Polimeni JR, Cauley SF, Bianciardi M, Adalsteinsson E, et al. Fast quantitative susceptibility mapping with L1-regularization and automatic parameter selection. Magn Reson Med. 2014;72(5):1444–59.

231. Yushkevich PA, Piven J, Hazlett HC, Smith RG, Ho S, Gee JC, et al. User-guided 3D active contour segmentation of anatomical structures: Significantly improved efficiency and reliability. Neuroimage. 2006;31(3):1116–28.

232. Barnes SRS, Haacke EM, Ayaz M, Boikov AS, Kirsch W, Kido D. Semiautomated detection of cerebral microbleeds in magnetic resonance images. Magn Reson Imaging. 2011;29(6):844–52.

233. Bian W, Hess CP, Chang SM, Nelson SJ, Lupo JM. Computer-aided detection of radiation-induced cerebral microbleeds on susceptibility-weighted MR images. Neuroimage Clin. 2013;2(1):282–90.

234. Chesebro AG, Amarante E, Lao PJ, Meier IB, Mayeux R, Brickman AM. Automated detection of cerebral microbleeds on T2*-weighted MRI. Sci Rep. 2021;11(1):1–13.

235. Elkady AM, Sun H, Wilman AH. Importance of extended spatial coverage for quantitative susceptibility mapping of iron-rich deep gray matter. Magn Reson Imaging. 2016;34(4):574–8.

236. Haller S, Vernooij MW, Kuijer JPA, Larsson EM, Jäger HR, Barkhof F. Cerebral Microbleeds: Imaging and clinical significance. Radiology. 2018;287(1):11–28.

237. Zhu X, Gao Y, Liu F, Crozier S, Sun H. Deep grey matter quantitative susceptibility mapping from small spatial coverages using deep learning. Z Med Phys. 2022;32(2):188–98.

238. Treit S, Steve T, Gross DW, Beaulieu C. High resolution in-vivo diffusion imaging of the human hippocampus. Neuroimage. 2018;182:479–87.

239. Deistung A, Jäschke D, Draganova R, Pfaffenrot V, Hulst T, Steiner KM, et al. Quantitative susceptibility mapping reveals alterations of dentate nuclei in common types of degenerative cerebellar ataxias. Brain Commun. 2022;4(1):fcab306.

240. Dimov A v., Gupta A, Kopell BH, Wang Y. High-resolution QSM for functional and structural depiction of subthalamic nuclei in DBS presurgical mapping. J Neurosurg. 2018;131(2):360–7.

241. Bilgic B, Gagoski BA, Cauley SF, Fan AP, Polimeni JR, Grant PE, et al. Wave-CAIPI for highly accelerated 3D imaging. Magn Reson Med. 2015;73(6):2152–62.

242. Bilgic B, Ye H, Wald LL, Setsompop K. Simultaneous time interleaved multislice (STIMS) for rapid susceptibility weighted acquisition. Neuroimage. 2017;155:577–86.

243. le Ster C, Moreno A, Mauconduit F, Gras V, Stirnberg R, Poser BA, et al. Comparison of SMS-EPI and 3D-EPI at 7T in an fMRI localizer study with matched spatiotemporal resolution and homogenized excitation profiles. PLoS One. 2019;14(11):e0225286.

244. Langkammer C, Schweser F, Shmueli K, Kames C, Li X, Guo L, et al. Quantitative susceptibility mapping: Report from the 2016 reconstruction challenge. Magn Reson Med. 2018;79(3):1661–73.

245. Lancione M, Donatelli G, Cecchi P, Cosottini M, Tosetti M, Costagli M. Echo-time dependency of quantitative susceptibility mapping reproducibility at different magnetic field strengths. Neuroimage. 2019;197:557–64.

246. Jezzard P, Balaban RS. Correction for geometric distortion in echo planar images from B0 field variations. Magn Reson Med. 1995;34(1):65–73.

247. Reber PJ, Wong EC, Buxton RB, Frank LR. Correction of off resonance-related distortion in echo-planar imaging using EPI-based field maps. Magn Reson Med. 1998;39(2):328–30.

248. Brey WW, Narayana PA. Correction for intensity falloff in surface coil magnetic resonance imaging. Med Phys. 1988;15(2):241–5.

249. Narayana PA, Brey WW, Kulkarni M v., Sievenpiper CL. Compensation for surface coil sensitivity variation in magnetic resonance imaging. Magn Reson Imaging. 1988;6(3):271–4.

250. Lindemeyer J, Worthoff WA, Shymanskaya A, Shah NJ. Iterative Restoration of the Fringe Phase (REFRASE) for QSM. Front Neurosci. 2021;15:474.

251. Rehman HZU, Hwang H, Lee S. Conventional and deep learning methods for skull stripping in brain MRI. Applied Sciences. 2020;10(5):1773.

252. Li H, Zhu Q, Hu D, Gunnala M, Johnson H, Hao Li al, et al. Human brain extraction with deep learning. In: Proc SPIE 12032, Medical Imaging 2022: Image Processing. SPIE; 2022. p. 369–75.

253. Fair MJ, Gatehouse PD, Firmin DN. Minimisation of slab-selective radiofrequency excitation pulse durations constrained by an acceptable aliasing coefficient. Magn Reson Imaging. 2021;81:94–100.

254. Li N. Magnetic susceptibility quantification for arbitrarily shaped objects in inhomogeneous fields. Magn Reson Med. 2001;46(5):907–16.

255. Uddin MN, Lebel RM, Wilman AH. Value of transverse relaxometry difference methods for iron in human brain. Magn Reson Imaging. 2016;34(1):51–9.

256. Langkammer C, Schweser F, Krebs N, Deistung A, Goessler W, Scheurer E, et al. Quantitative susceptibility mapping (QSM) as a means to measure brain iron? A post mortem validation study. Neuroimage. 2012;62(3):1593–9.

257. Zheng W, Nichol H, Liu S, Cheng YCN, Haacke EM. Measuring iron in the brain using quantitative susceptibility mapping and X-ray fluorescence imaging. Neuroimage. 2013;78:68–74.

258. Sun H, Walsh AJ, Lebel RM, Blevins G, Catz I, Lu JQ, et al. Validation of quantitative susceptibility mapping with Perls' iron staining for subcortical gray matter. Neuroimage. 2015;105:486–92.

259. Peterson ET, Kwon D, Luna B, Larsen B, Prouty D, de Bellis MD, et al. Distribution of brain iron accrual in adolescence: Evidence from cross-sectional and longitudinal analysis. Hum Brain Mapp. 2019;40(5):1480–95.

260. Persson N, Wu J, Zhang Q, Liu T, Shen J, Bao R, et al. Age and sex related differences in subcortical brain iron concentrations among healthy adults. Neuroimage. 2015;122:385–98.

261. Chen W, Zhu W, Kovanlikaya I, Kovanlikaya A, Liu T, Wang S, et al. Intracranial calcifications and hemorrhages: Characterization with quantitative susceptibility mapping. Radiology. 2014;270(2):496–505.

262. Bush AI. The metallobiology of Alzheimer's disease. Trends Neurosci. 2003;26(4):207–14.

263. Santin MD, Didier M, Valabrègue R, Yahia Cherif L, García-Lorenzo D, Loureiro de Sousa P, et al. Reproducibility of R2* and quantitative susceptibility mapping (QSM) reconstruction methods in the basal ganglia of healthy subjects. NMR Biomed. 2017;30(4):e3491.

264. Lin PY, Chao TC, Wu ML. Quantitative susceptibility mapping of human brain at 3T: A multisite reproducibility study. American Journal of Neuroradiology. 2015;36(3):467–74.

265. Wang R, Xie G, Zhai M, Zhang Z, Wu B, Zheng D, et al. Stability of R2∗and quantitative susceptibility mapping of the brain tissue in a large scale multi-center study. Sci Rep. 2017;7:45261.

266. Spincemaille P, Liu Z, Zhang S, Kovanlikaya I, Ippoliti M, Makowski M, et al. Clinical integration of automated processing for brain quantitative susceptibility mapping: Multi-site reproducibility and single-site robustness. Journal of Neuroimaging. 2019;29(6):689–98.

267. Voelker MN, Kraff O, Goerke S, Laun FB, Hanspach J, Pine KJ, et al. The traveling heads 2.0: Multicenter reproducibility of quantitative imaging methods at 7 Tesla. Neuroimage. 2021;232:117910.

268. Hinoda T, Fushimi Y, Okada T, Fujimoto K, Liu C, Yamamoto A, et al. Quantitative susceptibility mapping at 3 T and 1.5 T: Evaluation of consistency and reproducibility. Invest Radiol. 2015;50(8):522–30.

269. Spincemaille P, Anderson J, Wu G, Yang B, Fung M, Li K, et al. Quantitative susceptibility mapping: MRI at 7T versus 3T. Journal of Neuroimaging. 2020;30(1):65–75.

270. Headley AM, Grice J v., Pickens DR. Reproducibility of liver iron concentration estimates in MRI through R2* measurement determined by least-squares curve fitting. J Appl Clin Med Phys. 2020;21(12):295–303.

271. Lauzon ML, McCreary CR, McLean DA, Salluzzi M, Frayne R. Quantitative susceptibility mapping at 3 T: comparison of acquisition methodologies. NMR Biomed. 2017;30(4):e3492.

272. Pei M, Nguyen TD, Thimmappa ND, Salustri C, Dong F, Cooper MA, et al. Algorithm for fast monoexponential fitting based on Auto-Regression on Linear Operations (ARLO) of data. Magn Reson Med. 2015;73(2):843–50.

273. Manjón J v., Coupé P. Volbrain: An online MRI brain volumetry system. Front Neuroinform. 2016;10:30.

274. Koo TK, Li MY. A guideline of selecting and reporting intraclass correlation coefficients for reliability research. J Chiropr Med. 2016;15(2):155–63.

275. Gibbons RD, Hedeker D. Applications of mixed-effects models in biostatistics. Sankhyā: The Indian Journal of Statistics. 2000;Series B:70–103.

276. Klein R. Bland-Altman and Correlation Plot. MATLAB Central File Exchange. 2021.

277. Deh K, Nguyen TD, Eskreis-Winkler S, Prince MR, Spincemaille P, Gauthier S, et al. Reproducibility of quantitative susceptibility mapping in the brain at two field strengths from two vendors. Journal of Magnetic Resonance Imaging. 2015;42(6):1592–600.

278. Karsa A. Optimising MRI Magnetic Susceptibility Mapping for Applications in Challenging Regions of the Body. Doctoral thesis, London (UK): University College London; 2018.

279. Eskreis-Winkler S, Zhou D, Liu T, Gupta A, Gauthier SA, Wang Y, et al. On the influence of zero-padding on the nonlinear operations in Quantitative Susceptibility Mapping. Magn Reson Imaging. 2017;35:154–9.

280. Berg RC, Preibisch C, Thomas DL, Shmueli K, Biondetti E. Investigating the effect of flow compensation and quantitative susceptibility mapping method on the accuracy of venous susceptibility measurement. Neuroimage. 2021;240:118399.

281. Wharton S, Bowtell R. Whole-brain susceptibility mapping at high field: A comparison of multiple- and single-orientation methods. Neuroimage. 2010;53(2):515–25.

282. Bilgic B, Pfefferbaum A, Rohlfing T, Sullivan E v., Adalsteinsson E. MRI estimates of brain iron concentration in normal aging using quantitative susceptibility mapping. Neuroimage. 2012;59(3):2625–35.

283. Jung W, Bollmann S, Lee J. Overview of quantitative susceptibility mapping using deep learning: Current status, challenges and opportunities. NMR Biomed. 2022;35(4):e4292.

284. Sharma SD, Hernando D, Horng DE, Reeder SB. Quantitative susceptibility mapping in the abdomen as an imaging biomarker of hepatic iron overload. Magn Reson Med. 2015;74(3):673–83.